Collective motion with excluded-volume effects

Gayani Tennakoon

A thesis submitted in fulfilment of the requirements for the degree of Doctor of Philosophy in Mathematics, the University of Auckland, 2022.

Abstract

Many physical and biological systems consist of individuals with collective behaviour. In reality, these individuals have a finite size, or at least prevent others from interacting or becoming involved; hence, they exclude a volume in space. Volume exclusion can be considered the simplest possible interaction within a population. It plays an important role in determining transport properties from small-scale systems such as interior cell motion or ion channels to large-scale systems such as pedestrian motion or animal swarms. Individual-based models describe how interacting individuals give rise to collective behaviour; however, these models become computationally intractable for large systems. Our research aims to replace these expensive simulation models with continuum population-level models based on partial differential equations (PDEs). The diffusion of finite size hard-core interacting particles in one or two dimensions are examined systematically using asymptotic methods. The result is a coupled system of PDEs for the distribution functions of position, velocity and time. Due to size exclusion, the PDEs are nonlinear in the transport term.

Acknowledgements

First and foremost, I would like to express my sincere appreciation to my supervisor Dr Stephen W Taylor, for his support and guidance throughout this work. The continuous discussions with him during the period led to successful outcomes, inspiring me to pursue a career in research.

I am also indebted to Dr Tertius Ralph, a former student and my colleague, for his support and for having many productive discussions regarding this research. Another special thank should also go to Dr Marie Graff and Dr Andrus Giraldo for devoting their time to clarify some simulation techniques utilised in the thesis. I am blessed to be a part of this diverse mathematics research community at the University of Auckland, and I would like to thank all academic and professional staff for all the support given to me during the last few years.

Warmest gratitude to my parents, in-laws and friends for their blessings, encouragement, and love. Although many miles apart, they all spared their time to call me and see how I was doing. Last but certainly not least, I thank my beloved husband, Kushan, for the countless times he went out of his way to make sure I was happy and comfortable. He is the strong pillar behind me throughout the ups and downs of my journey.

Contents

1 Introduction

1.1 Excluded volume interactions

Many physical and biological systems consist of individuals with collective behaviour. In reality, these individuals have a finite size, and many living organisms tend to keep others at a distance; hence, they exclude a volume in space. Volume exclusion can be considered as the simplest possible interaction within a population. From small-scale systems such as interior cell motion or ion channels to large-scale systems like pedestrian motion or animal swarms, it influences the transport properties of diffusing particles through crowded conditions.
A short-range hard-core potential

$$\phi(r) = \begin{cases} \infty & d \leq 2r, \\ 0 & d > 2r, \end{cases}$$

where d is the inter-particle distance and $2r$ is the particles' diameter, is suitable for modelling excluded volume interactions in a system consisting of impenetrable spherical particles. Such systems classify as hard-sphere (HS) systems, which will be the subject of this thesis. A hard-sphere of radius r excludes a spherical volume of radius $2r$ around the sphere's centre as in Figure (1.1). When the particle concentration increases, this exclusion reduces the free volume in a hard-sphere system, which does not occur in a point particle system. Analysing such systems is our primary interest in the following three chapters. However, note that we do not allow penetrations; instead, a particle may

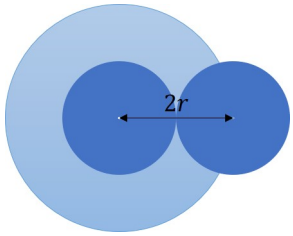

Figure 1.1: Excluded volume of radius $2r$ around the center of the sphere

have a chance to enter and leave the excluded region. This will allow us to model particle motion in a narrow channel by assuming that collisions occur with a certain probability; otherwise, particles can freely pass each other.

1.2 Theoretical approaches to HS systems

One of the intriguing questions is how to introduce a theoretically justified framework to analyse HS systems. A common approach is to incorporate volume exclusion to individual-based models (IBMs), also known as agent-based or microscopic models. IBMs treat each occupant as a discrete entity and describe their behaviour explicitly. This behaviour may include internal processes and interactions between individuals, which are mathematically explained by an evolution update rule given in the form of an algorithm or differential equation. For example, the application of overdamped Langevin stochastic differential equation (SDE) for cell chemotaxis with size exclusion [53]. IBMs are conceptually simple, linkable to experimental data and suitable for systems with a low number of occupants. However, in real applications, we find large systems of particles with complex behavioural patterns. At this stage, it is difficult to deal with IBMs as they are computationally intractable. This difficulty can be avoided by replacing them with continuum population-level models. Continuum models are responsive to large numbers as they consider group-level quantities rather than individual properties. For this reason, they might not capture details at discrete levels [86]; however, many preferred continuum over discrete scale because of their computational efficiency. Continuum models most commonly use partial differential equations (PDEs). For the derivation, one must consider the system variables such as number density or spatial population density. For instance, the overdamped Langevin SDE stated above has an associated Fokker-Planck (FP) equation in term of cell density [12].

Connecting individual and continuum levels is challenging and not evident in general, especially when the system includes particle-particle and particle-environmental interac-

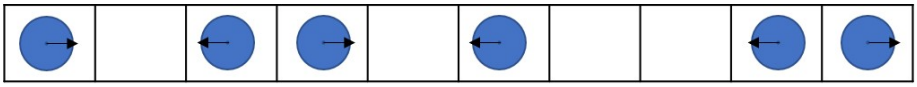

Figure 1.2: One-dimensional cellular automata consist of several uniform cells either occupied or empty.

tions. On the other hand, an individual-level model requires computationally intensive simulations to produce statistical results, and gain an accurate and deep understanding of population-level dynamics. Therefore many studies have focused on solely one of the two levels. Indeed one can either use a continuum model or a discrete model depending on the subject of relevance and available experimental data. Nevertheless, it is essential to understand the micro-macro link to get an insight into the diffusing systems.

1.2.1 Lattice-based models

In this section, we introduce modelling frameworks for lattice-based systems. We cite models like the cellular automaton and cellular potts to give insight into the vast on-lattice modelling techniques available in the literature. However, we avoid detailed explanations as this topic is not the scope of the present work.

Many studies have developed continuum models from interacting lattice-based models. These on-lattice IBMs restrict particles' motion to random walk on a grid. Two types of lattice-based models exist: interacting and non-interacting [68]. An interacting lattice-based model is the one that includes size exclusion during which the target site is occupied by, at most, a single particle; otherwise vacant. The simplest model is a random walk on the one-dimensional lattice with jumps (left/right) to the nearest vacant site [9]. In other words, a particle at site n will after one time step be either at site $n+1$ or at site $n-1$. The probabilities $P_n(t)$ of finding a particle at site n at time $t \geq 0$ obey the master equation,

$$\frac{dP_n}{dt} = W^+_{n-1}P_{n-1} + W^-_{n+1}P_{n+1} - (W^+_n + W^-_n)P_n \tag{1.1}$$

where $W^{\pm}_n$ are the nearest neighbour transition rates. By employing the Laplace transformation, one can find the long-time asymptotic behaviour of the average mean displacement.

Volume exclusion can be integrated to discrete space, velocity and time models, such as lattice gas automata (LGA), a special type of cellular automaton (CA). In a CA model, the discretised domain (grid or lattice) holds at most one particle at each lattice site and they evolve according to a set of rules based on neighbouring cells' states. The simplest is the one-dimensional updating rule (Figure (1.2)) known as elementary CA [105]. LGA differ somewhat from the CA as the update rule splits into collisions and propagation.

In other words, the microdynamics of LGA is described on a square or hexagonal lattice with updated rules for collision and propagation. They produce simplified models leading to mass and momentum conservation and yield the desired Navier-Stokes equation in the macroscopic limit [1], which was exploited to study complex fluid mechanics problems. In recent years, LGA has been applied in modelling pedestrian flows [65] and cell migration [59] incorporating size exclusion.

The Cellular Potts Model (CPM), which is also lattice-based, illustrates a modelling framework when the intercellular interactions are defined by the cell shape, size, and the area of the cell interfaces. Lushnikov et al. [53] established a connection between the stochastic cellular Potts model and the macroscopic nonlinear diffusion model. The cells are assumed to have a fluctuating rectangular shape, and the volume exclusion is imposed by setting the cell interaction potential to infinity during an overlap. The numerical solution to the macroscopic model agreed with Monte Carlo simulations of the microscopic model even for relatively large volume fractions. Both LGA and CPM are suitable to model cell-cell interaction and migration [33]. CPM catches the size fluctuation, thus suitable to study patterns of cells that often change the shape while LGA can simulate cells' movement in a correct and straightforward process.

Taylor et al. [96] studied a lattice model with volume exclusion implemented in each uniform compartment. A compartment may be occupied by a single particle (full exclusion), a finite number of particles (partially excluded/coarse-grained) or by infinitely many particles (no exclusion). The diffusion of particles is modelled as a series of jumps between compartments with jump rates

$$T_j^{\pm} = \frac{D}{(mh)^2}(1 - f^{(m)}(n_{j\pm1}^{(m)})) \tag{1.2}$$

where D is the diffusion coefficient, h is the particle length, $n_j^{(m)}$ is the number of particles in compartment j when each compartment has capacity m. The function $f^{(m)}$ specifies the proportion of jumps that fail due to the crowding effect. To clarify functional forms of this volume exclusion function, they consider equations for particle numbers' mean and variance derived from a master equation similar to (1.1). They observed a perfect agreement for the mean and variance between the full excluded and coarse-grained models. Later, the model was extended to study multi-scale systems, by considering non-uniform hybrid lattices [97]. Although the partially-excluding model reduced the computational cost, a one spatial dimension multi-species mix led the models to make irreconcilable

[1] Not all LGA models yield the Navier-Stokes equation in the macroscopic limit [104]

predictions in the fully-excluding and partially-excluding models [95]. Therefore, the authors reexamined the system in two spatial dimensions where mixing is possible and observed a good agreement in the models.

The continuum limit of an on-lattice hopping model in the context of multiple species leads to a system of nonlinear drift-diffusion equations with cross-diffusion [15, 87]. In the case of a single type of particle, the one-particle density function satisfies the Fokker Planck equation

$$\frac{\partial \rho}{\partial t} = \nabla \cdot (D\nabla\rho + \rho(1-\rho)\nabla F) \tag{1.3}$$

where D is the diffusion constant (independent of ρ) and F is the force acting on the particle. The first order closure approximation assumes independence between particles, and it is the simplest form of moment-closure. If the system is strongly correlated the assumption often generates errors in the population level model. In such a situation a higher order moment-closure approximation can be considered [5], where one has to deal with a series of unclosed coupled moment equations for each of the individuals' distribution that may be difficult to solve. The usual procedure is to close the system by setting the moments above a specific order equal to zero [34].

Some studies have used discrete space, continuous time master equation (1.1) with the volume filling approach [74]. In volume filling (a particle jumps to free spaces), the higher the density at a particular position, the less chance another particle accesses the same location; therefore, a new term for the probability of finding a space at its nearby location is introduced to the system. In particular, for the on-lattice cell density u and chemical concentration v, the transition rate $W_n^{\pm}$ takes the form

$$W_n^{\pm} = q(u_{n\pm1})(\alpha + \beta(\tau(v_{n\pm1}) - \tau(v_n))) \tag{1.4}$$

α, β are constants, τ represents the mechanism of signal detection and $q(u)$ is the probability of a particle finding space at its neighbouring site. As mentioned earlier, a master equation describes the probability of occupation; in the volume limitation, the continuum limit leads to a Keller-Segel (KS) type model. This method of establishing the micro-macro link is used in applications like ion transport through confined regions [16] and chemosensitive motion of a cell population [75].

KS models are widely used to describe aggregation [48] and pattern formation [41,101] in a cell population. However, the solution to the KS model in chemotaxis exists globally in time only if the mass is below its threshold, otherwise blows-up. Introducing a jumping probability q to the cross-diffusion term that depends on the density u at the position (volume-filling), Hillen and Painter prevent these blow-ups. In one dimension, every non-

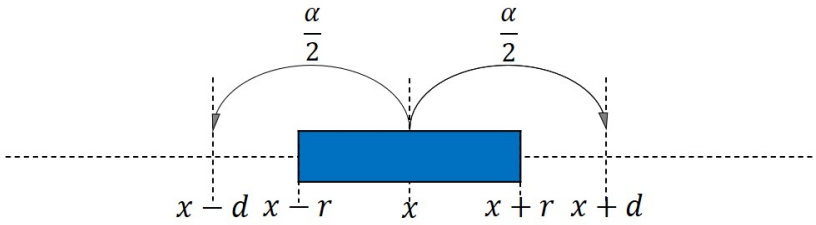

Figure 1.3: 1D hopping model where individuals' centre located at x move with a rate α, a distance d to the left or right

increasing q prevents blow-ups; however, in a higher dimension, existence depended on the choice of q.

1.2.2 Off-lattice models An off-lattice framework can also be employed to study IBMs. Here, particles do not jump on a lattice instead change its' position in a continuous space. Since this approach allows movement in any direction, IBMs capture the typical behaviour of cells and animals. Again, the challenge is to incorporate volume exclusion to the model.

Murray et al. investigated a one-dimensional spring-based model for interaction force being linear [63] and nonlinear [64]. The volume exclusion is introduced by denying the cells to pass the equilibrium distance, and the macroscopic limit produced a nonlinear diffusion equation. A mechanical spring model ignores stochasticity; hence the equations are deterministic. The resulting diffusion coefficient is compared with that derived by Lushnikov et al. [53] and found to be notably similar.

Dyson et al. [21] described an analytical approach to derive the continuum model from a one-dimensional off-lattice model. They considered an unbiased random walk where cell centres jump a distance d at a rate α. The idea is similar to the on-lattice hopping model, where particles only move to vacant sites, and at most, one particle can occupy the left or right site. However, a jump does not occur on a predefined grid (see Figure (1.3)). Later, Dyson and Baker [20] extended the ideas into two and three dimensions and incorporated the bias by assigning a higher probability for the favourable movement. The authors derive the continuum equations from the time evolution of the i^{th} cell centre's probability density function that closely resembles Brownian dynamics. Both studies make use of a moment-closure assumption where one of the lower order moments is set to zero.

Iron et al. [44] also considered an off-lattice framework with the above attempt-and-abort volume exclusion mechanism where overlaps abort when agent attempt to move with probability P_m. Although cells can migrate in a continuous space to preferred directions, the authors divide the domain into vertical strips of width Δ and calculate the average

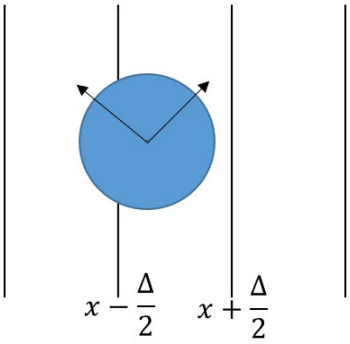

Figure 1.4: The spatial domain is discretised into strips of width Δ. The $C(x,t)$ is calculated by averaging the number of agents whose horizontal coordinate lies in the interval $\left[x - \frac{\Delta}{2}, x + \frac{\Delta}{2}\right)$ at time t, over number of realisations.

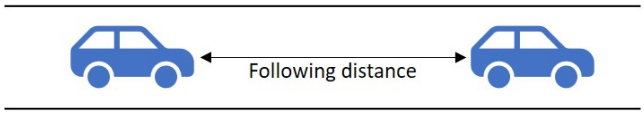

Figure 1.5: Maintain a distance between the rear and front bumpers of the preceding and the following vehicles respectively.

agent density $C(x,t)$ in the vertical direction so that the model simplifies the dynamics into a one-dimensional framework (see Figure (1.4)). They begin with an approximate conservation statement in terms of agents' density $C(x,t)$ in a strip and derive the mean-field nonlinear partial differential equation (PDE). Each term in the discrete conservation statement is interpreted as the product of P_m from a particular strip to a nearby and the probability that such an attempt will succeed ($P(C)$) during some time interval. Crowding effects in the mean-field description are represented by the function $P(C)$.
A continuum model may have limitations if the population size is low. As Tyagi [100] points out, the macroscopic variable *density* is defined for a sufficiently large number of particles; however, in traffic flows, the lanes might have a handful of vehicles which is inappropriate to model as a continuum using the notion of density. They consider the system as a countably infinite collection of homogenous, interconnected dynamical systems and model via a set of coupled ordinary differential equations. The interactions between vehicles occur according to *vehicle following behaviour* where the response is based on the state of the vehicle in front (see Figure (1.5)).

1.2.3 Brownian dynamics

Brownian motion is often used as a model for any movements or dynamics described as random, and it is the simplest stochastic model one can think of. As this topic is not our primary focus, we avoid full explanations, but definitions

can be found in various textbooks [36,102]. We are interested in the work on Brownian particles with excluded-volume effects that Bruna and Chapman [12] have already studied as we develop a method similar to their work. The authors introduced a method to a class of models consisting of diffusive particles with short-range interactions beginning with the overdamped Langevin stochastic differential Equation

$$dX_i(t) = f_i(\vec{X}(t))dt + \sqrt{2}dW_i(t) \tag{1.5}$$

which expresses the particle dynamics of a N-particles system. The centres of these spherical particles (diameter ϵ) are given by $X_i(t)$, $i = 1, ...N$ with the standard Brownian motions W_i. The above SDE has an associated FP equation (1.6) in term of the joint probability density function, which is high-dimensional and difficult to solve.

$$\frac{\partial P}{\partial t}(\vec{x}, t) = \vec{\nabla}_{\vec{x}} \cdot (\vec{\nabla}_{\vec{x}} P - \vec{F}(\vec{x})P) \tag{1.6}$$

Due to excluded volume effects, the above equation is defined in the hollow form of the domain (a domain with holes corresponding to overlaps). Under the low volume fraction (the ratio of the volume occupied by particles to the total volume) hypothesis, the authors apply the method of matched asymptotic expansions (MAE) to derive a nonlinear diffusion model from the particle-level model (1.6). The model can be thought of as a continuum equation derived from an off-lattice individual-based model and it is similar to what Dyson and Baker [20] obtained in their work under no external force. Lushnikov et al. [53], and Bodnar and Velazquez [11] are other studies that derive continuum limit starting from a stochastic equation similar to the Langevin equation. The former derived a KS type model which does not collapse in finite time, under higher volume fractions and the latter studies the limit equation under attractive and repulsive potentials; however, the macroscopic equation became ill-posed when the element for attractions was introduced. The above studies are limited to systems that resemble Brownian motion. In such systems, the particle velocity is ignored; the models focus on only the random path that particles follow.

1.3 Velocity jump processes

Behaviour in animal swarms and pedestrian flows are closely related to the random walk in the velocity, where individuals avoid each other without loss of energy. These events which have a spontaneous change in velocities can be described using transport equation

as it includes a term for the finite propagation speed. Transport equations are extensively used to study the motion of chemosensitive cells [4,71,92].

Throughout the thesis, we will repeatedly use the so-called velocity jump process, and the framework is presented in [71]. In a velocity jump process, stochastic changes are applied to the velocity rather than position. A particle may change its current velocity $\mathbf{v} \in V \subset \mathbb{R}^d$ at a small time-step dt with probability λdt, where λ is the turning frequency. This frequency may take different forms depending on various internal and external factors, which will be addressed later. The inverse is the mean run length time between the random choices of direction. Given that a jump occurred, a turning kernel $T(\mathbf{v}, \mathbf{u})$ defines the probability of a change in velocity from $\mathbf{u}$ to $\mathbf{v}$ (in the same velocity space V).

In light of the above information, the evolution of the density function $p(\mathbf{x}, \mathbf{v}, t)$ for individuals in 2d-dimensional ($d = 1, 2, ...$) phase space with coordinates $(\mathbf{x}, \mathbf{v})$, where $\mathbf{x} \in \Omega \subset \mathbb{R}^d$, is governed by the transport equation

$$\frac{\partial p}{\partial t} + \nabla_{\mathbf{x}} \cdot \mathbf{v} p(\mathbf{x}, \mathbf{v}, t) = \lambda \int_V T(\mathbf{v}, \mathbf{u}) p(\mathbf{x}, \mathbf{u}, t) d\mathbf{u} - \lambda p(\mathbf{x}, \mathbf{v}, t), \quad t \geq 0 \tag{1.7}$$

The above velocity jump process best describes the motion of flagellated bacteria such as E. coli that possess two behavioural modes; runs and tumbles. In one space dimension, this model recovers one of the earliest correlated random walk models proposed by Goldstein and Kac [35, 47]. When particles possess random motions with a constant speed, say c, and switch directions at an instantaneous time with an unbiased constant reversal rate λ, the authors write the following coupled hyperbolic system of PDEs,

$$\begin{aligned} \frac{\partial p^+}{\partial t} + c\frac{\partial p^+}{\partial x} + \lambda(p^+ - p^-) = 0 \\ \frac{\partial p^-}{\partial t} - c\frac{\partial p^-}{\partial x} + \lambda(p^- - p^+) = 0 \end{aligned} \tag{1.8}$$

where $p^{\pm} \equiv p(x, \pm c, t)$. By introducing the macroscopic density $\rho = p^+ + p^-$ and the flux $j = c(p^+ - p^-)$, the system reduces to a damped wave equation

$$\frac{\partial^2 \rho}{\partial t^2} + 2\lambda \frac{\partial \rho}{\partial t} = c^2 \frac{\partial^2 \rho}{\partial x^2} \tag{1.9}$$

In higher dimensions, when individuals change directions according to the turning kernel, the diffusion limit of the velocity jump process (1.7) is not straightforward. However, with appropriate scaling of space and time, the asymptotic behaviour of the transport model leads to its diffusion approximation [70]. At the same time, the turning kernel has to have

some properties that ensure the limit's existence. The macroscopic behaviour was further analysed by the same authors under a variety of biases in the turning rate and kernel, which led to either an anisotropic diffusion equation or a well-known KS type model [72]. We find various generalisations of the transport model (1.7). For instance, Erban and Othmer [26] introduced internal dynamics of E Coli bacteria to the microscopic model. Since these bacteria are chemosensitive, the internal state depended on an external signal and evolved according to an ordinary differential equation. They later generalised the analysis to a higher dimension [27] and applied it to a system which involves crawling cells [28] where the diffusion limit led to the classical macroscopic description for chemotaxis. Incorporation of a resting phase is another extension of the transport equation; this was investigated by Taylor-King et al. [98] for a group of swarm robotics: E-Puck. E-Puck robots also perform velocity-jumps; however, their tumbling time is not negligible as in cell migration. Therefore the authors introduced the time it takes for a particle to reorient from velocity $\mathbf{v}$ to $\mathbf{u}$ by a new function $K(\mathbf{v}, \mathbf{u})$ and included a resting state that defines the number of particles remaining in their turning time. They observed that models including finite turning delays match well with experimental data compared to the models without this delay.

Many previous velocity-jump processes are noninteracting; hence crowding effects are not taken into account. This means overlaps are permitted which is not realistic in a dense population. Treloar et al. [99] established a micro-macro link by incorporating three types of crowding interactions into a velocity-jump process. The first case is the simplest, where multiple agents on the same lattice site are prevented, similar to the on-lattice hopping models discussed earlier (see Figure (1.2)). In other cases, additional conditions are imposed apart from the first. They derived a system of advective PDEs in each case from the discrete conservation statements that describe the evolution of the subpopulations (left and right moving agents). The simulations for micro-macro comparison were performed on a one-dimensional lattice at a particular velocity. However, these models are lattice-based and may not be realistic in some scenarios, as the mechanism allows individuals to jump across. Also, the approximation restricts the choice of the model parameters and the initial condition.

Gavagnin and Yates [32] relaxed the above restrictions and generalized the model on a two-dimensional lattice to connect the microscopic model with the macroscopic description via the diffusive limit. A positive integer is interpreted as the agent's velocity, where magnitude is given by the number of lattice sites moved during a single movement event. An agent can move or reorient itself as independent Poisson processes with different intensities. They scale an additional parameter φ to bias the motion along the chosen

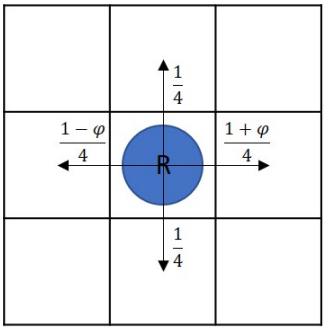

Figure 1.6: An R-polarised agent with unit velocity (jump one lattice site) has four potential configurations when a movement occurs with bias φ.

direction (see Figure (1.6)), considering four different exclusion properties consistent with that of Treloar et al. [99]. The diffusion limit leads to a series of coupled generalized diffusion equations consisting of an advective and a reactive term. Agreement between the continuum and discrete profiles holds for any arbitrary reorienting rates which were not achievable in Treloar's work.

Franz et al. [31] analysed the transport equation for N interacting hard-spheres in higher dimensions where the reflective (speed preserving) collisions dominate. The speed is a constant and the velocity jumps are defined as in the equation (1.7); therefore, this work's ideas are significantly linked to our work. The authors reduce the higher-dimensional PDE to a low-dimensional allowing the collision boundary term to be absorbed into the turning rate from three methods: under molecular chaos assumption, Boltzmann integral; an adjusted velocity-jump process using Cattaneo approximation; and an alternative transport equation with a correction term using matched asymptotic expansion. The effective diffusion properties investigated in this paper are consistent with those for Brownian particles studied in [12]. Estrada-Rodriguez and Gimperlein [29] obtained the macroscopic description of swarm robotics, starting from the kinetic equation, that incorporates alignment, collisions and long runs according to a Levy distribution. Unlike in Taylor-King et al. [98] work, this study assumes that tumbles are instantaneous; thus, no delays in turnings. However, both studies neglected the interdependence between individuals' velocities as the experiments were conducted under low robot density.

By following the ideas from [7,12], Ralph et al. [81] derived a model for chemotaxis with hard-core interactions. The author examined how the finite size of individuals affect the behaviour of groups of particles moving according to a velocity jump process in one dimension. The particles are identical hard rods that run back and forth with constant speed in a fixed-length single-file channel while interacting through reflective collisions. The velocity changes are controlled by a chemical gradient, meaning longer runs along

favourable directions with fewer turns. The author performed an asymptotic analysis of the associated transport equation using the method of MAE in the limit that the volume fraction of particles is small, and verified that the nonlinear PDE model captures the stochastic properties of the N-particle system.

1.3.1 Turning frequency Although the hyperbolic model was a notable explanation for biological interactions among individuals, with constant turning rates, it limits the knowledge about how correlation depends on the internal and external factors. In particular, the turns may occur due to the influence of conspecific densities or external signal (food/toxin). Thus more complicated models have been derived, incorporating more involved turning frequencies.

When nearby individuals' densities (e.g. left and right moving densities) directly influence the interactions, a density-dependent turning rate of the form $\lambda^{\pm} = \mu + \mu^{\pm}(p^+, p^-)$ (where turning rate μ is for independent turnings and $\mu^{\pm}(p^+, p^-)$ are for right and left turnings due to interactions) can be introduced to systems like (1.8) to investigate the formation and movement of bacterial aggregations. These models are capable of describing the rippling behaviour of bacteria such as myxobacteria [54]. In contrast, an extracellular signal (attractant/repellent) can cause indirect interactions among organisms; hence, the turning rates may depend not only on the signal S alone but also on the spatial gradient of S. In the presence of such non-vanishing signal gradient, $\lambda^+ \neq \lambda^-$ and particles will move in the direction of an increasing gradient resulting in a prolonged run-phase. Hillen and Stevens [42] investigated a slightly complicated form of (1.8).

$$\frac{\partial p^+}{\partial t} + c\frac{\partial p^+}{\partial x} + \lambda^+(S, S_x)p^+ - \lambda^-(S, S_x)p^- = 0 \tag{1.10a}$$

$$\frac{\partial p^-}{\partial t} - c\frac{\partial p^-}{\partial x} + \lambda^-(S, S_x)p^- - \lambda^+(S, S_x)p^+ = 0 \tag{1.10b}$$

$$\tau\frac{\partial S}{\partial t} - D\frac{\partial^2 S}{\partial x^2} - f(S, p^+ + p^-) = 0 \tag{1.10c}$$

where last equation describes the production, decay and diffusion of the external signal S. The authors established the global existence of positive solutions from positivity and boundedness of the turning rates. However, during the process of examining finite time blow-up solutions for the model, Hillen and Levine[40] observed that turning rates may vanish (*zero-turning-rate*) before the solution blows up, which leads to negative densities for $p^{\pm}$. They considered the following forms for turning rates based on the previous

experimental observations.

$$\lambda_1^{\pm} = \frac{c}{2D}(c \mp \chi(S)S_x) \tag{1.11a}$$

$$\lambda_2^{\pm} = \frac{c^2}{2D} exp\big(\mp \frac{\chi(S)}{c} S_x\big) \tag{1.11b}$$

where D is the diffusion coefficient, $c \in \mathbb{R}^+$ is the speed and χ is the chemotactic sensitivity coefficient. The former is suitable for shallow chemical gradients, or small chemotactic sensitivities, or higher speed while maintaining the positivity of the turning rate. The later is the most realistic model assumption which agreed well with the experimental observations.

1.4 Our research

1.4.1 Motivation and Intention Reviewing previous studies on collective dynamics and self-organisation in the physical and biological sciences, we understand the importance of advanced mathematical frameworks to capture fundamental characteristics in a system. Among these features, the excluded-volume effect is the simplest possible interaction arising from the mutual impenetrability of finite-size particles, and we recognised how this effect was incorporated into two classical modelling approaches: IBMs and continuum models.

In this thesis, we develop a method similar to studies [31] and [81], to analyse the impact of collisions between individuals on the behaviour of groups of particles, driven according to a velocity jump process. The ideas of the former study are applicable when analysing the two-dimensional model, while the latter is closely related to the one-dimensional model. In particular, we too examine a hard-core N-particle system, which gives rise to the so-called excluded volume effects that influence population dynamics; though, we change some aspects of the interacting systems.

Our model contains particles with unidirectional motion and instantaneous velocity changes, much like Ralph's model. However, the particles are now hard disks or spheres, and the domain is a fixed-length narrow channel where occupants are allowed to cross each other while collisions occur at random. During a pass, one particle has access to another particle's excluded region; therefore, an interaction occurs through interface conditions. This kind of setup is more vivid as individuals moving with constant speed will meet head-on or pass one another if there is enough space. Examples where particles are driven in a domain confined to a narrow channel, include various biological systems [8,67,85]

and polymer solutions [37,50]. The assumptions of a narrow channel are reasonable to model even pedestrian motion as unexpected contacts may occur on a pedestrian crossing [77,79].

We suppose that there are no electrostatic or hydrodynamic interaction forces between particles since our primary focus is on excluded volume effects. Once the particle-level model is set, the goal is to find a system that models the motion of a single particle, that is, the marginal density function with independent variables being the position, velocity and time of a single particle. To this end, we perform an asymptotic analysis of the associated transport equation under the low volume fraction assumption.

The system for the two-dimensional model can also be defined in a similar fashion, but rather than considering reflective collisions this time, as specified by Franz et al., we suppose an exchange of velocities after a collision. By doing so, we simplify the asymptotic analysis. For elastic or reflective collisions, one has to use the method of MAE and determine the terms in the collision integral [2]. Furthermore, they examine models employing a constant turning rate with an unbiased turning kernel, which is not the case in our models.

We consider velocity changes that are biased according to the individual's environment. In other words, the movement of an organism in response to a stimulus, a taxis. In particular, we consider chemotaxis, which is a directed motion along a chemical gradient. There are other types of taxes; for instance, Ha and Levy derive a hierarchy of mathematical models for phototactic bacteria (stimulation by light) employing a similar turning operator as in chemotaxis [38]. Mazzag et al. [58] incorporate experimental observations of the aerotactic bacteria (stimulation by oxygen) into a mathematical model similar to Goldstein and Kac; yet, chemotaxis is the most intensely studied by far [73].

To analyse the models derived in this thesis, we consider the following form of λ (similar to (1.11a)):

$$\lambda(\vec{x}, \vec{v}) = \lambda_0 - \chi(S)\vec{v} \cdot \nabla S(\vec{x}) \tag{1.12}$$

where λ_0 is a constant base-line turning frequency and $\vec{v}$ is the velocity. The term $\chi(S)\nabla S(\vec{x})$ describes the change in the turning frequency in the presence of an external chemical gradient. When $\chi > 0$, the stimulus S can be a chemoattractant which leads to a positive taxis. A particle is less likely to change direction when moving in a favourable direction; hence, returns a lower value for λ. The sample signal functions for

[2] Franz et al. [31] introduced MAE similar to what can be seen in [12]. However, due to the velocity component, the leading order terms in the asymptotic analysis may disagree at the collision boundaries.

S are taken from the the paper [26].

1.4.2 Outline of the thesis *Chapter 2* presents our core model, a system of N identical hard-core particles with unidirectional motion in a bounded narrow channel whose dimensions are large compared to the particles' size. This chapter allows us to introduce the method and techniques used in the subsequent chapters. Due to size exclusion, we find PDEs that are nonlinear in the transport term. To validate the model, we compare the numerical solutions of the PDE model with simulations of the full-particle model.
In *Chapter 3*, We extend our core model from identical particles to different particles, mainly two species. We call them blues and reds. Particles within one group are all identical, but a blue and a may red have different sizes. Our analysis at the particle-level model now produces a coupled system of nonlinear transport equations for the two one-particle densities. The equations incorporate terms from both interspecies and intraspecies interactions. We also take one species as an obstacle and study the diffusion of the other through the obstacle.
Going back to the N identical hard spheres system, we introduce resting particles in *Chapter 4*. That is, a finite-sized particle moving back and forth with a constant speed may suddenly stop its motion and enter into a resting state. We derive equations for both the collision and the narrow channel systems with symmetric and non-symmetric turning rates. Once again, we validate the models comparing the numerical solutions with their respective stochastic simulations of the full-particle system.
We carry the fundamental ideas from the collision model in [81] and create the two-dimensional problem in *Chapter 5*. In particular, the system has N identical hard-core particles moving with constant speed in a two-dimensional bounded domain. Particles switch their velocities due to collisions between each other or with the domain walls. Besides collisions, direct reversals occur according to an independent Poisson process. Under the low volume fraction assumption, we derive the population-level model analogous to those one-dimensional nonlinear PDEs derived earlier.

2

Velocity-jump process in a narrow channel

2.1 Introduction

In this chapter, we analyse our main model: a system of N identical hard cores (spheres or discs) on a narrow geometric configuration. The physical space is essentially a channel in $\mathbb{R}$ with a probability of occupants being able to pass each other. The system mimics what nature does, where individuals pass one another in a narrow channel while making incidental contact with those moving in the opposite direction. The passing probability depends on the size of the particles and the width of the channel. The extreme case in which particles' diameter is equal to the width of the channel is the so-called single-file diffusion [55]. One can also view this as a problem of finite-size particles diffusing through a confined domain; however, it is not to be confused with the particle densities being dependent on the vertical position [14].

Many examples of mathematical and computational efforts to understand confined domain systems solely focused on either stochastic models [19,43] or continuum population-level models developed for Brownian colloidal [3,14]. We establish the micro-macro link to a velocity jump process in a narrow channel, where waiting times between velocity jumps are exponentially distributed [71]. A single-file velocity jump process has already been examined [81]; the correlated motion with the ability of particles to bypass one another that was ignored in this work has now become important in the present work. The

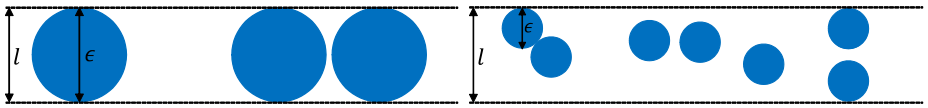

Figure 2.1: (a) A single-file channel where particle's diameter is same as the width of the channel. (b) A narrow channel where particles crossover and easily change order.

occupants exclude a volume in the channel, but in the passing regime, the occupied regions behave as interfaces that are no longer excluded; hence the interactions occur via interface conditions.

We begin in section (2.2) by writing down the particle-based description of the system, which consists of an N-dimensional PDE for the joint probability density function in the probability space.

2.2 Particle level model

In this section, we describe the stochastic system in compact velocity space with constant speed. We neglect the effect of background noise and assume that the system does not have external forces which restrict or prevent the particles' motion and turn velocity back to zero. The system has N interacting particles in a one-dimensional domain that does not change through time, meaning there is no birth/death. The particles are identical hard spheres of diameter ϵ and move either left or right with a constant speed $c \in \mathbb{R}^+$. In other words, the velocity space $V = \{-c, c\}$. The bounded domain $\Omega = [0, L]$ is the space available to a particle centre and for any particle centre $X_i(t) \in \Omega$ at time $t \geq 0$ with velocity $V_i(t) \in V$, we write the relation

$$\frac{dX_i}{dt} = V_i.$$

The stochastic changes are applied to the particle's velocity rather than to its position in space; therefore, a particle switches its direction based on N independent Poisson processes with rates $\lambda(x, v) > 0$. Collisions with another particle or with the domain wall may also change the velocity; however, we expect fewer collisions when the domain dimensions are larger than the particle's size. Due to unidirectional motion, particles will only interact with the left and the right ends of the domain. During a head-on collision, the initial velocities, say c and $-c$ of two interacting individuals will be reflected at a distance ϵ, and these collisions are both energy and momentum preserving, which

will not be the case in our two-dimensional model. The other important assumption is that particles occupy a small volume of the one-dimensional domain, so that pairwise interactions are dominated.

The equivalent PDE description in terms of the joint probability density function $P(\vec{x}, \vec{v}, t)$ for N particles to be found at the position $\vec{x} = (x_1, ..., x_N)$ with velocity $\vec{v} = (v_1, ..., v_N)$ at time t, given by

$$\frac{\partial P}{\partial t} + \vec{v} \cdot \nabla_{\vec{x}} P + \sum_{i=1}^{N} \big(\lambda(x_i, v_i) P(\vec{x}, \vec{v}, t) - \lambda(x_i, -v_i) P(\vec{x}, s_i \vec{v}, t)\big) = 0, \tag{2.1}$$

where $\nabla_{\vec{x}}$ stands for the gradient with respect to the N-particle position vector $\vec{x} \in \Omega^N$, $\vec{v} \in V^N$ and s_i is the operator for the velocity change in the i^{th} particle. The third (fourth) term is the loss (gain) due to the velocity jumps with the switching rate $\lambda(x_i, v_i) = \lambda_0 - \chi v_i D_{x_i} S(x_i)$, the one-dimensional form of (1.12). In the passing regime, the excluded area $\{\vec{x} \in \Omega^N : |x_i - x_j| \leq \epsilon, \forall i \neq j\}$ act as an interface where P has jumps at $x_i \pm \epsilon$, $\forall i$.

We now proceed to address the necessary initial and boundary conditions. If all the particles are initially distributed independently and identically in the domain, the initial condition

$$P(\vec{x}, \vec{v}, 0) = P_0(\vec{x}, \vec{v}) \tag{2.2}$$

is invariant to permutations of the particle labels; however, they do not preserve their initial ordering as the finite-size particles can pass each other.

The wall-particle boundary condition can be written as,

$$P(\vec{x}, \vec{v}, t) = P(\vec{x}, s_i \vec{v}, t) \quad \text{for} \quad x_i = 0, L. \tag{2.3}$$

Inside the domain, particles collide with probability δ, otherwise move independently. This collision probability is another small parameter that depends on the particle size and the channel width (say l) in a particular modelling situation. Here, we treat δ as an independent parameter. During a bypass, a particle can access one's excluded region from the left and right ends; consequently, an interface condition will replace the collision boundary condition. The one-dimensional domain with these interface conditions mimics particles' motion in a narrow channel. We detail these conditions in the following section.

Finally, $P(\vec{x}, \vec{v}, t)$ satisfies the normalization condition,

$$\int_{\Omega^N \times V^N} P(\vec{x}, \vec{v}, t) d\vec{x} d\vec{v} = 1 \tag{2.4}$$

The equation (2.1) together with the above conditions defines the individual-based model which is higher dimensional; hence difficult to solve directly.

2.3 Population level model

The aim is to reduce the higher-dimensional PDE for the joint density $P(\vec{x}, \vec{v}, t)$ to a low-dimensional PDE for the marginal density of a single particle which is the population-level model for $p(x, v, t)$. We begin with the transport equation for two particles and integrate it with respect to the configuration domain. Then through a systematic asymptotic expansion we derive a nonlinear hyperbolic equation for the marginal density.

2.3.1 Point particles Consider the simple case when $\epsilon = 0$. The domain Ω^N has no holes and particles are independent. Therefore, inserting

$$P(\vec{x}, \vec{v}, t) = \prod_{i=1}^{N} p(x_i, v_i, t)$$

in the transport equation, we get the evolution equations for the one-particle density functions $p^{\pm} \equiv p(x, \pm c, t)$ as

$$\frac{\partial p^+}{\partial t} + c\frac{\partial p^+}{\partial x} + \lambda^+(x)p^+ - \lambda^-(x)p^- = 0 \tag{2.5a}$$

$$\frac{\partial p^-}{\partial t} - c\frac{\partial p^-}{\partial x} + \lambda^-(x)p^- - \lambda^+(x)p^+ = 0 \tag{2.5b}$$

with the initial condition

$$p(x, v, 0) = p_0(x, v)$$

and the boundary conditions on the domain wall $x = 0, L$

$$p^{\pm}(x, t) = p^{\mp}(x, t)$$

The above system does not contain any confinement parameters. In fact, it is similar to that of Goldstein and Kac [35, 47], except now the turning rate is a function of x which can be replaced by the one-dimensional form of (1.12). Consequently, in terms of the total density $\rho(x,t) = p^+ + p^-$ and the flux $j(x,t) = c(p^+ - p^-)$, system (2.5) can be re-written as

$$\frac{\partial \rho}{\partial t} + \frac{\partial j}{\partial x} = 0 \tag{2.6a}$$

$$\frac{\partial j}{\partial t} + c^2 \frac{\partial \rho}{\partial x} - 2c^2 \chi \frac{\partial S}{\partial x} \rho + 2\lambda_0 j = 0 \tag{2.6b}$$

Differentiating (2.6a) with respect to time t and (2.6b) with respect to space x, we eliminate j and derive the telegraph equation

$$\frac{\partial^2 \rho}{\partial t^2} + 2\lambda_0 \frac{\partial \rho}{\partial t} = c^2 \frac{\partial^2 \rho}{\partial x^2} - 2c^2 \frac{\partial}{\partial x}\left(\rho \chi \frac{\partial S}{\partial x}\right) \tag{2.7}$$

Then taking the limit $\lambda_0 \to \infty$ and $c \to \infty$ in such a way that $\frac{c^2}{2\lambda_0} (= D)$ held constant results the following PKS (Patlak-Keller-Segel) type diffusion model [70].

$$\frac{\partial \rho}{\partial t} = D \frac{\partial^2 \rho}{\partial x^2} - \frac{c^2}{\lambda_0} \frac{\partial}{\partial x}\left(\rho \chi \frac{\partial S}{\partial x}\right) \tag{2.8}$$

We will compare (2.8) with the diffusion equation for finite-size particles in our subsequent analysis.

2.3.2 Finite-size particles When $\epsilon > 0$, the domain Ω^N has holes and particles are no longer independent. We find configurations in which two or more particles are approaching each other; however, in the low volume fraction regime, the volume in the integration space occupied by two particles dominates. A simple physical explanation in terms of geometric ideas will help to understand this statement.

As illustrated in Figure (2.1), consider a narrow flattened pipe where cores of the occupants are separated by $\mathcal{O}(\epsilon)$. Then the volume in the configuration space corresponding to when two disks are close to each other is $\mathcal{O}(\epsilon^2 N)$ (for $N-1$ pair interactions) whereas for three disks it is $\mathcal{O}(\epsilon^4 N^2)$ (for $(N-1)(N-2)/2$ triplets). Therefore, the dominant contribution to collisions corresponds to two-particle interactions. Consequently, instead of integrating the transport equation (2.1) over N-dimensional configuration space, we can illustrate the method for two-particle interactions and later extend for N.

We begin with two identical particles of diameter ϵ at position x_1 with velocity v_1 and at

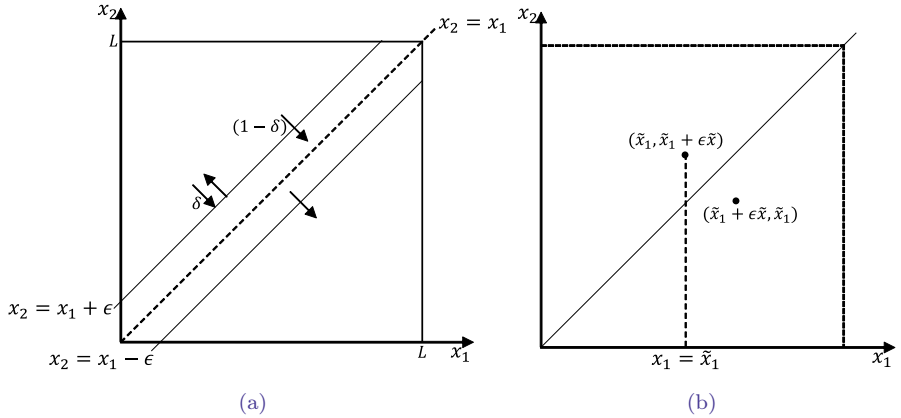

Figure 2.2: (a) Schematic of the excluded area $|x_1 - x_2| < \epsilon$ in the integration domain $[0, L]$ which is accessible to a second particle with the probability $1 - \delta$. (b) The boundary layer coordinates in the regions $x_1 < x_2$ (upper left) and $x_1 > x_2$ (lower right).

position x_2 with velocity v_2, which satisfy the transport equation

$$\frac{\partial P}{\partial t} + v_1\frac{\partial P}{\partial x_1} + v_2\frac{\partial P}{\partial x_2} + \lambda(x_1, v_1)P(\vec{x}, \vec{v}, t) - \lambda(x_1, -v_1)P(\vec{x}, -v_1, v_2, t) + \lambda(x_2, v_2)P(\vec{x}, \vec{v}, t) - \lambda(x_2, -v_2)P(\vec{x}, v_1, -v_2, t) = 0 \tag{2.9}$$

in the configuration space (2.2(a)). This configuration space is different from both the single-file channel and the independent-particle situation. In the former $(x_1-\epsilon, x_1+\epsilon)$ is an illegal configuration, while the latter does not have such regions. In the current situation, the second particle passes this inner region with the probability $1 - \delta$; otherwise, bounce back. Therefore, when particle one is at x_1, the space available for the second particle's centre is still $\Omega = [0, L]$, but with discontinuities at $x_1 \pm \epsilon$. We now write the conditions for the two particles that explain the situation near interfaces.
At the right interface,

$$P(x_1, x_1^+ + \epsilon, -c, c, t) = \delta P(x_1, x_1^+ + \epsilon, c, -c, t) + P(x_1, x_1^- + \epsilon, -c, c, t) \tag{2.10a}$$
$$P(x_1, x_1^- + \epsilon, c, -c, t) = (1 - \delta)P(x_1, x_1^+ + \epsilon, c, -c, t) \tag{2.10b}$$

and at the left interface,

$$P(x_1, x_1^- - \epsilon, c, -c, t) = \delta P(x_1, x_1^- - \epsilon, -c, c, t) + P(x_1, x_1^+ - \epsilon, c, -c, t) \tag{2.11a}$$
$$P(x_1, x_1^+ - \epsilon, -c, c, t) = (1 - \delta)P(x_1, x_1^- - \epsilon, -c, c, t) \tag{2.11b}$$

where $\delta \equiv \delta(\epsilon, l)$.

2.3.2.1 Integrated equation

Let us now integrate equation (2.9) over $\Omega \times V$ and derive the population-level model in terms of the marginal density p, where

$$p(x_1, v_1, t) = \int_{\Omega \times V} P(x_1, x_2, v_1, v_2, t) dx_2 dv_2$$

We rewrite the integral over subintervals $[0, x_1 - \epsilon)$, $(x_1 - \epsilon, x_1 + \epsilon)$ and $(x_1 + \epsilon, L]$ where necessary because the joint density function P has jumps at $x_1 \pm \epsilon$.
Begin by integrating the first term of (2.9) simply yields,

$$\int_{\Omega \times V} \frac{\partial P}{\partial t} dx_2 dv_2 = \frac{\partial p}{\partial t} \tag{2.12}$$

since the domain is independent of t. The integration of the second term of (2.9) requires the use of the Leibniz integral rule as each of the subinterval has an upper or lower limit that depends on x_1.

$$\int_{\Omega} \frac{\partial P}{\partial x_1} dx_2 = \frac{\partial}{\partial x_1} \int_{\Omega} P dx_2 + P(x_1, x_2, \vec{v}, t)|_{x_2 = x_1^- - \epsilon}^{x_2 = x_1^+ + \epsilon} - P(x_1, x_2, \vec{v}, t)_{x_2 = x_1^+ - \epsilon}^{x_2 = x_1^- + \epsilon}$$

The integral over v_2 is the summation over $\{-c, c\}$. That is,

$$\int_{\Omega \times V} v_1 \frac{\partial P}{\partial x_1} dx_2 dv_2 = \sum_{v_2 \in \{-c, c\}} v_1 \int_{\Omega} \frac{\partial P}{\partial x_1} dx_2$$

Hence, the second term of (2.9) reads

$$\begin{aligned} \int_{\Omega \times V} v_1 \frac{\partial P}{\partial x_1} dx_2 dv_2 = v_1 \frac{\partial p}{\partial x_1} + \sum_{v_2 \in \{-c, c\}} v_1 \Big(& P(x_1, x_2, \vec{v}, t)|_{x_2 = x_1^- - \epsilon}^{x_2 = x_1^+ + \epsilon} \\ & - P(x_1, x_2, \vec{v}, t)|_{x_2 = x_1^+ - \epsilon}^{x_2 = x_1^- + \epsilon} \Big) \end{aligned} \tag{2.13}$$

The third term of (2.9) generates

$$\begin{aligned}\int\limits_{\Omega\times V} v_2\frac{\partial P}{\partial x_2}dx_2dv_2 &= \int\limits_{\Omega}\sum_{v_2\in\{-c,c\}} v_2\frac{\partial P}{\partial x_2}dx_2\\ &= \sum_{v_2\in\{-c,c\}} v_2\Big(P(x_1,x_2,\vec{v},t)|_{x_2=0}^{x_2=x_1^-(x_1)-\epsilon}\\ &+ P(x_1,x_2,\vec{v},t)|_{x_2=x_1^+(x_1)-\epsilon}^{x_2=x_1^-(x_1)+\epsilon} + P(x_1,x_2,\vec{v},t)|_{x_2=x_1^+(x_1)+\epsilon}^{x_2=L}\Big)\end{aligned}$$

Using the wall-particle boundary conditions,

$$\sum_{v_2\in\{-c,c\}} v_2P(x_1,0,v_1,v_2,t)=0$$

and

$$\sum_{v_2\in\{-c,c\}} v_2P(x_1,L,v_1,v_2,t)=0$$

Consequently the third term simplifies to

$$\int\limits_{\Omega\times V} v_2\frac{\partial P}{\partial x_2}dx_2dv_2 = \sum_{v_2\in\{-c,c\}} -v_2\left(P(x_1,x_2,\vec{v},t)|_{x_2=x_1^-(x_1)-\epsilon}^{x_2=x_1^+(x_1)+\epsilon} - P(x_1,x_2,\vec{v},t)|_{x_2=x_1^+(x_1)-\epsilon}^{x_2=x_1^-(x_1)+\epsilon}\right) \quad (2.14)$$

The integral of the last term of (2.9) vanishes as for any v_1

$$\sum_{v_2\in\{-c,c\}} \lambda(x_2,v_2)P(\vec{x},\vec{v},t)-\lambda(x_2,-v_2)P(\vec{x},v_1,-v_2,t)=0$$

and the remaining term $\lambda(x_1,v_1)P(\vec{x},\vec{v},t)-\lambda(x_1,-v_1)P(\vec{x},-v_1,v_2,t)$ results

$$\begin{aligned}\int\limits_{\Omega\times V} \lambda(x_1,v_1)P(\vec{x},\vec{v},t)-\lambda(x_1,-v_1)P(\vec{x},-v_1,v_2,t)dx_2dv_2 =\\ \lambda(x_1,v_1)p(x_1,v_1,t)-\lambda(x_1,-v_1)p(x_1,-v_1,t)\end{aligned} \quad (2.15)$$

Now by adding (2.13) and (2.14), the right hand side yields

$$v_1\frac{\partial p}{\partial x_1} + \sum_{v_2\in\{-c,c\}} (v_1-v_2)\left(P(x_1,x_2,\vec{v},t)|_{x_2=x_1^+(x_1)-\epsilon}^{x_2=x_1^+(x_1)+\epsilon} - P(x_1,x_2,\vec{v},t)|_{x_2=x_1^+(x_1)-\epsilon}^{x_2=x_1^-(x_1)+\epsilon}\right)$$

From the summation term above, we get two separate terms $(v_1 + c)[...]$ and $(v_1 - c)[...]$; since v_1 also has the same two choices for the velocity, the above equation reduces to

$$v_1 \frac{\partial p}{\partial x_1} + 2v_1 \left(P(x_1, x_2, v_1, -v_1, t)|_{x_2 = x_1^- - \epsilon}^{x_2 = x_1^+ + \epsilon} - P(x_1, x_2, v_1, -v_1, t)|_{x_2 = x_1^+ - \epsilon}^{x_2 = x_1^- + \epsilon} \right) \tag{2.16}$$

Combining equations (2.12), (2.15) and (2.16) we find the integral of the equation (2.9) over $\Omega \times V$ as

$$\begin{aligned} \frac{\partial p}{\partial t} + v_1 \frac{\partial p}{\partial x_1} + 2v_1 \left(P(x_1, x_2, v_1, -v_1, t)|_{x_2 = x_1^- + \epsilon}^{x_2 = x_1^+ + \epsilon} + P(x_1, x_2, v_1, -v_1, t)|_{x_2 = x_1^- - \epsilon}^{x_2 = x_1^+ - \epsilon} \right) + \\ \lambda(x_1, v_1) p(x_1, v_1, t) - \lambda(x_1, -v_1) p(x_1, -v_1, t) = 0 \end{aligned} \tag{2.17}$$

The joint density P is not specified at the interfaces, but we expect an expression for P that is uniformly valid over the entire interval $[0, L]$. For freely moving particles, we may take $P(x_1, x_2, v_1, v_2, t) = p(x_1, v_1, t)p(x_2, v_2, t)$ (closure approximation); however, this approximation is invalid for a correlated system. Therefore we seek a more reliable interpretation for P asymptotically.

2.3.2.2 Evaluating the terms at the interfaces

An asymptotic expansion allows us to find an approximate P which does not breaks down in the interval $(x_1 - \epsilon, x_1 + \epsilon)$. We implement the idea that when two particles are far apart ($|x_1 - x_2| \gg \epsilon$), they are independent, whereas when they are close to each other ($|x_1 - x_2| \sim \epsilon$), they are correlated. So we identify two interior layers at $x_1 + \epsilon$ and at $x_1 - \epsilon$. Note that, when x_1 is close to $\partial\Omega$, it creates a boundary layer at $\partial\Omega$; however, since we assume that the length of the domain is higher than the particle's diameter, we may ignore this boundary layer.

In the outer region, where one particle lies further from the other particle ($|x_2 - x_1| \gg \epsilon$) define $P_{out}(x_1, x_2, v_1, v_2, t) = P(x_1, x_2, v_1, v_2, t)$. Since particles are identical and independent to leading order, for some distribution function q, we define the outer solution with δ dependency. Indeed, we may think of δ as a small parameter that depends on ϵ.

$$P_{out}(x_1, x_2, v_1, v_2, t) = q(x_1, v_1, t)q(x_2, v_2, t) + \delta P_{out}^{(1)}(x_1, x_2, v_1, v_2, t)$$

In the correlated region, we introduce the boundary layer coordinates $x_1 = \tilde{x}_1$ and $x_2 = \tilde{x}_1 + \epsilon\tilde{x}$ (see Figure 2.2(b)). Then the interface conditions (2.10) and (2.11) change

accordingly, such that

$$\begin{aligned}\tilde{P}(\tilde{x}_1,\tilde{x},v_1,v_2,t)|_{\tilde{x}=1^-}^{\tilde{x}=1^+} &= \delta\tilde{P}(\tilde{x}_1,1^+,c,-c,t)\\ \tilde{P}(\tilde{x}_1,\tilde{x},v_1,v_2,t)|_{\tilde{x}=-1^-}^{\tilde{x}=-1^+} &= -\delta\tilde{P}(\tilde{x}_1,-1^-,-c,c,t)\end{aligned} \tag{2.18}$$

Expanding the outer solution in terms of the inner variables, we get

$$P_{out}(\tilde{x}_1,\tilde{x},v_1,v_2,t) = q(\tilde{x}_1,v_1,t)q(\tilde{x}_1,v_2,t) + \epsilon\tilde{x}q\frac{\partial q}{\partial\tilde{x}_1} + \delta P_{out}^{(1)} + \delta\epsilon\tilde{x}\frac{\partial P_{out}^{(1)}}{\partial\tilde{x}_1} + ... \tag{2.19}$$

When $v_2 = -v_1$, the appropriate expansion for the boundary layer solution is in powers of δ; $\tilde{P}(\tilde{x}_1,\tilde{x},v_1,v_2,t) \approx \tilde{P}_0(\tilde{x}_1,\tilde{x}_1+\epsilon\tilde{x},v_1,v_2,t) + \delta\tilde{P}_1(\tilde{x}_1,\tilde{x}_1+\epsilon\tilde{x},v_1,v_2,t) + ...$ that matches with the outer solution at the interfaces as well as $|\tilde{x}| \to \infty$. Substituting the expansions into (2.18), the $\mathcal{O}(1)$ and $\mathcal{O}(\epsilon)$ terms yield

$$\tilde{P}_0 = q(\tilde{x}_1,v_1,t)q(\tilde{x}_1,v_2,t) + \epsilon\tilde{x}q(\tilde{x}_1,v_1,t)\frac{\partial}{\partial\tilde{x}_1}q(\tilde{x}_1,v_2,t)$$

If we suppose that $P_{out}^{(1)} \equiv P_r^{(1)}(\tilde{x}_1,\tilde{x}_1,\vec{v},t)$ for $\tilde{x} > 1$ and $P_{out}^{(1)} \equiv P_l^{(1)}(\tilde{x}_1,\tilde{x}_1,\vec{v},t)$ for $\tilde{x} < -1$ we get, at the right interface

$$\begin{aligned}\mathcal{O}(\delta) &: P_r^{(1)} - \tilde{P}_1 = q(\tilde{x}_1,c,t)q(\tilde{x}_1,-c,t),\\ \mathcal{O}(\delta\epsilon) &: \frac{\partial P_r^{(1)}}{\partial\tilde{x}_1} - \frac{\partial\tilde{P}_1}{\partial\tilde{x}_1} = q(\tilde{x}_1,c,t)\frac{\partial}{\partial\tilde{x}_1}q(\tilde{x}_1,-c,t),\end{aligned}$$

and at the left interface

$$\begin{aligned}\mathcal{O}(\delta) &: \tilde{P}_1 - P_l^{(1)} = -q(\tilde{x}_1,-c,t)q(\tilde{x}_1,c,t),\\ \mathcal{O}(\delta\epsilon) &: \frac{\partial P_l^{(1)}}{\partial\tilde{x}_1} - \frac{\partial\tilde{P}_1}{\partial\tilde{x}_1} = q(\tilde{x}_1,-c,t)\frac{\partial}{\partial\tilde{x}_1}q(\tilde{x}_1,c,t).\end{aligned}$$

We may now go back to the integrated equation (2.17) and use the above results to evaluate the terms at the interfaces.

$$
\begin{aligned}
P(x_1, x_2, v_1, -v_1, t)|_{x_2=x_1^+ +\epsilon}^{x_2=x_1^- +\epsilon} + P(x_1, x_2, v_1, -v_1, t)_{x_2=x_1^- -\epsilon}^{x_2=x_1^+ -\epsilon} = \\
\tilde{P}(\tilde{x}_1, \tilde{x}, v_1, v_2, t)|_{\tilde{x}=1^-}^{\tilde{x}=1^+} + \tilde{P}(\tilde{x}_1, \tilde{x}, v_1, v_2, t)|_{\tilde{x}=-1^-}^{\tilde{x}=-1^+} = \\
\delta\left(P_r^{(1)} - \tilde{P}_1 + \tilde{P}_1 - P_l^{(1)}\right) + \delta\epsilon\left(\frac{\partial P_r^{(1)}}{\partial \tilde{x}_1} - \frac{\partial \tilde{P}_1}{\partial \tilde{x}_1} + \frac{\partial P_l^{(1)}}{\partial \tilde{x}_1} - \frac{\partial \tilde{P}_1}{\partial \tilde{x}_1}\right) = \\
\delta\epsilon\left[q(\tilde{x}_1, c, t)\frac{\partial}{\partial \tilde{x}_1}q(\tilde{x}_1, -c, t) + q(\tilde{x}_1, -c, t)\frac{\partial}{\partial \tilde{x}_1}q(\tilde{x}_1, c, t)\right]
\end{aligned}
$$

Since particles are identical and indistinguishable, we can write the nonlinear term, in general, as

$$\delta\epsilon\frac{\partial}{\partial \tilde{x}_1}q(\tilde{x}_1, v_1, t)q(\tilde{x}_1, -v_1, t)$$

and change the variable from $\tilde{x}_1$ to x_1. From the normalization condition (2.4) on P we find, $q(x_1, v_1, t) = p(x_1, v_1, t) + \mathcal{O}(\epsilon)$ (Detailed description is given in appendix A.1.1). Hence, density $p(x_1, v_1, t)$ satisfies, to $\mathcal{O}(\epsilon)$, the nonlinear kinetic equation

$$
\begin{aligned}
\frac{\partial p}{\partial t} + v_1\frac{\partial p}{\partial x_1} + 2v_1\delta\epsilon\frac{\partial}{\partial x_1}\left(pp(x_1, -v_1, t)\right) + \lambda(x_1, v_1)p(x_1, v_1, t) \\
-\lambda(x_1, -v_1)p(x_1, -v_1, t) = 0
\end{aligned}
\tag{2.20}
$$

Recall that we began our analysis considering pairwise interactions at $\mathcal{O}(\epsilon)$ which can now be easily extended to N particles. For a particle interacting with $N-1$ remaining particles, we find

$$
\begin{aligned}
\frac{\partial p}{\partial t} + v_1\frac{\partial p}{\partial x_1} + 2v_1(N-1)\delta\epsilon\frac{\partial}{\partial x_1}\left(pp(x_1, -v_1, t)\right) + \lambda(x_1, v_1)p(x_1, v_1, t) - \\
\lambda(x_1, -v_1)p(x_1, -v_1, t) = 0
\end{aligned}
\tag{2.21}
$$

with the initial condition

$$p(x_1, v_1, 0) = p_0(x_1, v_1)$$

and the boundary condition

$$p(x_1, v_1, t) = p(x_1, -v_1, t)$$

Equation (2.21) describes the evolution of a particle at position x_1 with velocity v_1 at time $t \geq 0$. Due to excluded volume effects, the PDE is nonlinear in the transport term. If we separate the left and right moving densities $p^{\pm}$, the kinetic equation can also be

written as,

$$\frac{\partial p^+}{\partial t} + c\frac{\partial p^+}{\partial x} + 2c(N-1)\delta\epsilon\frac{\partial}{\partial x}(p^+p^-) + \lambda^+(x)p^+ - \lambda^-(x)p^- = 0 \tag{2.22a}$$

$$\frac{\partial p^-}{\partial t} - c\frac{\partial p^-}{\partial x} - 2c(N-1)\delta\epsilon\frac{\partial}{\partial x}(p^-p^+) + \lambda^-(x)p^- - \lambda^+(x)p^+ = 0 \tag{2.22b}$$

The above PDE system is fairly similar to the model in previous work [81], except now the nonlinear term incorporates a collision probability. Although we assumed a small δ for the first-order perturbative correction, the probability may take any value between zero and one as far as the model concerns; the extreme value resembles a collision system (or single-file channel). We later determine the expression for δ in terms of the sizes of the particle and the container. One can also think of this model as an off-lattice version examined in [99]; however, the reduced continuum model we have obtained for the population-level behaviour differs from the corresponding continuum limit of the discrete on-lattice counterpart model. Specifically, the nonlinear transport terms of the coupled system of hyperbolic PDEs obtained due to crowding effects do not agree with those derived in our model.

We will next look at some mathematical properties of the system (2.22), restricting our attention to the following nonlinear hyperbolic system of conservation laws (without velocity jumps)

$$\frac{\partial \vec{p}}{\partial t} + \frac{\partial}{\partial x}F(\vec{p}) = 0, \quad 0 \le x \le L, \quad 0 \le t \le T \tag{2.23}$$

where $\vec{p} = \begin{pmatrix} p^+ \\ p^- \end{pmatrix}$ and $F(\vec{p}) = \begin{pmatrix} cp^+ + c\xi p^+p^- \\ -cp^- - c\xi p^-p^+ \end{pmatrix}$ with $\xi = 2\delta\epsilon(N-1)$. The Jacobian of F, for a noninteracting system (2.5) yields linearly degenerate fields

$$\left\{ \left[c, \begin{pmatrix} 1 \\ 0 \end{pmatrix} \right], \left[-c, \begin{pmatrix} 0 \\ 1 \end{pmatrix} \right] \right\} \tag{2.24}$$

whereas for the interacting system produces genuinely nonlinear fields

$$\begin{aligned} &\left\{ \left[c(a+\sqrt{b}), \begin{pmatrix} -1 - \frac{\xi}{2}(p^+ + p^-) - \sqrt{b} \\ \xi p^- \end{pmatrix} \right], \right. \\ &\left. \left[c(a-\sqrt{b}), \begin{pmatrix} -1 - \frac{\xi}{2}(p^+ + p^-) + \sqrt{b} \\ \xi p^- \end{pmatrix} \right] \right\} \end{aligned} \tag{2.25}$$

where $a = -\frac{\xi(p^+ - p^-)}{2}$ and $b = 1 + \xi(p^+ + p^-) + \frac{1}{4}\left(\xi(p^+ - p^-)\right)^2$. Since the eigenvalues are real and distinct, the system (2.23) is strictly hyperbolic.
We assess the validity of both the models (2.22) and (2.23) by examining the solutions for both particle-level and population-level models in the following sections. The eigenvalues and its associated eigenvectors above are essential to understand these solutions from the numerical methods. This analysis shows the conditions under which the model can describe population-level behaviour emerging from the particle-level dynamics.

2.3.2.3 Long-time dynamics of the kinetic model

The reduction of the point-particle velocity-jump process to a telegraph equation was effortless; however, the process becomes more involved with finite-size particles due to nonlinearity of the transport term. In fact, we can only expect to obtain diffusion limit as an asymptotic description of the velocity-jump process.
We begin by rewriting the system in terms of the total density $\rho(x,t) = p^+ + p^-$ and the flux $j(x,t) = c(p^+ - p^-)$.

$$\begin{aligned} \frac{\partial \rho}{\partial t} + \frac{\partial j}{\partial x} &= 0 \\ \frac{\partial j}{\partial t} + c^2\frac{\partial \rho}{\partial x} + \delta\epsilon(N-1)\frac{\partial}{\partial x}(c^2\rho^2 - j^2) + c(\lambda^+ - \lambda^-)\rho + (\lambda^+ + \lambda^-)j &= 0 \\ &\text{with no flux boundary condition} \end{aligned} \tag{2.26}$$

From the representation (1.12) for the turning frequencies λ^+ and λ^-, we can further simplify the above equations. We then introduce the parabolic scaling $\zeta = \gamma x$ for space variable and $\tau = \gamma^2 t$ for time variable, where γ is a small dimensionless parameter [70]. This yields the scaled system of equations,

$$\begin{aligned} \gamma\frac{\partial \rho}{\partial \tau} + \frac{\partial j}{\partial \zeta} &= 0 \\ \gamma^2\frac{\partial j}{\partial \tau} + \gamma c^2\frac{\partial \rho}{\partial \zeta} + \gamma\delta\epsilon(N-1)\frac{\partial}{\partial \zeta}(c^2\rho^2 - j^2) - 2\gamma c^2\chi\frac{\partial S}{\partial \zeta}\rho + 2\lambda_0 j &= 0 \end{aligned} \tag{2.27}$$

Applying the regular perturbation expansions $\rho = \rho_0 + \gamma\rho_1 + ...$ and $j = j_0 + \gamma j_1 + ...$, we get

$$\mathcal{O}(1): \frac{\partial j_0}{\partial \zeta} = 0$$

$$2\lambda_0 j_0 = 0$$

which implies the trivial solution $j_0 = 0$

$$\mathcal{O}(\gamma): \frac{\partial \rho_0}{\partial \tau} + \frac{\partial j_1}{\partial \zeta} = 0$$

$$c^2 \frac{\partial \rho_0}{\partial \zeta} + \delta\epsilon(N-1)\frac{\partial}{\partial \zeta}(c^2\rho_0^2) - 2c^2\chi\frac{\partial S}{\partial \zeta}\rho_0 + 2\lambda_0 j_1 = 0$$

eliminating j_1 from the equations we get the drift-diffusion equation

$$\frac{\partial \rho_0}{\partial \tau} = \frac{\partial}{\partial \zeta}\left[\frac{c^2}{2\lambda_0}(1 + 2\epsilon\delta(N-1)\rho_0)\frac{\partial \rho_0}{\partial \zeta} - \frac{c^2\chi}{\lambda_0}\frac{\partial S}{\partial \zeta}\rho_0\right] \tag{2.28}$$

In the noninteracting system, we found a PKS type diffusion model with a constant diffusion coefficient (2.8). But here, we identify a density-dependent diffusion coefficient $D(\rho) = \frac{c^2}{2\lambda_0}(1+2\epsilon\delta(N-1)\rho)$ which coincides with the collective diffusion coefficient studied by Bruna ([12], chapter 2). The diffusion is increased relative to point particles by $\mathcal{O}(\epsilon)$, while the drift term remains the same in both models. This increment in the collective diffusion coefficient is because collisions influence propagation towards low particle density areas (see [12], section 2.5.1). We expect a close result from the two-dimensional kinetic model as well.

2.4 Time-dependent solutions

In this section, we study solution strategies based on characteristics for time-dependent hyperbolic balance laws. Rather than adhering to standard numerical methods, this approach is comprehensive and practical. Numerous work has contributed to understanding nonlinear hyperbolic systems of equations, such as the shallow water equations [1] and compressible Euler equations [69]. The main ingredients in the study of such systems are the concepts of characteristics and Riemann invariants. We apply them for both the theoretical and computational developments in the system we study. To begin with, the equations in (2.22) can be represented as a hyperbolic system

$$\frac{\partial \vec{p}}{\partial t} + \frac{\partial}{\partial x}F(\vec{p}) = \vec{g}(x, \vec{p}), \quad 0 \le x \le L, \quad 0 \le t \le T \tag{2.29}$$

where terms on the right-hand side have the same definitions as at (2.23) and the left-hand side has the source term $\vec{g}(x,\vec{p}) = \begin{pmatrix} \lambda^-(x)p^- - \lambda^+(x)p^+ \\ \lambda^+(x)p^+ - \lambda^-(x)p^- \end{pmatrix}$. When $\epsilon = 0$, the characteristic fields (2.24) of the uncoupled system (2.5) give rise to the following system of ODEs:

$$\begin{aligned} \frac{dp^+}{dt} &= g_1(x,\vec{p}) \quad \text{along} \quad x = ct + x_0 \\ \frac{dp^-}{dt} &= g_2(x,\vec{p}) \quad \text{along} \quad x = -ct + x_0 \end{aligned} \tag{2.30}$$

with the initial condition $p_0^{\pm}(x)$ and the reflective boundary conditions. The system can be solved by employing a numerical integration method with a fixed time step, which is not the case in a nonlinear system. When $\epsilon \neq 0$, for every $\vec{p} \in \mathbb{R}^2$ we found two distinct real eigenvalues paired with two linearly independent eigenvectors (2.25). But the structure of these eigenvectors does not provide much help for the latter computations; alternatively, we consider the periodic extensions for the marginal densities.
Let $u_1(x,t)$ be the odd extension of $p^+ - p^-$ and $u_2(x,t)$ be the even extension of $p^+ + p^-$. Then the solution domain changes to $[-L, L]$, and substituting $p^+ = \frac{u_1+u_2}{2}$ and $p^- = \frac{u_2-u_1}{2}$ in to (2.22), the non-conservative system reads

$$\begin{gathered} \frac{\partial \vec{u}}{\partial t} + J(\vec{u})\frac{\partial \vec{u}}{\partial x} = \vec{g}(x,\vec{u}), \quad -L \leq x \leq L, \quad 0 \leq t \leq T \\ \text{with the periodic boundary condition} \quad \vec{u}(-L,t) = \vec{u}(L,t), \end{gathered} \tag{2.31}$$

where $\vec{u} = \begin{pmatrix} u_1 \\ u_2 \end{pmatrix}$, $J(\vec{u}) = \begin{pmatrix} -c\xi u_1 & c(1+\xi u_2) \\ c & 0 \end{pmatrix}$ and the source term $\vec{g}(x,\vec{u}) = \begin{pmatrix} \mu_1 u_2 + \mu_2 u_1 \\ 0 \end{pmatrix}$ with $\mu_1 = \lambda^- - \lambda^+$ and $\mu_2 = -\lambda^- - \lambda^+$. We use this extended system to analyse time-dependent solutions. Essentially we expect to get two ODEs for some algebraic combinations of u_1 and u_2 along the characteristic curves.

2.4.1 $\lambda^{\pm} \equiv 0$ When particles do not experience random changes in the direction, we can simply ignore the source term in (2.31). In this particular situation, the solution of (2.30) is simply $p_0^{\pm}(x \mp ct)$. In an interacting system, we still find velocity changes due to collisions, but we expect the nonlinear system to behave like the noninteracting particles linear system at lower values of collision probabilities. Besides, the solution procedure becomes more involved in the presence of nonlinear transport terms. To solve the system (2.31), we first derive the characteristic ODEs from the eigenvalues and their associated

eigenvectors. We then find functions that are invariant along the characteristic directions and satisfy a set of convective equations.
The eigenvalues

$$\Lambda = c(a \pm \sqrt{b}) \quad \text{of} \quad J, \quad \text{where} \quad a = -\frac{\xi u_1}{2} \quad \text{and} \quad b = 1 + \xi u_2 + \frac{1}{4}(\xi u_1)^2 \tag{2.32}$$

represent the characteristic directions at which hard particles propagate, paired with the left eigenvectors

$$V = (1, -a \pm \sqrt{b}) \tag{2.33}$$

The system is strictly hyperbolic, because the eigenvalues are all real and distinct, as long as b remains positive. Also, the Λ_i-characteristic field is genuinely nonlinear as

$$\nabla\Lambda_1(u_1, u_2) \cdot V_1 = \frac{c\xi^2 u_1}{2\sqrt{b}} \quad \text{and} \quad \nabla\Lambda_2(u_1, u_2) \cdot V_2 = -\frac{c\xi^2 u_1}{2\sqrt{b}} \quad \text{for} \quad \xi \neq 0.$$

When the system (2.31) is multiplied by the eigenvectors, we derive the following PDEs

$$(u_1)_t + \Lambda_i (u_1)_x + V_{i2}[(u_2)_t + \Lambda_i (u_2)_x] = 0 \quad \text{for} \quad i = 1, 2$$

which then condenses and collapses down to two ODEs:
along the characteristics $x'(t) = \Lambda_i(u_1, u_2)$,

$$V_{i1}\frac{du_1}{dt} + V_{i2}\frac{du_2}{dt} = 0 \quad \text{for} \quad i = 1, 2 \tag{2.34}$$

Since the asymptotic expansion is accurate up to $\mathcal{O}(\epsilon)$, we expand $\sqrt{b}$ and include terms upto $\mathcal{O}(\xi)$. This approximation simplifies the above ODEs into

$$\begin{aligned} \frac{du_1}{dt} + \big(1 + \tfrac{\xi}{2}(u_1 + u_2)\big)\frac{du_2}{dt} &= 0, \\ \frac{du_1}{dt} + \big(\tfrac{\xi}{2}(u_1 - u_2) - 1\big)\frac{du_2}{dt} &= 0, \end{aligned}$$

which are integrable using an integrating factor. Hence, it follows that the Riemann invariants are

$$\begin{aligned} \mathcal{R}_1(u_1,u_2) &= (u_1+u_2)e^{\frac{\xi u_2}{2}} \quad \text{on characteristics} \quad x(t) = c\big(1+\tfrac{\xi}{2}(u_2-u_1)\big)t + x_0, \\ \mathcal{R}_2(u_1,u_2) &= (u_1-u_2)e^{\frac{\xi u_2}{2}} \quad \text{on characteristics} \quad x(t) = -c\big(1+\tfrac{\xi}{2}(u_2+u_1)\big)t + x_0 \end{aligned} \tag{2.35}$$

It is possible to obtain an exact solution for p^+ and p^- in the nonlinear system (2.22) during this unbiased situation. Since $\mathcal{R}_1$ and $\mathcal{R}_2$ are constant along their respective characteristics, given the initial conditions, say $u_1^0(x_0)$ and $u_2^0(x_0)$, we write

$$\begin{aligned} \mathcal{R}_1(u_1(x,t),u_2(x,t)) &= \mathcal{R}_1(u_1^0(x-\Lambda_1 t), u_2^0(x-\Lambda_1 t)) \\ \mathcal{R}_2(u_1(x,t),u_2(x,t)) &= \mathcal{R}_2(u_1^0(x-\Lambda_2 t), u_2^0(x-\Lambda_2 t)) \end{aligned}$$

Now solving the above system, we get

$$\begin{aligned} p^+ &= \frac{1}{4}(\mathcal{R}_1^0+\mathcal{R}_2^0)\exp\left[-\mathcal{W}\big(\tfrac{\xi}{4}(\mathcal{R}_1^0-\mathcal{R}_2^0)\big)\right] + \frac{1}{\xi}\mathcal{W}\big(\tfrac{\xi}{4}(\mathcal{R}_1^0-\mathcal{R}_2^0)\big) \\ p^- &= \frac{1}{\xi}\mathcal{W}\big(\tfrac{\xi}{4}(\mathcal{R}_1^0-\mathcal{R}_2^0)\big) - \frac{1}{4}(\mathcal{R}_1^0+\mathcal{R}_2^0)\exp\left[-\mathcal{W}\big(\tfrac{\xi}{4}(\mathcal{R}_1^0-\mathcal{R}_2^0)\big)\right] \end{aligned} \tag{2.36}$$

where $\mathcal{R}_1^0 = \mathcal{R}_1(u_1^0(x-\Lambda_1 t), u_2^0(x-\Lambda_1 t))$, $\mathcal{R}_2^0 = \mathcal{R}_2(u_1^0(x-\Lambda_2 t), u_2^0(x-\Lambda_2 t))$ and $\mathcal{W}$ is the Lambert W function.

2.4.2 $\lambda^\pm \neq 0$ When the system possessed by an external signal, the particles begin its' random turns unfolding the source term $\vec{g}(x,\vec{u})$ on the right-hand side of (2.31); hence, following the same reasoning as in zero turnings, the system of ODEs (2.34) returns

$$V_{i1}\frac{du_1}{dt} + V_{i2}\frac{du_2}{dt} = V_{i1}g_1 + V_{i2}g_2 \quad \text{for} \quad i=1,2$$

We can write the above system in a more concise form with the approximation to $\sqrt{b}$; the solutions propagate according to the differential equations

$$\begin{aligned} \frac{d\mathbf{R}}{dt} = e^{\frac{\xi u_2}{2}}\mathbf{G}(u_1,u_2) \quad &\text{along the characteristics} \\ &\mathbf{x}'(t) = \mathbf{Q}(u_1,u_2) \end{aligned} \tag{2.37}$$

where $\mathbf{R} = (\mathcal{R}_1, \mathcal{R}_2)$ as defined in (2.35), $\mathbf{G}$ is the source term whose entries are $V_i \cdot \vec{g} = \mu_1 u_2 + \mu_2 u_1$ for $i = 1,2$ and $\mathbf{Q}(u_1,u_2) = (\Lambda_1, \Lambda_2)$. The equations are integrable along the characteristics. So computing the solution of the kinetic model (2.22) is equivalent to

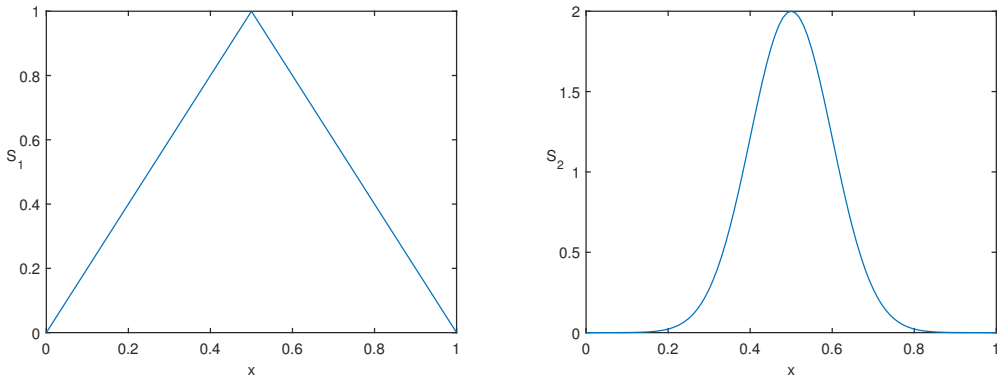

(a) (b)

Figure 2.3: Signal functions: (a) $S(x) = 1 - 2|x - 0.5|$ with $\lambda_0 = 2.5$, (b) $S(x) = 2e^{-50\,(x-0.5)^2}$ with $\lambda_0 = 20$.

numerically generating the characteristic paths in spacetime. In the following section, we discuss the methods of solving the full-particle systems and later match the results with the numerical integration.

2.5 Full-particle simulations

In this section, we develop algorithms necessary to perform simulations of velocity jump particles with (and without) hard-sphere interactions. We apply a simple time-stepping stochastic simulation algorithm for point particles and an event-driven kinetic Monte Carlo method for finite-size particles. To this end, we need to be more specific about the signal function S. In one dimension, the turning frequency (1.12) becomes

$$\lambda^{\pm} = \lambda_0 \mp c\chi D_x S(x) \tag{2.38}$$

and we consider two forms of signal functions which are given in Figure (2.3). The Gaussian function is also used as bias interaction kernels in IBMs, where the neighbouring individuals influence the travelling direction [94].

2.5.1 A Stochastic Simulation Algorithm (SSA) In a one-dimensional velocity jump model, a particle positioned at $X(t)$ evolves according to

$$V(t) = \frac{dX}{dt}$$

This can be discretised using a finite time step Δt as

$$X(t+\Delta t) = X(t) + V(t)\Delta t \tag{2.39}$$

The initial positions $X(0)$ are drawn from the initial density $P_0(\vec{x}, \vec{v})$. A point particle which undergoes a velocity jump process has only two possible events; reflection near boundaries and random turns. The reflective boundary conditions can be implemented as follows:

$$\begin{aligned} &\text{If} \quad X(t+\Delta t) < 0, \quad X(t+\Delta t) = -X(t) - V(t)\Delta t; \\ &\text{If} \quad X(t+\Delta t) > L, \quad X(t+\Delta t) = 2L - X(t) - V(t)\Delta t; \\ &\text{complemented with} \quad V(t+\Delta t) = -V(t). \end{aligned} \tag{2.40}$$

The above conditions are used to avoid particles moving outside the domain walls when stepping forward in time. However, they do not generate new positions; instead, detect the wall, switch the velocity and proceed the random walk (that performed outside walls) in the opposite direction. The final step is the execution of the random velocity jumps. During the time interval $(t + \Delta t)$ a particle will turn with the turning probability $\lambda\Delta t$; otherwise, advances with the same velocity. The turning rate λ has two possibilities based on the particle's direction of motion and is chosen according to the formula (2.38). (See appendix (A.2.1) for the complete algorithm.)

We observe particle-particle interactions apart from random jumps and wall collisions in a closed, narrow channel with finite-size particles. Therefore at the end of each time-step, every sphere must be checked over every other for overlaps. A system of N particles generate $\frac{N(N-1)}{2}$ such checks. If collision (one or more) occurred, the new velocities would be computed by turning back the clock to the collision time and then continue the simulation. It is essential to choose a small time step to avoid dropping any interaction. Despite the simplicity, these checks at a minimal time interval increase the computational cost of the method. In the next section, we present an improved algorithm to deal with finite-size particles.

2.5.2 Event-driven kinetic Monte Carlo (KMC) algorithm. To perform simulations on velocity jump particles with hard-core interactions, we use an event-based algorithm that fits into the general class of KMC methods. During this event-driven algorithm, realisations advance from event to event [52]. The time is calculated for the next possible event; hence automatically adjusts the time step and avoid missing any interactions.

There are three types of events in our problem; collision with another particle (with

probability δ), collision with boundaries, and random velocity jump. Again from the low volume fraction assumption, we can safely ignore three or more particle interactions. A particle can bypass its neighbours and interact with a distant individual or with the walls. Therefore, it is necessary to check the interactions of each particle with every other particle and walls. We may divide the domain into cells such that each section contains two or more particles. This way, we can compute interaction times within a cell; however, a higher number of occupants bring the step complexity back to an $\mathcal{O}(N^2)$. Moreover, an individual may experience instantaneous directional changes in between pair interactions. Consequently, we expect different event queues from two consecutive iterations.

Let us now closely look at the basic operations in the algorithm for a chaotically colliding N hard spheres in a narrow channel. The state of sphere i consists of position and velocity along with the last updated time $t_i \leq t$, where t is the current simulation time. The trajectory of the sphere is a unique straight line; thus, given the current configuration, we can calculate position $X(t + \Delta t)$ using the equation (2.39). If a particle reverses its direction in the presence of an external signal $S(x)$ at an instantaneous random time, we can compute the next turning time $t+\tau$. The derivation is adapted from the lecture note [25], where we replace the chemical reaction rate with the turning rate (2.38).

$$\begin{aligned} V(t)\ln\left(\frac{1}{r}\right) &= \int_{X(t)}^{X(t)+V(t)\tau} \lambda(y)dy \\ &= \int_{X(t)}^{X(t)+V(t)\tau} \lambda_0 - \chi V(t) S_y dy \\ &= \lambda_0 V(t)\tau - \chi V(t)\left(S(X+V\tau) - S(X)\right) \end{aligned}$$

where r is a uniform random number from the interval $(0, 1)$ and $V(t)$ is either c or $-c$. When the signal function is of the form 2.3(a), we have

$$\tau = \begin{cases} (\lambda_0 + 2V\chi)^{-1} \ln\left(\frac{1}{r}\right), & 0.5 \leq X(t) \leq 1 \\ (\lambda_0 - 2V\chi)^{-1} \ln\left(\frac{1}{r}\right), & 0 \leq X(t) < 0.5 \end{cases} \tag{2.41}$$

and the signal 2.3(b) yields,

$$\ln\left(\frac{1}{r}\right) = \lambda_0\tau - 2\chi\left(e^{-50(X+V\tau-0.5)^2} - e^{-50(X-0.5)^2}\right) \tag{2.42}$$

To find τ, one can use either Newton-Raphson (NR) method or MATLAB `fzero` function. Next suppose two hard spheres, i and j, positioned initially at X_{i0} and X_{j0} with velocities V_{i0} and V_{j0}. If two collide, given the collision probability δ, we can compute the collision time at $\epsilon = |X_j - X_i|$.

$$t_{coll} = \frac{|X_{j0} - X_{i0}| - \epsilon}{|V_{j0} - V_{i0}|} \tag{2.43}$$

The interaction time finds a finite value only if two particles move towards each other $(X_{j0} - X_{i0})(V_{j0} - V_{i0}) < 0$ and collide with the specified probability; otherwise, we assume a large value for t_{coll}. Besides, a collision does not occur at all if two particles moving the same direction, $|V_{j0} - V_{i0}| = 0$; or if already overlapped, $|X_{j0} - X_{i0}| < \epsilon$. After a collision, their velocities experience jumps. The final event time is the reflection on the walls, and it can be calculated by dividing the distance to the wall from its speed.

$$t_{wall} = \begin{cases} (L - X_i)/V_i, & V_i > 0; \\ X_i/V_i, & V_i < 0 \end{cases} \tag{2.44}$$

Due to unidirectional motion, a particle will only hit either end of the channel. The reflection time set to a large value if the particle moves away from the wall.
The above three functions create the event queue, and the algorithm picks the minimum next event time. Using equation (2.39), every sphere will advance their position according to this minimum time, but only the selected event's participants change their velocities. To avoid particles leaving the domain during the position advancement, we use the reflective boundary conditions (2.40) (the basic algorithm is given in appendix (A.2.2)).

2.6 Comparison of transient solutions

This section is dedicated to assess the validity of the kinetic model 2.21 from the transient solutions. The solution procedures studied under previous sections are illustrated through practical numerical examples and the numerical results are compared with particle simulations.

2.6.1 Numerical Integration Since an analytical solution for the nonlinear kinetic model (2.22) is not achievable with varying turning rates over x, we resort to a numerical integration method along the characteristics. This way, we avoid problems that occur when using standard numerical methods for solving PDEs. We have already established the equations for this numerical integration in section (2.4), where we have found a set of

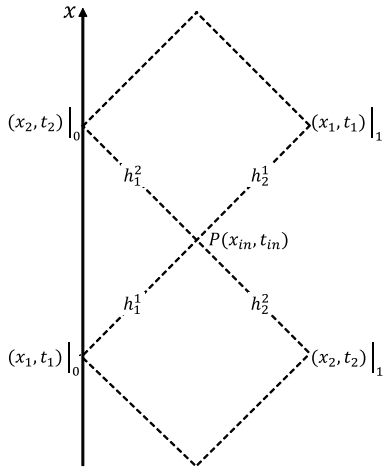

Figure 2.4: Two characteristics originating from $\mathbf{x}_0 = (x_1, x_2)|_0$ at time $\mathbf{t}_0 = (t_1, t_2)|_0$ intersect at $P(x_{in}, t_{in})$, then reach $\mathbf{x}_1 = (x_1, x_2)|_1$ at $\mathbf{t}_1 = (t_1, t_2)|_1$.

ODEs for the Riemann variables $\mathcal{R}_1$ and $\mathcal{R}_2$ on the characteristic directions (2.37). Given the initial conditions, we can obtain the solutions elsewhere by integrating along the characteristic curves, and the numerical procedure is the simple Euler's approximation. Each integration step requires information carried by both sets of characteristics, and they themselves depend on both u_1 and u_2 which leads to a nonuniform grid.
Let us now establish the algorithm according to (2.37).

S1 Determine the time and position of the intermediate crossover point $P(x_{in}, t_{in})$ of the two characteristics originating from $\mathbf{x}_0 \equiv \mathbf{x}(\mathbf{t}_0)$ (see Figure (2.4)). Here we use the two equations; $x_{in} = \mathbf{x}_0 + (h_1^1, h_1^2) \circ \mathbf{Q}$, the output from the Euler's step and $t_{in} = \mathbf{t}_0 + (h_1^1, h_1^2)$, where h_1^is are the time steps for their respective characteristics.

S2 Calculate the Riemann variables $\mathbf{R}$ at P using

$$\mathbf{R}(x_{in}, t_{in}) = \mathbf{R}(\mathbf{x}_0, \mathbf{t}_0) + (h_1^1, h_1^2) \circ \mathbf{G}$$

Each element in $\mathbf{R}$ is a combination of u_1 and u_2 along the two curves, which gives us two equations to solve and find the updated u_1 and u_2 at the crossover point.

S3 Using the updated u_1 and u_2 calculate the new positions $\mathbf{x}_1 \equiv \mathbf{x}(\mathbf{t}_1)$ beyond the intersection point. Similar to equations in S1, again from the Euler's step we have $\mathbf{x}_1 = x_{in} + (h_2^1, h_2^2) \circ \mathbf{Q}$, and $\mathbf{t}_1 = t_{in} + (h_2^1, h_2^2)$.

S4 Find $\mathbf{R}$ beyond intersections using

$$\mathbf{R}(\mathbf{x}_1, \mathbf{t}_1) = \mathbf{R}(x_{in}, t_{in}) + (h_2^1, h_2^2) \circ \mathbf{G}$$

Here h_1^i and h_2^i, for $i = 1, 2$ are calculated from the equations given in S1 and S3. The total time elapsed, say h, is the sum of h_1^i and h_2^i along each characteristic. We cannot maintain a fixed h since h_1^i and h_2^i are constantly changing during the process. We may start off with a uniform grid at $t = 0$, but subsequently follows the characteristics. Hence the curves will be approximate straight lines.

2.6.2 Numerical examples The numerical examples presented in this section aim to the followings: illustrate the behaviour of the systems under biased and unbiased conditions, investigate whether the model and associated discrete processes support travelling wave solutions, and examine the effect of changing parameters, such as the size of the particles and collision probability, on the solutions. Unless explicitly stated otherwise, we consider a set of $N = 100$ particles with speed $c = 1$ and chemotactic sensitivity coefficient $\chi = 1$, placed inside a channel of length one ($L = 1$). Given the size of the indistinguishable particles and the width of the channel, the formula A.3(iii) calculates the collision probabilities.

In the event-driven algorithm, we generate random initial positions for the particles at the beginning of each realisation; simultaneously, we avoid overlaps. The collision probability will take care of the overlaps during iterations. The histograms were produced by dividing the domain into 40 bins. At each step, we check the number of particles in each bin; subsequently, the cumulative average is calculated; dividing the resulting value in each bin by the number of steps, total particle count and bin width. For the two signal functions (2.3(a)) and (2.3(b)), respectively performed 5000 and 500 realisations. Effectively, this implies that we are using 5×10^5 (and 5×10^4) trajectories of all N particles to compute the one-particle distribution histogram.

For the numerical integration, the domain $[0, 1]$ is divided into $k = 200$ spaces. At the beginning of each time step h, two characteristics emerge from each grid point x_k while at the end, two characteristics meet at each x_k. As said in the earlier section, We may be only able to choose an equidistant grid at the beginning of time. The subsequent paths and time step will be computed automatically in the numerical procedure. At the boundaries, we impose periodic boundary conditions.

The solid lines and the circles represent solutions for the PDE models and the KMC simulations, respectively. In all figures, we follow the colour code (for both lines and circles): green, the point particle system; blue, the narrow channel system; red, the collision system. Figures (2.5) and (2.6) collate simulations of both noninteracting and interacting particles at time $t = 0.3$. Initially, all the particles are evenly distributed across the domain. We fix width of the channel (l) to 0.01 and examine the solutions for

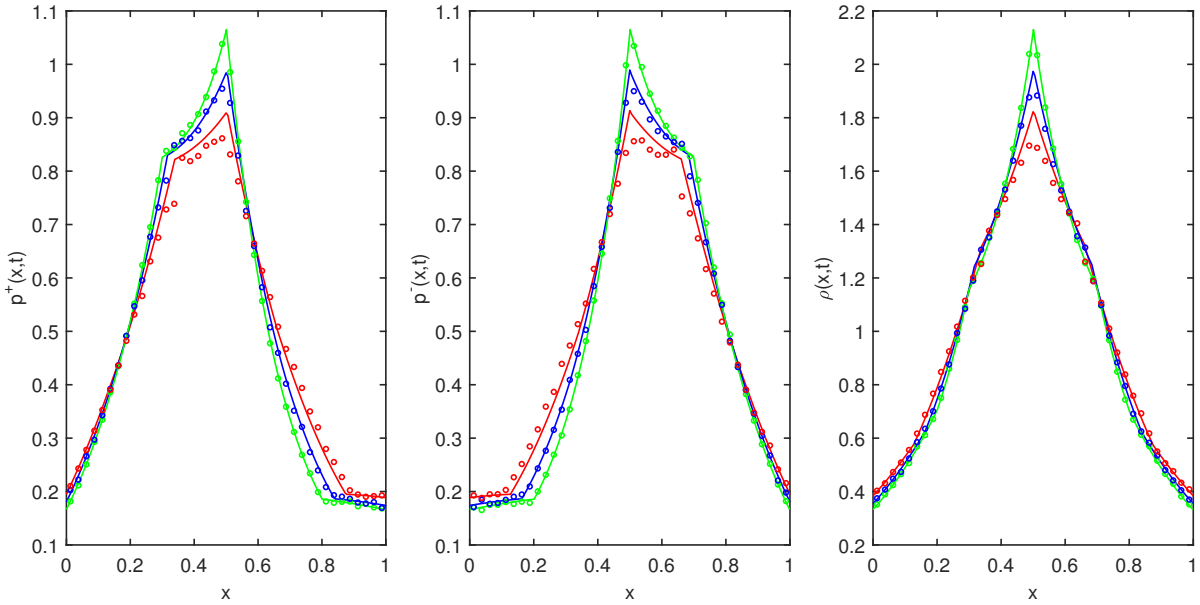

Figure 2.5: Transient marginal densities from the signal function (2.3(a)) when $\epsilon = 0$ (green), $\delta(0.002, 0.01) = 0.4375$ (blue) and $\delta(0.005, 0.01) = 1$ (red). The particle simulations (circles) are obtained by 5000 realisations.

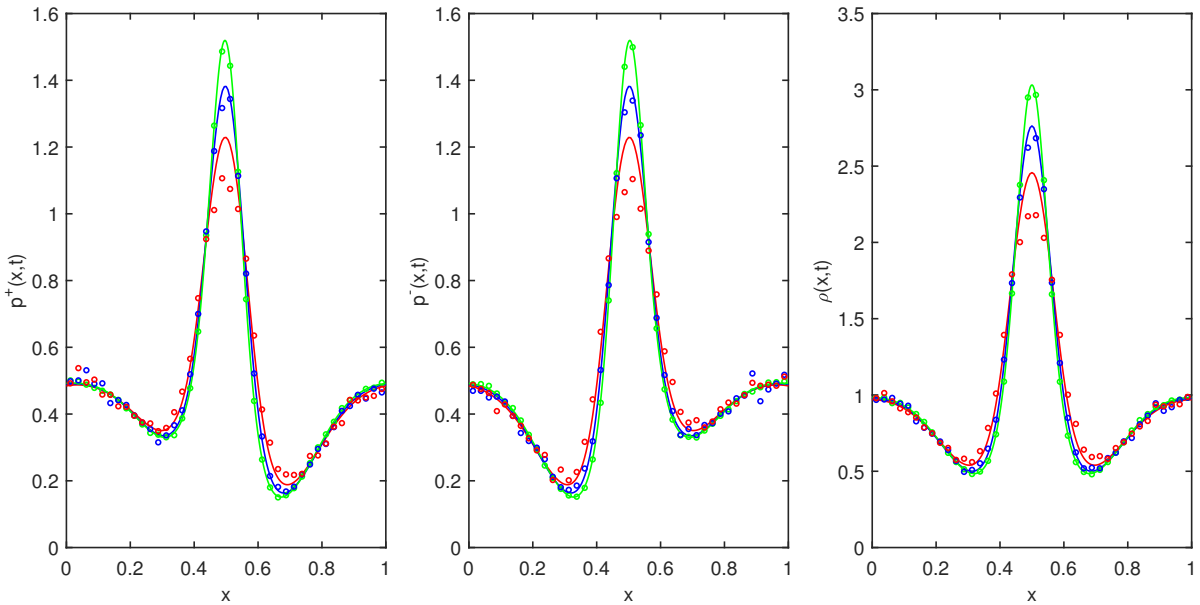

Figure 2.6: Transient marginal densities from the signal function (2.3(b)) when $\epsilon = 0$ (green), $\delta(0.002, 0.01) = 0.4375$ (blue) and $\delta(0.005, 0.01) = 1$ (red). The particle simulations (circles) are obtained by 500 realisations.

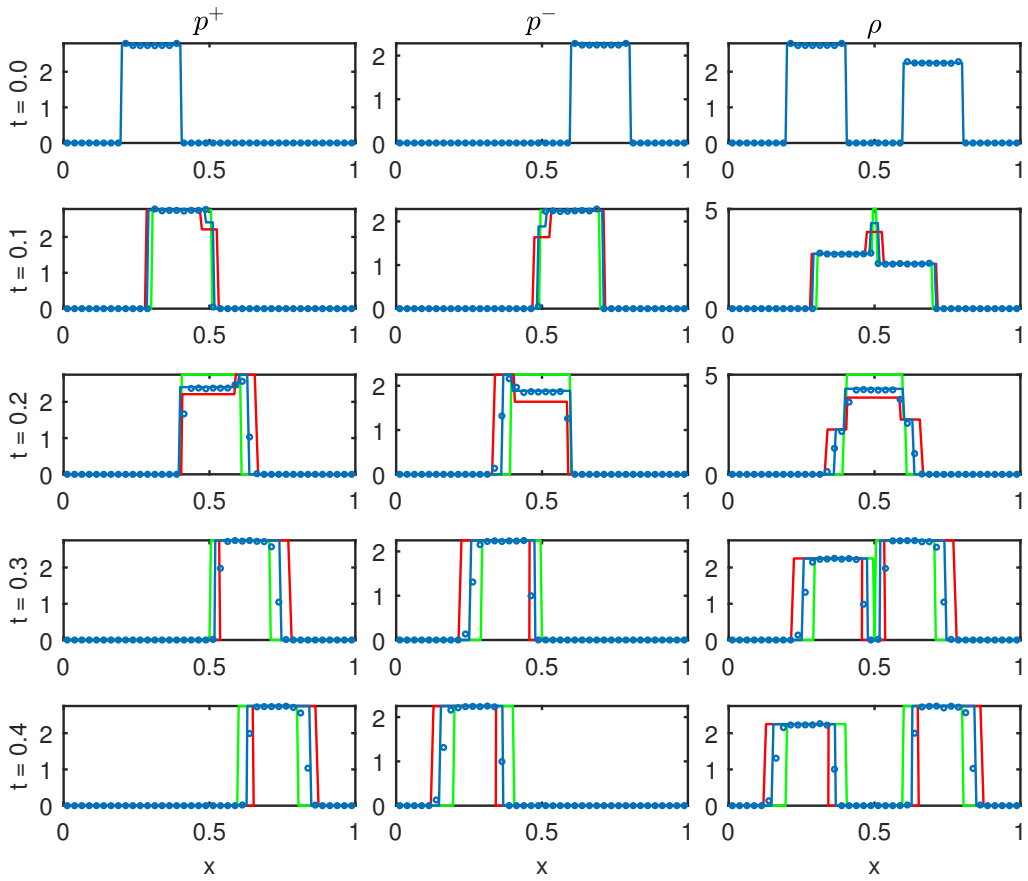

Figure 2.7: Transient marginal densities when $\lambda^{\pm} = 0$. Numerical results in the leftmost and middle columns show the band travels to the right and left, respectively. The particle simulations (circles) are obtained by 5000 realisations.

0.0314 and 0.1962 occupied fractions; the latter occupancy yields a collision system where $\delta(0.005, 0.01) = 1$.

We plot a subpopulation of right-moving p^+, a subpopulation of left-moving p^- and the total population $\rho = p^+ + p^-$ for a simple non-tumbling case in Figure (2.7), and with biases in Figures (2.8) and (2.9) upto time $t = 0.4$. The initial particle arrangement is given by

$$p_0^+(x) = \frac{55}{100}\mathbb{1}_{[0.2,0.4]} \quad \text{and} \quad p_0^-(x) = \frac{45}{100}\mathbb{1}_{[0.6,0.8]}$$

We compare the numerical predictions of the narrow channel system with those corresponding to both the point particles and the single-file models. For more readable graphs, we avoid particle simulations of the latter systems. The particle size is fixed to $\epsilon = 0.002$ so that $N\epsilon^2$ remains constant during model comparison. We, therefore, change

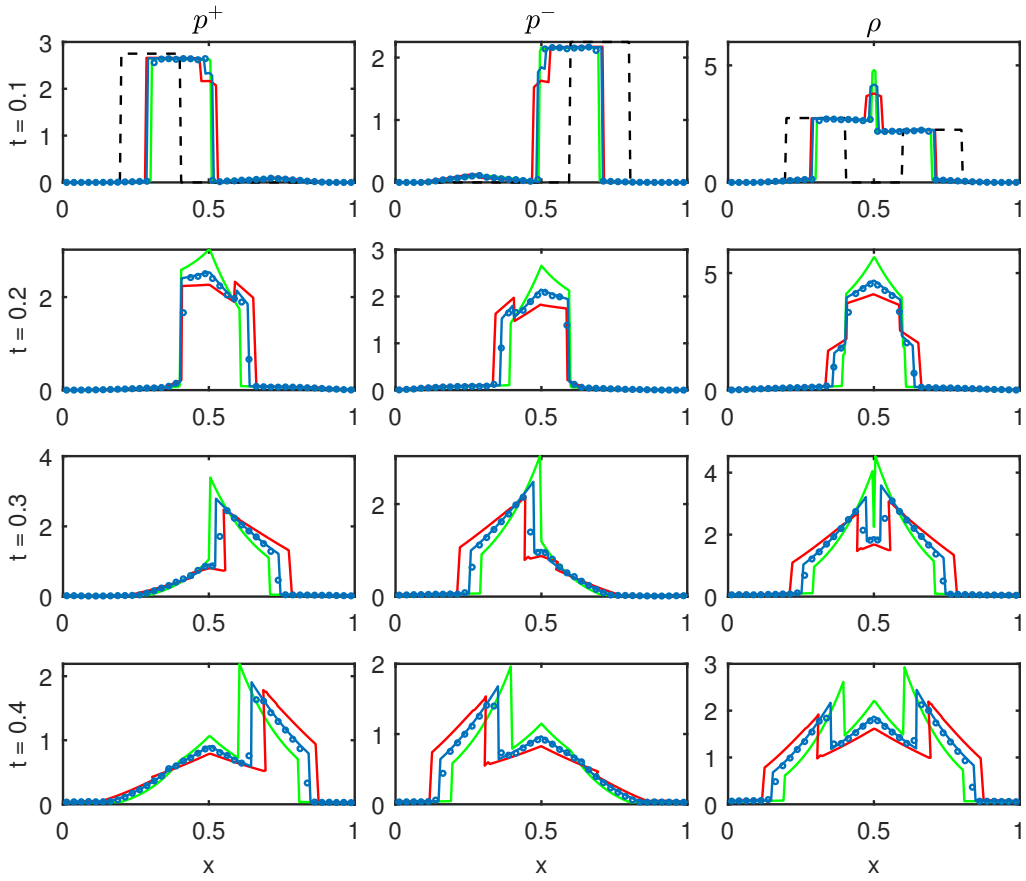

Figure 2.8: Transient marginal densities for the signal function (2.3(a)). Numerical results in the leftmost and middle columns show the band travels to the right and left, respectively. The particle simulations (circles) are obtained by 5000 realisations.

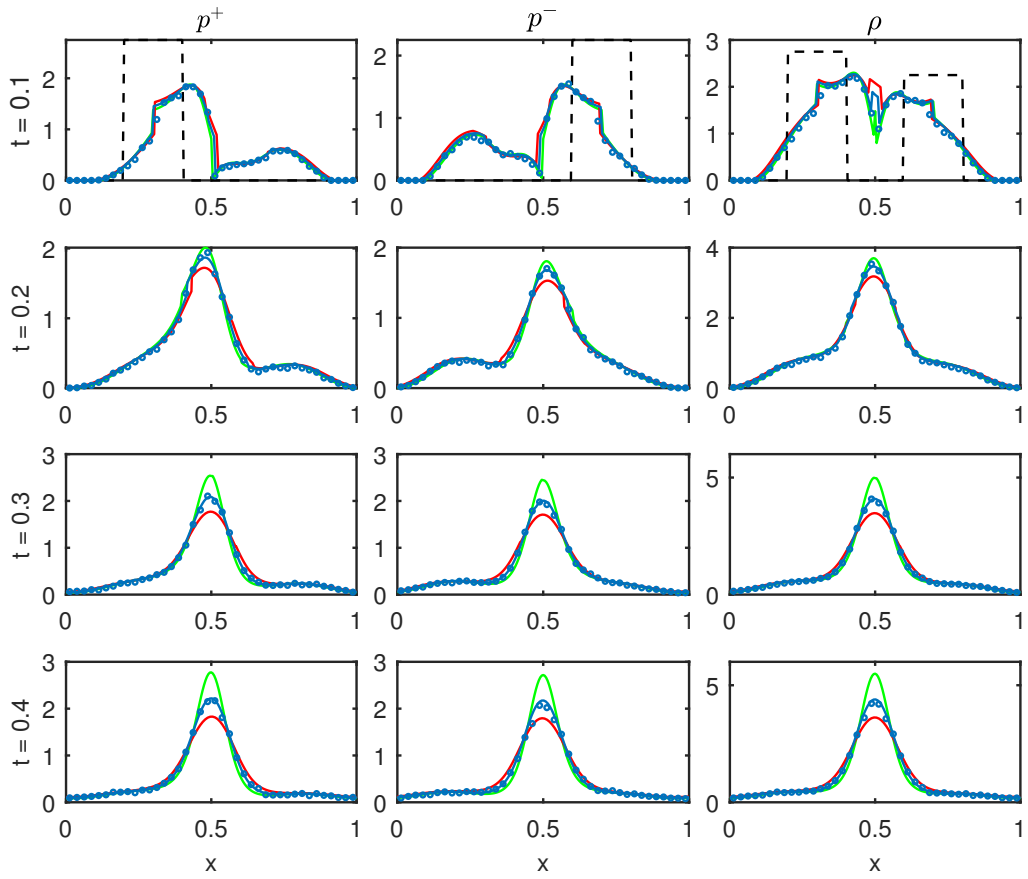

Figure 2.9: Transient marginal densities for the signal function (2.3(b)). Numerical results in the leftmost and middle columns show the band travels to the right and left, respectively. The particle simulations (circles) are obtained by 500 realisations.

the width of the channel to 0.004 to form a collision system. This comparison will explain the importance of excluded volume effects on the propagating wavefronts in biased and unbiased conditions.

2.6.2.1 Discussion

In the above numerical examples, we illustrate the time-dependent behaviour of the systems in the case of both vanishing and nonvanishing turning frequencies. In Figures (2.5) and (2.6), the theoretical predictions for both point (green) and finite-size particles in a narrow channel (blue) compare well with their simulation counterparts. Particularly in the narrow channel, when 3.14% of the domain is occupied we observe 56.25% overlaps. Due to this low volume fraction as well as more overlaps, the model and the simulations are essentially in a close convergence. However, excluded-volume effects are significant in the collision system, especially at the peaks [1]. An apparent reason for this observation is that the high volume fraction (19.62%) occupied by the particles. In fact, we expect approximately the same outcomes for the narrow channel under this large occupied fraction. Note that significantly fewer simulations were required for the signal function (2.3(b)) compared to (2.3(a)), as particles reorganize themselves rapidly under higher baseline frequency.

The collision-free and single-file channel plots are the reference points that allow us to see the competition between the most favourable signal environment and the volume exclusion of finite-size particles. In general, we find higher densities around the peaks of the signal functions as individuals aggregate into favourable regions. However, the peaks are reduced for the narrow channel system (blue) and further reduced for the collision system (red). In other words, the higher the collision probability lesser the peak. This is because not all particles can be in and around the highest point of the signal. A particle redistribution would also co-occur, allowing more particles closer to the ends of the channels (this can be clearly seen in the subpopulation plots of Figure (2.5)). Initially, particles are evenly distributed in the domain; therefore, we do not find deviations in the subpopulation densities about the centre after time t.

The idea of distinct waves for subpopulations is pursued in [26] and [88]. The former referred to travelling bands of point particles, while the latter suggested that in the case where the travelling wave speed coincides with the individual cell speed. The wavefronts of the point particle system (2.5) travel at constant speed c. Since $\epsilon = 0$, overlap within the band is not a factor. However, when $\epsilon \neq 0$, velocity changes due to collisions. From

[1] This effect is minor in Figures (2.5) compared to Figures (2.6) as the gradients of signal (2.3(a)) are much more shallow than those of signal (2.3(b)) around the centre of the domain [81]

the plots (2.7) and (2.8), we find the nonlinear system (2.22) match the noninteracting particles linear system up to $t = 0.1$; thereafter, two fronts collide. Specifically, in the narrow channel, only 43.75% collisions are involved in this. The rebounded waves at $t = 0.3$ are shifted outward; apparently, this shift progresses with the increasing collision probabilities, which the eigenvalues (2.25) describe. We find the characteristic speeds, to $\mathcal{O}(\epsilon)$, $\Lambda^+ = c + c\xi p^-$ and $\Lambda^- = -c - c\xi p^+$, where $\xi = 2\delta\epsilon(N-1)$. The maximum, $\delta = 1$ recovers the single-file nonlinear system [81].

When $\lambda \neq 0$, whether the particles are point or finite in size, they undergo instantaneous velocity changes; waves distort before collisions (Figures (2.8) and (2.9) at $t = 0.1$). The travelling bands further disrupted due to interactions between finite-size particles, and the difference between the linear and nonlinear PDE solutions become more noticeable at $t = 0.2$. The 56.25% overlaps again raise the crowd in and around the centre of the narrow channel domain compared to the single-file channel. Note that, higher baseline frequencies stimulate the kinetic waves to diffusion mode. Hence we do not observe continuing kinetic waves in Figure (2.9).

2.7 Stationary solution

In this section, we compare the steady-state solutions with the stochastic simulations of the full particle model. In one dimensional setting, it is feasible to derive an exact stationary solution. However, this is not the case in higher dimensions, and we will see this in the chapter (5). For the full particle system, we use an indirect sampling method known as the Metropolis Hastings (MH) algorithm.

When the system is at equilibrium, ρ is independent of time t; therefore, (2.26) yields $\frac{dj}{dx} = 0$. From the wall-particle boundary conditions it follows that, $j = 0$; hence, the stationary density p_{st} satisfies the ODE

$$c\frac{dp_{st}}{dx} + 2(N-1)c\delta\epsilon p_{st}\frac{dp_{st}}{dx} + (\lambda^+ - \lambda^-)p_{st} = 0 \tag{2.45}$$

Set $\xi = 2\delta\epsilon(N-1)$ and $\Lambda = \lambda^+ - \lambda^-$, then

$$\begin{aligned}
\frac{1}{p_{st}}\frac{dp_{st}}{dx} + \xi\frac{dp_{st}}{dx} &= -\frac{\Lambda}{c} \\
\ln p_{st} + \xi p_{st} &= -\int_0^x \frac{\Lambda(y)}{c}dy + \ln A \\
\ln(\xi p_{st} e^{\xi p_{st}}) &= \ln(A\xi e^{-\int_0^x \frac{\Lambda(y)}{c}dy}) \\
(\xi p_{st})e^{\xi p_{st}} &= A\xi e^{-\int_0^x \frac{\Lambda(y)}{c}dy} \\
p_{st} &= \frac{1}{\xi}\mathcal{W}(A\xi e^{-\int_0^x \frac{\Lambda(y)}{c}dy})
\end{aligned} \tag{2.46}$$

where $\mathcal{W}$ is the Lambert W function and A is a constant to be determined using the normalisation condition,

$$\int_0^L p_{st}(x)dx = 1$$

Note that, $\epsilon = 0$ returns the solution for the point particles $p_{st} = Ae^{-\int_0^x \frac{\Lambda(y)}{c}dy}$.

2.7.1 Full particle system To derive the stationary solution for the full particle system, we consider the higher dimensional PDE (2.1) for two particles travelling with velocity $v_1 = -v_2 \in \{c, -c\}$. To ease the notation, we use the superscripts $+-, -+$ for the velocities of the joint density $P(x_1, x_2, v_1, v_2, t)$ in the order of x_1 and x_2, and write

$$\begin{aligned}
\frac{\partial P^{+-}}{\partial t} + c\frac{\partial P^{+-}}{\partial x_1} - c\frac{\partial P^{+-}}{\partial x_2} &+ \lambda^+(x_1)P^{+-}(x_1,x_2) - \lambda^-(x_1)P^{--}(x_1,x_2) \\
&+\lambda^-(x_2)P^{+-} - \lambda^+(x_2)P^{++}
\end{aligned} \tag{2.47a}$$

$$\begin{aligned}
\frac{\partial P^{-+}}{\partial t} - c\frac{\partial P^{-+}}{\partial x_1} + c\frac{\partial P^{-+}}{\partial x_2} &+ \lambda^-(x_1)P^{-+}(x_1,x_2) - \lambda^+(x_1)P^{++}(x_1,x_2) \\
&+\lambda^+(x_2)P^{-+} - \lambda^-(x_2)P^{--}
\end{aligned} \tag{2.47b}$$

with the reflective boundary condition on $x_i = 0, L$ and the interface conditions (2.10) at the right interface, and (2.11) at the left interface.

Let the total density and flux be $(\rho_1, \rho_2) = (P^{+v} + P^{-v}, P^{v+} + P^{v-})$ and $(j_1, j_2) = c(P^{+v} - P^{-v}, P^{v+} - P^{v-})$, where v is either c or $-c$. Note that, the flux has no inflow towards the excluded region while the total density has jumps across interfaces. For instance, at the left interface, the sum and the difference of the two conditions (2.11a)

and (2.11b) yield, respectively,

$$j_1(x_1, x_1^- - \epsilon) = j_1(x_1, x_1^+ - \epsilon)$$

and

$$\rho_1(x_1, x_1^- - \epsilon) - \rho_1(x_1, x_1^+ - \epsilon) = 2\delta P^{-+}(x_1, x_1^- - \epsilon)$$

We use the latter to establish the steady state solution for interacting system. Adding equations (2.47), the kinetic model in terms of the flux at the steady state reads as

$$\frac{\partial j_2}{\partial x_1} + \frac{\partial j_1}{\partial x_2} + \frac{\lambda^+(x_1) - \lambda^-(x_1)}{c} j_2 + \frac{\lambda^+(x_2) - \lambda^-(x_2)}{c} j_1 = 0 \tag{2.48}$$

For two arbitrary functions ψ_1 and ψ_2, the exponential functions

$$j_1 = \psi_1(x_1) e^{-\int_0^{x_2} \frac{\lambda^+(u) - \lambda^-(u)}{c} du} \quad \text{and} \quad j_2 = \psi_2(x_2) e^{-\int_0^{x_1} \frac{\lambda^+(u) - \lambda^-(u)}{c} du}$$

satisfy equation (2.48) and the no-flux boundary condition yields $(j_1, j_2) = \mathbf{0}$ for all $x_1, x_2 \in [0, L]$. It follows that, $\rho_1 = 2P_{st}^{+v} = \rho_2 = 2P_{st}^{v+} = P_{st}(\vec{x})$, which yields the kinetic equation in terms of steady state P_{st} as

$$\frac{\partial P_{st}}{\partial x_1} - \frac{\partial P_{st}}{\partial x_2} + \frac{\Lambda(x_1) - \Lambda(x_2)}{c} P_{st} = 0 \tag{2.49}$$

where $\Lambda(x_1) = \lambda^+(x_1) - \lambda^-(x_1)$ and $\Lambda(x_2) = \lambda^+(x_2) - \lambda^-(x_2)$.
The solution for the above equation is

$$P_{st} = A e^{-\int_0^{x_1} \frac{\Lambda(u)}{c} du - \int_0^{x_2} \frac{\Lambda(u)}{c} du}, \quad \text{where } A \text{ is an arbitrary constant.}$$

In fact, there are three different arbitrary constants in the interacting system, one for each region excluded by the two particles connected by the interface conditions. Let A_1, A_2, and A_3 be those constants for left outer region, inner region and right outer region, respectively. For $x_1 > x_2$,

$$P_{st}(x_1, x_1^- - \epsilon)[1 - \delta] = P_{st}(x_1, x_1^+ - \epsilon)$$

$$A_1 e^{-\int_0^{x_1} \frac{\Lambda(u)}{c} du - \int_0^{x_1^- - \epsilon} \frac{\Lambda(u)}{c} du}[1 - \delta] = A_2 e^{-\int_0^{x_1} \frac{\Lambda(u)}{c} du - \int_0^{x_1^+ - \epsilon} \frac{\Lambda(u)}{c} du}$$

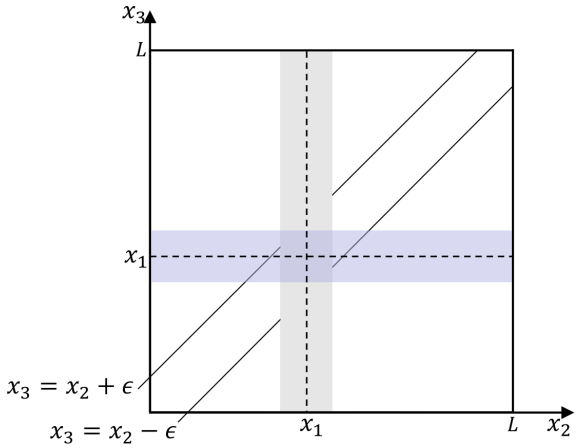

Figure 2.10: Schematic of the excluded domain for three interacting particles when one particle is fixed at x_1. The shaded areas show the inner slabs of width 2ϵ.

and since $\lambda(x)$ is continuous, we get $A_1[1-\delta] = A_2$.
For $x_1 < x_2$, the equation

$$P_{st}(x_1, x_1^+ + \epsilon)[1-\delta] = P_{st}(x_1, x_1^- + \epsilon)$$

$$A_3 e^{-\int_0^{x_1} \frac{\Lambda(u)}{c} du - \int_0^{x_1^+ + \epsilon} \frac{\Lambda(u)}{c} du}[1-\delta] = A_2 e^{-\int_0^{x_1} \frac{\Lambda(u)}{c} du - \int_0^{x_1^- + \epsilon} \frac{\Lambda(u)}{c} du}$$

implies $A_3[1-\delta] = A_2$.
Therefore, the stationary solution for a system with two identical particles can be written as,

$$P_{st} = A[1-\delta] e^{-\sum_{i=1}^{2} \int_0^{x_i} \frac{\Lambda(u)}{c} du}$$

where A is the arbitrary constant in the outer region. Note that, the collision probability δ is invariant to switch of particles, and we still adhere to the low volume fraction assumption. Using a similar approach, we can show that vector flux is zero for a system of three identical particles and establish the stationary solution

$$P_{st} = A[1-\delta]^2 e^{-\sum_{i=1}^{3} \int_0^{x_i} \frac{\Lambda(u)}{c} du}.$$

In two dimensions (two particles), the inner region is a diagonal of width 2ϵ (see Figure 2.2(a)), and we have already computed the density jump, which changes from a factor of $(1-\delta)$. In three dimension (three particles), a slab of the same width along the diagonals represent the inner regions. As depicted in Figure (2.10) when one particle is fixed at x_1, the density changes from $1-\delta$ when first enters from the inner slab of the second particle

and then from $(1-\delta)^2$ further from the inner slab of the third particle. If the system has $n(< N)$ interacting particles, one particle has $n-1$ inner regions.
i.e. for position index $i \neq j$, define

$$\phi(x_i, x_j) = \begin{cases} 1 & |x_i - x_j| \leq \epsilon \\ 0 & |x_i - x_j| > \epsilon \end{cases}$$

Then,

$$n(\phi) = \sum_{i=1}^{N-1} \sum_{j=i+1}^{N} \phi(x_i, x_j)$$

Thus, we can write the steady state solution as

$$\begin{aligned} P_{st}(\vec{x}) &= A[1-\delta]^{n(\phi)} e^{-\sum_{i=1}^{N} \int_0^{x_i} \frac{\Lambda(u)}{c} du} \\ \text{with the normalisation condition} \quad & \int_{\Omega^N} P_{st} d\vec{x} = 1 \end{aligned} \tag{2.50}$$

If all the particles are noninteracting, then $\delta \to 0$ and

$$P_{st}(\vec{x}) = A e^{-\sum_{i=1}^{N} \int_0^{x_i} \frac{\Lambda(u)}{c} du} \tag{2.51}$$

2.7.2 The Metropolis-Hastings algorithm Integrating (2.50) in higher-dimension and direct calculation of A may not be feasible; instead, let us move to the application of MH algorithm to the stationary state of our model. To begin, let $\Phi(\vec{x}) = \sum_{i=1}^{N} \int_0^{x_i} \frac{\Lambda(u)}{c} du$ be the energy associated with the configuration $\vec{x} \in \Omega^N$. Then, the stationary density (2.50) becomes

$$P_{st}(\vec{x}) = A[1-\delta]^{n(\phi)} e^{(-\Phi(\vec{x}))} \quad \text{for} \quad \vec{x} \in \Omega^N \tag{2.52}$$

Note that Φ is not defined outside the domain; therefore, we set $\Phi(\vec{x}) = \infty$ for $\vec{x} \notin \Omega^N$. The MH algorithm samples configurations according to the density P_{st} as follows:

S1 Select a particle i at random and calculate the close encounters with the other $\mathbf{x}_j$s for $i \neq j = 1, 2, ..., N$.

S2 Generate a candidate $\mathbf{y}_i = \mathbf{x}_i + hX$ where $X \sim N(0,1)$ and h a tunable parameter.

S3 Count the close encounters with $\mathbf{y}_i$ and $\mathbf{x}_j$s for $i \neq j = 1, 2, ..., N$. (the difference of above counts in step 1 and 3 $= (n-1)$)

S4 Compute the difference $\Delta\Phi$ between the current and modified configurations

S5 Accept $\mathbf{y}_i$ with probability $p = \min(1,(1-\delta)^{n-1}\exp(\text{-}\Delta\Phi))$ and set $\mathbf{x}_{i+1} = \mathbf{y}_i$, otherwise set $\mathbf{x}_{i+1} = \mathbf{x}_i$

At the i^{th} iteration, the candidate $\mathbf{y}$ is generated from a randomly chosen particle and displaced it by a normal random distance. It is essential to understand how the density function changes with the randomly chosen particle. Therefore, in steps S1-S3, we compare the close encounters before and after modifying each selection. Both the displacement of the randomly chosen particle and the acceptance rate controls by the tunable parameter h. If it is too small, the chain will converge slowly; on the other hand, if it is too large more likely to get a lower acceptance rate. It has been established that for high-dimensional target distributions formed by independent and identically distributed components, the optimal acceptance rate approaches 0.234 [82]. We used $h = 0.1$, and it does not change the rate of convergence drastically. The calculation of the acceptance probability does not require knowledge of the normalisation constant. Moreover, the higher the $\Delta\Phi$, the lower the probability of acceptance.

2.7.3 Numerical comparison of stationary solutions

From the one dimensional form of the turning frequency (1.12), we get $\Lambda = -2c\chi D_x S$. Then, the equilibrium solution (2.46) becomes

$$p_{st} = \frac{1}{\xi} W(A\xi e^{2\chi(S(x)-S(0))})$$

With the signal function $S(x)$, the expression for the Lambert W function is too complicated to be analysed by the ordinary calculus; therefore, we use Matlab function `fminsearch` of `norm` of the integral to estimate the constant A. Nevertheless, one can also use the NR method.

Figure (2.11) shows the model and simulation results with N = 100 for both point and finite-size particles of size $\epsilon = 0.002$ and unit speed. In a narrow channel of length $[0, 1]$ this corresponds to 0.0314 fraction of filled volume. The width of the channel determines the collision probability; for $l > 0.004$, particles can pass each other, while $l = 0.004$ turns it into a full-collision system. In accordance with the transient solutions, we choose $l = 0.01$ which returns $\delta = 0.4375$. The histograms for the MH algorithm are produced by dividing the domain into 40 bins, and initially the particles are evenly spaced in the domain. An acceptance rate in the 0.1 order of magnitude, and 10^6 steps of the algorithm produce the desired results. We monitor the number of particles in each bin at

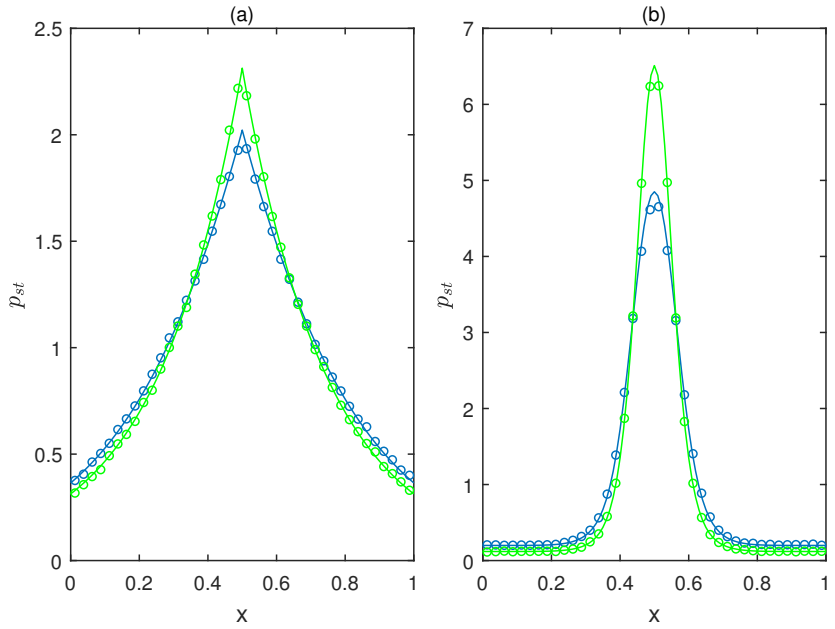

Figure 2.11: Stationary marginal density p_{st} (solid lines) and the simulations from the MH algorithm (circles) for $\epsilon = 0$ (green) and $\epsilon = 0.002$ (blue). (a) Solutions corresponding to the signal function (2.3(a)). (b) Solutions corresponding to (2.3(b)).

every step: when a proposed move is rejected, the old configuration is added over to the count, whereas if the move is accepted, the new configuration is added. At the end of the process, the cumulative average is calculated; dividing the resulting value in each bin by the number of steps, total particle count and bin width.

The stationary solution of the kinetic model agrees well with the particle simulation results for both interacting and noninteracting systems. As in time-dependent solutions, we see a lower density around the peak of the signal functions for finite-size particles. Even though we did not include stationary solutions from the single-file channel, we expect a much lower peak in this situation unless for considerably smaller particle size [2]. A narrow channel allows some overlaps based on the passing probability around the maximum point of the signal while the colliding individuals redistribute to other accessible areas in the domain.

2.8 Summary

This chapter has considered a system of N identical interacting hard-cores of size ϵ and unit speed in a narrow bounded channel that undergoes a velocity-jump process. These

[2]Stationary solutions for the single-file channel (collision system) has already been studied in [81]

random changes in the velocity are instantaneous and distributed according to a Poisson process. The finite-size of particles means that the motions are correlated; the interactions in a narrow channel give rise to the so-called interface conditions. From a high-dimensional PDE, we obtained the kinetic model under the small volume fraction assumption whilst considering the interactions at the particle level. The equations are nonlinear in the transport term, and it incorporates a collision probability that resembles a collision system at its maximum value. We have verified the model with numerical simulations, comparing its solutions with the corresponding stochastic simulations of the underlying particle system as well as against the interaction-free linear system. The plots confirm that the model captures the features at the particle level rather well. Besides, we have implemented both time-dependent and stationary simulations of the system. The time-dependent solutions are non-dissipative as we have considered a systematic approach based on characteristics for hyperbolic balance laws. Note that, we do not comment on the collision system's outputs as they are examined already in [81] following different conditions. The study of this core model allows extensions in many directions. In the following chapter, we will be considering distinguishable particles in a narrow channel. Another interesting but complicated extension is that considering anisotropic particles to examine how the transport model changes with noncircular particles [78].

3

Multiple species in a narrow channel

3.1 Introduction

This chapter extends the model of identical hard cores in a narrow channel to several particles. Specifically, we allow two species in the system and each population to have a different number of particles with different sizes. We name these species the blues and reds [13] and intend to derive a continuum model that describes the evolution of each species' population density. The analysis will yield a coupled system of nonlinear transport equations, one for each species. The procedure is similar to Chapter 2, although now interactions among identical species as well as opposite species are possible. Only the latter type of interactions involving one blue particle and one red particle must be computed; the former is similar to what we did for one species. The integration step produces an unknown collision term to be determined using the asymptotic expansion.
The common lattice-based modelling approach for multi-species size exclusion has been employed to develop models for facing pedestrian traffic on a passage [65], interacting bath-tracer particles inside a narrow channel [60] and subpopulation cell motility within a large population of cells [90], in which the particle's motion is restricted, and one defines hopping rules to estimate the interactions. Nevertheless, we have already learned the drawbacks of these kinds of on-lattice models. Surendran et al. [94] investigated a lattice-free IBM and its macroscale continuum approximation considering interactions between individuals in a population consists of two distinct species; chasers and escapees. Unlike our finite-size exclusion model, the interplays are attractions or repulsions, leading

to four types of interactions.
We begin the next section by writing down the particle level model for the two species in the population. The species have a small memory effect allowing them to sense the chemical concentrations along their trajectory and respond to gradients of concentrations. We then derive the continuum model for the one-particle density functions. This setting of keeping two distinct densities in the continuum model enables us to describe the evolution of a single tagged particle and transport through static obstacles. As in the previous chapter, we compare numerical solutions of the coupled system with the full particle simulations and validate the model; however, we use a standard numerical method this time as the characteristics are much more complicated in the balance laws.

3.2 Two species particle-level model

Consider a system which consists of N_b blue and N_r red hard discs (or spheres) of non-dimensional diameters ϵ_b and ϵ_r, respectively. The total number of particles $N = N_b + N_r$, and they are diffusing in a bounded one-dimensional domain of length $\Omega = [0, L]$. Regardless of the kind, every particle move either left or right with a constant speed $c \in \mathbb{R}^+$, and the blue (and red) particles switch their direction based on Poisson processes with rate $\lambda_b(x_i, v_i)$ (and $\lambda_r(x_i, v_i)$) where $x_i \in \Omega$ and $v_i \in V = \{-c, c\}$ for $i = 1, ..., N$. As before, we assume a low particle occupied fraction, so that $N_b\epsilon_b^d + N_r\epsilon_r^d \ll 1$. To give an instance, the occupied volume fraction in a narrow flattened pipe is $\pi\left(\left(\frac{\epsilon_b}{2}\right)^2 N_b + \left(\frac{\epsilon_r}{2}\right)^2 N_r\right)/lL$, where l is the width of the pipe.
Three types of pairwise interactions are possible: blue-blue, red-red, and blue-red; the lattermost is the one that needs to be computed. The two interacting individuals involving one blue particle and one red particle will be reflected at a distance $\epsilon_{br} = \frac{1}{2}(\epsilon_b + \epsilon_r)$ preserving both momentum and energy.
We may divide the position and velocity vectors to represent blue and red indices separately and re-write equation (2.1) for a two species system. Particularly, the higher-dimensional PDE in terms of the joint probability density $P(\vec{x}, \vec{v}, t)$ in space $(x_1, x_2, ..., x_{N_b}, x_{N_{b+1}}, ..., x_N) \in \Omega^N$ and velocity $(v_1, v_2, ..., v_{N_b}, v_{N_{b+1}}, ..., v_N) \in V^N$ at time t can be written as follows:

$$\frac{\partial P}{\partial t} + \vec{v}_b \cdot \nabla_{\vec{x}_b} P + \vec{v}_r \cdot \nabla_{\vec{x}_r} P + \sum_{i=1}^{N_b} [\lambda_b(x_i, v_i)P(\vec{x}, \vec{v}, t) - \lambda_b(x_i, -v_i)P(\vec{x}, s_i^b\vec{v}, t)] + \sum_{i=N_b+1}^{N} [\lambda_r(x_i, v_i)P(\vec{x}, \vec{v}, t) - \lambda_r(x_i, -v_i)P(\vec{x}, s_i^r\vec{v}, t)] = 0 \tag{3.1}$$

with the initial condition,

$$P(\vec{x}, \vec{v}, 0) = P_0(\vec{x}, \vec{v})$$

wall-particle boundary condition,

$$P(\vec{x}, \vec{v}, t) = P(\vec{x}, s_i\vec{v}, t) \quad \text{for} \quad x_i = 0, L$$

where s_i is the operator that switches the i^{th} velocity component regardless of the species, whereas s_i^b and s_i^r correspond to each species' turn. In other words,

$$s_i^b\vec{v} = (v_1, v_2, ..., -v_i, ..., v_{N_b}, ..., v_N) \quad \text{and} \quad s_i^r\vec{v} = (v_1, v_2, ..., v_{N_b}, ..., -v_i, ..., v_N).$$

In this chapter, we define switching rate (1.12) for different chemotactic sensitivity coefficient χ_b and χ_r. The initial distribution is invariant to the particle labels' permutations in that same species as they are identically distributed within the same kind. The configuration space now contains three different holes that are reachable by another or the same kind. It can generally be taken as $\left\{x_i \in \Omega^N : ||x_i - x_j|| > \frac{1}{2}(\epsilon_i + \epsilon_j), \quad \forall i \neq j\right\}$ where $\epsilon_i = \epsilon_b$ for $i \leq N_b$ and $\epsilon_i = \epsilon_r$ otherwise. In the passing regime, equation (3.1) is defined in Ω^N. There are four interface conditions for each particle type; that is when red particle entering (leaving) the excluded region of the blue (placed at x_i) and vice versa. These interface conditions are coupled as well as identical upon exchange of the blue and red labels.
At the left interface,

$$P^{+-}(x_i, x_i^- - \epsilon_{br}, t) = \delta P^{-+}(x_i, x_i^- - \epsilon_{br}, t) + P^{+-}(x_i, x_i^+ - \epsilon_{br}, t) \tag{3.2a}$$
$$P^{-+}(x_i, x_i^+ - \epsilon_{br}, t) = [1 - \delta]P^{-+}(x_i, x_i^- - \epsilon_{br}, t) \tag{3.2b}$$

and at the right interface,

$$P^{-+}(x_i, x_i^+ + \epsilon_{br}, t) = \delta P^{+-}(x_i, x_i^+ + \epsilon_{br}, t) + P^{-+}(x_i, x_i^- + \epsilon_{br}, t) \tag{3.3a}$$
$$P^{+-}(x_i, x_i^- + \epsilon_{br}, t) = [1 - \delta]P^{+-}(x_i, x_i^+ + \epsilon_{br}, t) \tag{3.3b}$$

where δ is the red-blue collision probability that depends on the particle sizes of blue, red and the width of the channel. Moreover, in a mixture of the two species, the interface conditions for a single variety also hold; hence requires collision probabilities α_b and α_r from ϵ_b and ϵ_r, respectively.
As seen in one species system, our goal is to reduce the higher-dimensional PDE (3.1) for

the joint density P to a low-dimensional PDEs for the marginal densities of one particle. In particular, we now have two marginal density functions, one for each blue and red particles. Since all the particles are identical within the same population, the marginal densities b and r for the first blue and last red can be written as,

$$b(x_1, v_1, t) = \int_{\Omega_{\epsilon_{br}}^{N-1}(x_1)\times V^{N-1}} P(\vec{x}, \vec{v}, t) dx_2 ... dx_N dv_2 ... dv_N$$

$$r(x_N, v_N, t) = \int_{\Omega_{\epsilon_{br}}^{N-1}(x_N)\times V^{N-1}} P(\vec{x}, \vec{v}, t) dx_1 ... dx_{N-1} dv_1 ... dv_{N-1}$$

where $\Omega^N(x_1)$ and $\Omega^N(x_N)$ denote slices of the configuration space Ω^N when blue particle is fixed at x_1 and red at x_N.

3.3 Population-level model

As in the previous chapter, we derive the low-dimensional PDEs for the marginal density of each species. The model reduction is straightforward for point particles. For finite-size particles, we begin with the transport equation for one blue particle and one red particle, and integrate it with respect to the configuration domain. Then from the systematic asymptotic expansion, we derive a coupled system of nonlinear hyperbolic equations.

3.3.1 Point particles When ϵ_b and ϵ_r are zero, the domain has no holes; thus, no interface conditions. The product solution

$$P(\vec{x}, \vec{v}, t) = \prod_{i=1}^{N_b} b(x_i, v_i, t) \prod_{i=N_b+1}^{N} r(x_i, v_i, t)$$

corresponds to N independent particles yields the evolution equations for the one-particle density functions b and r as

$$\frac{\partial b}{\partial t}(x, v_b, t) + v_b \frac{\partial b}{\partial x}(x, v_b, t) + \lambda_b(x, v_b) b(x, v_b, t) - \lambda_b(x, -v_b) b(x, -v_b, t) = 0 \qquad (3.4a)$$

$$\frac{\partial r}{\partial t}(x, v_r, t) + v_r \frac{\partial r}{\partial x}(x, v_r, t) + \lambda_r(x, v_r) r(x, v_r, t) - \lambda_r(x, -v_r) r(x, -v_r, t) = 0 \qquad (3.4b)$$

in $\Omega \times V$, with the initial conditions

$$b(x, v_b, 0) = b_0(x, v_b) \quad \text{and} \quad r(x, v_r, 0) = r_0(x, v_r) \qquad (3.5)$$

and the reflective boundary conditions

$$b(x, v_b, t) = b(x, -v_b, t), \qquad r(x, v_r, t) = r(x, -v_r, t) \quad \text{on} \quad x = 0, L \tag{3.6}$$

3.3.2 Interacting particles When $\epsilon_b, \epsilon_r > 0$, the particles are no longer independent, and the volume associate when they are close to each other is $\mathcal{O}(\epsilon_{br}^2 N)$ (for disks in a narrow flattened pipe). Here too, we assume a small occupied volume that leads to dominant pairwise interactions. Since we have already examined equations for identical particle pair interactions in the previous chapter, we now begin with one blue and one red particle. The system derives for a pair $N_b = 1$ and $N_r = 1$ can be readily extended to an arbitrary N.

For one blue particle (diameter ϵ_b) at position x_1 with velocity v_1 and one red particle (diameter ϵ_r) at position x_2 with velocity v_2, the transport equation (3.1) reads as

$$\begin{aligned}\frac{\partial P}{\partial t} + v_1\frac{\partial P}{\partial x_1} + v_2\frac{\partial P}{\partial x_2} + \lambda_b(x_1, v_1)P(\vec{x}, \vec{v}, t) - \lambda_b(x_1, -v_1)P(\vec{x}, -v_1, v_2, t) + \\ \lambda_r(x_2, v_2)P(\vec{x}, \vec{v}, t) - \lambda_r(x_2, -v_2)P(\vec{x}, v_1, -v_2, t) = 0\end{aligned} \tag{3.7}$$

with the interface conditions (3.2) and (3.3) defined for x_1 and x_2. The distinctive sizes of the individuals make the configuration space (2.2(a)) asymmetric along $x_2 = x_1$. In light of that, the space available to red particle when blue is fixed at x_1, explicitly, $\Omega = [0, L]$ with discontinuities at $x_1 \pm \epsilon_{br}$, where we define $\epsilon_{br} = \frac{1}{2}(\epsilon_b + \epsilon_r)$ for the convenience. The red passes the inner region of the blue with probability $1 - \delta$, where $\delta \equiv \delta(\epsilon_b, \epsilon_r, l)$.

The marginal density functions $b(x_1, v_1, t)$ and $r(x_2, v_2, t)$ are now read as

$$b(x_1, v_1, t) = \int_{\Omega \times V} P(\vec{x}, \vec{v}, t) dx_2 dv_2 \tag{3.8a}$$

$$r(x_2, v_2, t) = \int_{\Omega \times V} P(\vec{x}, \vec{v}, t) dx_1 dv_1 \tag{3.8b}$$

We proceed to obtain an equation for $b(x_1, v_1, t)$ with the support of the interface conditions and reflective boundary conditions; a similar procedure would yield the equation for the red marginal density $r(x_2, v_2, t)$. Integrating equation (3.7) over $\Omega \times V$, and following the steps in section (2.3.2.1) we derive the first three terms

$$\frac{\partial b}{\partial t} + v_1\frac{\partial b}{\partial x_1} + 2v_1[P(x_1, x_2, \vec{v}, t)|_{x_2 = x_1^+ - \epsilon_{br}}^{x_2 = x_1^+ + \epsilon_{br}} - P(x_1, x_2, \vec{v}, t)_{x_2 = x_1^+ - \epsilon_{br}}^{x_2 = x_1^- + \epsilon_{br}}] \tag{3.9}$$

Since $\sum_{v_2\in\{-c,c\}} \lambda_r(x_2,v_2)P(\vec{x},\vec{v},t) - \lambda_r(x_2,-v_2)P(\vec{x},v_1,-v_2,t) = 0$, the integral of the last term is zero. The remaining term $\lambda_b(x_1,v_1)P(\vec{x},\vec{v},t) - \lambda_b(x_1,-v_1)P(\vec{x},-v_1,v_2,t)$ results

$$\begin{aligned}\int_{\Omega\times V} \lambda_b(x_1,v_1)P(\vec{x},\vec{v},t) - \lambda_b(x_1,-v_1)P(\vec{x},-v_1,v_2,t)dx_2dv_2 = \\ \lambda_b(x_1,v_1)b(x_1,v_1,t) - \lambda_b(x_1,-v_1)b(x_1,-v_1,t)\end{aligned} \tag{3.10}$$

Combining equations (3.9) and (3.10) we get the integral of (3.7) over $\Omega\times V$ as

$$\begin{aligned}\frac{\partial b}{\partial t} + v_1\frac{\partial b}{\partial x_1} + 2v_1[P(x_1,x_2,\vec{v},t)|_{x_2=x_1^-+\epsilon_{br}}^{x_2=x_1^++\epsilon_{br}} + P(x_1,x_2,\vec{v},t)_{x_2=x_1^-+\epsilon_{br}}^{x_2=x_1^+-\epsilon_{br}}] + \\ \lambda_b(x_1,v_1)b(x_1,v_1,t) - \lambda_b(x_1,-v_1)b(x_1,-v_1,t) = 0\end{aligned} \tag{3.11}$$

Consequently, we can write the corresponding equation for $r(x_2,v_2,t)$ as well

$$\begin{aligned}\frac{\partial r}{\partial t} + v_2\frac{\partial r}{\partial x_1} + 2v_2[P(x_1,x_2,\vec{v},t)|_{x_1=x_2^-+\epsilon_{br}}^{x_1=x_2^++\epsilon_{br}} + P(x_1,x_2,\vec{v},t)_{x_1=x_2^-+\epsilon_{br}}^{x_1=x_2^+-\epsilon_{br}}] + \\ \lambda_r(x_2,v_2)r(x_2,v_2,t) - \lambda_r(x_2,-v_2)r(x_2,-v_2,t) = 0\end{aligned} \tag{3.12}$$

The next step is to find the unknown interaction term at the interfaces, and this can be proceeded according to section (2.3.2.2). The expression deriving for P is now depends on both the marginal densities b and r and it is not invariant to a switch of blue and red particle labels. Therefore when blue is fixed at x_1 (red moves independently on $[0,x_1-\epsilon_{br})$ and $(x_1+\epsilon_{br},L]$), for two arbitrary functions q_b and q_r we define

$$P_{out}(x_1,x_2,\vec{v}) = q_b(x_1,v_1)q_r(x_2,v_2) + \delta P_{out}^{(1)}(x_1,x_2,\vec{v})$$

in the outer region. In the inner region, the boundary layer coordinates changes to $x_1=\tilde{x}_1$ and $x_2=\tilde{x}_1+\epsilon_{br}\tilde{x}$, and the interface conditions (2.18) (the boundary layer coordinates produce the same interface conditions from (3.2) and (3.3)) yields following relations to $\mathcal{O}(\delta)$ and $\mathcal{O}(\delta\epsilon_{br})$ terms:

At the right interface,

$$\begin{aligned}\mathcal{O}(\delta) &: P_r^{(1)} - \tilde{P}_1 = q_b(\tilde{x}_1,c,t)q_r(\tilde{x}_1,-c,t) \\ \mathcal{O}(\delta\epsilon_{br}) &: \frac{\partial P_r^{(1)}}{\partial\tilde{x}_1} - \frac{\partial\tilde{P}_1}{\partial\tilde{x}_1} = q_b(\tilde{x}_1,c,t)\frac{\partial}{\partial\tilde{x}_1}q_r(\tilde{x}_1,-c,t)\end{aligned}$$

At the left interfarce,

$$\mathcal{O}(\delta) : \tilde{P}_1 - P_l^{(1)} = -q_b(\tilde{x}_1, -c, t) q_r(\tilde{x}_1, c, t)$$
$$\mathcal{O}(\delta\epsilon_{br}) : \frac{\partial P_l^{(1)}}{\partial \tilde{x}_1} - \frac{\partial \tilde{P}_1}{\partial \tilde{x}_1} = q_b(\tilde{x}_1, -c, t) \frac{\partial}{\partial \tilde{x}_1} q_r(\tilde{x}_1, c, t)$$

Now we evaluate the unknown interaction term at the two interfaces from the above outcomes.

$$\begin{aligned}
P(x_1, x_2, \vec{v})|_{x_2 = x_1^+ + \epsilon_{br}}^{x_2 = x_1^- + \epsilon_{br}} + P(x_1, x_2, \vec{v})_{x_2 = x_1^- - \epsilon_{br}}^{x_2 = x_1^+ - \epsilon_{br}} = \\
\tilde{P}(\tilde{x}_1, \tilde{x}, v_1, v_2, t)|_{\tilde{x}=1^-}^{\tilde{x}=1^+} + \tilde{P}(\tilde{x}_1, \tilde{x}, v_1, v_2, t)|_{\tilde{x}=-1^-}^{\tilde{x}=-1^+} = \\
\delta\big(P_r^{(1)} - \tilde{P}_1 + \tilde{P}_1 - P_l^{(1)}\big) + \delta\epsilon\Big(\frac{\partial P_r^{(1)}}{\partial \tilde{x}_1} - \frac{\partial \tilde{P}_1}{\partial \tilde{x}_1} + \frac{\partial P_l^{(1)}}{\partial \tilde{x}_1} - \frac{\partial \tilde{P}_1}{\partial \tilde{x}_1}\Big) = \\
\delta[q_b(\tilde{x}_1, c, t) q_r(\tilde{x}_1, -c, t) - q_b(\tilde{x}_1, -c, t) q_r(\tilde{x}_1, c, t)] + \\
\delta\epsilon_{br}\big[q_b(\tilde{x}_1, c, t) \frac{\partial q_r}{\partial \tilde{x}_1}(\tilde{x}_1, -c, t) + q_b(\tilde{x}_1, -c, t) \frac{\partial q_r}{\partial \tilde{x}_1}(\tilde{x}_1, c, t)\big]
\end{aligned}$$

We observe a significant difference in the resulting expression compared to the nonlinear term derived under identical and indistinguishable conditions, in which we found only the $\mathcal{O}(\delta\epsilon)$ contribution. We drop "$\sim$" on x_1 and use the normalisation condition on P to determine the functions q_b and q_r (see Appendix (A.1.2)). Thus, the evolution of blue marginal density is given by the nonlinear kinetic equation (omitting the time variable and use subscript notation for partial derivatives for ease of notation), to $\mathcal{O}(\epsilon_{br})$,

$$\begin{aligned}
\partial_t b + v_b \partial_x b + 2v_b N_r \delta[b(x,c) r(x,-c) - b(x,-c) r(x,c)] + 2v_b N_r \delta\epsilon_{br}\big[b(x,c)\partial_x r(x,-c) \\
+ b(x,-c)\partial_x r(x,c)\big] + 2v_b(N_b - 1)\alpha_b \epsilon_b \partial_x b b(x, -v_b) + \lambda_b(x, v_b) b(x, v_b) \\
- \lambda_b(x, -v_b) b(x, -v_b) = 0
\end{aligned} \tag{3.13a}$$

coupled with the kinetic equation for the red marginal density

$$\begin{aligned}
\partial_t r + v_r \partial_x r + 2v_r N_b \delta[r(x,c) b(x,-c) - r(x,-c) b(x,c)] + 2v_r N_b \delta\epsilon_{br}\big[r(x,c)\partial_x b(x,-c) \\
+ r(x,-c)\partial_x b(x,c)\big] + 2v_r(N_r - 1)\alpha_r \epsilon_r \partial_x r r(x, -v_r) + \lambda_r(x, v_r) r(x, v_r) \\
- \lambda_r(x, -v_r) r(x, -v_r) = 0
\end{aligned} \tag{3.13b}$$

in $\Omega \times \mathbb{R}^+$ and complemented with the initial condition (3.5), and the boundary condition (3.6). The δ, α_b and α_r are collision probabilities of red-blue, blue-blue and red-red, respectively. The above coupled system is the extended model for N_b blue and N_r red particles. This extension is possible up to $\mathcal{O}(\epsilon_{br})$ as pairwise interactions dominate at this order. For instance, in equation (3.13a) the N_r copies of the nonlinear term are from the blue-red inner regions. Similarly, the $N_b - 1$ copies of the nonlinear term are a contribution of pairwise interactions between identical particles.

Comparing the terms in distinguishing particles' nonlinear system with that of identical particles, we find the additional $\mathcal{O}(\epsilon_{br})$ transport term that enhances (or diminish) the diffusion. The third term is the leading-order contribution, and it did not appear in the indistinguishable particle situation. One can think of this term as a contribution to the density changes due to a collision, that simply vanishes when particles are identical.[1] The last two terms in both equations (3.13) are the loss and gain terms corresponding to the velocity jumps, explicitly given by

$$\lambda(x, v_b) = \lambda_0 - \chi_b v_b D_x S(x) \quad \text{and} \quad \lambda(x, v_r) = \lambda_0 - \chi_r v_r D_x S(x).$$

When the two species are identical, say $v_b = v_r$, $\epsilon_b = \epsilon_r$ and $\chi_b = \chi_r$, the collision probabilities $\delta = \alpha_b = \alpha_r$, as well as the governing equations of the densities b and r are the same. Then, if we begin with equal densities $b_0(x, v_b) = r_0(x, v_b)$ for $v_b \in \{-c, c\}$, we may set $b(x, v_b) = r(x, v_b) \quad \forall t > 0$. Consequently, the two species model retrieves the system for a single species.

$$\partial_t b + v_b \partial_x b + 2v_b(N_r + N_b - 1)\alpha_b \epsilon_b \partial_x b b(x, -v_b, t) + \lambda_b(x, v_b) b(x, v_b) \\ -\lambda_b(x, -v_b) b(x, -v_b) = 0$$

Note that, we will not connect the parameters (above stated) in the model (3.13); hence, they can be chosen independently.

3.3.3 Equilibria We compute the stationary solutions of the coupled nonlinear kinetic model (3.13), which we denote by b_{st} and r_{st}. In the case of point particles ($\epsilon_b = \epsilon_r = 0$),

[1] In the initial ordering, whether $x_1 < x_2$ or $x_1 > x_2$, one cannot distinguish between the particles after a collision when they are identical.

the equilibria are trivial as the system for b_s and r_s decouples and we get

$$b_{st}(x) = A_b e^{-\int_0^x \frac{\Lambda_b(y)}{c} dy} \tag{3.14a}$$

$$r_{st}(x) = A_r e^{-\int_0^x \frac{\Lambda_r(y)}{c} dy} \tag{3.14b}$$

where $\Lambda_b = \lambda_b^+ - \lambda_b^-$, $\Lambda_r = \lambda_r^+ - \lambda_r^-$ and A_b, A_r are constants to be determined using the normalisation condition. For finite-size particles, we rewrite the system in terms of the first two moments; the total densities $\rho_b = b^+ + b^-$, $\rho_r = r^+ + r^-$ and the fluxes $j_b = c(b^+ - b^-)$, $j_r = c(r^+ - r^-)$. Then the system become

$$\begin{aligned}
\frac{\partial \rho_b}{\partial t} + \frac{\partial j_b}{\partial x} &= 0 \\
\frac{\partial j_b}{\partial t} + c^2 \frac{\partial \rho_b}{\partial x} + 2cN_r\delta(\rho_r j_b - \rho_b j_r) + 2N_r\delta\epsilon_{br}\big(c^2\rho_b\frac{\partial \rho_r}{\partial x} - j_b\frac{\partial j_r}{\partial x}\big) + \\
\alpha_b\epsilon_b(N_b - 1)\frac{\partial}{\partial x}(c^2\rho_b^2 - j_b^2) + c(\lambda_b^+ - \lambda_b^-)\rho_b + (\lambda_b^+ + \lambda_b^-)j_b &= 0 \\
\frac{\partial \rho_r}{\partial t} + \frac{\partial j_r}{\partial x} &= 0 \\
\frac{\partial j_r}{\partial t} + c^2 \frac{\partial \rho_r}{\partial x} + 2cN_b\delta(\rho_b j_r - \rho_r j_b) + 2N_b\delta\epsilon_{br}\big(c^2\rho_r\frac{\partial \rho_b}{\partial x} - j_r\frac{\partial j_b}{\partial x}\big) + \\
\alpha_r\epsilon_r(N_r - 1)\frac{\partial}{\partial x}(c^2\rho_r^2 - j_r^2) + c(\lambda_r^+ - \lambda_r^-)\rho_r + (\lambda_r^+ + \lambda_r^-)j_r &= 0
\end{aligned}$$

Then continuing with the same procedure as in section (2.7), we get the coupled system of ODEs,

$$\begin{aligned}
c\frac{db_{st}}{dx} + 2cN_r\delta\epsilon_{br}b_{st}\frac{dr_{st}}{dx} + 2c\alpha_b\epsilon_b(N_b - 1)b_{st}\frac{db_{st}}{dx} + (\lambda_b^+ - \lambda_b^-)b_{st} &= 0 \\
c\frac{dr_{st}}{dx} + 2cN_b\delta\epsilon_{br}r_{st}\frac{db_{st}}{dx} + 2c\alpha_r\epsilon_r(N_r - 1)r_{st}\frac{dr_{st}}{dx} + (\lambda_r^+ - \lambda_r^-)r_{st} &= 0
\end{aligned}$$

where we set the equilibrium states of ρ_b and ρ_r to b_{st} and r_{st}, respectively. Observe the multi-species interaction addition to each equation in the system (compared with (2.45)). Integrating above, the resulting equations can be written as

$$\begin{aligned}
\ln b_{st} + 2N_r\delta\epsilon_{br}r_{st} + 2\alpha_b\epsilon_b(N_b - 1)b_{st} + \int_0^x \frac{\Lambda_b(y)}{c}dy &= A_b \\
\ln r_{st} + 2N_b\delta\epsilon_{br}b_{st} + 2\alpha_r\epsilon_r(N_r - 1)r_{st} + \int_0^x \frac{\Lambda_r(y)}{c}dy &= A_r
\end{aligned} \tag{3.15}$$

with the normalisation conditions $\int_0^L b_{st}(x)dx = \int_0^L r_{st}(x)dx = 1$. We find solutions for b_{st} and r_{st} with the Newton-Raphson method, discretising the domain into K grid points, approximating the normalisation integrals with a quadrature, and solving for $2K + 2$ unknowns.

3.3.3.1 Multiple species system via MH algorithm

Similar to (2.50), we first find the stationary density for the multi-species particle-level model. Then use the MH algorithm as in (2.7.2), though as particles can have different chemotactic sensitivity, care must be taken when defining the energy associated with each configuration. Note that, the candidate y_i generated in the second step of the algorithm may be either red or blue. Based on this selection, we count the distinct close encounters with x_j for $j = 1, 2, ..., N_b$ and for $j = N_b + 1, ..., N$ in the third step. In the fifth step, the acceptance probability of y_i is replaced by these reformulated stationary densities. We derive the following forms for the close encounters among identical and different species within the population.

Blue-Blue (or red-red): $n(\phi_k) = \sum_{i=1}^{N_k-1} \sum_{j=i+1}^{N_k} \phi_k(x_i, x_j)$,

where $\phi_k(x_i, x_j) = \begin{cases} 1, & |x_i - x_j| \leq \epsilon_k \\ 0, & |x_i - x_j| > \epsilon_k \end{cases}$ for $k = b$ or r.

Blue-Red (or red-blue): $n(\phi_{br}) = \sum_{i=1}^{N_k} \sum_{j=N_k+1}^{N} \phi_{br}(x_i, x_j)$,

where $\phi_{br}(x_i, x_j) = \begin{cases} 1, & |x_i - x_j| \leq \epsilon_{br} \\ 0, & |x_i - x_j| > \epsilon_{br} \end{cases}$

Imitating the process established in the section (2.7.1), under no-flux boundary conditions, the stationary densities become

$$\begin{aligned} B_{st}(\vec{x}) &= A_b[1-\delta]^{n(\phi_{br})}[1-\alpha_b]^{n(\phi_b)} \exp\{-\Phi(\vec{x})\} \\ R_{st}(\vec{x}) &= A_r[1-\delta]^{n(\phi_{rb})}[1-\alpha_r]^{n(\phi_r)} \exp\{-\Phi(\vec{x})\}, \end{aligned} \tag{3.16}$$

where Φ is the energy associated to configurations given by

$$\Phi(\vec{x}) = \sum_{i=1}^{N_b} \int_0^{x_i} \frac{\Lambda_b(y)}{c} dy + \sum_{i=N_b+1}^{N} \int_0^{x_i} \frac{\Lambda_r(y)}{c} dy \quad \text{for} \quad \vec{x} \in \Omega^N$$

To gain more insight into the expression (3.16), let us consider a system containing two blues and one red. For a blue particle (say fixed at x_1 as in Figure (3.1)), the density

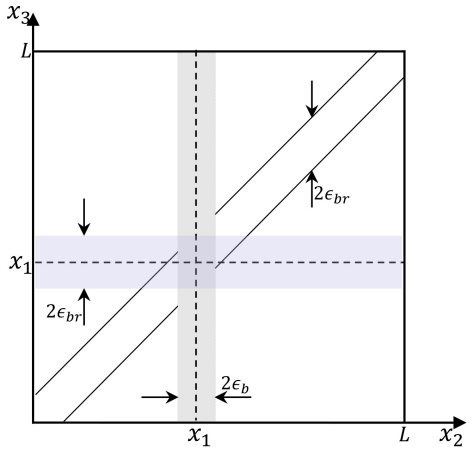

Figure 3.1: Schematic of the excluded domain for three interacting particles (two blues and one red) when a blue particle is fixed at x_1. The shaded areas show the inner slabs of width $2\epsilon_b$ and $2\epsilon_{br} = \epsilon_b + \epsilon_r$.

changes from $1-\delta$ when first enters from the inner slab of the red particle and then from $1-\alpha_b$ through the inner slab of the second blue particle, whereas for the red particle, the density changes from $1-\delta$ when first enters from the inner slab of the blue particle and then from $(1-\delta)^2$ further from the inner slab of the second blue particle. Therefore, we find

$$B_{st}(\vec{x}) = A_b[1-\delta][1-\alpha_b]\exp\{-\Phi(\vec{x})\} \quad \text{and} \quad R_{st}(\vec{x}) = A_r[1-\delta]^2\exp\{-\Phi(\vec{x})\}.$$

3.3.3.2 Numerical comparison

Eight examples of stationary solutions are shown in Figures (3.2) and (3.3) from the two signal functions (2.3(a)) and (2.3(b)), respectively. We have taken $N_b = 40$ blue particles of size $\epsilon_b = 0.002$ and $N_r = 60$ red particles of size $\epsilon_r = 0.001$ moving with a constant speed $c = 1$ inside a channel of length $L = 1$. Given the width of the channel and the sizes of the particles, the formula (A.3) produces the collision probabilities between identical as well as opposite species. We first take width $l = 0.01$ to add more overlaps and then narrow it down to $l = 0.003$ to increase collisions in the system. The red and blue solid lines (and dashed lines) indicate the stationary solutions derived from the equations (3.15) using NR method. Since this method is sensitive to the initial guess, we define initial densities through signal functions which provide estimates that are reasonably close to the solutions of the coupled system. When discretising the domain into K grid points, and approximating the normalisation integrals with quadrature, the density values

$b_{st}(x_i), r_{st}(x_i)$ for $1 \leq i \leq K$ and the two constants A_b, A_r yields a system of equations for $2K+2$ unknowns as follows:

$$\begin{aligned}
\ln Q_{\{1\leq k\leq K\}} + 2N_r\delta\epsilon_{br}Q_{\{K+1\leq k\leq 2K\}} + 2\alpha_b\epsilon_b(N_b-1)Q_{\{1\leq k\leq K\}} \\
-2\chi_b(S(x)-S(0)) - Q_{2K+1} = 0 \\
\ln Q_{\{K+1\leq k\leq 2K\}} + 2N_b\delta\epsilon_{br}Q_{\{1\leq k\leq K\}} + 2\alpha_r\epsilon_r(N_r-1)Q_{\{K+1\leq k\leq 2K\}} \\
-2\chi_r(S(x)-S(0)) - Q_{2K+2} = 0 \\
m\cdot Q_{\{1\leq k\leq K\}} - 1 = 0 \quad \text{and} \quad m\cdot Q_{\{K+1\leq k\leq 2K\}} - 1 = 0
\end{aligned} \tag{3.17}$$

where $Q = (b_{st}(:), r_{st}(:), A_b, A_r)$ and $m = \begin{pmatrix}1 & 4 & 2 & 4 & \dots & 4 & 1\end{pmatrix}$, the one dimensional quadrature. The simulations were initiated with orderly distributed blue ($i \leq N_b$) and red ($N_b < i \leq N$) particles in the domain. The domain is then divided into 40 bins and the histograms are computed with 10^7 steps of the MH algorithm. Again, the tuneable parameter 0.1 gives the desired outputs.

3.3.3.3 Discussion

The effect of reflective collisions on the equilibrium of a group of species that follow a velocity jump process has been examined in this section. We have computed the stationary solutions (3.14) and (3.15) for the respective point and finite-size particles systems. In Figures (3.2) and (3.3), we have included the results for latter case with different chemotactic sensitivity coefficients. We omit interaction-free plots from this figure as the results would be similar to those green plots in Figure (2.11), but one can still use them as the point of reference to understand the competition between the most favourable signal environment and the volume exclusion of finite-size particles; particularly, the blue plot in Figures (3.2 (a)) and (3.3 (a)), for $\chi_b = 1$.

Although the system contains more red particles, the domain occupied by blue (0.0126) is higher than the red (0.0047). This is because the size of a blue particle is twice the size of a red. Even so, we find a good agreement between the model (3.15) and the stochastic simulations for the narrow channel system throughout the domain. Besides, the higher passing rates encourage overlaps and hence the agreement. When the channel width is reduced to $l = 0.003$, only red particles overlap themselves; the rest of the interactions (red-blue and blue-blue) will end up being collisions. Note that, we have derived the equations for the perturbed system using the fact that $\delta \ll 1$, but we examine solutions for higher probabilities (closer to 1) as far as the model concerned.

Both species aggregate in and around the centre of the domain as expected, but each

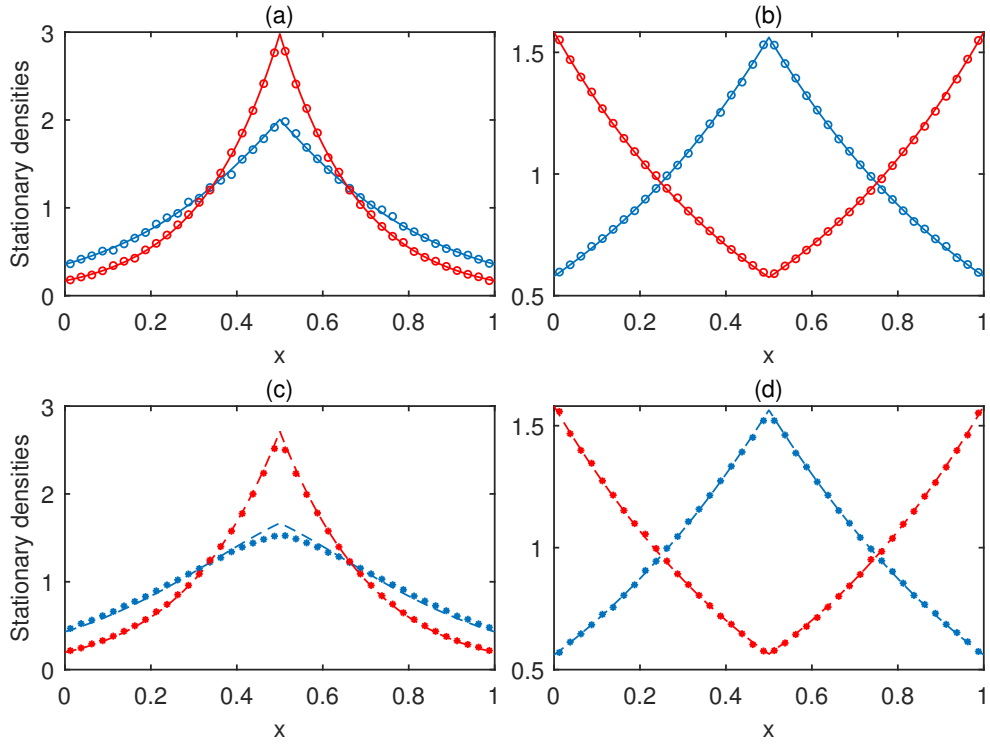

Figure 3.2: Stationary marginal densities b_{st} (blue) and r_{st} (red) from the signal function (2.3(a)) for particles in a channel of width 0.01 (solid lines) and 0.003 (dashed lines). Circles depict the histograms from the MH algorithm for the former model, while asterisks describe that for the latter model. Solutions in (a) and (c) are for $\chi_b = 1$ and $\chi_r = 1.5$; in (b) and (d) are for $\chi_b = 0.5$ and $\chi_r = -0.5$.

species' densities change according to its sensitivity toward the signal. One can think of the signal as a chemoattractant for positive chemotactic sensitivity coefficient while a chemorepellent for negative of that. In the first column of the Figures (3.2) and (3.3), $\chi_r > \chi_b > 0$; therefore, red densities are higher than that of blue where the signal maximise. The peaks are reduced in the collision system, and we see a noticeable deviation in the simulation results in Figure (3.3 (c)). This is because not all particles can aggregate at the centre according to the steep signal gradients of the signal (2.3(b)).

The red and blue particles accumulating to opposite ends for $\chi_r < 0$ and $\chi_b > 0$, and the outcomes are illustrated in the second column of the Figures (3.2) and (3.3). Particularly blues are attracted, and reds are repelled in the central part of the domain. A blue does not block a red at the centres and vice versa. However, particles disperse to less crowded areas. Consequently, we find a higher density of reds at either end of the domain. We do not observe significant changes in the densities from the collision system compared to the narrow channel. In fact, we see a reasonable closeness between the solutions and the particle simulations.

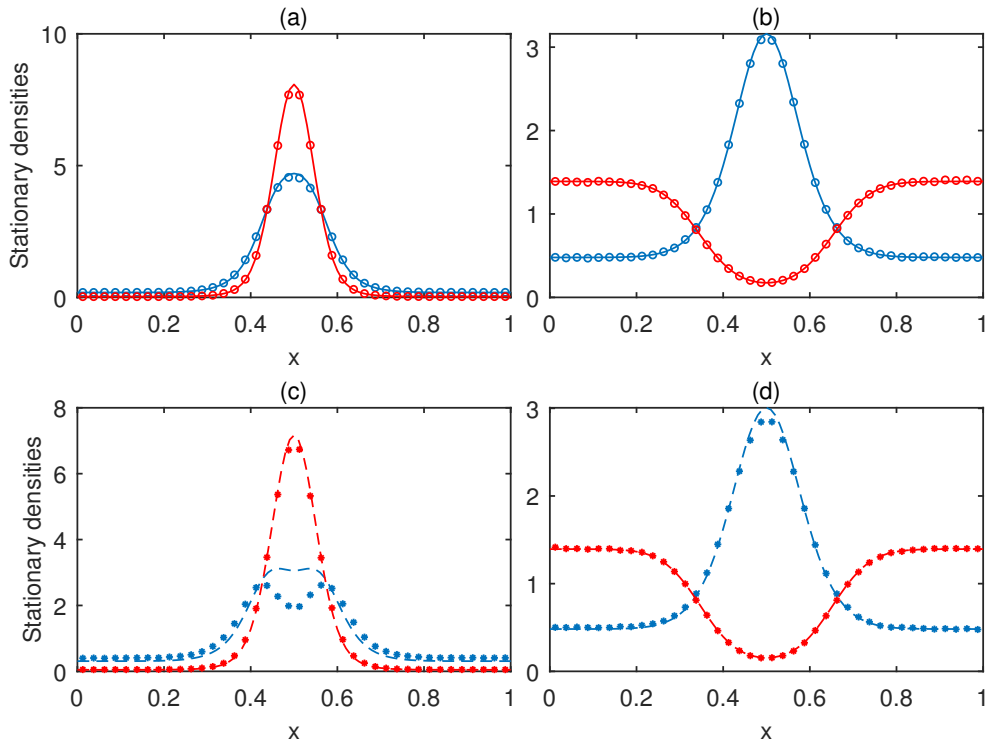

Figure 3.3: Stationary marginal densities b_{st} (blue) and r_{st} (red) from the signal function (2.3(b)) for particles in a channel of width 0.01 (solid lines) and 0.003 (dashed lines). Circles depict the histograms from the MH algorithm for the former model, while asterisks describe that for the latter model. Solutions in (a) and (c) are for $\chi_b = 1$ and $\chi_r = 1.5$; in (b) and (d) are for $\chi_b = 0.5$ and $\chi_r = -0.5$.

3.4 Multiple species time-dependent solutions

This section illustrates the time-dependent behaviour of the particle-based model and the population-based system with numerical simulations. We applied a solution strategy based on characteristics as eigenvalues and eigenvectors were readily available in the single-species model. However, with the nonlinear transport term from the opposite species interactions, the method becomes more complicated. Therefore, we resort to a standard numerical method to find transient solutions. We begin by writing the coupled system of equations in terms of the left- and right- moving densities and applying the periodic extensions as in (2.4). This initiation yields a non-conservative product due to $\mathcal{O}(\epsilon_{br})$ terms.

The system (3.13) may be rewritten in the form

$$\begin{aligned}
&\partial_t b^+ + c\partial_x b^+ + 2cN_r\delta[b^+r^- - b^-r^+] + 2cN_r\delta\epsilon_{br}\left[b^+\partial_x r^- + b^-\partial_x^+\right] + \\
&\qquad 2c(N_b-1)\alpha_b\epsilon_b\partial_x b^+b^- + \lambda_b(x,c)b^+ - \lambda_b(x,-c)b^- = 0 \\
&\partial_t b^- - c\partial_x b^- - 2cN_r\delta[b^+r^- - b^-r^+] - 2cN_r\delta\epsilon_{br}\left[b^+\partial_x r^- + b^-\partial_x^+\right] - \\
&\qquad 2c(N_b-1)\alpha_b\epsilon_b\partial_x b^-b^+ + \lambda_b(x,-c)b^- - \lambda_b(x,c)b^+ = 0
\end{aligned}$$

$$\begin{aligned}
&\partial_t r^- - c\partial_x r^- - 2cN_b\delta[r^+b^- - r^-b^+] - 2cN_b\delta\epsilon_{br}\left[r^+\partial_x b^- + r^-\partial_x b^+\right] - \\
&\qquad 2c(N_r-1)\alpha_r\epsilon_r\partial_x r^+r^- + \lambda_r(x,-c)r^- - \lambda_r(x,c)r^+ = 0 \\
&\partial_t r^+ + c\partial_x r^+ + 2cN_b\delta[r^+b^- - r^-b^+] + 2cN_b\delta\epsilon_{br}\left[r^+\partial_x b^- + r^-\partial_x b^+\right] + \\
&\qquad 2c(N_r-1)\alpha_r\epsilon_r\partial_x r^-r^+ + \lambda_r(x,c)r^+ - \lambda_r(x,-c)r^- = 0
\end{aligned}$$

Let $u_{b_1}(x,t)$ be the odd extension of $b^+ - b^-$ and $u_{b_2}(x,t)$ be the even extension of $b^+ + b^-$ together with the extensions $u_{r_1}(x,t)$ and $u_{r_2}(x,t)$ for the red densities. Then the modified system reads

$$\begin{aligned}
&\frac{\partial \vec{U_b}}{\partial t} + \frac{\partial F_b}{\partial x}(\vec{U_b}) + K_b(\vec{U_b})\frac{\partial \vec{U_r}}{\partial x} + S_b = G_b(x)\cdot\vec{U_b}, \\
&\frac{\partial \vec{U_r}}{\partial t} + \frac{\partial F_r}{\partial x}(\vec{U_r}) + K_r(\vec{U_r})\frac{\partial \vec{U_b}}{\partial x} + S_r = G_r(x)\cdot\vec{U_r}, \\
&\text{with the periodic boundary condition} \quad \vec{U_i}(-L,t) = \vec{U_i}(L,t)
\end{aligned} \tag{3.18}$$

where $\vec{U_i} = \begin{pmatrix} u_{i_1} \\ u_{i_2} \end{pmatrix}$ and flux terms $F_i(\vec{U_i}) = \begin{pmatrix} cu_{i_2} + c\alpha_i\epsilon_i(N_i-1)(u_{i_2}^2 - u_{i_1}^2) \\ cu_{i_1} \end{pmatrix}$ for $i = b, r$; $K_b(\vec{U_b}) = \begin{pmatrix} -2c\delta\epsilon_{br}N_r u_{b_1} & 2c\delta\epsilon_{br}N_r u_{b_2} \\ 0 & 0 \end{pmatrix}$ and $K_r(\vec{U_r}) = \begin{pmatrix} -2c\delta\epsilon_{br}N_b u_{r_1} & 2c\delta\epsilon_{br}N_b u_{r_2} \\ 0 & 0 \end{pmatrix}$ are the terms in the non-conservative products; $S_b = \begin{pmatrix} 2cN_r\delta \det(\vec{U_b}, \vec{U_r}) \\ 0 \end{pmatrix}$ and $S_r = \begin{pmatrix} 2cN_b\delta \det(\vec{U_r}, \vec{U_b}) \\ 0 \end{pmatrix}$; $G_i(x) = \begin{pmatrix} \mu_{i_2} & \mu_{i_1} \\ 0 & 0 \end{pmatrix}$ the source terms with $\mu_{i_1} = \lambda_i^- - \lambda_i^+$ and $\mu_{i_2} = -\lambda_i^- - \lambda_i^+$ for $i = b, r$.

Note that, the flux terms are similar to those in the single species system; hence, the Jacobian $\frac{\partial F_i}{\partial \vec{U_i}}$ produces eigenvalues for each separate system analogous to those in (2.32). The coupled equations in (3.18) can be further combined and written under the form:

$$\frac{\partial \mathbf{U}}{\partial t} + \mathcal{J}(\mathbf{U})\frac{\partial \mathbf{U}}{\partial x} = \mathbf{G}(x, \mathbf{U}) \tag{3.19}$$

where $\mathbf{U} = \begin{pmatrix} \vec{U_b} \\ \vec{U_r} \end{pmatrix}$, $\mathcal{J}(\mathbf{U}) = \begin{pmatrix} \frac{\partial F_b}{\partial \vec{U_b}} & K_b \\ K_r & \frac{\partial F_r}{\partial \vec{U_r}} \end{pmatrix}$ and $\mathbf{G} = \begin{pmatrix} G_b & O \\ O & G_r \end{pmatrix} \cdot \mathbf{U} - \begin{pmatrix} S_b \\ S_r \end{pmatrix}$. This integrated system's eigencharacteristics are more involved than that of the single-species model, leaving us no choice other than adapting one of the usual numerical schemes. To this end we follow the Roe-type path conservative schemes proposed by Parés and Castro [76].

We define an equidistant mesh size Δx with mesh interfaces $x_i = i\Delta x$ for $i \in \mathbb{N}$. As usual, the cell average at time t is given by

$$\mathbf{U}(x_i, t) = \frac{1}{\Delta x} \int_{x_i - \Delta x/2}^{x_i + \Delta x/2} \mathbf{U}(y, t) dy$$

Since the method is based on the theoretical notion of path, we first define a family of paths $\phi : [0,1] \times \mathbb{R}^4 \times \mathbb{R}^4 \to \mathbb{R}^4$ that satisfies the properties in ([76], Definition 1). We confine ourself to the simplest choice:

$$\phi(s; \mathbf{U}_L, \mathbf{U}_R) = \mathbf{U}_L + s(\mathbf{U}_R - \mathbf{U}_L) \quad \text{for} \quad s \in [0,1]$$

then a Roe linearisation $\mathcal{J}_\phi(\mathbf{U}_L, \mathbf{U}_R)$ can be defined such that ([76], Definition 3),

- $\mathcal{J}_\phi(\mathbf{U}_L, \mathbf{U}_R)$ has four distinct eigenvalues for any $\mathbf{U}_L, \mathbf{U}_R$,
- $\mathcal{J}_\phi(\mathbf{U}, \mathbf{U}) = \mathcal{J}(\mathbf{U}) \ \forall \ \mathbf{U}$,

- $\mathcal{J}_\phi(\mathbf{U}_L, \mathbf{U}_R) \cdot (\mathbf{U}_R - \mathbf{U}_L) = \int_0^1 \mathcal{J}(\phi(s; \mathbf{U}_L, \mathbf{U}_R))\partial_s\phi(s; \mathbf{U}_L, \mathbf{U}_R)ds$ for any $\mathbf{U}_L, \mathbf{U}_R$.

From the specified path, $\partial_s\phi = \mathbf{U}_R - \mathbf{U}_L$; hence, the elements of Roe matrix are simply the averages of $\mathbf{U}_L$ and $\mathbf{U}_R$. In the descretized system, the intermediate matrix is $\mathcal{J}_{i+1/2} = \mathcal{J}_\phi(U_i, U_{i+1})$ for $i \in \mathbb{N}$, and the CFL condition has the form

$$C = \frac{\Delta t}{\Delta x} \max\{|\Lambda_j|, 1 \leq j \leq 4\} \quad \text{for} \quad 0 < C \leq 1$$

where Λ_js are the eigenvalues of the matrix and Δt is the time step. We may now adapt the numerical scheme ([76], 4.63) as

$$\begin{aligned} \mathbf{U}_i(t + \Delta t) = \mathbf{U}_i(t) - \frac{\Delta t}{\Delta x}\left[F_{i+1/2} - F_{i-1/2}\right] - \frac{\Delta t}{2\Delta x}\left[B_{i+1/2} \cdot (\mathbf{U}_{i+1} - \mathbf{U}_i) + \right. \\ \left. B_{i-1/2} \cdot (\mathbf{U}_i - \mathbf{U}_{i-1})\right] + \frac{\Delta t}{2}\left[\mathbf{G}_{i+1/2} + \mathbf{G}_{i-1/2}\right] \end{aligned} \tag{3.20}$$

where $F_{i+1/2} = \frac{1}{2}\left[F(\mathbf{U}_{i+1}) + F(\mathbf{U}_i)\right] - \frac{1}{2}\left[\max\{|\Lambda_j^{i+1}, \Lambda_j^i|, 1 \leq j \leq 4\}\right](\mathbf{U}_{i+1} - \mathbf{U}_i)$, the Rusanov flux and
$B_{i+1/2} = \int_0^1 B(\phi(s; \mathbf{U}_i, \mathbf{U}_{i+1}))ds$, with B being the block matrix $\begin{pmatrix} O & K_b \\ K_r & O \end{pmatrix}$. The last term is obtained by applying the trapezoidal rule to the integral of $\mathbf{G}(x, \mathbf{U})$ over the interval $[x_i - \Delta x/2, x_i + \Delta x/2]$.

The solution of the particle-level model is obtained using the event-driven KMC method described in section (2.5.2). The only difference is that now we count interactions among red-blue particles by computing the collision times between reds and blues. Distinguishing between the two species, we must now construct two histograms, one for each population. The histograms were produced by dividing the domain into 40 bins. At each step, we count the number of blue and red particles in each bin; subsequently, the cumulative averages are calculated.

To corroborate our methods and to understand the importance of volume exclusions, we perform simulations of the discrete and continuum models for finite-size particles. The Figures (3.4),(3.5), (3.6) and (3.7) shows the results of time-dependent simulations of each species under different chemotactic sensitivity coefficients when $N_b = 60$, $N_r = 40$ and width of the flattened channel $l = 0.01$. To generate the plots in the first two figures, we set $\epsilon_b = 0.002$ and $\epsilon_r = 0.001$ that yields 31.95% red-blue, 43.75% blue-blue and 20.99% red-red collisions. Then halve the sizes of the species for the latter plots. Initially, the blue particles are uniformly distributed, that is $b_0(x) = 1$, and the red particles are normally distributed with 0.5 mean and standard deviation 1. The distribution is truncated so that

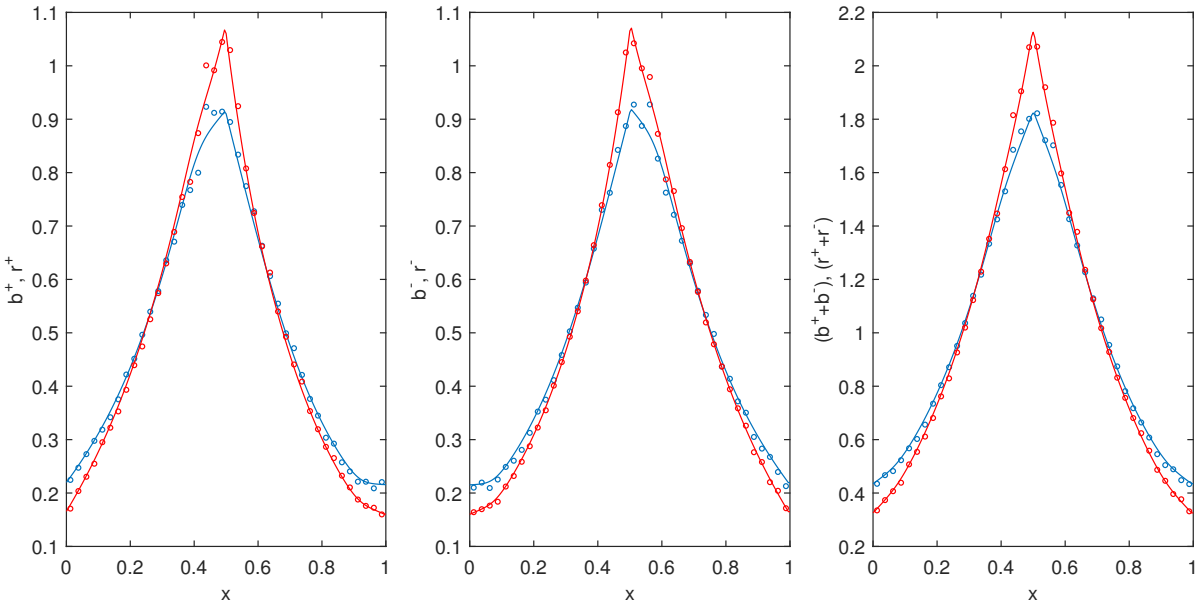

Figure 3.4: Transient marginal densities for the signal function (2.3(a)) at time $t = 0.4$. Blue particles of size $\epsilon_b = 0.002$ with $\chi_b = 0.5$ (blue line) and red particles of size $\epsilon_r = 0.001$ with $\chi_r = 1$ (red line). The collision probabilities $\delta(0.002, 0.001, 0.01) = 0.3195$, $\alpha_b(0.002, 0.002, 0.01) = 0.4375$ and $\alpha_r(0.001, 0.001, 0.01) = 0.2099$. Histograms computed from 5000 realisations (circles).

its integral over the domain Ω is one.

The theoretical predictions for finite-size particles compare well with their simulations in both types of external biases, while excluded volume effects are noticeable for opposite chemotactic sensitivities even though the volume fraction of particles is only 0.0055 (see Figure 3.6). This discrepancy is because the impediment is high from one species to another when they are moving away from each other. However, the agreement between the model solution and particle simulation is reasonable for steeper gradients (see Figure 3.7). For positive chemotactic sensitivities, subpopulations flow towards the maximum of the signal functions. Besides, the higher the sensitivity, the higher the aggregation at this location.

3.4.1 Without tumbling and bias In the simple case where $\lambda_i^{\pm} \equiv 0$ for $i = b, r$, no random changes will occur in the velocities of particles; the only changes are due to collisions. The solutions for noninteracting particles (3.4) are simply waves travelling at constant speed; $b^{\pm}(x,t) = b_0^{\pm}(x \mp ct)$ and $r^{\pm}(x,t) = r_0^{\pm}(x \mp ct)$. We expect the coupled nonlinear system to behave like the noninteracting particles linear system up to the point when the two fronts collide. Figure (3.8) shows the results of time-dependent simulations for point particles as well as finite-size particles ($\epsilon_b = 0.002$ and $\epsilon_r = 0.001$) with $N_b = 20$,

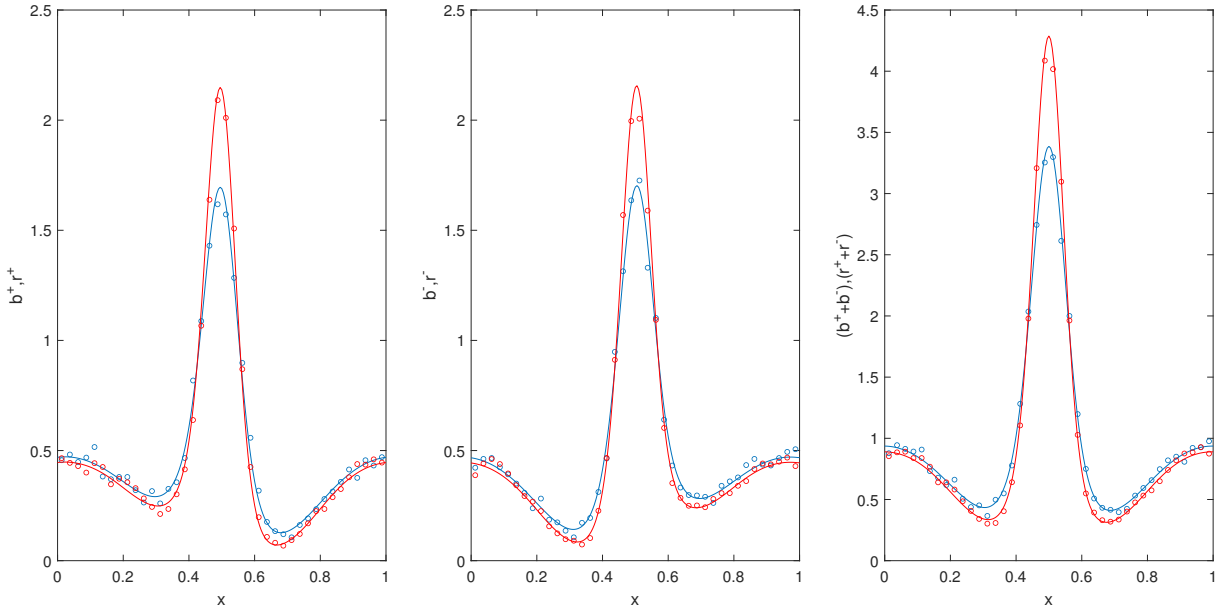

Figure 3.5: Transient marginal densities for the signal function (2.3(b)) at time $t = 0.4$. Blue particles of size $\epsilon_b = 0.002$ with $\chi_b = 1.0$ (blue line) and red particles of size $\epsilon_r = 0.001$ with $\chi_r = 1.5$ (red line). The collision probabilities $\delta(0.002, 0.001, 0.01) = 0.3195$, $\alpha_b(0.002, 0.002, 0.01) = 0.4375$ and $\alpha_r(0.001, 0.001, 0.01) = 0.2099$. Histograms computed from 500 realisations (circles).

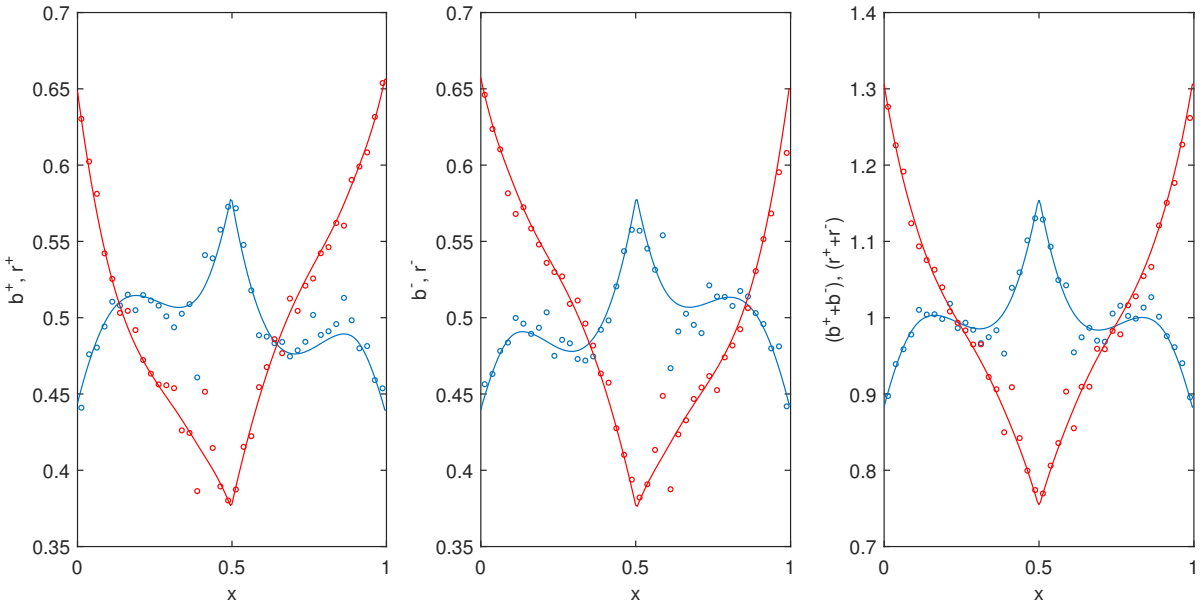

Figure 3.6: Transient marginal densities for the signal function (2.3(a)) at time $t = 0.4$. Blue particles of size $\epsilon_b = 0.001$ with $\chi_b = 0.5$ (blue line) and red particles of size $\epsilon_r = 0.0005$ with $\chi_r = -0.5$ (red line). The collision probabilities $\delta(0.001, 0.0005, 0.01) = 0.1550$, $\alpha_b(0.001, 0.001, 0.01) = 0.2099$ and $\alpha_r(0.0005, 0.0005, 0.01) = 0.1025$. Histograms computed from 5000 realisations (circles).

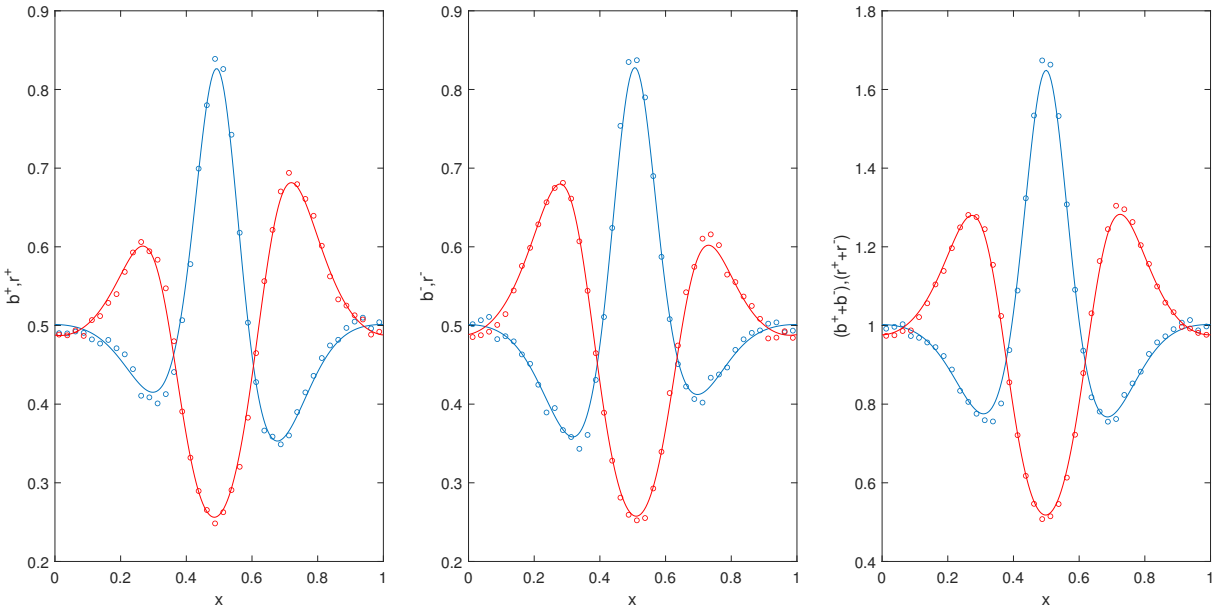

Figure 3.7: Transient marginal densities for the signal function (2.3(b)) at time $t = 0.4$. Blue particles of size $\epsilon_b = 0.001$ with $\chi_b = 0.5$ (blue line) and red particles of size $\epsilon_r = 0.0005$ with $\chi_r = -0.5$ (red line). The collision probabilities $\delta(0.001, 0.0005, 0.01) = 0.1550$, $\alpha_b(0.001, 0.001, 0.01) = 0.2099$ and $\alpha_r(0.0005, 0.0005, 0.01) = 0.1025$. Histograms computed from 500 realisations (circles).

$N_r = 100$ and $l = 0.01$. We initiate with the same initial conditions mentioned earlier and collate plots at different times.

It is evident from the plots that the initial uniform density of the blue particles does not change in time when size-exclusion effects are ignored (blue dash-dot line). In contrast, the non-uniform density of red particles pushes blue particles towards the domain edges when they are of finite size. The shift depends on the red's travelling direction; particularly, the red travelling to the right (or left) pushes blue to the right (or left) end. On the other hand, the red particles' initial profile, in which particles are dense in the centre of the domain, spreads faster when excluded-volume effects are included compared to interaction-free case (at time $t = 0.3$ and $t = 0.5$). This indicates that the collisions bias the spread towards areas of low particle densities.

3.4.2 Tagged particle

With a tagged particle, it is not the collective motion we are looking at anymore; it is now the movement of an individual particle. But higher densities of background particles impede the tagged particle diffusion, and excluded volume effects become complex. The Lorentz and Rayleigh gases are well studied in this context, where one assumes the only interactions present are between a unique particle of one species and a collection of particles of another species [57]. The linear Boltzmann equation has

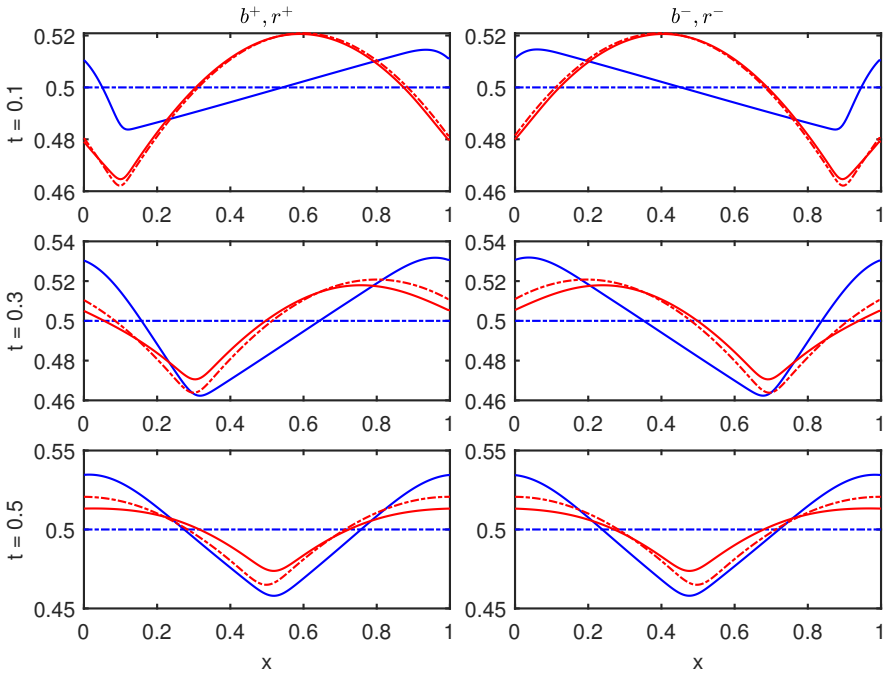

Figure 3.8: Transient marginal densities for the non-tumbling point (dash-dot lines) and finite-size particles (solid lines) when $N_b = 20$ (blue) and $N_r = 100$ (red). The collision probabilities $\delta(0.002, 0.001, 0.01) = 0.3195$, $\alpha_b(0.002, 0.002, 0.01) = 0.4375$ and $\alpha_r(0.001, 0.001, 0.01) = 0.2099$.

given the macroscopic evolution of the tagged particle density.

The advancement of a tagged particle over time is often monitored by the particle's mean-square displacement that can be related to the self-diffusion coefficient. It is well known that the mean square displacement scales linearly with time for interaction-free diffusion. However, when the tagged particle is immersed in a crowded system, it exhibits so-called anomalous subdiffusion diffusion. This effect is more apparent in narrow channel systems, especially single-file [6,49].

We compare the time-dependent solutions of an individual tagged particle in a crowded environment. We do this by colouring one particle in red, leaving the remaining particles to be blue. Setting $N_r = 1, N_b = N$, and $\epsilon_b = \epsilon_r = \epsilon$ in (3.13), under non-tumbling conditions give

$$\begin{aligned} \partial_t b + v_b \partial_x b + 2v_b \delta[b(x,c)r(x,-c) - b(x,-c)r(x,c)] + 2v_b \delta\epsilon\big[b(x,c)\partial_x r(x,-c) \\ + b(x,-c)\partial_x r(x,c)\big] + 2v_b(N-1)\delta\epsilon\partial_x b b(x,-v_b) = 0 \\ \partial_t r + v_r \partial_x r + 2v_r N\delta[r(x,c)b(x,-c) - r(x,-c)b(x,c)] + 2v_r N\delta\epsilon\big[r(x,c)\partial_x b(x,-c) \\ + r(x,-c)\partial_x b(x,c)\big] = 0 \end{aligned} \tag{3.21}$$

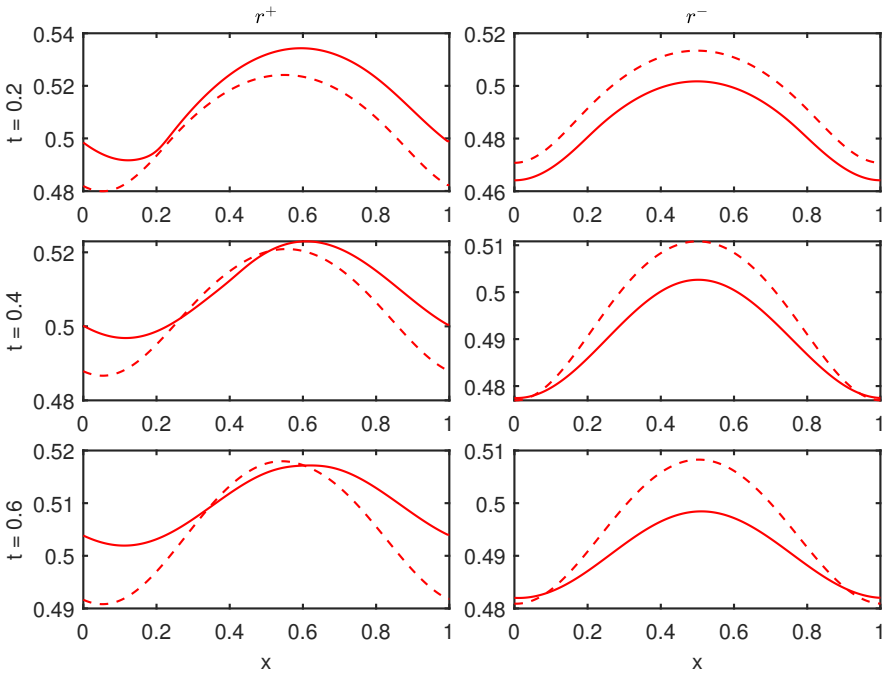

Figure 3.9: Transient marginal densities for the non-tumbling tagged red particle when $N = 50$ (solid lines) and $N = 100$ (dashed lines) blue particles. The particle's size is $\epsilon = 0.001$ and the channel width is $l = 0.01$ yields the collision probability $\delta(0.001, 0.001, 0.01) = 0.2099$.

Looking at the equation for the tagged red where particle's velocity changes are solely depended on the collisions, we see that mobility is affected by the crowders, the blues. For a better understanding, we compare the results of $N = 50$ and $N = 100$ crowders at a longer run time in Figure (3.9). All the particles are of size 0.001 and placed in a channel of width 0.01. At $t = 0$, the blues are uniformly distributed, while the tagged particle is normally distributed with 0.5 mean and standard deviation 1 with a positive velocity. That implies, initial $r^-(x)$ is zero. The tagged particle moves to the right until it collides with the crowders. This shift is more vivid in the solid line compared to the dashed at $t = 0.2$, because the red will be less unobstructed from a fewer number of crowders. The diffusion of tagged particles immersed in a densely populated domain gives rise to immediate collisions; therefore, $r^-(x, t)$ value rises and the dashed line is lies above the solid line in the top right plot. We do not observe a notable shift after time $t = 0.2$; instead, the tagged particle's density begins to spread. Although the concentrations are higher in the centre, the spread slows down with more crowders (see left plots at times $t = 0.4$ and $t = 0.6$).

In Figure (3.10), we compare tagged particle situation to the one-species collective motion. Since the red particle is identical to all the blue particles except in colour, we unlabeled it so that if the initial densities are the same, then $r^\pm \equiv b^\pm$ for all $x \in \Omega$ and the coupled

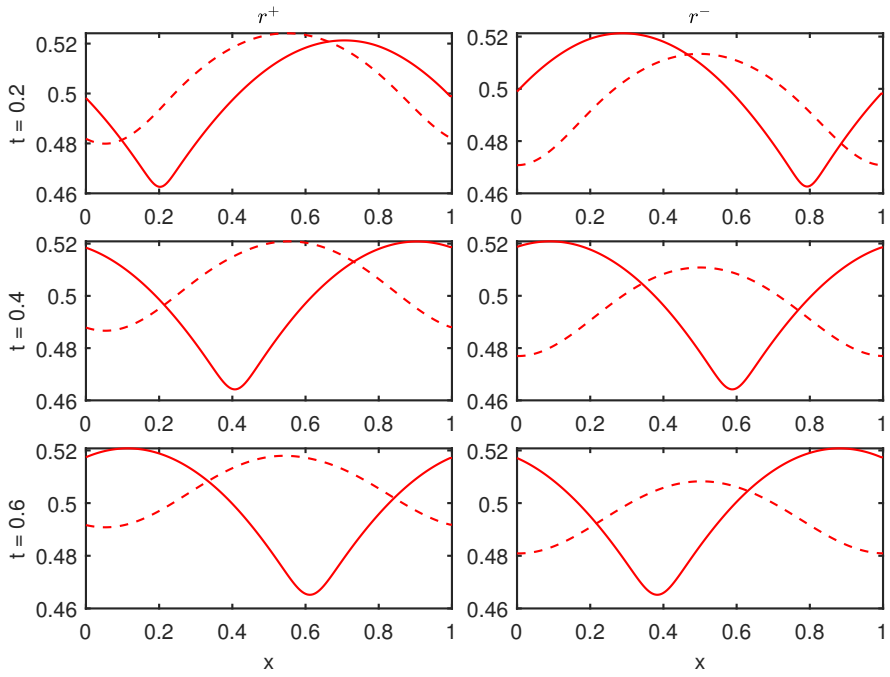

Figure 3.10: Transient marginal densities for the non-tumbling tagged red particle with $N = 100$ blue particles (dashed lines) and collective motion (solid lines) when $r^{\pm} \equiv b^{\pm}$ at $t = 0$. The collision probability $\delta(0.001, 0.001, 0.01) = 0.2099$.

system (3.21) yields

$$\partial_t r + v_r \partial_x r + 2 v_r N \delta \epsilon \partial_x r r(x, -v_r, t) = 0$$

that coincides with the equation (2.21) without switching rates. We consider a 0.79% occupied fraction for the comparison as the models perform well under small volume fractions. The same initial condition is applied to red particles and the subpopulation densities are plotted. We observe left and right moving travelling bands in the collective motion since particles are identical and indistinguishable (solid lines). In comparison, the tagged red concentration spread over the domain from the initial profile (dashed line) and the crowders undergo collective motion.

3.4.3 Transport through obstacles

The two species model (3.13) itself can be considered as one species diffusing through an obstacle. The only difference is that the obstacles are mobile crowders. We may use the same model to study the impact of having static obstacles in a system. This has been found in many different contexts: bacterial motility in porous media in which individual cells are hopping and intermittently trapping for a short time as they move through the pore space; the instantaneous speed

calculations of each cell differentiate the two modes [10], diffusion of probe molecules into absorbed polymer layers where the diffusion rate is reduced with the density of surface obstacles encountered by tracer molecules [83], protein transport in the plasma membrane where hopping becomes the primary transport mechanism under a high area fraction of obstacles [93], and in anomalous subdiffusion of inert tracer particles in the cytoplasm of mammalian cells where the embedded proteins provide an obstacle-rich environment [103].

Starting from the particle-level model described in section (3.2) for two interacting species; red and blue, we set the blue particle to be the static obstacle. The red particles switch their velocities due to collisions among themselves as well as with obstacles. While the former collisions are both momentum and speed preserving, the latter only preserve the speed. According to the new settings, we should re-evaluate the interaction term because the interface conditions change considerably. Particularly a red particle that passes the obstacle or reflects at the obstacle satisfies

$$\begin{aligned} P(x_r, x_b, v_r, 0, t)\big|_{x_b=x_r^-+\epsilon}^{x_b=x_r^++\epsilon} &= \delta P(x_r, x_r^+ + \epsilon, c, 0, t) \\ P(x_r, x_b, v_r, 0, t)\big|_{x_b=x_r^--\epsilon}^{x_b=x_r^+-\epsilon} &= -\delta P(x_r, x_r^- - \epsilon, -c, 0, t) \end{aligned}$$

as well as the integral (3.9) for red marginal density $r(x_r, v_r, t)$ reads

$$\frac{\partial r}{\partial t} + v_r \frac{\partial r}{\partial x_r} + v_r \left[P(x_r, x_b, v_r, 0, t)\big|_{x_b=x_r^-+\epsilon_{br}}^{x_b=x_r^++\epsilon_{br}} - P(x_r, x_b, v_r, 0, t)_{x_b=x_r^+-\epsilon_{br}}^{x_b=x_r^-+\epsilon_{br}} \right] \tag{3.22}$$

The obstacles' distribution $b(x, 0, t)$ is given by $b_0(x), t > 0$; hence, we find the equation

$$\begin{aligned} \partial_t r + v_r \partial_x r + v_r N_b \delta b_0(x)[r(x, c) - r(x, -c)] + v_r N_b \delta \epsilon_{br} \big[r(x, c) + r(x, -c)\big] \partial_x b_0(x) \\ +2v_r(N_r - 1)\alpha_r \epsilon_r \partial_x r r(x, -v_r) + \lambda_r(x, v_r) r(x, v_r) - \lambda_r(x, -v_r) r(x, -v_r) = 0 \end{aligned} \tag{3.23}$$

in $\Omega \times \mathbb{R}^+$, where δ is the collision probability of red-blue interaction, together with reflective boundary condition $r(x, v_r, t) = r(x, -v_r, t)$ on $\partial\Omega \times \mathbb{R}^+$. It is apparent that the result is the same as setting $b^{\pm}(x, t) = b^0(x)$ in (3.13b). Accordingly, we only need to consider equations for $\vec{U}_r$ from the extended system (3.18), where

$$K_r(\vec{U}_r) \frac{\partial \vec{U}_b}{\partial x} = \begin{pmatrix} 2c\delta\epsilon_{br} N_b u_{r_2} \partial_x b_0 \\ 0 \end{pmatrix} \quad \text{and} \quad S_r = \begin{pmatrix} 2c\delta N_b u_{r_1} b_0 \\ 0 \end{pmatrix}.$$

The two Figures (3.11) and (3.12) show the results of time-dependent simulations when $N_r = 60$ and $N_b = 40$ placed in a narrow channel of width $l = 0.01$. Blue obstacles

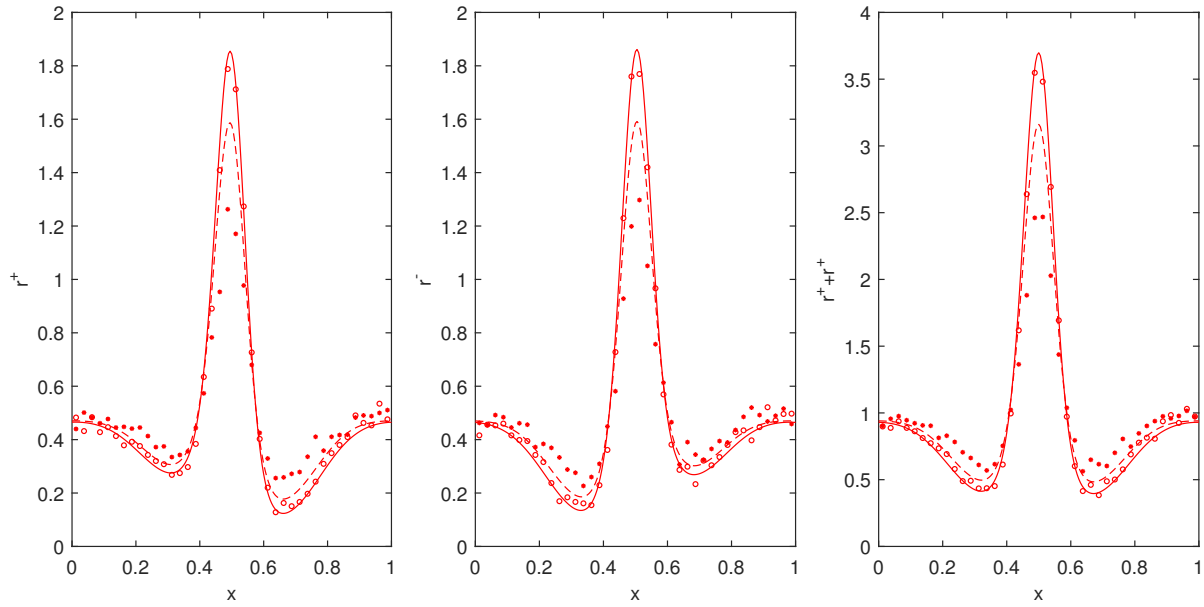

Figure 3.11: Marginal density of mobile red particles at time $t = 0.4$ when the blue obstacle sizes are $\epsilon_b = 0.002$ (solid line & circles) and $\epsilon_b = 0.005$ (dashed line & asterisks). Histograms computed from 500 realisations. The red particle size is $\epsilon_r = 0.001$ that yields collision probabilities $\delta = 0.3194$ for $\epsilon_b = 0.002$ and $\delta = 0.6444$ for $\epsilon_b = 0.005$. The collision probability α_r remains at 0.2099.

are uniformly distributed; $b \equiv 1$, and the initial density of the red particles is a one-dimensional Gaussian of mean 0.5 and standard deviation 1. In Figure (3.11), the solutions of the kinetic model (3.23) are compared with event-driven KMC simulations of the N-dimensional system for the obstacle sizes 0.002 and 0.005 at time $t = 0.4$. The size of the red particle is 0.001 with chemotactic sensitivity coefficient $\chi_r = 1.5$. Regardless of the obstacle size, the reds cluster around the signal's peak, but the density is reduced for the larger obstacle size as they block piling more reds in the centre of the domain. In fact, we do not see a good agreement between the model and the particle simulations. In contrast, there is a better agreement on the reduced obstacle size. Note that, red-red interactions influence the outputs in the same way for both cases as the collision likelihood among themselves does not change, whichever the obstacle size.

The plots in Figure (3.12) are generated assuming that the reds are under no external influence. Thus we concentrate on the behaviour of red subpopulations as they interact with the blue obstacles and themselves via excluded volume interactions. Here we compare both point ($\epsilon_r = 0$) and finite-size ($\epsilon_r = 0.001$) particles' solutions of (3.23) by setting the obstacle size to 0.002. For non-tumbling point red particles, the equation transforms to

$$\partial_t r + v_r \partial_x r + v_r N_b \delta b_0(x)[r(x,c) - r(x,-c)] + v_r N_b \delta \epsilon_{br}\big[r(x,c) + r(x,-c)\big]\partial_x b_0(x) = 0$$

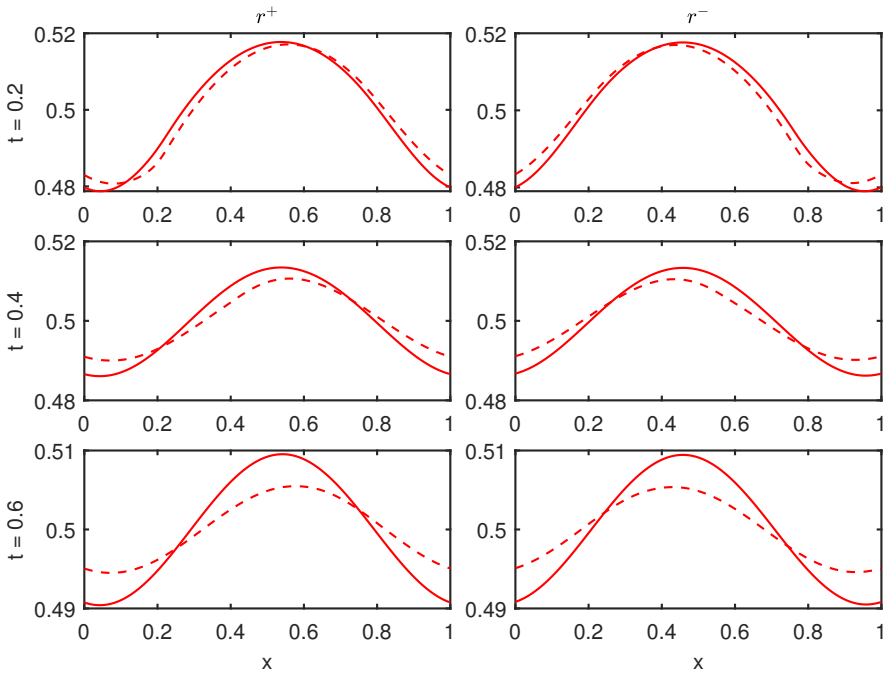

Figure 3.12: Transient marginal densities for red point particles (dashed lines) and finite-size particles (solid lines) at different times. The obstacle size is set to $\epsilon_b = 0.002$. The collision probabilities for the finite-size red-red $\alpha_r(0.001, 0.001, 0.01) = 0.2099$ and red-obstacle $\delta(0.002, 0.001, 0.01) = 0.3194$.

where $\epsilon_{br} = \epsilon_b/2$ and $\delta = \epsilon_b/l$. Their movement is unobstructed until it meets an obstacle, whereas a finite-size particle can be blocked by its kind. Therefore point particle's sub-populations are shifted more in their respective directions (dashed lines in Figure 3.12 at $t = 0.2$). The initial profile, in which red particles are concentrated in the centre, spreads more slowly for finite-size particles than for point particles indicating that the overall distribution of red is reduced. This behaviour is evident in both left- and right-moving reds after $t = 0.2$ (solid and dashed lines at $t = 0.4$ and $t = 0.6$).

3.5 Summary and discussion

We find many efforts to describe multiple species with size exclusion processes that have been directed at on-lattice models, where one takes the continuum limit of a discrete model and obtain a PDE describing the average occupancy of the agent population. However, less attention has been given to off-lattice systems with several species experience instantaneous tumbles or random changes in velocity. In this chapter, we examined such a scenario by predicting the macroscopic description of the particle-level attributes. Specifically, we allowed two interacting species of hardcore to have different sizes and chemosensitivities,

and extended the model derived in the previous chapter. The result is a coupled system of nonlinear transport equations for the two marginal probability densities associated to each species. Both identical and opposite species interactions emerge as nonlinear transport terms, involving coupling terms to interpret the inter-species communications in the narrow channel.

We have assessed the validity of our kinetic model to predict the system's behaviour by comparing its numerical solutions with the simulations of the discrete particle-based model. Both the stationary and time-dependent simulations agree well under low occupied fractions, supporting the notion that our PDE system captures the same population-level behaviour observed under expensive particle simulations. Our two-component nonlinear transport model is used to characterise the transport properties of a tagged particle system. A single tagged particle exhibits outspreading from its initial order rather than travelling bands (collective behaviour of identical particles). We also studied the motion of finite-size particles through static obstacles. In fact, one species itself can be considered as some sort of a mobile obstacle in our original model. The difference is that collisions bias the spread towards areas of low particle densities during the latter case, while immobile obstacles adversely affect the overall spread.

An interesting extension of two-species model is to study the role of the interactions and the speed synchronization of the travelling pulses when each population travels at different speeds in the channel [23,24]. The interface conditions can be handled assuming elastic collisions while reflecting at the solid boundaries. The summation term $\sum_{v_2 \in \{-c,c\}} (v_1 - v_2)[...]$ does not simplify to $2v_1[...]$; instead, it will produce additional terms corresponding to each velocity. One can also extended the model to examine heterogeneous population that is composed of agents from three different subpopulations [45].

4

Velocity-jumps with a finite set of speeds

4.1 Introduction

This chapter goes back to the velocity jump process analysed in Chapter 2 and introduces the zero velocity to the compact velocity space. That is, particles can now move either to the left or the right with a fixed speed c or suddenly become motionless. This transition from one velocity to another is reasonable since several organisms may tend to take a rest for a short time during the motion; a particular case could be narrow bands of chemical pheromone trails formation by ants while foraging for food [86]. The system still accounts for the excluded volume, and upon collisions, particles block each other until eventually a random velocity switch or a bypass frees them. We study the effect of elastic collisions between hard cores where particles exchange velocities after a collision. The speeds typically change during fully elastic collisions, but the total momentum of the system is preserved. If the system has at most two velocities $\{c, -c\}$, reflective and elastic collisions are equivalent. It should be noted that the set-up here is to introduce zero velocity to the system and is not to be confused with the case when one species is appearing as a static obstacle that has already been studied in section (3.4.3).

We begin by writing the PDE in terms of the joint probability density for the individual-based model description. As in previous chapters, we aim to reduce this high-dimensional PDE to a practical low dimensional description for the one-particle density under two

channel domains: single-file and a channel with a sufficiently large width so that occupants can easily change order. Asymptotic analysis in the limit of small volume fraction is performed, resulting in nonlinear transport terms that describe pairwise interactions among the three subpopulations. We adopt the characteristics method applied in the section (2.4) to find numerical solutions of the coupled system and compare them with the full particle simulations to validate the model. For a more comprehensive understanding, we generalise the derived nonlinear model for a velocity-jump process that comprises a finite set of speeds in section (4.3.3), and also reexamine the original system under reflective pair collisions in section (4.3.4). Interestingly, the resulting PDE for the latter system is similar to that of multiple species model when one species blocks the motion of the other.

4.2 Formulation of the particle-level model

To begin with, we consider a random motion of a point particle either at rest or moving at a constant speed c in one dimensional domain. That is, the system has a finite set of three possible velocities with the transition rate $\lambda_{v_2}^{v_1}$ in $[t, t+\Delta t]$, where $v_1, v_2 \in \{+c, 0, -c\}$ and $v_1 \neq v_2$. Denoting the one-particle density by $p(x, c, t)$ with position x and velocity c at time t, the probability of finding the particle in the interval $[a, b]$ can be written as

$$P\left(X(t) \in [a,b], V(t) = c\right) = \int_a^b p(x,c,t)dx$$

So we write the rate of change $\frac{dP}{dt}$ as

$$\int_a^b \frac{\partial p^+}{\partial t}(x,t)dx = cp^+(a,t) - cp^+(b,t) + \int_a^b p^0(x,t)\lambda_+^0(x)dx + \int_a^b p^-(x,t)\lambda_+^-(x)dx - \int_a^b p^+(x,t)\lambda_0^+(x)dx - \int_a^b p^+(x,t)\lambda_-^+(x)dx$$

where first two terms of the right hand side are for the rates of change when a particle enters at the boundary a and leaves from the boundary b; third and fourth are gain terms when switching to c; the last two terms are the loss terms when switching from c to 0 and $-c$. There is no contribution from the terms λ_+^+, λ_0^0 and λ_-^-.

By rearranging the terms we get

$$\int_a^b \left(\frac{\partial p^+}{\partial t} + c\frac{\partial p^+}{\partial x} - p^0\lambda_+^0 - p^-\lambda_+^- + p^+\lambda_0^+ + p^+\lambda_-^+ \right) dx = 0$$

Since $[a, b]$ is an arbitrary interval from $\mathbb{R}_0^+$, we get

$$\frac{\partial p^+}{\partial t} + c\frac{\partial p^+}{\partial x} - p^0\lambda_+^0(x) - p^-\lambda_+^-(x) + p^+\lambda_0^+(x) + p^+\lambda_-^+(x) = 0$$

Similarly, for the subpopulations with velocities 0 and $-c$, we have

$$\begin{aligned} \frac{\partial p^0}{\partial t} + p^0\lambda_+^0(x) + p^0\lambda_-^0(x) - p^+\lambda_0^+(x) - p^-\lambda_0^-(x) = 0 \\ \frac{\partial p^-}{\partial t} - c\frac{\partial p^-}{\partial x} + p^-\lambda_0^-(x) + p^-\lambda_+^-(x) - p^+\lambda_-^+(x) - p^0\lambda_-^0(x) = 0 \end{aligned}$$

where the transport term for a stationary particle disappears, and the rate of change only depends on velocity-jumps. Hence the above system of equations can be written in the following compact form for a point particle.

$$\frac{\partial p}{\partial t}(x, v, t) + v\frac{\partial p}{\partial x}(x, v, t) + \sum_{v' \in \{c,0,-c\}} \lambda_{v'}^v(x)p(x, v, t) - \lambda_v^{v'}(x)p(x, v', t) = 0 \tag{4.1}$$

An extension of the above model (4.1) for two particles is provided in the appendix (A.4). Thus for a system of N particles, the evolution of joint probability density $P(\vec{x}, \vec{v}, t)$, where $\vec{x} \in \Omega^N$ and $\vec{v} \in V^N = \{c, 0, -c\}^N$, is governed by the following transport equation:

$$\frac{\partial P}{\partial t} + \vec{v} \cdot \nabla_{\vec{x}} P + \sum_{i=1}^{N} \sum_{v' \in \{c,0,-c\}} \left(\lambda_{v'}^{v_i}(x_i)P(\vec{x}, \vec{v}, t) - \lambda_{v_i}^{v'}(x_i)P(\vec{x}, s_i'\vec{v}, t) \right) = 0, \tag{4.2}$$

where s_i' is the operator that changes the i^{th} velocity component to v'. Compared to particle level model (2.1) in Chapter 2, the reaction term (due to a random choice of velocity) contains additional transition terms as a result of the zero velocity component. The model completes with the initial condition

$$P(\vec{x}, \vec{v}, 0) = P_0(\vec{x}, \vec{v}) \tag{4.3}$$

and the wall-particle boundary condition (assuming reflective collisions at the solid boundaries)

$$P(\vec{x}, \vec{v}, t) = P(\vec{x}, s_i\vec{v}, t) \quad \text{for} \quad x_i = 0, L \tag{4.4}$$

where s_i is the operator that switches the sign of the i^{th} velocity component. It is now remaining to specify the conditions during interactions. These conditions may vary depending on the channel domain; particularly, particle interactions occur through collision boundary conditions in a single-file channel switches to interface conditions when particles collide with a certain probability that mimics the narrow channel. We intend to look through these interaction conditions between moving and stationary particles in-depth in the following section, and derive the population-level model for the marginal density p of one particle in a reduced dimensional space.

4.3 Population-level model

We derive the population-level model for identical hard disks of non-dimensional diameter $\epsilon \ll L$ in a bounded domain $\Omega = [0, L]$ that satisfies the linear, but higher-dimensional PDE model (4.2). We expect two nonlinear transport terms from the subpopulation interactions in the resulting PDE. The collision (single-file) and the narrow channel systems are studied under separate sections, and for both, we assume that the volume fraction is small. This assumption allows us to write down an integral equation for the one-particle density in terms of the two-particle joint density and later generalise for N.

4.3.1 Collision system In a one-dimensional collision system, particles cannot pass each other and remain ordered in the same manner as for the initial time. The hard cores create holes in the domain; hence, equation (4.2) is defined everywhere except at illegal configurations. So we redefine the configuration space as

$$\Omega_\epsilon^N = \{\vec{x} \in \Omega^N : |x_i - x_j| > \epsilon, \forall i \neq j\}.$$

Therefore, P satisfies the normalisation condition

$$\int\limits_{\Omega_\epsilon^N \times V^N} P(\vec{x}, \vec{v}, t) = 1.$$

Since particle-particle collisions are elastic, the collision boundary condition can be written as

$$P(\vec{x},\vec{v},t) = P(\vec{x},s_j^i\vec{v},t) \tag{4.5}$$

where s_j^i is an operator that swaps the velocity components i,j at $|x_i - x_j| = \epsilon$. We can now progress to obtain the population-level description for the one-particle density

$$p(x,v,t) = \int\limits_{\Omega_\epsilon^{N-1}(x)\times V^{N-1}} P(\vec{x},\vec{v},t)dx_2...dx_N dv_2...dv_N.$$

4.3.1.1 Integrated equation for a collision system

A system consist of two particles at (x_1,v_1) and (x_2,v_2) satisfy the transport equation

$$\begin{aligned}\frac{\partial P}{\partial t} + v_1\frac{\partial P}{\partial x_1} + v_2\frac{\partial P}{\partial x_2} + \sum_{v'\in\{c,0,-c\}} &\big(\lambda_{v'}^{v_1}(x_1)P(\vec{x},\vec{v},t) - \lambda_{v_1}^{v'}(x_1)P(\vec{x},s_1'\vec{v},t) \\ &+\lambda_{v'}^{v_2}(x_2)P(\vec{x},\vec{v},t) - \lambda_{v_2}^{v'}(x_2)P(\vec{x},s_2'\vec{v},t)\big) = 0\end{aligned} \tag{4.6}$$

Let $\Omega(x_1)$ be the space available for the second particle when first particle is at x_1; explicitly it is comprised of the left region $[0, x_1-\epsilon)$ and the right region $(x_1+\epsilon, L]$. Then integration of (4.6) over $\Omega(x_1)\times V$ produces a similar result as in section (2.3.2.1).

$$\begin{aligned}\frac{\partial p}{\partial t} + v_1\frac{\partial p}{\partial x_1} + \sum_{v_2\in V}(v_1-v_2)P(x_1,x_2,\vec{v},t)|_{x_2=x_1-\epsilon}^{x_2=x_1+\epsilon} + \sum_{v'\in V} &\big(\lambda_{v'}^{v_1}(x_1)p(x_1,v_1,t) \\ &-\lambda_{v_1}^{v'}(x_1)p(x_1,v',t)\big) = 0\end{aligned} \tag{4.7}$$

The first term comes from the independence of the configuration domain from time. The second and third terms come from integrating the transport terms $v_1\frac{\partial P}{\partial x_1}$ and $v_2\frac{\partial P}{\partial x_2}$, applying the Leibniz integral rule and wall-particle boundary conditions. Continuing to integral of the summation over the velocity-jumps,

$$\begin{aligned}&\int\limits_{\Omega(x_1)\times V}\sum_{v'\in V}\Big(\lambda_{v'}^{v_1}P(\vec{x},\vec{v},t) - \lambda_{v_1}^{v'}P(\vec{x},s_1'\vec{v},t) + \lambda_{v'}^{v_2}P(\vec{x},\vec{v},t) - \lambda_{v_2}^{v'}P(\vec{x},s_2'\vec{v},t)\Big) \\ &= \sum_{v'\in V}\Big(\lambda_{v'}^{v_1}p(x_1,v_1,t) - \lambda_{v_1}^{v'}p(x_1,v',t)\Big) + \int\limits_{\Omega(x_1)\times V}\sum_{v'\in V}\Big(\lambda_{v'}^{v_2}P(\vec{x},\vec{v},t) - \lambda_{v_2}^{v'}P(\vec{x},s_2'\vec{v},t)\Big)\end{aligned}$$

we note that

$$\sum_{v_2\in V}\sum_{v'\in V}\left(\lambda_{v'}^{v_2}(x_2)P(\vec{x},\vec{v},t)-\lambda_{v_2}^{v'}(x_2)P(\vec{x},s_2'\vec{v},t)\right)$$
$$=\sum_{v'\in V}\Big(\lambda_{v'}^{c}P(\vec{x},v_1,c,t)-\lambda_{c}^{v'}P(\vec{x},v_1,v',t)+\lambda_{v'}^{0}P(\vec{x},v_1,0,t)-\lambda_{0}^{v'}P(\vec{x},v_1,v',t)$$
$$+\lambda_{v'}^{-c}P(\vec{x},v_1,-c,t)-\lambda_{-c}^{v'}P(\vec{x},v_1,v',t)\Big)=0$$

Hence the only term remaining will be the loss and gain terms due to the velocity jumps of particle 1, which is the last term of (4.7).

4.3.1.2 Evaluating the collision term

To evaluate the collision term $P(x_1,x_2,\vec{v},t)|_{x_2=x_1-\epsilon}^{x_2=x_1+\epsilon}$, when two particles are far apart ($|x_1-x_2|\gg\epsilon$), we define $P_{out}(x_1,x_2,v_1,v_2,t)=P(x_1,x_2,v_1,v_2,t)$ as

$$P_{out}(x_1,x_2,v_1,v_2,t)=q(x_1,v_1,t)q(x_2,v_2,t)+\epsilon P_{out}^{(1)}(x_1,x_2,v_1,v_2,t)$$

for some distribution function q. In the inner region where $|x_1-x_2|\sim\epsilon$, we define the inner coordinates $x_1=\tilde{x}_1$ and $x_2=\tilde{x}_1+\epsilon\tilde{x}$. Then $\tilde{P}(\tilde{x}_1,\tilde{x},v_1,v_2,t)=P(x_1,x_2,v_1,v_2,t)$ and the collision boundary condition (4.5) becomes

$$\tilde{P}(\tilde{x}_1,\tilde{x},v_1,v_2,t)=\tilde{P}(\tilde{x}_1,\tilde{x},v_2,v_1,t)\quad\text{at}\quad\tilde{x}=\pm1 \tag{4.8}$$

Now expanding the outer solution in terms of the inner variables, we get

$$P_{out}(\tilde{x}_1,\tilde{x},v_1,v_2,t)=q(\tilde{x}_1,v_1,t)q(\tilde{x}_1,v_2,t)+\epsilon\left[\tilde{x}q\frac{\partial q}{\partial\tilde{x}_1}+P_{out}^{(1)}(\tilde{x}_1,v_1,v_2,t)\right] \tag{4.9}$$

We look for a solution in powers of ϵ; $\tilde{P}\approx\tilde{P}_0+\epsilon\tilde{P}_1+...$ that matches with the outer solution as $|\tilde{x}|\to\infty$. Since the leading order term satisfies (4.8), we find $\tilde{P}_0=q(\tilde{x}_1,v_1,t)q(\tilde{x}_1,v_2,t)$. If we suppose that $P_{out}^{(1)}\equiv P_r^{(1)}(\tilde{x}_1,\tilde{x}_1,\vec{v},t)$ for $\tilde{x}\geq1$ and $P_{out}^{(1)}\equiv P_l^{(1)}(\tilde{x}_1,\tilde{x}_1,\vec{v},t)$ for $\tilde{x}\leq-1$, the collision boundary condition (4.8) requires that $\mathcal{O}(\epsilon)$ terms to satisfy;
at the right boundary ($\tilde{x}=1$),

$$q(\tilde{x}_1,v_1,t)\partial_{\tilde{x}_1}q(\tilde{x}_1,v_2,t)+P_r^{(1)}=q(\tilde{x}_1,v_2,t)\partial_{\tilde{x}_1}q(\tilde{x}_1,v_1,t)+P_r^{(1)}(\tilde{x}_1,\tilde{x}_1,v_2,v_1,t) \tag{4.10}$$

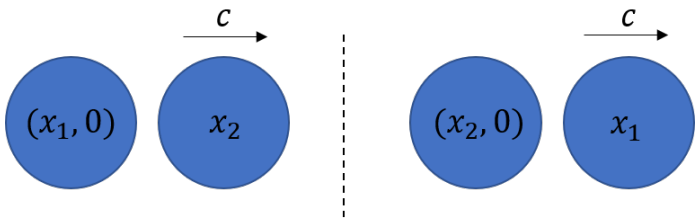

Figure 4.1: Configurations for identical and indistinguishable particles when $x_2 > x_1$ and $x_2 < x_1$.

and at the left boundary ($\tilde{x} = -1$),

$$-q(\tilde{x}_1, v_1, t)\partial_{\tilde{x}_1} q(\tilde{x}_1, v_2, t) + P_l^{(1)} = -q(\tilde{x}_1, v_2, t)\partial_{\tilde{x}_1} q(\tilde{x}_1, v_1, t) + P_l^{(1)}(\tilde{x}_1, \tilde{x}_1, v_2, v_1, t) \quad (4.11)$$

Therefore, we find the inner solution, to $\mathcal{O}(\epsilon)$,

$$\tilde{P}(\tilde{x}_1, \tilde{x}, v_1, v_2, t) = q(\tilde{x}_1, v_1, t)q(\tilde{x}_1, v_2, t) + \epsilon\left[\tilde{x}q\frac{\partial q}{\partial \tilde{x}_1} + P_{out}^{(1)}(\tilde{x}_1, \tilde{x}_1, v_1, v_2, t)\right] \quad (4.12)$$

that satisfies (4.10) and (4.11). We can relate $P_r^{(1)}$ and $P_l^{(1)}$ using the fact that particles are identical and indistinguishable. For instance, suppose $v_1 = 0$ and $v_2 = c$, then at the right outer region $P_{out}^{(1)} \equiv P_r^{(1)}(x_1, x_2, 0, c, t)$, but the same configuration can be obtained in the left outer region when $P_{out}^{(1)} \equiv P_l^{(1)}(x_1, x_2, c, 0, t)$ (see Figure (4.1)). Therefore, more generally we can write,

$$P_r^{(1)}(x_1, x_2, v_1, v_2, t) = P_l^{(1)}(x_1, x_2, v_2, v_1, t) \quad (4.13)$$

We may now evaluate the collision term $P(x_1, x_2, \vec{v}, t)|_{x_2=x_1-\epsilon}^{x_2=x_1+\epsilon} = \tilde{P}(\tilde{x}_1, \tilde{x}, \vec{v}, t)|_{\tilde{x}=-1}^{\tilde{x}=1}$, where $\mathcal{O}(\epsilon)$ terms yield,

$$\begin{aligned}
&q(\tilde{x}_1, v_1, t)\frac{\partial q}{\partial \tilde{x}_1}(\tilde{x}_1, v_2, t) + P_r^{(1)}(\tilde{x}_1, \vec{v}, t) + q(\tilde{x}_1, v_1, t)\frac{\partial q}{\partial \tilde{x}_1}(\tilde{x}_1, v_2, t) - P_l^{(1)}(\tilde{x}_1, \vec{v}, t) \\
&= q(\tilde{x}_1, v_1, t)\frac{\partial q}{\partial \tilde{x}_1}(\tilde{x}_1, v_2, t) + P_l^{(1)}(\tilde{x}_1, v_2, v_1, t) + q(\tilde{x}_1, v_1, t)\frac{\partial q}{\partial \tilde{x}_1}(\tilde{x}_1, v_2, t) - P_l^{(1)}(\tilde{x}_1, \vec{v}, t) \\
&= q(\tilde{x}_1, v_1, t)\frac{\partial q}{\partial \tilde{x}_1}(\tilde{x}_1, v_2, t) + q(\tilde{x}_1, v_2, t)\frac{\partial q}{\partial \tilde{x}_1}(\tilde{x}_1, v_1, t) \\
&= \frac{\partial}{\partial \tilde{x}_1}\left[q(\tilde{x}_1, v_1, t)q(\tilde{x}_1, v_2, t)\right]
\end{aligned}$$

We have used the inner solution (4.12), the relation (4.13) and the left boundary condition (4.11) in the first, second and third lines, respectively. From the normalisation condition (A.1.1) we find $q(x_1, v_1, t) = p(x_1, v_1, t) + \mathcal{O}(\epsilon)$; consequently, the nonlinear kinetic model

(4.7) for N interacting particles in a single-file channel can be written as,

$$\frac{\partial p}{\partial t} + v_1 \frac{\partial p}{\partial x_1} + \sum_{v_2 \in V} (v_1 - v_2)(N-1)\epsilon \frac{\partial}{\partial x_1} [p(x_1, v_1, t) p(x_1, v_2, t)] + \sum_{v' \in V} \left(\lambda_{v'}^{v_1}(x_1) p(x_1, v_1, t) - \lambda_{v_1}^{v'}(x_1) p(x_1, v', t) \right) = 0 \tag{4.14}$$

4.3.2 Narrow channel The idea is very much similar to the narrow channel model discussed earlier in Chapter (2), albeit we have stationary hard cores with elastic collisions. Since particles have three possible velocities, let us redefine the interface conditions (2.10) and (2.11) in a more general setting.
If two particles have velocities v_1 and v_2 that exchange after collisions; at the right interface,

$$P(x_1, x_1^+ + \epsilon, v_2, v_1, t) = \delta P(x_1, x_1^+ + \epsilon, v_1, v_2, t) + P(x_1, x_1^- + \epsilon, v_2, v_1, t) \tag{4.15a}$$

$$P(x_1, x_1^- + \epsilon, v_1, v_2, t) = [1 - \delta] P(x_1, x_1^+ + \epsilon, v_1, v_2, t) \tag{4.15b}$$

and at the left interface,

$$P(x_1, x_1^- - \epsilon, v_1, v_2, t) = \delta P(x_1, x_1^- - \epsilon, v_2, v_1, t) + P(x_1, x_1^+ - \epsilon, v_1, v_2, t) \tag{4.16a}$$

$$P(x_1, x_1^+ - \epsilon, v_2, v_1, t) = [1 - \delta] P(x_1, x_1^- - \epsilon, v_2, v_1, t) \tag{4.16b}$$

where $v_1, v_2 \in \{c, 0, -c\}$ and $\delta \equiv \delta(\epsilon, l)$ is the probability of collision. Mimicking the derivation process in section (2.3.2.1) with the above interface conditions and the boundary condition (4.4), integral of (4.6) over $\Omega \times V$ produces the PDE for the marginal density $p(x, v, t)$ analogous to (4.7):

$$\frac{\partial p}{\partial t} + v_1 \frac{\partial p}{\partial x_1} + \sum_{v_2 \in V} \delta(v_1 - v_2)(P(x_1, x_1^+ + \epsilon, v_1, v_2, t) - P(x_1, x_1^- - \epsilon, v_2, v_1, t)) + \sum_{v' \in V} \left(\lambda_{v'}^{v_1}(x_1) p(x_1, v_1, t) - \lambda_{v_1}^{v'}(x_1) p(x_1, v', t) \right) = 0 \tag{4.17}$$

Evaluating joint densities at the interfaces (see section (2.3.2.2)) and using the normalisation condition, we derive the population-level model for a narrow channel system that

contains stationary particles as

$$\frac{\partial p}{\partial t} + v_1 \frac{\partial p}{\partial x_1} + \sum_{v_2 \in V} \delta(v_1 - v_2)(N-1)\epsilon \frac{\partial}{\partial x_1}\left[p(x_1, v_1, t)p(x_1, v_2, t)\right] + \sum_{v' \in V} \left(\lambda_{v'}^{v_1}(x_1)p(x_1, v_1, t) - \lambda_{v_1}^{v'}(x_1)p(x_1, v', t)\right) = 0 \tag{4.18}$$

Both the systems (4.14) and (4.18) are complemented with no-flux boundary conditions on $\partial\Omega$ and the initial condition $p(x_1, v_1, 0) = p_0(x_1, v_1)$. The nonlinear transport terms obtained by the asymptotic expansion are accurate up to the first order ϵ, and the term count depend on the velocities (v_2 s) that the first particle, at x_1 with v_1, possibly contact. As far as the model concerned, when $\delta = 1$ we recover the kinetic model for the collision system; therefore, we consider the latter model to analysis time-dependent and stationary solutions. We expect a good agreement between stochastic simulations of the full particle system with the solution of the population-level equation.

From the given set of velocities $\{c, 0, -c\}$ equation (4.18) can also be written in terms of the subpopulation densities:

$$\frac{\partial p^+}{\partial t} + c\frac{\partial p^+}{\partial x_1} + c(N-1)\delta\epsilon\frac{\partial}{\partial x_1}(p^+p^0) + 2c(N-1)\delta\epsilon\frac{\partial}{\partial x_1}(p^+p^-) + \lambda_0^+(x_1)p^+ - \lambda_+^0(x_1)p^0 + \lambda_-^+(x_1)p^+ - \lambda_+^-(x_1)p^- = 0 \tag{4.19a}$$

$$\frac{\partial p^0}{\partial t} - c(N-1)\delta\epsilon\frac{\partial}{\partial x_1}(p^+p^0) + c(N-1)\delta\epsilon\frac{\partial}{\partial x_1}(p^0p^-) + \lambda_+^0(x_1)p^0 - \lambda_0^+(x_1)p^+ + \lambda_-^0(x_1)p^0 - \lambda_0^-(x_1)p^- = 0 \tag{4.19b}$$

$$\frac{\partial p^-}{\partial t} - c\frac{\partial p^-}{\partial x_1} - c(N-1)\delta\epsilon\frac{\partial}{\partial x_1}(p^-p^0) - 2c(N-1)\delta\epsilon\frac{\partial}{\partial x_1}(p^+p^-) + \lambda_0^-(x_1)p^- - \lambda_-^0(x_1)p^0 + \lambda_+^-(x_1)p^- - \lambda_-^+(x_1)p^+ = 0 \tag{4.19c}$$

where each equation consists of two nonlinear transport terms from the existing subpopulation interactions. In vectorial form with $\vec{p} = (p^+, p^0, p^-)$, we can write the gain terms as $\begin{pmatrix} 0 & \lambda_+^0 & \lambda_+^- \\ \lambda_0^+ & 0 & \lambda_0^- \\ \lambda_-^+ & \lambda_-^0 & 0 \end{pmatrix}$ that can be rewritten in terms of a constant (or constant matrix) κ: $\kappa \begin{pmatrix} 0 & \tilde{\lambda}_+^- & \tilde{\lambda}_+^0 \\ \tilde{\lambda}_-^+ & 0 & \tilde{\lambda}_-^0 \\ \tilde{\lambda}_0^+ & \tilde{\lambda}_0^- & 0 \end{pmatrix}$, where $\tilde{\lambda}_{v_1}^{v_2}$ s are transition probabilities such that each row adds upto one. This idea is similar to the turning kernel T defined in [71]. We assume non-zero transitions rates which are independent of time; therefore, transition probabilities are

stationary.

For bidirectional moving particles in section (2.3.2.3), we discussed the long-time dynamics of the kinetic model by taking the parabolic limit. The approach works for the current system (4.19) with the same flux function $j(x,t)$ and total density $\rho(x,t) = p^+ + p^0 + p^-$ (see Appendix (A.5) for details), returning the drift-diffusion equation

$$\frac{\partial \rho_0}{\partial \tau} = \frac{\partial}{\partial \zeta}\left[\frac{c^2}{3\lambda_0}(1+3\epsilon\delta(N-1)\rho_0)\frac{\partial \rho_0}{\partial \zeta} - \frac{c^2\chi}{\lambda_0}\frac{\partial S}{\partial \zeta}\rho_0\right] \tag{4.20}$$

which is very similar to the equation (2.28). The only difference is that the additional term in the density-dependent diffusion coefficient (proportional to the excluded volume) is multiplied by a factor of 3. This means the collective diffusion is increased relative to point particles in the presence of finite size particles.

4.3.3 The discrete velocity-jump model In this section, we generalise our nonlinear model (4.18) for a system that comprises a finite set of speeds. The common modelling approach that suggests itself pertaining to discrete distributions of velocities is the use of a discrete-velocity Boltzmann (DVB) system [17]. The system consists of PDEs that essentially describe the evolution of discrete distribution functions in term of elementary interactions. These interactions are included in the collision operator as loss and gain of particles' velocities due to collisions. With the molecular chaos hypothesis, these systems are more straightforward than the Boltzmann equation on a continuous velocity space.

Boltzmann-type approaches have been used in the context of traffic flows, where the collision operator is replaced with a probability distribution representing interactions that lead to the gain or loss of the test speed depending on the local traffic conditions [80]. With a small number of discrete velocities, the authors prove the existence of a class of quantized equilibrium distributions and their uniqueness. In an arbitrary finite set of speeds, the generalised Goldstein-Kac model is also a DVB system where random transitions from one velocity to another replace the pairwise collisions [56]. Hence, this system closely resembles our interaction-free model.

Here, attention is drawn to a class of nonlinear hyperbolic equations that describes a system with a family of n velocities, $V = \{-c_{\frac{n-1}{2}}, ..., -c_1, 0, c_1, ..., c_{\frac{n-1}{2}}\}$ and transition rates $\lambda_v^{v_i} \geq 0$ for $v_i, v \in V$; $v_i \neq v$. The dynamics of such a system, with interaction

treatment, is dictated by the generalised model

$$\frac{\partial p_i}{\partial t} + v_i \frac{\partial p_i}{\partial x} + \sum_{v \in V} \delta(v_i - v)(N-1)\epsilon \frac{\partial}{\partial x}\left[p(x, v_i, t)p(x, v, t)\right] + \sum_{\substack{v \in V \\ v_i \neq v}} \left(\lambda_v^{v_i}(x)p(x, v_i, t) - \lambda_{v_i}^{v}(x)p(x, v, t)\right) = 0, \quad i = 1, ..., n \tag{4.21}$$

where $p_i \equiv p(x, v_i, t)$ is the i^{th} subpopulation density and δ, ϵ, N have usual meaning. It is important to include both positive and negative values of the speed c_i in order to apply the wall-particle boundary condition in the integrated equation (4.17) (see 2.14 for details). Besides, simplifying the integral of the summation over the velocity-jumps also requires possessing these states for the velocities. In (4.21) the nonlinear transport term retains all terms up to first-order due to pairwise interactions. If we consider higher-order interactions where three particles or two particles and the boundary are close, additional correction terms will appear in the model.

4.3.4 Interactions through reflective collisions When elastic collisions are not applicable in biological applications, especially if living organisms do not transfer momentum when interacting with each other, reflective collisions are a valid alternative. At this point, stationary particles may act as static obstacles until, eventually, a random velocity switch frees them. We cleave to the system derived in section (4.3.2) and re-evaluate the interaction term because the change in the interface conditions corresponding to one moving and one obstacle requires some derivation steps to be modified. Interestingly, the resulting PDE is similar to the multiple species model when one variety obstructs the passage of the other.

For particles travelling in opposite directions in a narrow channel, the interface conditions (4.15) and (4.16) remain the same as there is no distinction between elastic and reflective collisions. When a mobile particle interacts with an obstacle, it will pass or bounce back; hence, the following changes occur:

$$P(x_1, x_2, v_1, 0, t)\big|_{x_2 = x_1^- + \epsilon}^{x_2 = x_1^+ + \epsilon} = \delta P(x_1, x_1^+ + \epsilon, c, 0, t)$$
$$P(x_1, x_2, v_1, 0, t)\big|_{x_2 = x_1^- - \epsilon}^{x_2 = x_1^+ - \epsilon} = -\delta P(x_1, x_1^- - \epsilon, -c, 0, t)$$

We may now go back to the asymptotic expansion discussed in section (2.3.2.2), set $v_2 = 0$ and re-evaluate the term for the obstacle at the interfaces. In this way we derive

the kinetic model, to $\mathcal{O}(\epsilon)$

$$\frac{\partial p}{\partial t} + v_1 \frac{\partial p}{\partial x_1} + \delta v_1 p^0 \left(p^+ - p^-\right) + \delta v_1 \epsilon \left(p^+ + p^-\right) \frac{\partial p^0}{\partial x_1} + 2 v_1 \delta \epsilon \frac{\partial}{\partial x_1} pp(x_1, -v_1, t) + \sum_{v' \in V} \left(\lambda_{v'}^{v_1}(x_1) p(x_1, v_1, t) - \lambda_{v_1}^{v'}(x_1) p(x_1, v', t) \right) = 0 \quad \text{for} \quad v_1 \in V \tag{4.22}$$

in $\Omega \times \mathbb{R}^+$. The stationary particle density p^0 changes with time as occupants are allowed to randomly choose directions according to the external stimuli and move along. At the same time, any moving occupant can quiet motion.

4.4 Transient solution

In this section, we consider the time-dependent evolution of the system. As in previous chapters, the particle-level system is solved using the event-driven KMC algorithm, while the kinetic model is integrated using characteristics. Below we give details of the algorithms used and numerical examples.

4.4.1 Balance laws When $\epsilon = 0$, the characteristic fields of the uncoupled system (4.1) give rise to the simple ODE system

$$\begin{aligned}
\frac{dp^+}{dt} &= \lambda_+^0(x)p^0 + \lambda_+^-(x)p^- - \lambda_0^+(x)p^+ - \lambda_-^+(x)p^+ \quad \text{along} \quad x = ct + x_0 \\
\frac{dp^0}{dt} &= \lambda_0^+(x)p^+ + \lambda_0^-(x)p^- - \lambda_+^0(x)p^0 - \lambda_-^0(x)p^0 \quad \text{along} \quad x = x_0 \\
\frac{dp^-}{dt} &= \lambda_-^0(x)p^0 + \lambda_-^+(x)p^+ - \lambda_0^-(x)p^- - \lambda_+^-(x)p^- \quad \text{along} \quad x = -ct + x_0
\end{aligned} \tag{4.23}$$

which can be numerically integrated with a fixed time step. For finite-size particles, we may write the nonlinear hyperbolic system (4.19) in matrix form and examine the solutions. However, we recall the less supportive structure of the eigenvectors in our previous constant speed models; in fact, here we get even more complex eigenvalues due to zero velocity component. Therefore, we begin with the periodic extensions for the marginal densities.

Let $u_1(x,t)$ be the odd extension of $p^+ - p^-$, $u_2(x,t)$ be the even extension of $p^+ + p^- + p^0$ and $u_3 = p^0$. Then the solution domain changes to $[-L, L]$, and substituting $p^+ = \frac{u_1 + u_2 - u_3}{2}$

and $p^- = \frac{u_2-u_1-u_3}{2}$ into (4.19), we find the system in a nonconservative form

$$\begin{gathered}\frac{\partial \vec{u}}{\partial t} + J(\vec{u})\frac{\partial(\vec{u})}{\partial x} = \vec{g}(x,\vec{u}), \quad -L \le x \le L, \quad 0 \le t \le T \\ \text{with the periodic boundary condition} \quad \vec{u}(-L,t) = \vec{u}(L,t),\end{gathered} \tag{4.24}$$

where $\vec{u} = \begin{pmatrix} u_1 \\ u_2 \\ u_3 \end{pmatrix}$, $J(\vec{u}) = \begin{pmatrix} -2c\xi u_1 & c(1+2\xi u_2 - \xi u_3) & -c(1+\xi u_2) \\ c & 0 & 0 \\ -c\xi u_3 & 0 & -c\xi u_1 \end{pmatrix}$

with $\xi = (N-1)\delta\epsilon$, and

$$\vec{g}(x,\vec{u}) = \begin{pmatrix} (\frac{\lambda_0^-}{2} - \frac{\lambda_0^+}{2} + \lambda_+^- - \lambda_-^+)(u_2-u_3) - (\frac{\lambda_0^-}{2} + \frac{\lambda_0^+}{2} + \lambda_+^- + \lambda_-^+)u_1 + (\lambda_+^0 - \lambda_-^0)u_3 \\ 0 \\ (\frac{\lambda_0^-}{2} + \frac{\lambda_0^+}{2})(u_2-u_3) + (\frac{\lambda_0^+}{2} - \frac{\lambda_0^-}{2})u_1 - (\lambda_+^0 + \lambda_-^0)u_3 \end{pmatrix}.$$

Due to complexity of the exact eigenvalues and eigenvectors of J, we try to find approximate values, upto $\mathcal{O}(\epsilon)$, using asymptotic expansion. This time we expect three ODEs for some algebraic combinations of u_1, u_2 and u_3 along characteristic curves.
Notice the exact eigencharacteristics

$$\left\{ \left[0, \begin{pmatrix} 0 \\ 0 \\ 1 \end{pmatrix}\right], \left[c, \begin{pmatrix} -1 \\ -1 \\ 1 \end{pmatrix}\right], \left[-c, \begin{pmatrix} 1 \\ -1 \\ 1 \end{pmatrix}\right] \right\} \tag{4.25}$$

of the simple non-interacting system. When $\epsilon \neq 0$, we introduce ϵ-dependency to the above and use the characteristic polynomial and eigenequation to evaluate each element. Accordingly for the nonlinear system, we find approximations

$$\begin{aligned}\left\{ \left[-c\xi u_1, \begin{pmatrix} 0 \\ \xi u_3 \\ 1 \end{pmatrix}\right], \left[c - c\xi\,(u_1-u_2)\,, \begin{pmatrix} -1 \\ -\xi(u_1+u_2-u_3)-1 \\ 1 \end{pmatrix}\right], \right. \\ \left. \left[-c - c\xi\,(u_1+u_2)\,, \begin{pmatrix} 1 \\ \xi(u_1-u_2+u_3)-1 \\ 1 \end{pmatrix}\right] \right\}\end{aligned} \tag{4.26}$$

that reduce the balance laws to the following ODEs:

$$\begin{aligned}
\xi u_3 \frac{du_2}{dt} + \frac{du_3}{dt} &= \mathcal{G}_1 \quad \text{on} \quad C_1 : x'(t) = -c\xi u_1 \\
-\frac{du_1}{dt} - [\xi(u_1 + u_2 - u_3) + 1]\frac{du_2}{dt} + \frac{du_3}{dt} &= \mathcal{G}_2 \quad \text{on} \quad C_2 : x'(t) = c - c\xi\,(u_1 - u_2) \\
\frac{du_1}{dt} + [\xi(u_1 - u_2 + u_3) - 1]\frac{du_2}{dt} + \frac{du_3}{dt} &= \mathcal{G}_3 \quad \text{on} \quad C_3 : x'(t) = -c - c\xi\,(u_1 + u_2)
\end{aligned} \tag{4.27}$$

where $\vec{\mathcal{G}}(x,\vec{u}) = \begin{pmatrix} (\frac{\lambda_0^-}{2} + \frac{\lambda_0^+}{2})(u_2 - u_3) + (\frac{\lambda_0^+}{2} - \frac{\lambda_0^-}{2})u_1 - (\lambda_+^0 + \lambda_-^0)u_3 \\ (\lambda_+^- - \lambda_-^+ - \lambda_0^+)(u_3 - u_2) + (\lambda_+^- + \lambda_-^+ + \lambda_0^+)u_1 - 2\lambda_+^0 u_3 \\ (\lambda_+^- - \lambda_-^+ + \lambda_0^-)(u_2 - u_3) - (\lambda_+^- + \lambda_-^+ + \lambda_0^-)u_1 - 2\lambda_-^0 u_3 \end{pmatrix}$.
With no direct velocity transitions, particles change their course only after a collision; the Riemann invariants

$$\left\{u_3 e^{\xi u_2}, (u_3 - u_1 - u_2)e^{\xi u_2}, (u_3 + u_1 - u_2)e^{\xi u_2}\right\}$$

satisfy such ODE system and, hence, simplifies the left hand side of (4.27). The simplified system is integrable along the characteristics. So computing the solution of the kinetic model (4.19) is equivalent to numerically generating the characteristic paths in spacetime. We will compare these solutions with the full-particle simulations under zero, symmetric and non-symmetric transition rates.

4.4.2 Discrete model The solution of the discrete model can be obtained using the event-driven KMC method described in (2.5.2). The only difference is that now we must assign zero velocity for some set of particles in the system and work out on times for each velocity transition. However, in a collision system, it is not necessary to compute collision times of each particle with every other particle or wall. Because we are working on a restricted domain (one dimensional), it is suffice to examine interaction times with the neighbouring particle or wall. This reduces the complexity of the algorithm. We also noticed that all event times of particles that are not involved in the current event remained unchanged. Therefore, we calculate them once before the time loop and update the stored data according to the new velocities of the interacting particles as time evolves. That is, the number of events to update per particle is two neighbouring interactions and one turn event. These changes significantly reduce the run time of a collision system compared to a narrow channel as fewer collision times are to be calculated.

4.4.3 Numerical Examples The numerical study aims to illustrate the behaviour of the systems under symmetric and asymmetric transition rates apart from examining the effect of biased and unbiased conditions. Unless explicitly stated otherwise, for all the numerical examples we take particles of speed $c = 1$ and chemotactic sensitivity coefficient $\chi = 1$, and place them inside a narrow channel of length 1 and width $l = 0.01$. The solid lines and the circles depict solutions for the PDE model and the KMC simulations, respectively.

We utilise the system of ODEs established in section (4.4.1) to find the solutions of the nonlinear kinetic model (4.18). The numerical integration procedure discussed in section (2.6.1) would work except now we have three characteristic curves emerging from each grid point in the domain. These curves are approximate straight lines; hence, there will be two intermediate crossover points. The first point is the intersection of C_2 and C_3 in (4.27), followed by the second intersection of C_1 with C_2 (or C_3) based on the inclination of the curve. At each crossover point, we compute the respective Riemann variables and update u_1, u_2 and u_3.

In the event-driven algorithm, we generate random initial positions for the particles at the beginning of each realisation while avoiding overlaps. The collision probability calculates from the formula A.3(iii) handles the overlaps during iterations. To construct the histograms for the full-particle model, we use 40 bins and compute bin averages using accumulated mobile and immobile particles at each realisation. For the two signal functions (2.3(a)) and (2.3(b)) we perform 5000 and 500 realisations, respectively.

Figures (4.2) and (4.3) collate simulations of both noninteracting (green) and interacting states at $t = 0.3$ when $N = 102$ particles are evenly distributed in the domain at the beginning of time. Here we cleave to the turning frequency (1.12) where we define asymmetric transition rates as

$$\lambda_0^+ = \lambda_-^+ = \lambda_0 - c\chi S_x, \quad \lambda_0^- = \lambda_+^- = \lambda_0 + c\chi S_x, \quad \lambda_+^0 = \lambda_-^0 = \lambda_0 \tag{4.28}$$

We find 43.75% collisions when 3.2% of the narrow channel is occupied (blue) while fully collisions when 20% is occupied (red). As in previous chapters, the purpose of having collision-free and single-file diffusion plots is to use them as reference points to see the competition between the most favourable signal environment and the volume exclusion of finite-size particles. We see a good match between the kinetic models (solid lines) and the particle simulations (circles) for noninteracting and narrow channel systems in all the subpopulation and total density plots. But the usual discrepancy between the two for a collision system is vivid in the domain centre. Here, the signal gradient is high, and

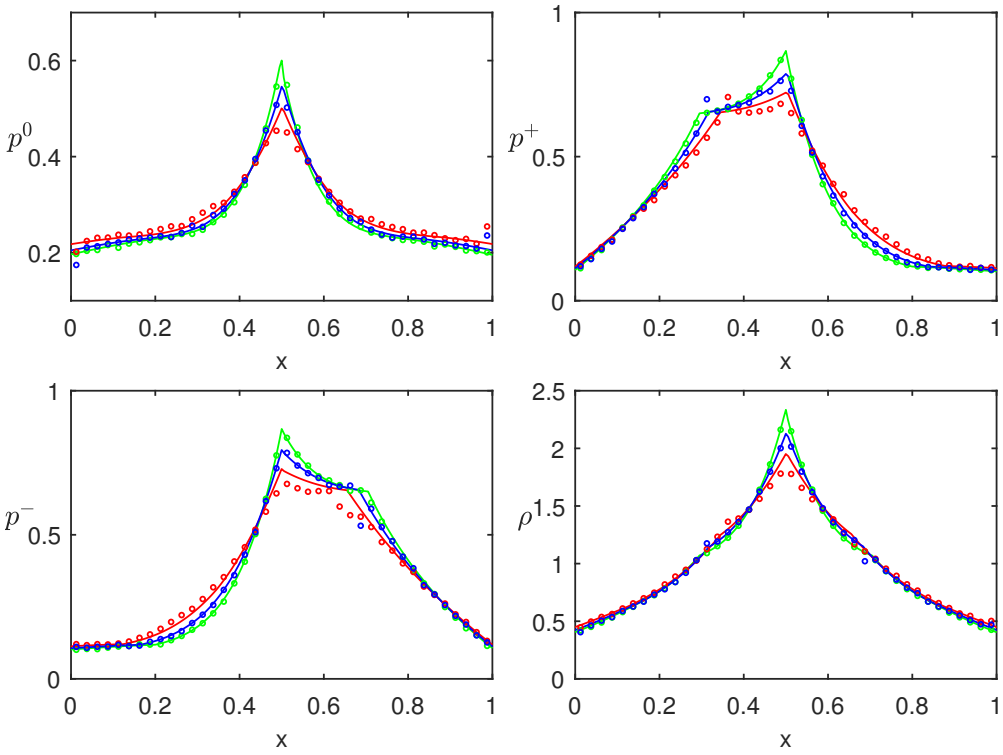

Figure 4.2: Transient marginal densities from the signal function (2.3(a)) when $\epsilon = 0$ (green), $\delta(0.002, 0.01) = 0.4375$ (blue) and $\delta(0.005, 0.01) = 1$ (red) at $t = 0.3$. The particle simulations (circles) are obtained by 5000 realisations.

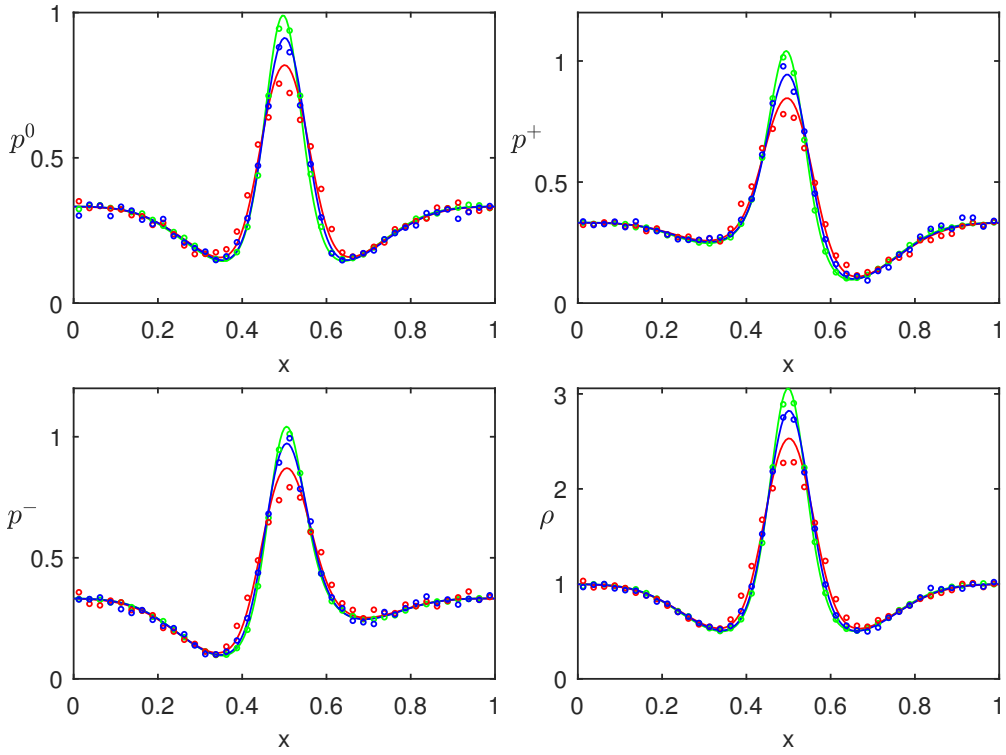

Figure 4.3: Transient marginal densities from the signal function (2.3(b)) when $\epsilon = 0$ (green), $\delta(0.002, 0.01) = 0.4375$ (blue) and $\delta(0.005, 0.01) = 1$ (red) at $t = 0.3$. The particle simulations (circles) are obtained by 500 realisations.

that results in notable excluded-volume effects. Initially, 1/3 of the total population is uniformly distributed stationary particles with a constant transition rate; however, they behave according to the extracellular chemical concentration. In fact, we find higher densities around the peaks of the signal functions (top left graphs in Figures (4.2) and (4.3)). The physical interpretation of such output one can think of is that it counts the density of immobile particles that have already moved in the favourable direction (direction of increasing S) with the random speed transformations.

The next four figures illustrate travelling bands of subpopulations under different transition rates. For all the plots, we begin by taking a set of $N = 135$ particles and distributing them according to a step function:

$$p_0^+(x) = (55/N)\mathbb{1}_{[0.1,0.3]}, \quad p_0^0(x) = (35/N)\mathbb{1}_{[0.4,0.6]}, \quad p_0^-(x) = (45/N)\mathbb{1}_{[0.7,0.9]}$$

The particle size is fixed to $\epsilon = 0.002$ so that the volume fraction remains constant during model comparison. We, therefore, change the width of the channel to 0.004 to form a collision system. We avoid full-particle simulation results to produce more concise graphs. In Figure (4.4), we have considered the simple case where particles do not undergo velocity transitions. This comparison purely explains the importance of excluded volume effects on the propagating wavefronts. In particular, solutions of the noninteracting system are simply waves travelling right and left at constant speed c and the initial distribution $p_0^0(x)$ itself. We find the nonlinear system obey the noninteracting particles linear system up to $t = 0.05$; thereafter, both right and left moving fronts collide with the stationary wave. The disturbances move along the characteristic curves at speeds $\{c\xi(p^- - p^+), c + c\xi(p^0 + 2p^-), -c - c\xi(p^0 + 2p^+)\}$, indicating that the existing speed of a particle is increased or decreased by other particles moving in different directions ($\mathcal{O}(\xi)$ terms). These shifts are apparent at $t = 0.3$; however, ignorable for $p^0(x, 0.5)$ (see bottom left plot in Figure 4.4).

To produce Figure (4.5), we let the symmetric transition rates be positive constants such that $\lambda_-^+ = \lambda_+^- = \alpha$, $\lambda_0^+ = \lambda_+^0 = \beta$, $\lambda_-^0 = \lambda_0^- = \gamma$. This means, we are looking at particles moving in one-dimension subject to an unbiased velocity jump process. This is the dominating process that dictates the behaviour of the particles until $t = 0.05$. Let us correlate those outputs with the transition rates in the following way. In $p^0(x, 0.05)$, the left density, corresponding to β, is lower than the right density, corresponding to γ, because $\beta < \gamma$. For $p^+(x, 0.05)$ and $p^-(x, 0.05)$, the gain from stationary particles is higher than that of oppositely moving particles as $\alpha < \beta < \gamma$. Despite the subpopulation density fluctuations, the total density does not vary much from the initial profile. After

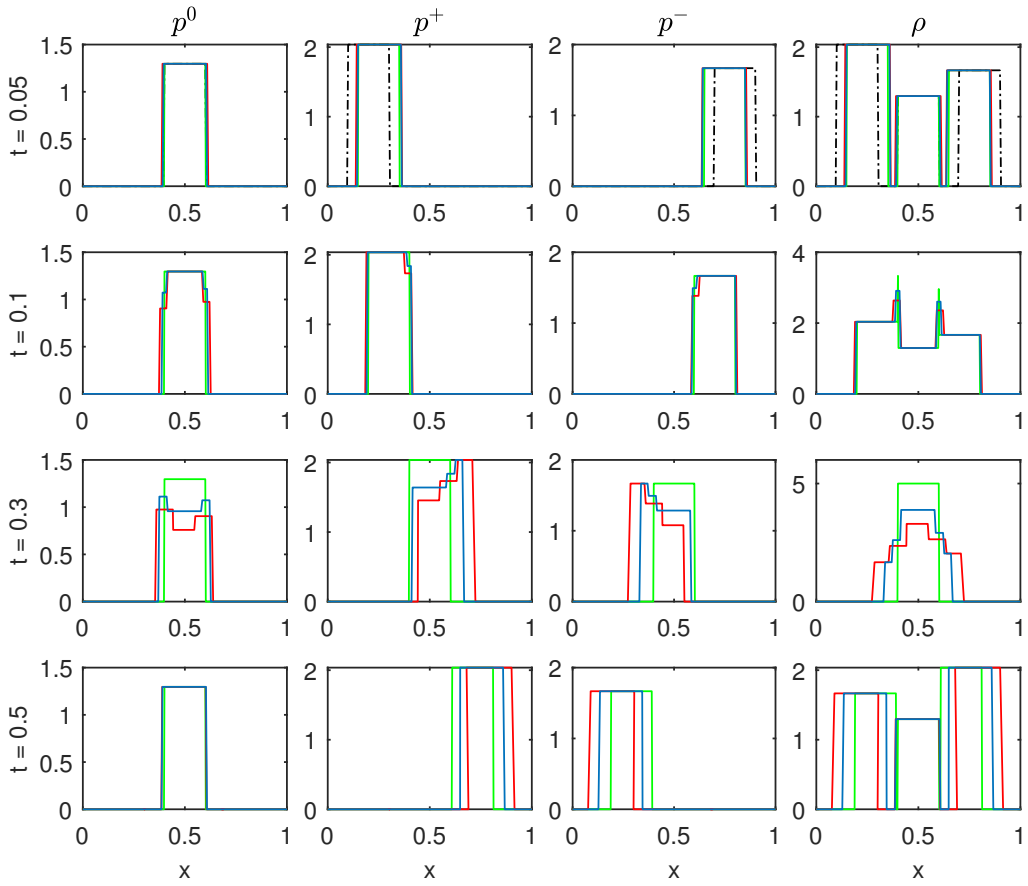

Figure 4.4: Transient marginal densities at various times without velocity transitions. Solid lines; green when $\delta(0, 0.01) = 0$, blue when $\delta(0.002, 0.01) = 0.4375$ and red when $\delta(0.002, 0.004) = 1$. The dash-dot black line is the initial travelling band.

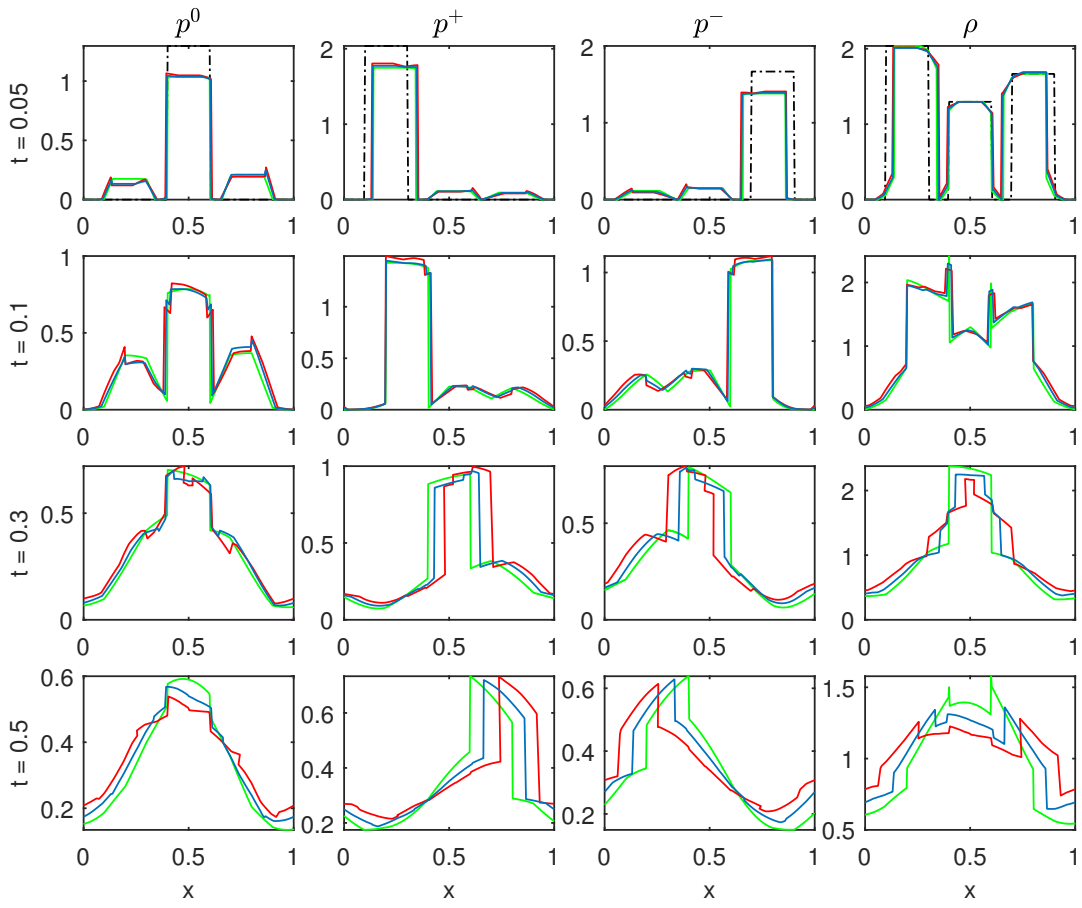

Figure 4.5: Transient marginal densities for symmetric transition rates $\alpha = 1.5$, $\beta = 2.5$ and $\gamma = 3.5$. Solid lines; green when $\delta(0, 0.01) = 0$, blue when $\delta(0.002, 0.01) = 0.4375$ and red when $\delta(0.002, 0.004) = 1$. The dash-dot black line is the initial travelling band.

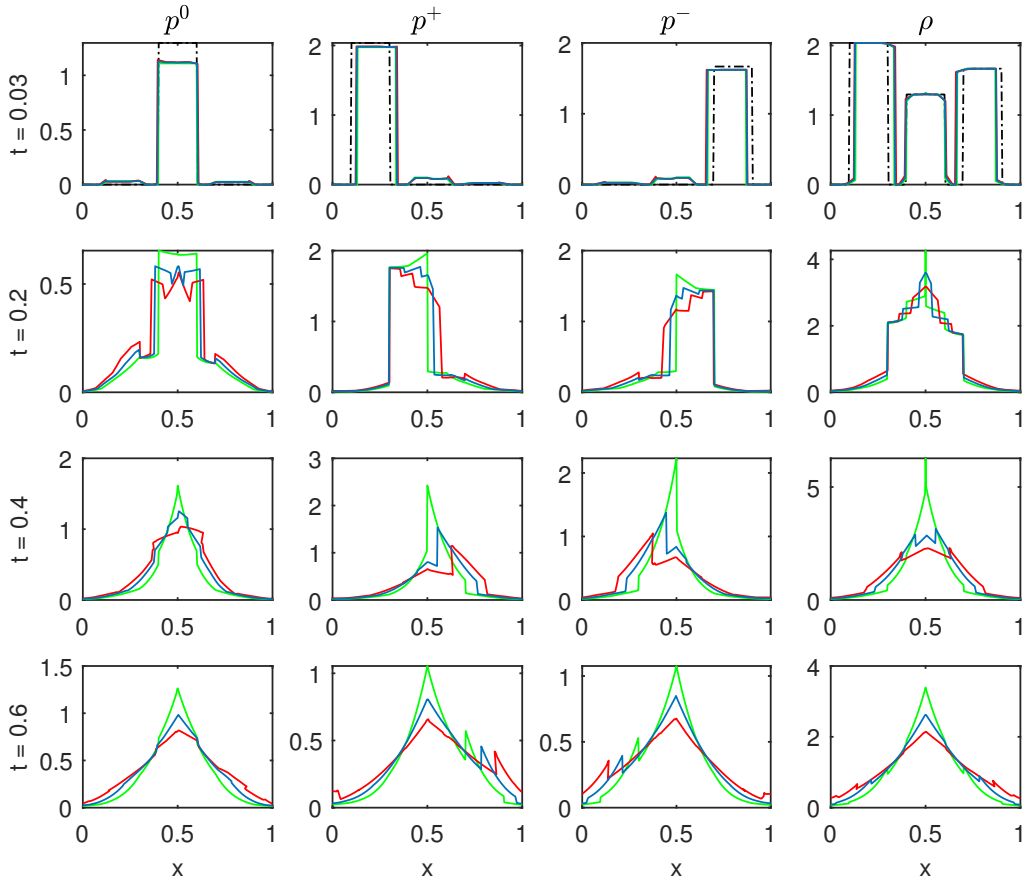

Figure 4.6: Transient marginal densities for the signal function (2.3(a)). Solid lines; green when $\delta(0, 0.01) = 0$, blue when $\delta(0.002, 0.01) = 0.4375$ and red when $\delta(0.002, 0.004) = 1$. The dash-dot black line is the initial travelling band.

$t = 0.1$, waves distort due to particle interactions, and wave shifts become noticeable even in stationary particle's densities (see plots in Figure 4.5 at $t = 0.5$).

Figures (4.6) and (4.7) are generated from the non-symmetric transition rates (4.28) to analyse travelling bands during biased velocity jump processes. The outcomes for left and right moving wavefronts are similar to those in the constant speed model (see Figures 2.8 and 2.9), except now we have distribution curves for immobile particles. The initial profile, in which stationary particles are concentrated in a strip in the centre, spreads more slowly for point particles than for finite-size particles, indicating that immobile point particles have already moved in the direction of increasing S with the random velocity transformations. Moreover, we find continuing kinetic waves (see plots in Figure 4.6 at $t = 0.2$) and a low number of velocity transitions (the dashed blue lines in Figure 4.7 at $t = 0.03$) under lower baseline frequencies.

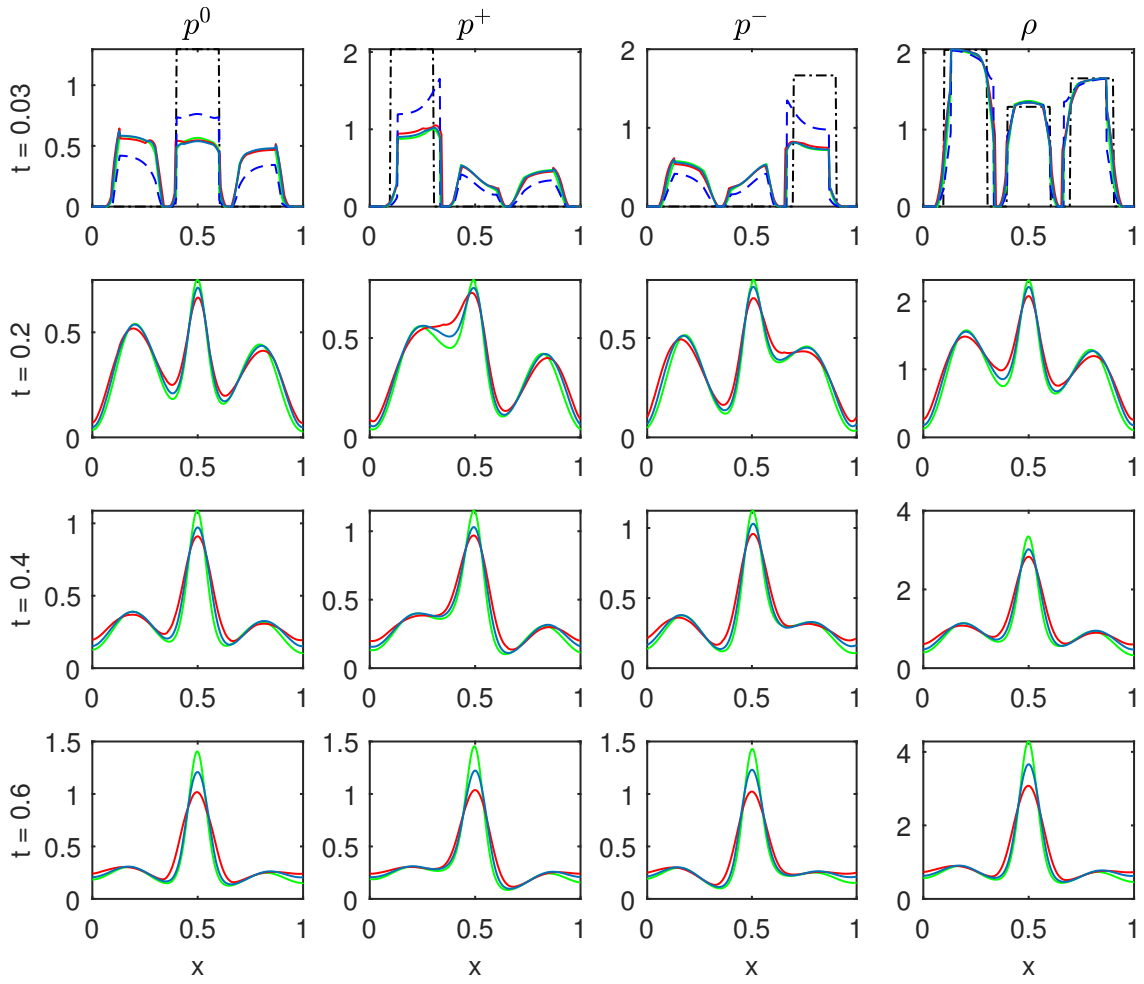

Figure 4.7: Transient marginal densities for the signal function (2.3(b)). Solid lines; green when $\delta(0, 0.01) = 0$, blue when $\delta(0.002, 0.01) = 0.4375$ and red when $\delta(0.002, 0.004) = 1$. The dash-dot black line is the initial travelling band, and the dashed blue line is for base frequency $\lambda_0 = 10$.

4.5 Stationary solutions

In section (2.7), we discussed the equilibria of a system which consists of bidirectional moving particles with a constant speed. The approach works for the current system with the same flux function as the immobile particles do not contribute to it. From the reflective boundary condition, the flux vanishes, and if $p^+ = p^- = p$ (say), the equation (4.19b) returns

$$p^0 = \Lambda p, \quad \text{where} \quad \Lambda = \frac{(\lambda_0^+ + \lambda_0^-)}{(\lambda_+^0 + \lambda_-^0)}.$$

Since the total stationary density $p_{st}(x) = p^+ + p^- + p^0$, we get $p = \frac{p_{st}}{(2+\Lambda)}$. Inserting these results into (4.19a) (or 4.19c) and rearranging the terms gives the following ODE for p_{st}:

$$c\frac{dp_{st}}{dx} + 2c\xi p_{st}\frac{dp_{st}}{dx} + (\lambda_0^+ - \lambda_+^0\Lambda + \lambda_-^+ - \lambda_+^-)p_{st} = 0,$$

where $\xi = \delta\epsilon(N-1)$. Hence, the stationary solution for the kinetic model (4.18) satisfies the nonlinear equation

$$\ln p_{st} + 2\xi p_{st} + \frac{1}{c}\int_0^x (\lambda_0^+ - \lambda_+^0\Lambda + \lambda_-^+ - \lambda_+^-)dy = \ln A$$

for an arbitrary constant A. When $\epsilon \to 0$, the above equation produces the stationary solution for the interaction-free system

$$p_{st}(x) = A\exp(-\tfrac{1}{c}\textstyle\int_0^x(\lambda_0^+ - \lambda_+^0\Lambda + \lambda_-^+ - \lambda_+^-)dy), \tag{4.29}$$

while finite-size particles yield

$$\begin{aligned} p_{st}(x) &= \frac{1}{2\xi}\mathcal{W}\left[2\xi A\exp(-\tfrac{1}{c}\textstyle\int_0^x(\lambda_0^+ - \lambda_+^0\Lambda + \lambda_-^+ - \lambda_+^-)dy)\right] \\ &\text{with the normalisation condition} \quad \int_0^L p_{st}(x)dx = 1 \end{aligned} \tag{4.30}$$

The solution (4.30) is valid for both the collision ($\delta = 1$) and narrow channel systems.

4.5.1 Comparison with the full-particle system The microscopic stationary density of the collision system is different from that of the narrow channel due to illegal configurations. The MH algorithm (2.7.2) defined in the second chapter works for the

current narrow channel system in the same fashion, except now we have a different energy function. However, for the collision system, we must redefine the N-dimensional microscopic density and modify the algorithm accordingly.

Up until the point of illegal configurations, we can define the stationary density for the full-particle system (4.2) as

$$P_{st}(\vec{x}) = A \exp\left(-\tfrac{1}{c}\sum_{i=1}^{N}\int_0^{x_i}(\lambda_0^+ - \lambda_+^0\mathbf{\Lambda} + \lambda_-^+ - \lambda_+^-)dy\right) \quad \text{for} \quad \vec{x} \in \Omega_\epsilon^N$$

Since a single-file channel prevents overlaps, P_{st} is not defined for configurations $\vec{x} \in \Omega^N \setminus \Omega_\epsilon^N$. However, it is possible to extend it in the entire configuration space Ω^N as

$$P_{st}(\vec{x}) = A \exp(-\Phi(\vec{x})) \tag{4.31}$$

by introducing the energy associated to arrangements

$$\Phi(\vec{x}) = \begin{cases} \frac{1}{c}\sum_{i=1}^{N}\int_0^{x_i}(\lambda_0^+ - \lambda_+^0\mathbf{\Lambda} + \lambda_-^+ - \lambda_+^-)dy, & \vec{x} \in \Omega_\epsilon^N \\ \infty, & \text{otherwise.} \end{cases}$$

Hence, the MH algorithm allows us to sample configurations directly from the density (4.31) as follows:

S1 Select a particle i at random and generate a candidate $\mathbf{y}_i = \mathbf{x}_i + hX$ where $X \sim N(0,1)$ and h a tunable parameter.

S2 Compute the difference $\Delta\Phi$ between the current and modified configurations

S3 Accept $\mathbf{y}_i$ with probability $p = \min(1,\exp(-\Delta\Phi))$ and set $\mathbf{x}_{i+1} = \mathbf{y}_i$, otherwise set $\mathbf{x}_{i+1} = \mathbf{x}_i$

For the numerical example, we consider following two cases:

Symmetric transition rates

When $\lambda_j^i = \lambda_i^j \; \forall i \neq j$, the multiplier $\mathbf{\Lambda}$ becomes one, and the reaction term (due to the random choice of velocity) vanishes. Hence the symmetry between turning rates leads to the outcomes; $p^0 = p$, and constant stationary density $p_{st} = \frac{1}{2\xi}W(2\xi A)$. Then applying the normalisation condition yields, $p_{st} = \frac{1}{L}$. That is, distribution fall into a uniform steady state.

Asymmetric transition rates

Inserting transition rates (4.28) to the multiplier $\mathbf{\Lambda}$, we get $p^0 = p$, resulting in the

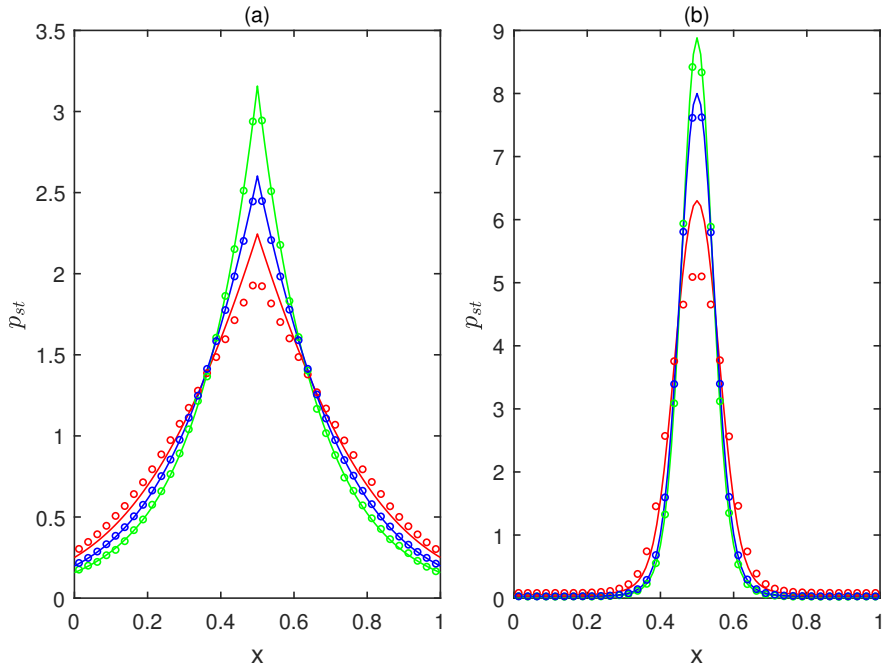

Figure 4.8: Stationary solutions of the kinetic model for $N = 102$ point (green), narrow channel (blue) and collision (red) particles. Densities in (a) from signal (2.3(a)) with $\epsilon = 0.002$ and in (b) from signal (2.3(b)) with $\epsilon = 0.001$. The results from the MH algorithm (circles) use 10^6 MH steps for noninteracting particles and 10^7 for hard-core particles.

equilibrium solution $p_{st} = \frac{1}{2\xi}\mathcal{W}\left[2\xi A e^{3\chi(S(x)-S(0))}\right]$ from (4.30). We use Matlab function `fminsearch` of `norm` of the integral to estimate the constant A.

Figure (4.8) compares the model and simulation results for the latter case with $N = 102$ and $\chi = 1$. We take two different particle sizes for the signal functions, $\epsilon = 0.002$ for (2.3(a)) and $\epsilon = 0.001$ for (2.3(b)), to reduce the disparity between the model predictions and the stochastic simulations, especially in the collision system. Both point and finite-size particles are distributed inside a narrow flattened pipe of length 1, which form a narrow channel at width $l = 0.01$ and a collision system at $l = 2\epsilon$. The histograms for the MH algorithm are produced by dividing the domain into 40 bins. An acceptance rate in the 0.1 order of magnitude, and 10^7 steps of the algorithms produce the desired outputs. As in time-dependent solutions, we see a lower density around the peak of the signal functions for finite-size particles. The peaks are even much lower in the single-file channel unless for considerably smaller particle size. The stationary solutions of the kinetic model agrees well with the particle simulations except in this situation. In fact, the discrepancy is notable in 4.8(b) relative to 4.8(a) despite having only half of the occupied fraction. This is because the gradients of signal function (2.3(b)) are steeper near the centre than that of (2.3(a)).

4.6 Summary and discussion

We find many efforts to describe interacting systems with discrete velocity distributions, specifically collision systems, using a discrete-velocity Boltzmann (DVB) system where a collision operator describes relations for velocities before and after encounters. However, to our knowledge, no attention has been given to finite-size species that experience both collisions and instantaneous velocity changes at a given set of speed values. In this chapter, we examined such a scenario by predicting the macroscopic descriptions of the particle-level attributes in a single-file and narrow channel. Specifically, we allowed immobile species of hardcore to interact with the same species of having a constant speed and extended that model for a finite set of speeds. The result is a system of nonlinear transport equations for the marginal probability density associated with each subpopulation. The number of nonlinear transport terms depended on the pairwise subpopulation interactions.

We have assessed the validity of our kinetic models to predict the system's behaviour by comparing its numerical solutions with the simulations of the discrete particle-based model. Both the stationary and time-dependent simulations agreed well under low occupied fractions, particularly in the narrow channel, supporting the notion that our PDE model captures the features at the particle level rather well. With suitable initial conditions, the subpopulation densities exhibit travelling bands under non-tumbling, symmetric and bias asymmetric transition rates. These time-dependent solutions are non-dissipative as we have considered a systematic approach based on characteristics for hyperbolic balance laws. The characteristic speeds were enhanced further by the stationary particle density causing outward shifts in the subpopulations.

An interesting extension in future work would be introducing a soft-core potential for particle interactions in the discrete velocity jump processes. Individuals in a real-life system may repel (or attract) each other over a region rather than on an excluded volume created by the particle's finite size. A simple repulsive soft pair potential like the exponential [61] or a repulsive–attractive potential like the Lennard–Jones [91] is appropriate for such systems to account for the softness.

5

Hard-core interactions in two dimensions

5.1 Introduction

Hard-core interactions in velocity-jump processes are typically observed in a two or three-dimensional domain, whereas we have thus far introduced them only in one dimension. Let us, therefore, extend the one-dimensional collision system examined by Ralph et al. [81] in a higher-dimensional setting. Particularly, we focus on the two-dimensional analysis, but the methods would easily work out in a three-dimensional regime. The equations derived in the previous work are quite similar to the kinetic model we have derived in Chapter 2, though we allowed particles to pass each other like in a narrow channel. In a much larger domain, an ample amount of space will be available for the occupants to move freely and pass each other without overlapping. Nevertheless, a collision may occur if one particle blocks the others' trajectory. Although it is demanding, we can consider this work as a direct extension of a one-dimensional collision system.

The behaviour of groups of particles moving according to a velocity-jump process is a classical problem in higher-dimensional domains. However, as we stated before, many models ignore excluded-volume effects; if one wishes to incorporate volume exclusion, just as in unidirectional motion, a common approach is to use agent-based models (ABM). For instance, one can write the mean-field approximation model for the four-directional motion on a lattice (pedestrian flow [66]) and derive the diffusive continuum description [32].

The travel directions are pre-defined, like left, right, up and down; therefore, ABM models may be restrictive and sometimes unreliable. The recent researches by Franz et al. [31], and Estrada-Rodriguez and Gimperlein [29] derived population-level models for velocity jumps in two dimensions which aligns with our work. Both studies adopted the molecular chaos assumption, and collision treatment has emerged in the source term. Besides, the former utilised the hypothesis with a first-order correction term that emerged in Bruna's work [12] from the method of matched asymptotic expansion, which may not be directly applicable to the velocity changes at the collision boundaries.

As in previous chapters, we begin by writing the particle-based description of the system, which consists of, in the probability space, a PDE for the joint probability density function. Reduction of this high-dimensional model from N interacting finite-size particles to the evolution of the one-particle marginal density explained in section (5.3). In the limit of small volume fraction, asymptotic analysis is performed, resulting in a nonlinear hyperbolic equations for the one-particle density function analogous to the one-dimensional model (33) derived in [81].

Generally, two types of collisions often consider in higher dimensions; reflective and elastic. In the one-dimensional constant speed case, elastic and reflective collisions were one in the same thing. We are interested in systems with speed preserving collisions where particles always maintain a constant speed $c \in \mathbb{R}^+$. Therefore, we examine the system when particles exchange their velocities during close encounters. We shall detail later the situation when particles reflect directly off each other. Note that, exchanging velocities are different from reflective collisions as they preserve both total momentum and energy in the system. For example, take $\mathbf{v} = (c, 0)$ and $\mathbf{u} = (0, c)$ to be the initial velocities, and suppose the collision occurred perpendicular to x direction. Then resulting velocities can be derived as follows.

For exchange velocities:

$$\begin{aligned} &\mathbf{v}' = \mathbf{u}; && \mathbf{u}' = \mathbf{v} \\ &\mathbf{v}' = (0, c); && \mathbf{u}' = (c, 0) \end{aligned}$$

For reflective collisions:

$$\begin{aligned} &\mathbf{v}' = \mathbf{v} - 2(\mathbf{v} \cdot \mathbf{n})\mathbf{n}; && \mathbf{u}' = \mathbf{u} - 2(\mathbf{u} \cdot \mathbf{n})\mathbf{n} \\ &\mathbf{v}' = (c, 0) - 2[(c, 0) \cdot (0, 1)](0, 1); && \mathbf{u}' = (0, c) - 2[(0, c) \cdot (0, -1)](0, -1) \\ &\mathbf{v}' = (c, 0); && \mathbf{u}' = (0, -c) \end{aligned}$$

For elastic collisions:

$$\mathbf{v}' = \mathbf{v} - [(\mathbf{v}-\mathbf{u})\cdot\mathbf{n}]\mathbf{n}; \qquad \mathbf{u}' = \mathbf{u} + [(\mathbf{v}-\mathbf{u})\cdot\mathbf{n}]\mathbf{n}$$
$$\mathbf{v}' = (c,0) - [(c,-c)\cdot(0,1)](0,1); \qquad \mathbf{u}' = (0,c) + [(c,-c)\cdot(0,-1)](0,-1)$$
$$\mathbf{v}' = (c,c); \qquad \mathbf{u}' = (0,0)$$

5.2 Particle level model

Let us consider a system of N identical disks in a two dimensional domain, $\Omega = [0,L]\times[0,L]$. This is the space available to a particle centre $X_i(t)$ at time $t \geq 0$ with no-flux boundary condition and it does not exactly correspond to the physical domain. The particles are hard cores of diameter $\epsilon(\ll L)$; therefore, the actual free space is somewhat smaller than Ω. When a particle's speed is constant, the dynamics of the particle is governed by

$$\frac{dX_i}{dt} = V_i \quad \text{for} \quad 1 \leq i \leq N$$

where $V_i = c(\cos\theta_i, \sin\theta_i)$ with c being any positive real value and $\theta_i \in [0, 2\pi]$; the set of possible orientations that can be defined through physical limitations in applications. We assume that the system does not have external forces limiting or preventing the particles' motion and turning velocity back to zero. But as before, particles switches its direction of motion according to independent Poisson processes with rates $\lambda(X_i, V_i) > 0$ or collision with another particle or the domain wall. If the domain dimensions are larger than the particle's size, we cannot expect many collisions.
Now we can write the equivalent higher dimensional transport equation in terms of the joint probability density $P(\mathbf{r}, \boldsymbol{v}, t)$ for the system described above.

$$\frac{\partial P}{\partial t} + \sum_{i=1}^{N} \vec{v_i}\cdot\nabla_{\vec{r_i}}P + \sum_{i=1}^{N}\big(\lambda(\vec{r_i},\vec{v_i})P(\mathbf{r},\boldsymbol{v},t) - \lambda(\vec{r_i},-\vec{v_i})P(\mathbf{r},s_i\boldsymbol{v},t)\big) = 0 \tag{5.1}$$

where $\mathbf{r} = (\vec{r}_1, \vec{r}_2, ..., \vec{r}_N) \in \Omega^N$ with $\vec{r}_i = (x_i, y_i)$ and $\boldsymbol{v} = (\vec{v}_1, \vec{v}_2, ..., \vec{v}_N) \in V^N$. Since a particle can only change its orientation, we can define the velocity space $V = c\Theta$, where Θ contains unit vectors. The term $\lambda(\vec{r_i}, -\vec{v_i})$ is the rate at which particle i reverses it's direction and s_i is the operator which represents this transformation in the density function. Due to hard-core interactions, equation (5.1) is defined in the configuration space (different from the physical domain) $\Omega_\epsilon^N \times V^N$, where

$$\Omega_\epsilon^N = \{\mathbf{r} \in \Omega^N : ||\vec{r_i} - \vec{r_j}|| > \epsilon \quad \forall i \neq j\}.$$

Initially, the particles are independently and identically distributed in the domain; hence, the initial condition

$$P(\mathbf{r}, \boldsymbol{v}, 0) = P_0(\mathbf{r}, \boldsymbol{v}) \tag{5.2}$$

is invariant to permutations of the particle labels. We assume reflective collisions with the wall; hence, the probability density satisfies the wall-particle boundary condition,

$$P(\mathbf{r}, \boldsymbol{v}, t) = P(\mathbf{r}, s_i\boldsymbol{v}, t) \quad \text{on} \quad \partial\Omega \tag{5.3}$$

where s_i is the operator that changes the angle when i^{th} particle hit the wall. During particle interactions, two particles collide at a distance ϵ and exchange their velocities. So the boundary condition for the collision between particles i and j is

$$P(\mathbf{r}, \boldsymbol{v}, t) = P(\mathbf{r}, s_{ij}\boldsymbol{v}, t) \quad \text{on} \quad ||\vec{r}_i - \vec{r}_j|| = \epsilon \tag{5.4}$$

where s_{ij} is the operator that swaps the angles of the interacting particles. The above system is higher dimensional, and we have dealt with such systems in our previous chapters. In the next section, we derive the population-level model using similar techniques.

5.3 Population level model

We are interested in a lower-dimensional model given in terms of the marginal density $p(\vec{r}_1, \vec{v}_1, t) = \int P(\mathbf{r}, \boldsymbol{v}, t) d\vec{r}_2 ... d\vec{r}_N d\vec{v}_2 ... d\vec{v}_N$, which is much more realistic and solvable. As before, the reduction process begins with the low volume fraction assumption. If N particles occupy the two dimensional domain, chosen a particle, there are $N-1$ possible pair interactions and $\frac{(N-1)(N-2)}{2}$ triplets. Since the particle centres are separated by a distance of $\mathcal{O}(\epsilon)$, in the configuration space, the total volume occupied by two particles is $\mathcal{O}(N\epsilon^2)$ and three particles is $\mathcal{O}(N^2\epsilon^4)$ [1]. During particle-particle-wall encounter, the volume fraction is $\mathcal{O}(N\epsilon^3)$. We take the domain to be large enough (volume of $\mathcal{O}(1)$) so that under low volume fraction, the dominant contribution is when two particles are close.

So let us restate the individual-based model and the boundary conditions for two disks at $(\vec{r}_1, \vec{r}_2) \in \Omega_\epsilon^2$ with velocities $(\vec{v}_1, \vec{v}_2) \in V^2$. The space available for disk 2 when disk 1 is fixed at $\vec{r}_1$ defines as $\Omega(\vec{r}_1) = \Omega \setminus B_\epsilon$, where $B_\epsilon = \{\vec{r}_2 \in \Omega : ||\vec{r}_1 - \vec{r}_2|| \leq \epsilon\}$. On the configuration space, $\Omega(\vec{r}_1)$ is a slice at $\vec{r}_1$. The excluded area defines here split the boundary into two: ∂B_ϵ, the collision boundary; and $\partial\Omega \setminus \partial B_\epsilon$, the reflective boundary.

[1] A more general description is given in [12]

Then equation (5.1) reads

$$\frac{\partial P}{\partial t} + \vec{v}_1 \cdot \nabla_{\vec{r}_1} P + \vec{v}_2 \cdot \nabla_{\vec{r}_2} P + \lambda(\vec{r}_1, \vec{v}_1)P - \lambda(\vec{r}_1, -\vec{v}_1)P(\vec{r}_1, \vec{r}_2, -\vec{v}_1, \vec{v}_2, t) + \lambda(\vec{r}_2, \vec{v}_2)P - \lambda(\vec{r}_2, -\vec{v}_2)P(\vec{r}_1, \vec{r}_2, \vec{v}_1, -\vec{v}_2, t) = 0 \tag{5.5a}$$

$$P(\vec{r}_1, \vec{r}_2, \vec{v}_1, \vec{v}_2, t) = P(\vec{r}_1, \vec{r}_2, \vec{v}_1, \vec{v}_*, t), \quad \vec{r}_2 \in \partial\Omega \tag{5.5b}$$

$$P(\vec{r}_1, \vec{r}_2, \vec{v}_1, \vec{v}_2, t) = P(\vec{r}_1, \vec{r}_2, \vec{v}_2, \vec{v}_1, t) \quad \text{on} \quad ||\vec{r}_1 - \vec{r}_2|| = \epsilon \tag{5.5c}$$

where $\vec{v}_*$ is the reflected velocity for wall collision given by $\vec{v}_* = \vec{v}_2 - 2(\vec{v}_2 \cdot \vec{n})\vec{n}$.
As has been the case throughout this thesis, we aim to reduce the equation (5.5a) term by term and derive the population level model for the marginal density

$$p(\vec{r}_1, \vec{v}_1, t) = \int\limits_{\Omega(\vec{r}_1)\times V} P(\vec{r}_1, \vec{r}_2, \vec{v}_1, \vec{v}_2, t) d\vec{r}_2 d\vec{v}_2.$$

Begin integrating the the first term yields

$$\int\limits_{\Omega(\vec{r}_1)\times V} \frac{\partial P}{\partial t} d\vec{r}_2 d\vec{v}_2 = \frac{\partial p}{\partial t} \tag{5.6}$$

as $\Omega(\vec{r}_1) \times V$ is independent of t. For the second integral, we use the Reynold's transport theorem.

$$\begin{aligned} \int\limits_{\Omega(\vec{r}_1)\times V} (\vec{v}_1 \cdot \nabla_{\vec{r}_1} P) d\vec{r}_2 d\vec{v}_2 &= \vec{v}_1 \cdot \nabla_{\vec{r}_1} \int\limits_{\Omega\times V} P d\vec{r}_2 d\vec{v}_2 - \int\limits_{\partial B_\epsilon \times V} (\vec{v}_1 \cdot \vec{n}) P dS_{\vec{r}_2} d\vec{v}_2 \\ &= \vec{v}_1 \cdot \nabla_{\vec{r}_1} p - \int\limits_{\partial B_\epsilon \times V} (\vec{v}_1 \cdot \vec{n}) P(\vec{r}_1, \vec{r}_2, \vec{v}_1, \vec{v}_2, t) dS_{\vec{r}_2} d\vec{v}_2 \end{aligned} \tag{5.7}$$

Here $dS_{\vec{r}_2}$ is the surface component with respect to $\vec{r}_2$. On the collision surface, the outward normal is $\vec{n} = (\vec{r}_1 - \vec{r}_2)/||\vec{r}_1 - \vec{r}_2||$ and it is pointing into the ball B_ϵ. In fact, we have a second outward pointing normal at the boundary of Ω, which we denote by $\vec{n}_\Omega$. Also note that, $\partial B_\epsilon(\vec{r}_1)$ is the only moving boundary which contributes to the theorem. Since the particle size is fixed over time, the velocity of the boundary is the same as its centre.
Now, using the Divergence theorem,

$$\int\limits_{\Omega(\vec{r}_1)\times V} (\vec{v}_2 \cdot \nabla_{\vec{r}_2} P) d\vec{r}_2 d\vec{v}_2 = \int\limits_{\partial\Omega \cup \partial B_\epsilon \times V} (\vec{v}_2 \cdot \vec{n}) P dS_{\vec{r}_2} d\vec{v}_2$$

To evaluate the integral along the wall $\partial\Omega$, we define two subsets

$$V^+(\vec{n}_\Omega) = \{\vec{v} \in V : \vec{v}\cdot\vec{n}_\Omega > 0\} \quad \text{and} \quad V^-(\vec{n}_\Omega) = \{\vec{v} \in V : \vec{v}\cdot\vec{n}_\Omega < 0\}.$$

Then,

$$\begin{aligned}\int\limits_{\partial\Omega\times V} (\vec{v}_2\cdot\vec{n}_\Omega)PdS_{\vec{r}_2}d\vec{v}_2 &= \int\limits_{\partial\Omega\times V^+} (\vec{v}_2\cdot\vec{n}_\Omega)PdS_{\vec{r}_2}d\vec{v}_2 + \int\limits_{\partial\Omega\times V^-} (\vec{v}_2\cdot\vec{n}_\Omega)PdS_{\vec{r}_2}d\vec{v}_2 \\ &= -\int\limits_{\partial\Omega\times V^-} (\vec{v}_2\cdot\vec{n}_\Omega)P(\mathbf{r},\vec{v}_1,\vec{v}_*,t)dS_{\vec{r}_2}d\vec{v}_2 + \int\limits_{\partial\Omega\times V^-} (\vec{v}_2\cdot\vec{n}_\Omega)PdS_{\vec{r}_2}d\vec{v}_2 \\ &= 0 \quad \text{(from (5.5b))}\end{aligned}$$

Therefore, the third term simplifies to

$$\int\limits_{\Omega(\vec{r}_1)\times V} (\vec{v}_2\cdot\nabla_{\vec{r}_2}P)d\vec{r}_2d\vec{v}_2 = \int\limits_{\partial B_\epsilon\times V} (\vec{v}_2\cdot\vec{n})P(\vec{r}_1,\vec{r}_2,\vec{v}_1,\vec{v}_2,t)dS_{\vec{r}_2}d\vec{v}_2 \tag{5.8}$$

In the fourth term, λ is independent of $\vec{r}_2$; therefore, one can simply integrate to obtain

$$\begin{aligned}\int\limits_{\Omega(\vec{r}_1)\times V} \lambda(\vec{r}_1,\vec{v}_1)P - \lambda(\vec{r}_1,-\vec{v}_1)P(\vec{r}_1,\vec{r}_2,-\vec{v}_1,\vec{v}_2,t)d\vec{r}_2d\vec{v}_2 = \\ \lambda(\vec{r}_1,\vec{v}_1)p - \lambda(\vec{r}_1,-\vec{v}_1)p(\vec{r}_1,-\vec{v}_1,t)\end{aligned} \tag{5.9}$$

Since $-\vec{v}_2 = c\,(\cos(\pi+\theta_2),\sin(\pi+\theta_2))$, the integral of $\lambda(\vec{r}_2,-\vec{v}_2)P(\vec{r}_1,\vec{r}_2,\vec{v}_1,-\vec{v}_2,t)$ over V when $\{\theta_2 : \pi \le \theta_2 \le 2\pi\}$ is same as the integral of $\lambda(\vec{r}_2,\vec{v}_2)P(\vec{r}_1,\vec{r}_2,\vec{v}_1,\vec{v}_2,t)$ when $\{\theta_2 : 0 \le \theta_2 \le \pi\}$. Thus, integral of the fifth term over V vanishes. Now combining (5.6), (5.7), (5.8) and (5.9), a single particle transport equation takes the form

$$\begin{aligned}\frac{\partial p}{\partial t}(\vec{r}_1,\vec{v}_1,t) + \vec{v}_1\cdot\nabla_{\vec{r}_1}p(\vec{r}_1,\vec{v}_1,t) + \int\limits_{\partial B_\epsilon(\vec{r}_1)\times V} [(\vec{v}_2-\vec{v}_1)\cdot\vec{n}]P(\vec{r}_1,\vec{r}_2,\vec{v}_1,\vec{v}_2,t)dS_{\vec{r}_2}d\vec{v}_2 \\ + \lambda(\vec{r}_1,\vec{v}_1)p - \lambda(\vec{r}_1,-\vec{v}_1)p(\vec{r}_1,-\vec{v}_1,t) = 0\end{aligned} \tag{5.10}$$

The next step is to find an estimation for the collision integral over the collision surface $\partial B_\epsilon(\vec{r}_1)$, where particles are more correlated. We first transform the integral into a surface integral over unit disk by taking the normal $\vec{n}$ such that $\vec{r}_2 = \vec{r}_1 + \epsilon\vec{n}$. Then, further

separate the collision boundary into sub-boundaries, ∂B_1^+ and ∂B_1^-. This yield

$$\begin{aligned}\mathcal{I} &= \int\limits_{\partial B_\epsilon(\vec{r}_1)\times V} [(\vec{v}_2-\vec{v}_1)\cdot\vec{n}]P(\vec{r}_1,\vec{r}_2,\vec{v}_1,\vec{v}_2,t)dS_{\vec{r}_2}d\vec{v}_2 \\ &= \int\limits_{\partial B_1(0)\times V} [(\vec{v}_2-\vec{v}_1)\cdot\vec{n}]P(\vec{r}_1,\vec{r}_1+\epsilon\vec{n},\vec{v}_1,\vec{v}_2,t)(-\epsilon)dS_{\vec{n}}d\vec{v}_2 \\ &= \int\limits_{\partial B_1^+(0)\times V} [(\vec{v}_2-\vec{v}_1)\cdot\vec{n}]P(\vec{r}_1,\vec{r}_1+\epsilon\vec{n},\vec{v}_1,\vec{v}_2,t)(-\epsilon)dS_{\vec{n}}d\vec{v}_2 \\ &+ \int\limits_{\partial B_1^-(0)\times V} [(\vec{v}_2-\vec{v}_1)\cdot\vec{n}]P(\vec{r}_1,\vec{r}_1+\epsilon\vec{n},\vec{v}_1,\vec{v}_2,t)(-\epsilon)dS_{\vec{n}}d\vec{v}_2\end{aligned}$$

where $\partial B_1^-(0) = \{\vec{n} : (\vec{v}_2-\vec{v}_1)\cdot\vec{n} < 0\}$ and $\partial B_1^+(0) = \{\vec{n} : (\vec{v}_2-\vec{v}_1)\cdot\vec{n} > 0\}$. From the collision boundary condition (5.5c), we find

$$\mathcal{I} = \int\limits_{\partial B_1^-(0)\times V} \epsilon[(\vec{v}_2-\vec{v}_1)\cdot\vec{n}]\big(P(\vec{r}_1,\vec{r}_1-\epsilon\vec{n},\vec{v}_2,\vec{v}_1,t) - P(\vec{r}_1,\vec{r}_1+\epsilon\vec{n},\boldsymbol{v},t)\big)dS_{\vec{n}}d\vec{v}_2$$

which still contains the unknown joint density function P. So to evaluate $\mathcal{I}$, we suppose the independent motion of far off particles whereas their correlation at nearby. The methodology is similar to what we have discussed in section 4.3.1.2, except that now it should be implemented in two dimensions. Hence, we get

$$P(\vec{r}_1,\vec{r}_1+\epsilon\vec{n},\mathbf{v},t) = q(\vec{r}_1,\vec{v}_1,t)q(\vec{r}_1,\vec{v}_2,t) + \epsilon\left[q(\vec{r}_1,\vec{v}_1,t)\vec{n}\cdot\nabla_{\vec{r}_1}q(\vec{r}_1,\vec{v}_2,t) + P_{out}^{(1)}(\vec{r}_1,\mathbf{v},t)\right] \tag{5.11}$$

where $P_{out}^{(1)}$ is the first order correction of the outer solution. However, the same approximation would not work for every interacting system. According to the physical description of our model, particles exchange their velocities during close encounters meaning the leading order term satisfies the collision boundary condition (5.5c), enabling us to write this approximation. On the contrary, when the system experiencing reflective (or elastic) collisions, the order $\mathcal{O}(1)$ terms may not satisfy the collision boundary condition. For example, let us recall the velocities during reflective collisions given in the introduction: when $\vec{v}_1 = (c,0)$, $\vec{v}_1{}' = (c,0)$ and $\vec{v}_2 = (0,c)$, $\vec{v}_2{}' = (0,-c)$. Then it is apparent that the leading orders $q(\vec{r}_1,\vec{v}_1,t)q(\vec{r}_2,\vec{v}_2,t) \neq q(\vec{r}_1,\vec{v}_1{}',t)q(\vec{r}_2,\vec{v}_2{}',t)$. At that point, one can utilise the method of matched asymptotic expansion to evaluate the collision integral.

Now, substituting the approximation (5.11) to the integral $\mathcal{I}$, $\mathcal{O}(\epsilon)$ terms vanishes and

$\mathcal{O}(\epsilon^2)$ terms yield,

$$\begin{aligned}\mathcal{O}(\epsilon^2): &\int_{\partial B_1^-(0)\times V} [(\vec{v}_2-\vec{v}_1)\cdot\vec{n}]\big(-q(\vec{r}_1,\vec{v}_2,t)\vec{n}\cdot\nabla_{\vec{r}_1}q(\vec{r}_1,\vec{v}_1,t)-q(\vec{r}_1,\vec{v}_1,t)\vec{n}\cdot\nabla_{\vec{r}_1}q(\vec{r}_1,\vec{v}_2,t)\\ &+P^{(1)}_{out}(\vec{r}_1,\vec{v}_2,\vec{v}_1,t)-P^{(1)}_{out}(\vec{r}_1,\vec{v}_1,\vec{v}_2,t)\big)dS_{\vec{n}}d\vec{v}_2\\ =&\int_{\partial B_1^-(0)\times V} [(\vec{v}_2-\vec{v}_1)\cdot\vec{n}]\big(-\nabla_{\vec{r}_1}[q(\vec{r}_1,\vec{v}_1,t)q(\vec{r}_1,\vec{v}_2,t)]\cdot\vec{n}\big)dS_{\vec{n}}d\vec{v}_2\\ +&\int_{\partial B_1^-(0)\times V} [(\vec{v}_2-\vec{v}_1)\cdot\vec{n}]\big(P^{(1)}_{out}(\vec{r}_1,\vec{v}_2,\vec{v}_1,t)-P^{(1)}_{out}(\vec{r}_1,\vec{v}_1,\vec{v}_2,t)\big)dS_{\vec{n}}d\vec{v}_2\\ =&\int_V \frac{\pi}{2}(\vec{v}_1-\vec{v}_2)\cdot\nabla_{\vec{r}_1}[q(\vec{r}_1,\vec{v}_1,t)q(\vec{r}_1,\vec{v}_2,t)]d\vec{v}_2\end{aligned}$$

To write the expression back in the original variables we use the normalisation condition on P which yields, $q(\vec{r}_1,\vec{v}_1,t)=p(\vec{r}_1,\vec{v}_1,t)+\mathcal{O}(\epsilon^2)$. Moreover, in a system of N individuals, pairwise interactions leads to $N-1$ excluded regions. Hence derives the following two dimensional kinetic model for $p(\vec{r}_1,\vec{v}_1,t)$ to $\mathcal{O}(\epsilon^2)$,

$$\begin{aligned}\frac{\partial p}{\partial t}(\vec{r}_1,\vec{v}_1,t)+\vec{v}_1\cdot\nabla_{\vec{r}_1}p(\vec{r}_1,\vec{v}_1,t)+\int_V\frac{\pi}{2}\epsilon^2(N-1)(\vec{v}_1-\vec{v}_2)\cdot\nabla_{\vec{r}_1}[p(\vec{r}_1,\vec{v}_1,t)p(\vec{r}_1,\vec{v}_2,t)]d\vec{v}_2\\ +\lambda(\vec{r}_1,\vec{v}_1)p(\vec{r}_1,\vec{v}_1,t)-\lambda(\vec{r}_1,-\vec{v}_1)p(\vec{r}_1,-\vec{v}_1,t)=0\end{aligned}\tag{5.12}$$

together with the initial condition

$$p(\vec{r}_1,\vec{v}_1,0)=p_0(\vec{r}_1,\vec{v}_1),\quad \text{where } p_0(\vec{r}_1,\vec{v}_1)=\int_{\Omega_\epsilon^{N-1}(\vec{r}_1)\times V^{N-1}} P_0(\mathbf{r},\mathbf{v})d\vec{r}_2...d\vec{r}_N d\vec{v}_2...d\vec{v}_N$$

and the reflective boundary condition $p(\vec{r}_1,\vec{v}_1,t)=p(\vec{r}_1,\vec{v}_*,t)$ on $\partial\Omega$.
In the particular case of $\epsilon=0$, N particles are independent in the domain Ω^N and we recover the noninteracting linear model from (5.12). This is the long-established velocity-jump model that describes the motion of organisms undergoing a stochastic reorientation event in higher dimensions [30, 71].

5.3.1 Velocity-space discretisation The nonlinear transport model can also be used to analyse systems that consist of a finite set of velocities. Such systems mimic the motion of persistent walkers on a lattice when each lattice site is occupied by at most one particle

or none. For instance, when individuals have an assigned direction of motion; vertically or horizontally, we may take $V = \{c(\cos\theta, \sin\theta) : \theta = \frac{k\pi}{2}, k = 0, 1, 2, 3\}$, possibly the simplest extension of the one-dimensional collision system. This is a well-known square lattice structure studied by Gavagnin and Yates [32] when each agent has been assigned a polarisation in one of the four directions of the lattice. The agent's velocity defined by the number of lattice sites moved during a single movement event. Moving on to the next example, the case when $V = \{c(\cos\theta, \sin\theta) : \theta = \frac{k\pi}{3}, k = 0, 1, 2, 3, 4, 5\}$ is more like an agent attempting to undergo a migration event choosing a target site from six nearest neighbour lattice sites [89].

In general, we can discretise the angular domain $[0, 2\pi]$ into m intervals of size $\Delta\theta = 2\pi/m$ and reformulate an equation capable of describing any situation like the above. In the divided domain, set $I_i = [\theta_{i-1/2}, \theta_{i+1/2}]$ for $i = 0, 1, ..., m-1$, and approximate $p(\vec{r}_1, \theta, t)$ by a piecewise constant function $p_i(\vec{r}_1, t)/\Delta\theta$, where $p_i(\vec{r}_1, t) = \int_{I_i} p(\vec{r}_1, \theta, t)d\theta$. We further ease the notations by setting $\theta_1 = \theta$ and $\theta_2 = \phi$ correspond to $\vec{v}_1$ and $\vec{v}_2$ in (5.12) and integrate it with respect to $\theta \in I_i$ to obtain the PDE for $p_i(\vec{r}_1, t)$.

Begin integrating the first term:

$$\int_{I_i} \frac{\partial p}{\partial t}(\vec{r}_1, \theta, t)d\theta = \frac{\partial p_i}{\partial t}(\vec{r}_1, t) \tag{5.13}$$

Integrating the second term,

$$\begin{aligned} \int_{I_i} \vec{v}_1 \cdot \nabla_{\vec{r}_1} p(\vec{r}_1, \theta, t)d\theta &= \frac{c}{\Delta\theta} \int_{I_i} (\cos\theta, \sin\theta) \cdot \nabla_{\vec{r}_1} p_i d\theta \\ &= \frac{\sin(\Delta\theta/2)}{\Delta\theta/2} \vec{v}_{\theta_i} \cdot \nabla_{\vec{r}_1} p_i(\vec{r}_1, t) \end{aligned} \tag{5.14}$$

where $\vec{v}_{\theta_i} = c(\cos\theta_i, \sin\theta_i)$. By discretising the existing integral V and applying the second integral over I_i, the third term simplifies as

$$\begin{aligned} &\int_{I_i} \int_0^{2\pi} \pi\epsilon^2(N-1)(\vec{v}_1 - \vec{v}_2) \cdot \nabla_{\vec{r}_1}[p(\vec{r}_1, \theta, t)p(\vec{r}_1, \phi, t)]d\phi d\theta \\ &\quad = \frac{c\pi\epsilon^2(N-1)}{\Delta\theta^2} \sum_{j=0}^{m-1} \nabla_{\vec{r}_1} p_i p_j \cdot \int_{I_i} \int_{I_j} [(\cos\theta, \sin\theta) - (\cos\phi, \sin\phi)]d\phi d\theta \\ &\quad = \pi\epsilon^2(N-1)\frac{\sin(\Delta\theta/2)}{\Delta\theta/2} \sum_{j=0}^{m-1} (\vec{v}_{\theta_i} - \vec{v}_{\theta_j}) \cdot \nabla_{\vec{r}_1} p_i p_j \quad \text{for} \quad i \neq j \end{aligned} \tag{5.15}$$

Substituting the bias term for λ, the fourth term becomes

$$\begin{aligned}\int_{I_i} \lambda(\vec{r}_1,\theta)p(\vec{r}_1,\theta,t)d\theta &= \int_{I_i} \big(\lambda_0 - c\chi(\cos\theta,\sin\theta)\cdot\nabla_{\vec{r}_1}S(\vec{r}_1)\big)p(\vec{r}_1,\theta,t)d\theta \\ &= p_i\lambda_0 - \frac{c\chi p_i}{\Delta\theta}\nabla_{\vec{r}_1}S(\vec{r}_1)\cdot\int_{I_i}(\cos\theta,\sin\theta)d\theta \\ &= \lambda_i(\vec{r}_1)p_i(\vec{r}_1,t)\end{aligned} \tag{5.16}$$

where $\lambda_i(\vec{r}_1) = \lambda_0 - \frac{\sin(\Delta\theta/2)}{\Delta\theta/2}\chi\vec{v}_{\theta_i}\cdot\nabla_{\vec{r}_1}S(\vec{r}_1)$. Similarly, we can evaluate the fifth term and write

$$\int_{I_i} \lambda(\vec{r}_1,\theta+\pi)p(\vec{r}_1,\theta+\pi,t)d\theta = \lambda_{i+\pi}(\vec{r}_1)p_{i+\pi}(\vec{r}_1,t) \tag{5.17}$$

where $\lambda_{i+\pi}(\vec{r}_1) = \lambda_0 + \frac{\sin(\Delta\theta/2)}{\Delta\theta/2}\chi\vec{v}_{\theta_i}\cdot\nabla_{\vec{r}_1}S(\vec{r}_1)$. Combining (5.13), (5.14), (5.15), (5.16) and (5.17), we get the discretised version of (5.12):

$$\begin{aligned}\frac{\partial p_i}{\partial t}(\vec{r}_1,t) + \frac{\sin(\Delta\theta/2)}{\Delta\theta/2}\vec{v}_{\theta_i}\cdot\nabla_{\vec{r}_1}p_i(\vec{r}_1,t) + \pi\epsilon^2(N-1)\frac{\sin(\Delta\theta/2)}{\Delta\theta/2}\sum_{j=0}^{m-1}(\vec{v}_{\theta_i}-\vec{v}_{\theta_j})\cdot\nabla_{\vec{r}_1}p_ip_j + \\ \lambda_i(\vec{r}_1)p_i(\vec{r}_1,t) - \lambda_{i+\pi}(\vec{r}_1)p_{i+\pi}(\vec{r}_1,t) = 0\end{aligned} \tag{5.18}$$

5.4 Diffusion limit

To analyse systems on a macroscopic scale, one can compute the diffusion limit of a transport equation. In fact, with a high frequency of directional changes, the motion resembles diffusion. In our previous discrete velocity-jump models, we investigated the long-time dynamics of the system by applying algebraic operations on the subpopulation probability distributions following up with an asymptotic expansion. In higher dimensions, one needs to use the analogous first two velocity moments:
the number density (zeroth moment): $\rho(\vec{r},t) = \int_V p(\vec{r},\vec{v},t)d\vec{v}$; and
the momentum flux (first moment) : $\mathbf{j}(\vec{r},t) = \rho(\vec{r},t)\mathbf{u}(\vec{r},t) = \int_V p(\vec{r},\vec{v},t)\vec{v}d\vec{v}$,
where $\mathbf{u}$ is the average velocity. The process yields a system of two equations that includes the third moment, and it is essential to close this system before investigating the parabolic limit. To this end, we use the Cattaneo approximation, which is studied by Hillen [39].

To begin with, let us first integrate (5.12) over V[2]:

$$\frac{\partial}{\partial t}\int_V p(\vec{v}_1)d\vec{v}_1 + \nabla_{\vec{r}_1}\cdot\int_V p(\vec{v}_1)\vec{v}_1 d\vec{v}_1 + \frac{\pi}{2}\epsilon^2(N-1)\nabla_{\vec{r}_1}\cdot\int_V\int_V(\vec{v}_1-\vec{v}_2)[p(\vec{v}_1)p(\vec{v}_2)]d\vec{v}_1 d\vec{v}_2 + \int_V\big(\lambda(\vec{r}_1,\vec{v}_1)p(\vec{v}_1)-\lambda(\vec{r}_1,-\vec{v}_1)p(-\vec{v}_1)\big)d\vec{v}_1 = 0$$

The third and the fourth integrals vanishes; therefore, we obtain the continuity equation

$$\frac{\partial\rho}{\partial t} + \nabla_{\vec{r}_1}\cdot\mathbf{j} = 0 \tag{5.19}$$

Next, multiplying (5.12) by $\vec{v}_1$ and again integrating over V,

$$\frac{\partial\mathbf{j}}{\partial t} + \nabla_{\vec{r}_1}\cdot\int_V p(\vec{v}_1)\vec{v}_1\vec{v}_1 d\vec{v}_1 + \frac{\pi}{2}\epsilon^2(N-1)\nabla_{\vec{r}_1}\cdot\left\{\rho\int_V p(\vec{v}_1)\vec{v}_1\vec{v}_1 d\vec{v}_1 - |\mathbf{j}|^2\right\} + 2\lambda_0\mathbf{j} - 2\nabla_{\vec{r}_1}S\cdot\int_V p(\vec{v}_1)\vec{v}_1\vec{v}_1 d\vec{v}_1 = 0 \tag{5.20}$$

where $\int_V p(\vec{v}_1)\vec{v}_1\vec{v}_1 d\vec{v}_1$ is the second velocity moment. To close the system we replace this higher moment from the Cattaneo approximation (see appendix (A.6)):

$$\int_V p(\vec{v}_1)\vec{v}_1\vec{v}_1 d\vec{v}_1 = \frac{c^2}{2}\rho I \tag{5.21}$$

where I is the 2×2 identity matrix. Substituting (5.21) and the turning frequency (1.12) in the integrated equation (5.20), we derive the moment system

$$\frac{\partial\rho}{\partial t} + \nabla_{\vec{r}_1}\cdot\mathbf{j} = 0 \tag{5.22a}$$

$$\frac{\partial\mathbf{j}}{\partial t} + \frac{c^2}{2}\nabla_{\vec{r}_1}\rho + \frac{\pi}{2}\epsilon^2(N-1)\nabla_{\vec{r}_1}\left(\frac{(c\rho)^2}{2} - |\mathbf{j}|^2\right) + 2\lambda_0\mathbf{j} - c^2\chi(S)\rho\nabla_{\vec{r}_1}S = \mathbf{0} \tag{5.22b}$$

$$\text{with the boundary condition}\quad \boldsymbol{\eta}\cdot\mathbf{j} = 0 \quad\text{on}\quad \partial\Omega \tag{5.22c}$$

[2] we write $p(\vec{r}_1,\vec{v}_1,t) = p(\vec{v}_1)$ to ease the notation

where $\boldsymbol{\eta}$ is the outward normal. We now apply the parabolic scaling $t = \tau/\gamma^2$ and $\vec{r}_1 = \vec{r}/\gamma$ for a sufficiently small parameter $\gamma > 0$. So the system (5.22) becomes

$$\gamma \frac{\partial \rho}{\partial \tau} + \nabla_{\vec{r}} \cdot \mathbf{j} = 0$$
$$\gamma^2 \frac{\partial \mathbf{j}}{\partial \tau} + \frac{c^2}{2}\gamma \nabla_{\vec{r}}\rho + \frac{\pi}{2}\epsilon^2(N-1)\gamma \nabla_{\vec{r}}\left(\frac{(c\rho)^2}{2} - |\mathbf{j}|^2\right) + 2\lambda_0 \mathbf{j} - c^2\chi(S)\gamma\rho\nabla_{\vec{r}}S = \mathbf{0}$$

Now using the regular perturbation expansion $\rho = \rho_0 + \gamma\rho_1 + \ldots$ and $\mathbf{j} = \mathbf{j}_0 + \gamma\mathbf{j}_1 + \ldots$, we get

$$\begin{aligned}
\mathcal{O}(1) :& \nabla_{\vec{r}} \cdot \mathbf{j}_0 = 0 \\
& 2\lambda_0 \mathbf{j}_0 = 0 \\
& \text{which implies the trivial solution} \quad \mathbf{j}_0 = 0 \\
\mathcal{O}(\gamma) :& \frac{\partial \rho_0}{\partial \tau} + \nabla_{\vec{r}} \cdot \mathbf{j}_1 = 0 \\
& \frac{c^2}{2}\nabla_{\vec{r}}\rho_0 + \frac{\pi}{4}\epsilon^2(N-1)\nabla_{\vec{r}}(c\rho_0)^2 + 2\lambda_0\mathbf{j}_1 - c^2\chi(S)\rho_0\nabla_{\vec{r}}S = 0 \\
& \text{eliminating } \mathbf{j}_1 \text{ from the equations we get the drift-diffusion equation}
\end{aligned}$$

$$\frac{\partial \rho_0}{\partial \tau} = \nabla_{\vec{r}} \cdot \left[\frac{c^2}{4\lambda_0}\left(1 + \pi\epsilon^2(N-1)\rho_0\right)\nabla_{\vec{r}}\rho_0 - \frac{c^2\rho_0}{2\lambda_0}\chi(S)\nabla_{\vec{r}}S\right], \tag{5.24}$$

where the effective diffusion coefficient $D(\rho)$ is given by $\frac{c^2}{4\lambda_0}\big(1 + \pi\epsilon^2(N-1)\rho\big)$ and the drift $F = \frac{c^2}{2\lambda_0}\chi(S)\nabla_{\vec{r}}S$. When $c, \lambda_0 \to \infty$

$$D(\rho) = D_0\big(1 + \pi\epsilon^2(N-1)\rho\big), \quad \text{where} \quad D_0 = \frac{c^2}{4\lambda_0} \tag{5.25}$$

The above drift-diffusion equation is consistent with that for Brownian particles which is investigated by Bruna and Chapman (see eq.(11) in [12]) but differs from the continuum population-level description of the on-lattice model used by Gavagnin and Yates [32]. The noninteracting system, however, aligns with our reduced linear model.

5.5 Eigenstructure of the two-dimensional system

In this thesis, a fair amount of work has been devoted to understanding the 1D nonlinear hyperbolic system using the concept of characteristic lines. We were able to write more transparent characteristic relations in terms of directional differentials along a sin-

gle characteristic direction (see section (2.4)) that were eventually supported us when establishing time-dependent solutions. However, the situation is more complicated in 2D problems. The characteristic curves become characteristic surfaces that involve two independent directions of directional differentiation described as bicharacteristic directions [51]. Moreover, a simple decoupling of the equations is not possible since the Jacobian matrices in the x- and y-direction cannot be diagonalized simultaneously. Therefore, in the present section, we discuss the eigenstructure of the 2D model following the ideas from the study [51], though we will not extend those in examining Riemann invariant manifolds.

The system (5.22) can be written in terms of three unknown functions on 3-dimensional spacetime that give rise to the differential conservative form

$$\frac{\partial U}{\partial t}+\frac{\partial F(U)}{\partial x}+\frac{\partial G(U)}{\partial y}=\mathbf{0},\quad -L\leq x,y\leq L,\quad 0\leq t\leq T \tag{5.26}$$

where $U=\begin{pmatrix}\rho\\ \rho u\\ \rho v\end{pmatrix}$ with (u,v) being the directional velocity,

$F(U)=\begin{pmatrix}\rho u\\ \frac{c^2\rho}{2}(1+\frac{\xi\rho}{2})-\frac{\xi}{2}|\mathbf{j}|^2\\ 0\end{pmatrix}$ and $G(U)=\begin{pmatrix}\rho v\\ 0\\ \frac{c^2\rho}{2}(1+\frac{\xi\rho}{2})-\frac{\xi}{2}|\mathbf{j}|^2\end{pmatrix}$ with $\xi=\pi\epsilon^2(N-1)$.

It is noted that, for the flux Jacobians J_F and J_G, the differential operator $\mathcal{D}=I\frac{\partial}{\partial t}+J_F\frac{\partial}{\partial x}+J_G\frac{\partial}{\partial y}$ is hyperbolic if real characteristic surfaces exist, and any characteristic surface $\psi(\mathbf{r},t)=0$, for $\mathbf{r}\in\mathbb{R}^2$ satisfies the characteristic function

$$\det\left(I\frac{\partial}{\partial t}\psi+J_F\frac{\partial}{\partial x}\psi+J_G\frac{\partial}{\partial y}\psi\right)=0 \tag{5.27}$$

Consequently, substituting the Jacobian matrices $J_F=\begin{pmatrix}0 & 1 & 0\\ \frac{c^2}{2}(1+\xi\rho) & -\xi\rho u & -\xi\rho v\\ 0 & 0 & 0\end{pmatrix}$ and $J_G=\begin{pmatrix}0 & 0 & 1\\ 0 & 0 & 0\\ \frac{c^2}{2}(1+\xi\rho) & -\xi\rho u & -\xi\rho v\end{pmatrix}$ in (5.27), a straightforward calculation derives the following factors for a polynomial in the derivatives of ψ:

$$\frac{\partial\psi}{\partial t}\left(\frac{\partial\psi}{\partial t}-\frac{\mathbf{j}\xi}{2}\cdot\nabla\psi-\frac{\sigma}{2}\|\nabla\psi\|\right)\left(\frac{\partial\psi}{\partial t}-\frac{\mathbf{j}\xi}{2}\cdot\nabla\psi+\frac{\sigma}{2}\|\nabla\psi\|\right)=0 \tag{5.28}$$

where $\sigma = \sqrt{2c^2 + 2\rho c^2 \xi + \xi^2 \left(\mathbf{j} \cdot \frac{\nabla\psi}{\|\nabla\psi\|}\right)^2}$. We may expand the square root in powers of ϵ, but we only add terms up to $\mathcal{O}(\epsilon^2)$ as the PDEs obtained by the perturbation method are expected to be accurate to this order. This simplification eliminates the spatial gradient of ψ in σ itself, which would be helpful in our following calculations.
We find each factor in (5.28) is in the general form of the Hamilton-Jacobi equation, where the Hamiltonian can be identified as

$$H(\mathbf{r}, p) = -\frac{\mathbf{j}\xi}{2} \cdot p \pm \frac{\sigma}{2}\|p\| \quad \text{for} \quad \nabla\psi \equiv p$$

From Hamilton's canonical equations, we then derive the bicharacteristics for the nonlinear system (5.26):

$$\dot{\mathbf{r}}(t) = \frac{\partial H}{\partial p} = -\frac{\mathbf{j}\xi}{2} \pm \frac{\sigma}{2}\frac{p}{\|p\|} = -\frac{\mathbf{j}\xi}{2} \pm \frac{\sigma}{2}\mathbf{n}$$

where $\mathbf{n} \equiv \frac{\nabla\psi}{\|\nabla\psi\|}$ is the spatial unit vector, and σ is independent of p. The eigenvalues of the matrix $\mathbf{n} \cdot (J_F, J_G)$ are given by the formula $\Lambda = -\frac{1}{\|\nabla\psi\|}\frac{\partial\psi}{\partial t} = \frac{H(\mathbf{r},p)}{\|p\|}$; therefore, we have the eigenvalues analogous to those in 1D form (2.32):

$$\left\{0, -\frac{\mathbf{j}\xi}{2} \cdot \mathbf{n} - \frac{\sigma}{2}, -\frac{\mathbf{j}\xi}{2} \cdot \mathbf{n} + \frac{\sigma}{2}\right\}$$

5.6 Stationary solution

In the present as well as in the following sections, we assess the validity of the two-dimensional velocity jump model, comparing both stationary and time-dependent solutions of (5.22) with particle-level simulations. The numerical techniques for both the particle- and the population-level models are similar to the ones used in the previous chapters, yet we detail the modifications that support the higher-dimensional applications. For the numerical examples, we consider the two-dimensional forms of the two signal functions 2.3(a) and 2.3(b), where the maximum indicates a higher amount of nutrients (see Figure (5.1)).
When the system is at equilibrium, the time derivative in the equation (5.22a) can be set to zero. This implies, $\mathbf{j}$ satisfies

$$\begin{aligned} \nabla_{\vec{r}_1} \cdot \mathbf{j} = 0 \quad &\text{in} \quad \Omega, \quad \text{and} \\ \boldsymbol{\eta} \cdot \mathbf{j} = 0 \quad &\text{on} \quad \partial\Omega \end{aligned}$$

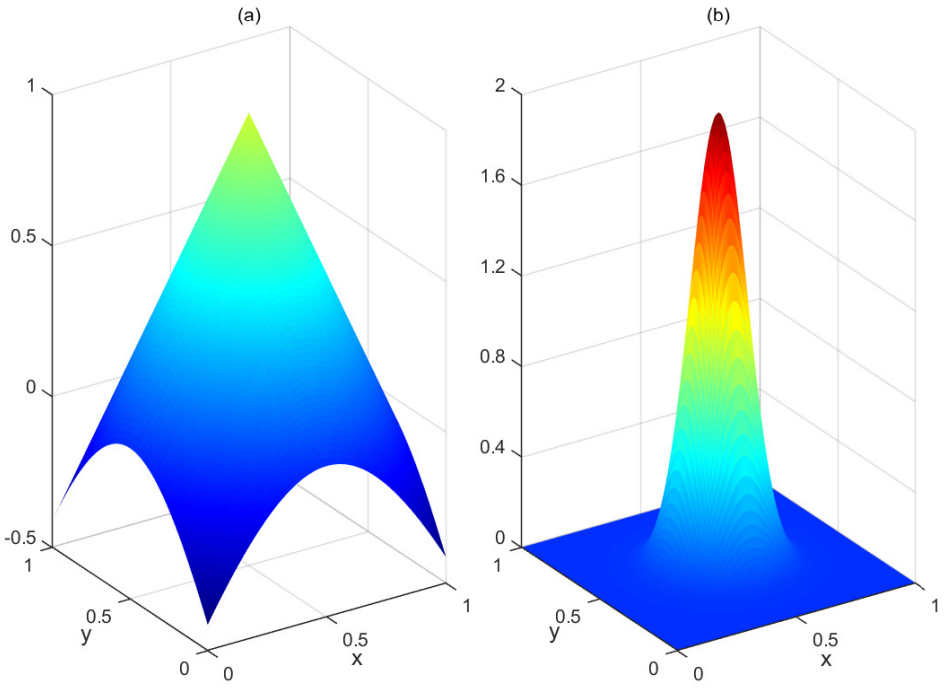

Figure 5.1: (a). $S(\vec{r}) = 1 - 2||\vec{r} - 0.5||$, with $\lambda_0 = 2.5$ and (b). $S(\vec{r}) = 2e^{-50\,||\vec{r}-0.5||^2}$, with $\lambda_0 = 20$

Consequently, the flux vanishes and the equation (5.22b) yields

$$\big(1 + \pi\epsilon^2(N-1)\rho_{st}\big)\nabla_{\vec{r}_1}\rho_{st} - 2\rho_{st}\chi(S)\nabla_{\vec{r}_1}S = \mathbf{0}$$
$$\text{with the normalisation condition} \quad \int_{\Omega} \rho_{st} d\vec{r}_1 = 1$$

The solution to the above equation is

$$\ln \rho_{st}(\vec{r}_1) + \pi\epsilon^2(N-1)\rho_{st}(\vec{r}_1) - 2\chi(S)(S(\vec{r}_1) - S(\vec{0})) = A, \tag{5.29}$$

where A is an arbitrary constant which can be determined from the normalisation condition. Note that, when $\epsilon \to 0$ we simply obtain the stationary state for the point particles:

$$\begin{aligned} \rho^0_{st} &= e^{\big(2\chi(S(\vec{r}_1)-S(\vec{0}))+A\big)} \\ &= \frac{e^{\big(2\chi(S(\vec{r}_1)-S(\vec{0}))\big)}}{\int e^{\big(2\chi(S(\vec{r}_1)-S(\vec{0}))\big)}} \end{aligned} \tag{5.30}$$

Although Lambert W function worked for (5.29) in one dimension, it is unlikely to find a closed form solution in higher dimension because of the nonlinearity; hence, we obtain

numerically.

5.6.1 The Metropolis–Hastings algorithm When the system consists of point particles, the stationary solution for the N-particle model (5.1) is

$$\begin{aligned} P_{st} &= \prod_{i=1}^{N} \rho_{st}^{0}(\vec{r}_i, t) \quad \text{in} \quad \Omega^N \\ &= A \exp\left\{ \sum_{i=1}^{N} \Big(2\chi(S)(S(\vec{r}_i) - S(\vec{0})) \Big) \right\} \end{aligned}$$

The same solution works for finite-sized particles in Ω_ϵ^N; however, we will face the same difficulty as in the one-dimensional situation. That is, integrating P_{st} over a complicated domain Ω_ϵ^N to find the arbitrary constant A. We have already overcome this problem in our previous models by using an indirect sampling method: the MH algorithm. In the two dimensional setting, the definition of P_{st} can be extended to all Ω^N as $P_{st} = A \exp(-\Phi(\mathbf{r}))$, by introducing the energy Φ associated with each configuration:

$$\Phi(\mathbf{r}) = \begin{cases} -\sum_{i=1}^{N} \Big(2\chi(S)(S(\vec{r}_i) - S(\vec{0})) \Big), & \mathbf{r} \in \Omega_\epsilon^N \\ \infty, & \text{otherwise} \end{cases}$$

We then follow the MH algorithm described under section (4.5.1) to sample configurations according to the density P_{st} by constructing a Markov chain over the configuration space.

5.6.2 Numerical example Since an exact stationary solution for the nonlinear PDE is not feasible, we solve (5.29) numerically using the Newton-Raphson method, discretising both x and y directions into K grid points. From these discrete counterparts, the density values $\rho_{st}(x_i, y_j)$ for $1 \le i, j \le K$ and the constant A yields a system of K^2 equations with $K^2 + 1$ unknowns. Approximating the normalisation condition using the composite Simpson's rule, we can write the $(K^2+1)^{th}$ equation. So the resulting system can be written as

$$\begin{aligned} \ln Q_k + \pi\epsilon^2(N-1)Q_k - 2(S(x_i, y_j) - S(\vec{0})) - Q_{K^2+1} = 0 \quad \text{for} \quad 1 \le k \le K^2 \\ \sum_{k=1}^{K^2} M_k Q_k - 1 = 0 \end{aligned} \tag{5.31}$$

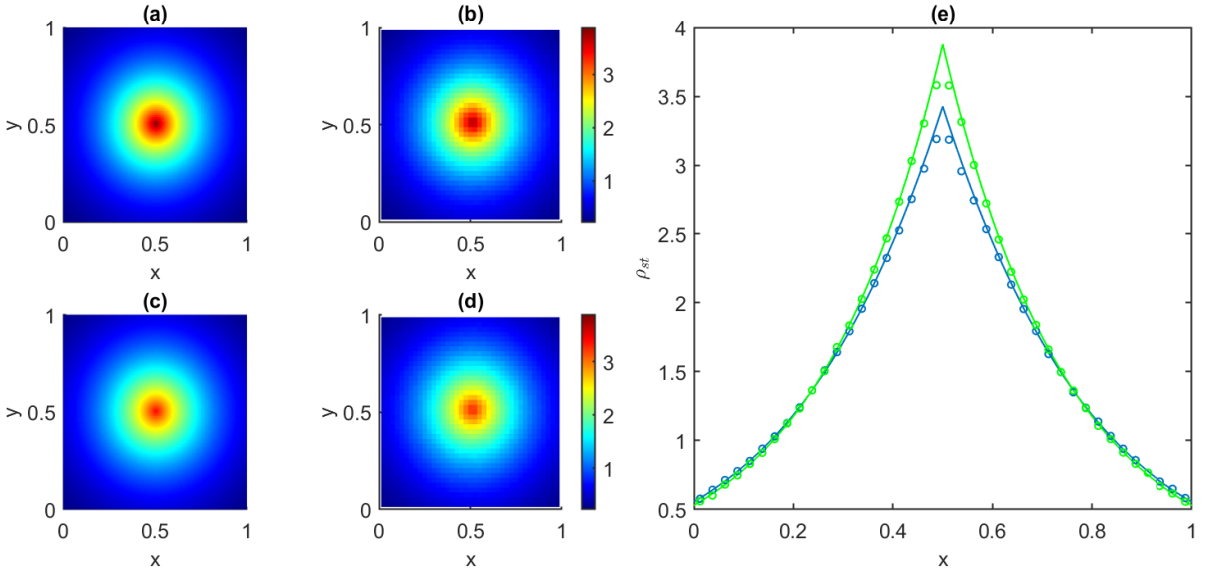

Figure 5.2: Stationary marginal densities ρ_{st} under the extracellular signal function (5.1(a)) for finite-size particles. (a) ρ_{st} from (5.29) for $\epsilon = 0.002$. (b) Histogram from the MH algorithm for $\epsilon = 0.002$. (c) ρ_{st} from (5.29) for $\epsilon = 0.01$. (b) Histogram from the MH algorithm for $\epsilon = 0.01$. Plots (a)-(d) have the same colour bar. (e) Stationary marginal density (solid line) and the particle simulation (circles) at $y = 0.5$. The green indicates $\epsilon = 0.002$ and blue $\epsilon = 0.01$.

where $Q = (\rho_{st}(:), C)$ and M_k is the k^{th} entry of the linearised matrix $\frac{h^2}{9}(m^\top m)$ with m being the one dimensional quadrature $\begin{pmatrix}1 & 4 & 2 & 4 & \dots & 4 & 1\end{pmatrix}$. The Jacobian is a $(K^2{+}1)$-by-(K^2+1) matrix given by,

$$Jacobian = \begin{pmatrix} \frac{1}{Q_1} + \pi\epsilon^2(N-1) & 0 & \cdots & 0 & -1 \\ 0 & \frac{1}{Q_2} + \pi\epsilon^2(N-1) & \cdots & 0 & -1 \\ \vdots & \vdots & \ddots & \vdots & \vdots \\ M_1 & M_2 & \cdots & M_{K^2} & 0 \end{pmatrix}$$

The Figures (5.2) and (5.3) show the model and simulation results of randomly positioned $N = 200$ particles of size $\epsilon = 0.002$ and $\epsilon = 0.01$ inside the square domain, whose chemotactic sensitivity coefficient χ is one. The histograms are produced at an acceptance rate in the 0.234 [82] order of magnitude with 10^8 steps of the MH algorithm, dividing the domain Ω into 40 bins along each dimension. At the end of the process, we divide the resulting value in each bin by the number of steps, the number of particles, and the bin area. In both figures, the stationary solutions preserve the radial shape and centres of their respective signal functions, indicating that the particle densities are higher in and around the centres of the domain. In fact, the densities are significantly high for steeper gradients (see Figure (5.3)). Although there is competition between finite-size

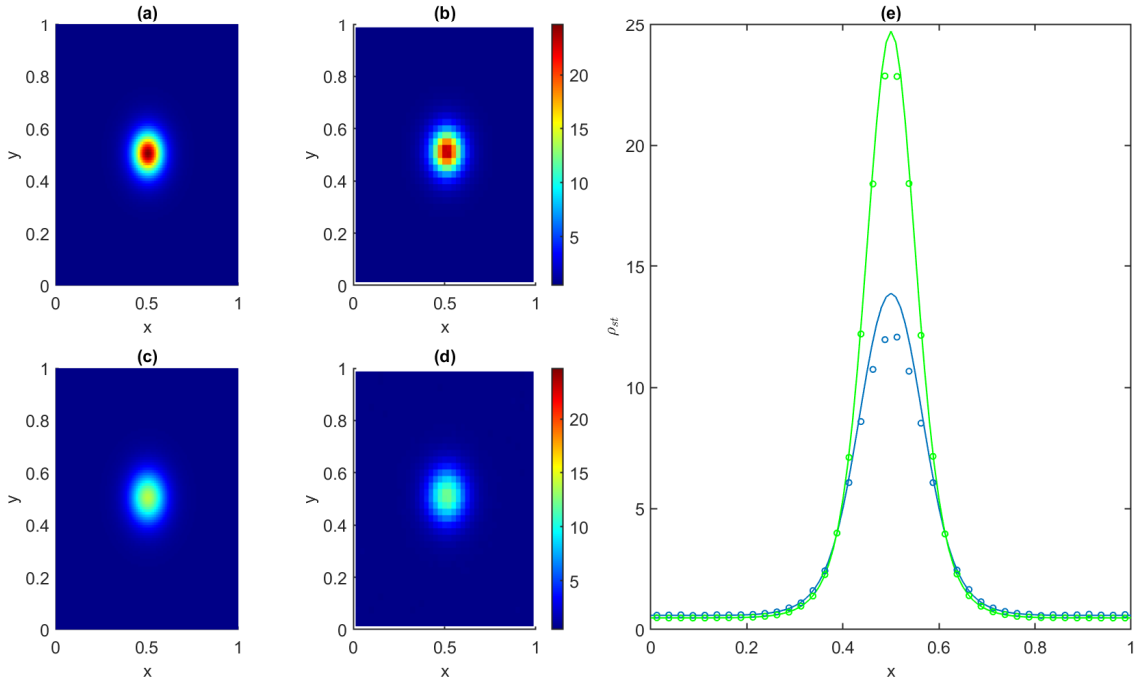

Figure 5.3: Stationary marginal densities ρ_{st} under the extracellular signal function (5.1(b)) for finite-size particles. (a) ρ_{st} from (5.29) for $\epsilon = 0.002$. (b) Histogram from the MH algorithm for $\epsilon = 0.002$. (c) ρ_{st} from (5.29) for $\epsilon = 0.01$. (b) Histogram from the MH algorithm for $\epsilon = 0.01$. Plots (a)-(d) have the same colour bar. (e) Stationary marginal density (solid line) and the particle simulation (circles) at $y = 0.5$. The green indicates $\epsilon = 0.002$ and blue $\epsilon = 0.01$.

particles, the agreement between the model (5.29) and the stochastic simulations is good when $\epsilon = 0.002$. Essentially the outputs are in close convergence with the point particle solution due to the low occupied fraction (≈ 0.000628). However, when we raise the dimension of the particle to 0.01 (keeping the number of particles the same), the model deviates noticeably from the simulation result around the centre of the domain (see Figure 5.3 (e)). This result confirms that the equilibrium of the kinetic model (5.12) works well under the strict condition: $N\epsilon^2 \ll 1$.

5.7 Transient solution

In this numerical study, we compare the time-dependent solutions of the kinetic models (5.12) with the simulations of the full particle system. We use the algorithm explained in section (2.5.2) that counts the frequency of collisions to perform full-particle simulations in two dimensions, and this is detailed in the next section. The numerical solutions of the model is achieved applying a first order explicit finite volume scheme in the discretised velocity space (5.18).

5.7.1 Event-driven KMC algorithm For the simulations, the KMC algorithm would work based on the three events: random turns, collisions with the wall and collisions with each other. We assume positions and velocities of the N particles are $X_i = (x_i, y_i)$ and $V_i = (u_i, v_i)$ with no two particles overlap at any time. That is $||X_i - X_j|| > \epsilon$ for $i \neq j$. The algorithm jumps from one minimum time to another; therefore, we calculate the event times as follows.

Turn time (τ_{turn}): $\lambda_0\tau - \chi\left(S(X + V\tau) - S(X)\right) - \ln\left(\frac{1}{r}\right) = 0$, where r is a uniform random number. When a turn event happens, the particle rotates by 180^{deg} and proceed in the new direction.

Boundary collision time (τ_{wall}): Particles rebound at the hard boundaries. We can simply calculate this rebound time, dividing the distance from the relevant collision wall ($x, y = 0$ or $x, y = L$) by its velocity component (horizontal or vertical). We can identify the collision wall by checking the sign of each velocity component and update the reflected velocities accordingly. Here we use the inward normal.

Particle interaction time (τ_{coll}): Computing future collisions of an individual with every other occupant increase the computational cost. Besides a particle is more likely to interact with neighbouring particles, rather than faraway ones. To identify one's neighbours, we first get the minimum time from turn times and wall collision times. Then, calculate the distance (d_{min}) that a particle can run during this minimum time. Pairs that fit into

the range which is created by d_{min} are counted for collision time calculations; otherwise, time is set to infinity. If two particles, say at X_i and X_j with velocities V_i and V_j, collide at a future time τ_{coll},

$$||(X_i + V_i\tau_{coll}) - (X_j + V_j\tau_{coll})||^2 = \epsilon^2$$

Therefore, we find the collision time through

$$\tau_{coll} = \begin{cases} \frac{-b-\sqrt{b^2-ac}}{a}, & a \neq 0, b \leq 0 \quad \text{and} \quad b^2 - ac \geq 0 \\ \infty, & \text{otherwise} \end{cases}$$

where $a = ||V_i - V_j||^2$, $b = (X_i - X_j) \cdot (V_i - V_j)$ and $c = ||X_i - X_j||^2 - \epsilon^2$. Note that, if $a = 0$, the particles are moving in the same direction. The value c may also be zero if two particles are already at the collision site. After the interaction, the two particles will exchange their velocities.

The above three events create the event queue, where we find the next minimum event time. Interestingly, all event times of particles that are not involved in this chosen event persist. Therefore, we can calculate them once before the time loop and update the stored data according to the new velocities of the interacting particles as time evolves. That is, the number of updated events per particle is N collisions and one turn event. These changes reduce the complexity of the algorithm to $\mathcal{O}(N)$ and hence the run time.

5.7.2 Numerical examples The numerical examples presented in this section aim to illustrate the behaviour of the systems under biased and unbiased conditions and examine the effect of changing parameters on the solutions. Unless explicitly stated otherwise, we take 400 particles of speed $c = 1$ and $\chi = 1$ in a unit square domain $\Omega = [0, 1] \times [0, 1]$ with no-flux boundary conditions. To generate model solutions, we discretise the velocity space into 20 velocity directions and the spatial domain into control volumes of size $dx = dy = 0.005$. We then approximate the numerical flux at each interface using the so called local Lax-Friedrichs (Rusanov) scheme. To produce histograms, we divide the domain into 40×40 bins and calculate the cumulative bin averages, performing 10^4 realisations. Essentially this implies that we are plotting a distribution of 4×10^6 particle positions. In all figures, we collate simulations of both noninteracting (green) and interacting particles (blue) at time $t = 0.2$; the solid lines and the circles indicate solutions for the PDE models and the KMC simulations, respectively.

Figure (5.4) illustrates the time-dependent behaviour of the system in the case of vanishing turning rates. In other words, we are examining only the effect of collisions. The particles are initialised uniformly at random inside a 0.5×0.5 square with centre at $(0.5, 0.5)$, that

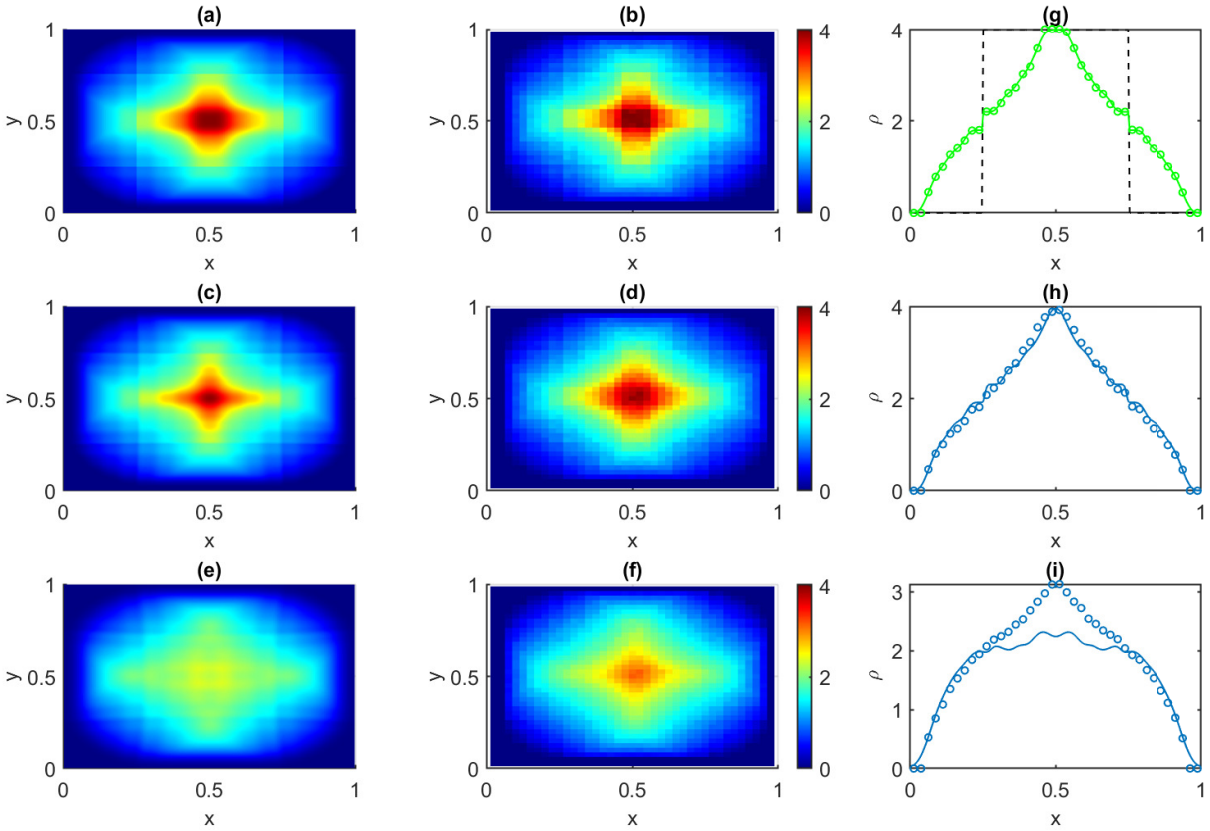

Figure 5.4: Transient marginal densities ρ at time $t = 0.2$ under no external stimulus. The first column shows model solutions for (a) point (c) $\epsilon = 0.005$ and (e) $\epsilon = 0.01$ particles with their respective histograms (from the KMC algorithm) in the second column. Plots (a)-(f) have the same colour bar. Plots (g)-(i) represent a cross section at $y = 0.5$ where the green indicates point and blue indicates finite-size particles. The dashed black line is the initial condition.

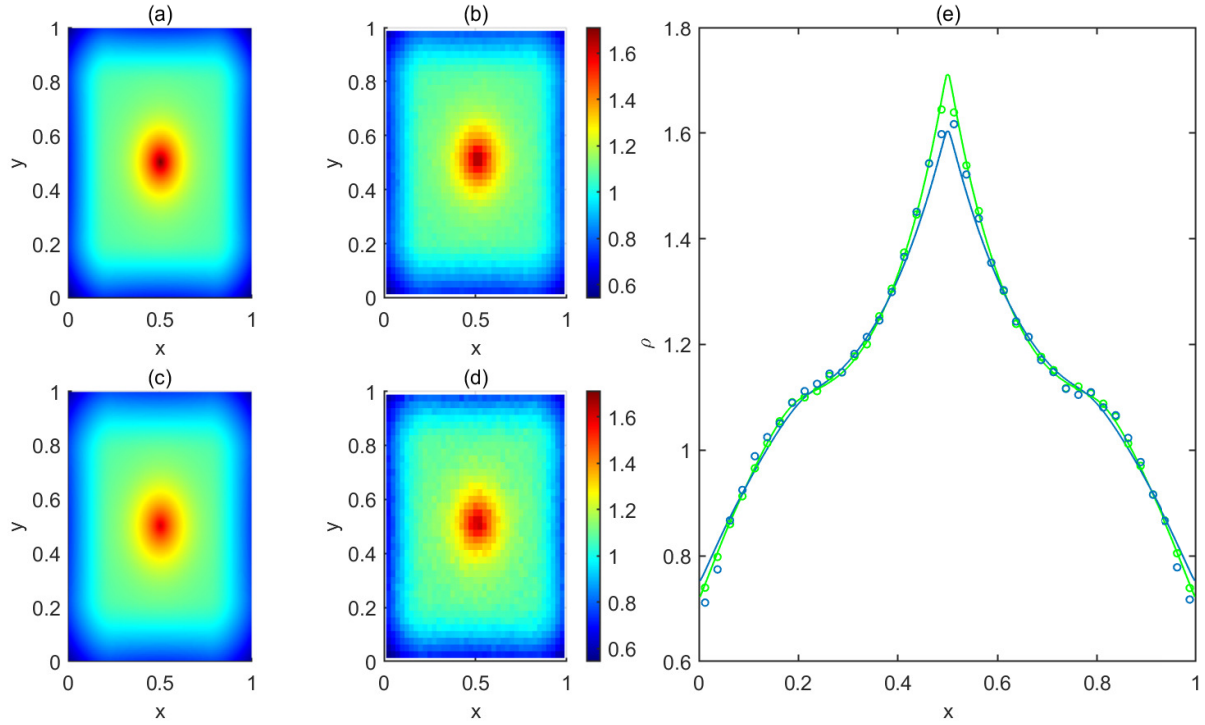

Figure 5.5: Transient marginal density $\rho(\vec{r}, t)$ under the extracellular signal function (5.1(a)). (a) ρ from (5.18) for $\epsilon = 0$. (b) Histogram from the KMC algorithm for $\epsilon = 0$. (c) ρ from (5.18) for $\epsilon = 0.01$. (b) Histogram from the KMC algorithm for $\epsilon = 0.01$. Plots (a)-(d) have the same colour bar. (e) Transient marginal density (solid line) and the particle simulation (circles) at $y = 0.5$.

is,

$$p(\vec{r}, \theta, 0) = \mathbb{1}_D, \quad \theta \in [0, 2\pi]$$

where $D = [0.25, 0.75] \times [0.25, 0.75]$. Care was taken to avoid overlapping of finite-size particles during this initialisation. The initial profile spreads out with time, maintaining an excellent match between the model solution and the simulation for point particles (see first row of Figure (5.4)). In fact, the theoretical prediction for size $\epsilon = 0.005$ also compares well with their simulation counterparts because of the low occupied fraction of particles. However, excluded-volume effects are significant for size $\epsilon = 0.01$ (see Figure 5.4(i)). This discrepancy can also be attributed to additional numerical diffusion in the PDE solution.

To generate Figures (5.5) and (5.6), we introduced the extracellular signals (5.1(a)) and (5.1(b)) to both point and finite-size particle systems. We started simulation by evenly distributing particles across the domain. After $t = 0.2$, we find higher densities in and around the most favourable location, the centre. In both figures, the point particle model seems to give a good approximation to the KMC results; however, when looking at the

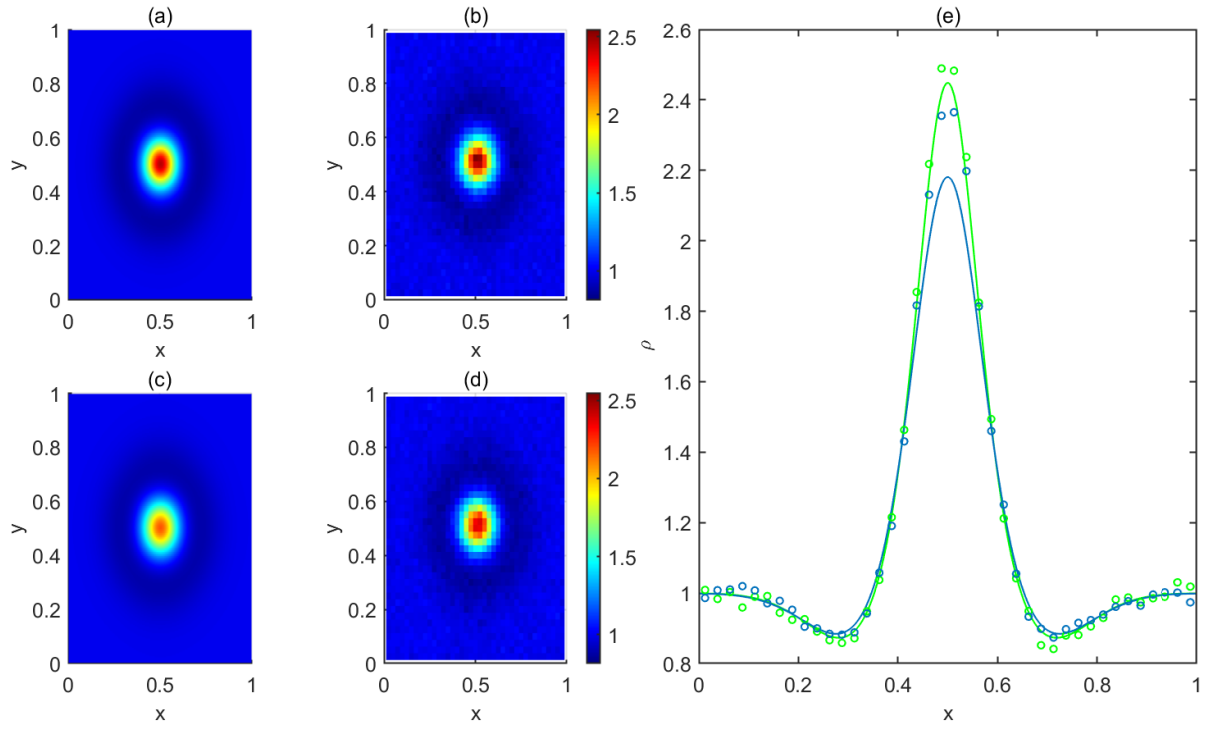

Figure 5.6: Transient marginal density $\rho(\vec{r}, t)$ under the extracellular signal function (5.1(a)). (a) ρ from (5.18) for $\epsilon = 0$. (b) Histogram from the KMC algorithm for $\epsilon = 0$. (c) ρ from (5.18) for $\epsilon = 0.01$. (b) Histogram from the KMC algorithm for $\epsilon = 0.01$. Plots (a)-(d) have the same colour bar. (e) Transient marginal density (solid line) and the particle simulation (circles) at $y = 0.5$.

slice in Figure 5.6(e), we see a slight disparity. In addition, the same slice plot confirms that the model solutions for $\epsilon = 0.01$ differ significantly from the particle simulation under steeper gradients. The main reason for this discrepancy is the appreciable volume fraction in the test problem even though it is only 0.0314; besides, one can attribute the steepness of the signal function that may further enhance numerical diffusion in the PDE solution. Overall, these results confirm the validity of the adjusted system (5.12) as a reasonable approximation under low occupied fractions for particles undergoing a velocity jump process with exchange velocity hard-sphere collisions in the considered parameter region.

5.8 Summary and discussion

The aim of this chapter was to extend the one-dimensional collision system examined by Ralph et al. [81] in a two-dimensional setting, examining the effect of exchange-velocity collisions on the general behaviour of a group of particles. These collisions differ greatly from the reflective and fully elastic collisions as they preserve both total momentum and energy in the system while maintaining the existing speed. While this chapter conceptually differs slightly from the one-dimensional work, it fits well into the context of classical velocity-jump processes in higher-dimensional domains. In the absence of random velocity switches, the system solely defines a hard-core collision system.

As in previous chapters, under the hypothesis that the occupied volume fraction is small, we obtained the population-level description through a systematic asymptotic expansion in ϵ while accurately considering the interactions at the particle level. The exchange-velocity collisions simplified the analysis as the leading orders satisfied the collision boundary conditions. On the contrary, when the system experiencing reflective (or elastic) collisions, one has to use some other systematic method to find solutions that are valid in the whole domain, including the region where particles are correlated [31].

The low-dimensional transport equation we have derived is for the one-particle probability density that measures the probability of finding any particle at a given position and velocity (given that the particles are identical and indistinguishable), and it carries a nonlinear transport term accounting for the excluded volume in the system. From this kinetic model, we then derived moments equations using the Cattaneo approximation technique, where parabolic scaling led to the collective diffusion constant, which is consistent with that for Brownian particles investigated by Bruna and Chapman [12].

Finally, the theoretical predictions of the derived model are compared with full-particle simulations and against the interaction-free case of point particles. We have performed

stationary and time-dependent simulations of the system; to this end, we adopted the two algorithms: MH and event-driven KMC, which were introduced in one dimension, with modifications to the 2D system. In both cases, the nonlinear PDE has captured the particle level's features well under low occupied fractions.

6
Conclusion

In this thesis, we have studied systems of hard-core particles with short-range interactions and stochastic changes applied to the velocity. Velocity jumps in collective behaviour under external impetus could arise in many different contexts and be analysed using different techniques. Out of the two classical modelling techniques, agent-based and continuum PDEs, we focused on the latter. Specifically, we intended to introduce a method that allows for a more accurate way of studying general dispersing systems without using any ad hoc closure assumptions. We introduced our core model in the second chapter, including the method and many of the techniques we used throughout this thesis. In the subsequent chapters, we removed limitations from this model and extended those techniques accordingly.

The model derivation procedure is initiated by writing down the particle-based description of the system in the probability space, a PDE for the joint probability density function. The cases considered in each chapter, respectively, are as follows:

Chapter 2 focussed on a system of N identical and indistinguishable finite-size particles moving in a narrow channel with a fixed speed.

Chapter 3 eliminated the assumption of identical the particles and introduced two types of particles or species to the system; namely, the blues and the reds.

Chapter 4 primarily studied both one-dimensional collision and narrow channel systems consisting of stationary particles and later extended the model to allow a finite set of speeds.

Chapter 5 extended the one-dimensional velocity-jump model with hard-core interactions in higher dimensions, where pairwise collisions swapped velocities.

The high-dimensional particle-based description was then reduced to a practical low-dimensional description for the one-particle density under the small volume fraction assumption. Here we used the regular perturbation expansion from the interaction-free case to find a solution to the system that is valid throughout the domain, including the correlated region. The resulting population-level model is nonlinear in the transport term due to excluded volume effects, and it is manifested in all of the above cases. The nonlinearities are all pair-products of subpopulation densities. This can be explained by the fact that they represent pairwise interactions and come from the outer solution. If we had considered three-particle interactions, we would expect to obtain a product of three subpopulation densities in the continuum model.

In order to assess the validity of the PDE models, we compared their numerical solutions with simulations of the N-particle system. This involved a numerical integration method along the characteristics to find transient solutions for our core model. The technique was successfully adopted for the model in the fourth chapter as well. This way, we avoided problems that occur during standard numerical methods for solving PDEs. However, in the third and fifth chapters, we had no choice but to resort to standard numerical methods due to the complexity of the eigenstructures. During particle-level simulations, we utilised Metropolis-Hastings for the equilibrium state calculations and the event-driven kinetic Monte Carlo method for the transient state calculations. We modified the steps of these algorithms in accordance with the dynamics of the systems: collision and narrow channel. The adjusted models seemed to give a good approximation to the averaged stochastic simulations of the particle-level model. Note that we have only included the leading-order nonlinear term in the PDE; however, it is possible to go back to the asymptotic expansions and algebraically calculate the next higher-order correction terms. These augmented models could match the simulations more firmly.

The main assumption that entered the models' derivation and validation procedure is the occupants' low occupied fraction. It should be low enough so that pairwise interactions are the dominant ones, and the agreement between model solutions and the particle simulations are acceptable. On the other hand, we discussed how the choice of particle's size could lead to problematic convergence behaviour in the numerical examples. We also assumed that the dimension of the container (with solid boundaries) is much larger than the particle length to avoid wall-particle-particle interactions. This way, the holes from illegal configurations may be hidden from the outside. In its simplest form, the velocity-jump process assumed that particles move at a constant speed; however, we managed to

extend that for a finite set of speeds in Chapter 4.
We repeatedly applied our test systems to chemotaxis, where entities adjust their motion according to an extracellular chemical. The time-independent turning (or transition) rates were defined using the fact that an agent is less likely to change when moving in a favourable direction; however, if the frequency of these changes becomes large, then the motion looks more like diffusion. We were able to formally derive the macroscopic limit under the diffusion-dominated regime via parabolic scaling and a regular perturbation expansion. In the numerical examples, we exercised two forms of signals, and in both, nutrients were found about the peak of the function. In most models, we used a positive chemotactic sensitivity coefficient that led to positive taxis. But we examined how this coefficient directs the chemotactic substance (positive or negative) in general from the multiple species model. We have also accompanied the one-dimensional kinetic models to examine travelling bands. Here we only considered PDE solutions for several specific examples instead of having exhaustive numerical tests to assess the validity of our continuum models against the simulations of the discrete models. We were able to obtain travelling wave type solutions for the subpopulations in one dimension as well as the two special cases: tagged particle and transport through obstacles in the two-species model. Despite the restriction of a low-volume fraction, our models provided insight into the mechanisms by which particle-level characteristics emerge at the population level, particularly the nonlinear terms.
This work bridges the existing statistical techniques and a PDE modelling framework for finite-size particles' random walk systems. The modelling techniques and model extensions presented help one to understand direct interactions through interfaces and collision boundaries, as well as indirect interactions via a chemotactic medium. The methods can, in theory, be applied to a range of systems on different scales and analyse the results against those already known in statistical mechanics. However, it is crucial to describe the dynamics in each situation. This is where we believe our work could have significant contributions. Furthermore, since all the models are based on simple one or two-dimensional PDEs, they are accessible and ready-to-use tools for any discipline.

6.1 Future work

One of the important future works would be the extension of the two-dimensional model when particles reflect directly off each other. This type of collision might be the most relevant for biological applications as organisms do not usually transfer momentum during interactions. We can carry out the ideas of the two-dimensional problem in Chapter 5

with changes to the collision boundary condition. That is, rewriting condition (5.5c) as

$$P(\vec{r}_1, \vec{r}_2, \vec{v}_1, \vec{v}_2, t) = P(\vec{r}_1, \vec{r}_2, \vec{v}_1{}', \vec{v}_2{}', t) \quad \text{on} \quad ||\vec{r}_1 - \vec{r}_2|| = \epsilon$$

where $\vec{v}_1{}'$ and $\vec{v}_2{}'$ are the velocity updates after a reflective collision. Franz et al. [31] have already studied this problem, but complications arose from using the same outer solution as Bruna's work without implementing it in the velocity space.

To systematically determine the collision integral $\mathcal{I}$, we can use the method of matched asymptotic expansion that accounts for both the independent (outer) region and the correlated (inner) region. It is successfully utilised to tackle the one-dimensional chemotaxis model by Ralph et al. [81]. The method involves finding a solution in the outer region and hence obtaining the matching inner solution. This way, we will find a solution that satisfies boundary conditions and is valid throughout the domain. We expect a qualitative difference in the resulting kinetic model, especially in the nonlinear transport term.

So far, we have considered hard-core interactions that assumed impenetrable particles where the potential is infinity for overlaps. But it is often the case that particles interact via two-body soft-core potentials where they attract or repel each other over a region rather than at a particular distance. Such interactions were examined within systems of self-propelling particles [2,22]. The most common soft-core potentials adopted in physical and biological applications are the Lennard–Jones [46] and Morse [62] potentials. They explicate both the situation where particles repel each other in a shorter range and attract each other in a longer range. Introducing these pair potentials to the velocity jump model would be another extension of our previous work. Interestingly the N-dimensional PDE in probability space is now defined in the whole space since there are no illegal configurations with a soft-core potential. The hard-core collision boundary condition is replaced by the interaction rule [18]:

$$\vec{v}_i{}' = \vec{v}_i - \nabla U(||\vec{r}_i - \vec{r}_j||) \quad \text{for} \quad i \neq j$$

where $\vec{v}_i{}'$ is the velocity update of the i^{th} particle and $U : \mathbb{R}^d \to \mathbb{R}$ is a given potential which is a function of the separation distance (since particles are isotropic). We suppose that the particle–wall interactions are hard-core; therefore, we still have the reflecting boundary conditions. As has been the case throughout this work, we reduce the dimensionality of the problem by looking at the marginal density function of one particle. Presumably, we expect the resulting transport equation to have the same structure as its hard-spheres counterpart, except that now the nonlinear term might depend on the pair

interaction potential.

In Chapter 4, we derived a model for a collision system with a finite set of velocities via asymptotic expansion. It would be interesting to produce a comparable result by applying Rost's method [84] to this system and explore the two methods' solutions. Ralph et al. [81] successfully used this compression method to derive a model for the constant speed interacting-particles problem. The idea is to eliminate the excluded regions among particles and convert the system into an interaction-free problem using a coordinate change. One can then easily write the kinetic equation for the marginal density under this compression; consequently, decompress back to the original variables. In contrast to the asymptotic approach, this method works well under constant (≥ 0) transition rates (the position-dependent rate would become discontinuous in the mapped problem).

A Appendix

A.1 Normalisation conditions

In this section we establish the relationships between marginal densities and the outer functions.

A.1.1 Identical particles To obtain a closed equation for the one-particle density $p(x, v, t)$, we used $q(x, v, t) = p(x, v, t) + \mathcal{O}(\epsilon)$ in section (2.3.2.2). Although there is no sharp boundaries at the left and right interfaces, we begin by introducing an imaginary radius γ, with $\epsilon < \gamma \ll 1$, that divides the region Ω into two; the inner region: $\Omega_{in} = \{x_2 \in \Omega : \epsilon < |x_1 - x_2| < \gamma\}$, and the outer region $\Omega_{out} = \Omega \backslash \Omega_{in}$.
From the definition of the marginal density (in terms of the joint density) and using the imaginary separation between inner and outer regions, we can then split the integral.

$$\begin{aligned} p(x_1, v_1, t) &= \int_{\Omega \times V} P(x_1, x_2, v_1, v_2, t) dx_2 dv_2 \\ &= \int_{\Omega_{in} \times V} P(x_1, x_2, v_1, v_2, t) dx_2 dv_2 + \int_{\Omega_{out} \times V} P(x_1, x_2, v_1, v_2, t) dx_2 dv_2 \end{aligned}$$

Since particles are independent in the outer region, we replace the second integrand by the product solution and transform the first integral to inner variables.

$$p(x_1,v_1,t) = \int\limits_{\{1<|\tilde{x}|<\gamma_\epsilon\}\times V} \epsilon P(\tilde{x}_1,\tilde{x},v_1,v_2,t)d\tilde{x}dv_2 + q(x_1,v_1,t)\int\limits_{\Omega_{out}\times V} q(x_2,v_2,t)dx_2dv_2$$

where $\gamma_\epsilon = \gamma/\epsilon$. Using the fact that $\Omega_{out} = \Omega\backslash\{x_2 \in \Omega : |x_1 - x_2| < \gamma\}$ in the second integral, and inserting the leading order inner solution $q(\tilde{x}_1,v_1,t)q(\tilde{x}_1,v_2,t)$ to the first integral, we can write

$$\begin{aligned}
p(x_1,v_1,t) &= \epsilon q(\tilde{x}_1,v_1,t)\rho(\tilde{x}_1,t)\int\limits_{\{1<|\tilde{x}|<\gamma_\epsilon\}} d\tilde{x} + q(x_1,v_1,t)\left(\int\limits_{\Omega\times V} q(x_2,v_2,t)dx_2dv_2\right.\\
&\quad\left. - \int\limits_{\{|x_1-x_2|<\gamma\}\times V} q(x_2,v_2,t)dx_2dv_2\right)\\
&= 2\epsilon(\gamma_\epsilon - 1)q(x_1,v_1,t)\rho(x_1,t) + \mathcal{O}(\epsilon^2) + q(x_1,v_1,t)\int\limits_{\Omega\times V} q(x_2,v_2,t)dx_2dv_2\\
&\quad - 2\gamma q(x_1,v_1,t)(\rho(x_1,t) + \mathcal{O}(\gamma))
\end{aligned}$$

$$p(x_1,v_1,t) = q(x_1,v_1,t)\int\limits_{\Omega\times V} q(x_2,v_2,t)dx_2dv_2 - 2\epsilon q(x_1,v_1,t)\rho(x_1,t) + \mathcal{O}(\epsilon^2,\gamma^2) \quad \text{(A.1.1)}$$

where $\rho(...,t) = q(...,c,t) + q(...,-c,t)$ and we drop $\sim$ on x_1 in the second line. Imposing the normalisation condition above and applying the binomial theorem for the fractional power, we get

$$\begin{aligned}
1 &= \int\limits_{\Omega\times V} q(x_1,v_1,t)dx_1dv_1\int\limits_{\Omega\times V} q(x_2,v_2,t)dx_2dv_2 - 2\epsilon\int\limits_{\Omega\times V} q(x_1,v_1,t)\rho(x_1,t)dx_1dv_1 + ...\\
&\left[\int\limits_{\Omega\times V} q(z,u,t)dzdu\right]^2 = 1 + 2\epsilon\int\limits_{\Omega\times V} q(z,u,t)\rho(z,t)dzdu + \mathcal{O}(\epsilon^2,\gamma^2)\\
&\int\limits_{\Omega\times V} q(z,u,t)dzdu = 1 + \epsilon\int\limits_{\Omega}\rho^2(z,t)dz + \mathcal{O}(\epsilon^2,\gamma^2)
\end{aligned} \quad \text{(A.1.2)}$$

Substituting this result in (A.1.1)

$$p(x_1, v_1, t) = q(x_1, v_1, t) + \epsilon q(x_1, v_1, t) \left(\int_\Omega \rho^2(z, t) dz - 2\rho(x_1, t) \right) + \mathcal{O}(\epsilon^2, \gamma^2)$$

Set $\gamma = \sqrt{\epsilon}$, then we get $p(x_1, v_1, t) = q(x_1, v_1, t) + \mathcal{O}(\epsilon)$ as required.

A.1.2 Multiple species To obtain a closed equation for two types of particles, a similar result required to relate the outer functions q_b and q_r with the marginal densities b and r. The same procedure as outlined above (upto (A.1.1)) yields

$$b(x_1, v_1, t) = q_b(x_1, v_1, t) \int_{\Omega \times V} q_r(x_2, v_2, t) dx_2 dv_2 + \mathcal{O}(\epsilon_{br})$$

and

$$r(x_2, v_2, t) = q_r(x_2, v_2, t) \int_{\Omega \times V} q_b(x_1, v_1, t) dx_1 dv_1 + \mathcal{O}(\epsilon_{br})$$

Then applying the normalisation condition, we get

$$\int_{\Omega \times V} q_b(z, u, t) dz du \int_{\Omega \times V} q_r(z, u, t) dz du = 1 + \mathcal{O}(\epsilon_{br})$$

This relation determines the leading orders of the integrals upto a constant. Without loss of generality setting one integral to 1, we find $b(x_1, v_1, t) = q_b(x_1, v_1, t) + \mathcal{O}(\epsilon_{br})$ and $r(x_2, v_2, t) = q_r(x_2, v_2, t) + \mathcal{O}(\epsilon_{br})$ as required.

A.1.3 2D system We may extend the work in (A.1.1) to relate the outer function $q(\vec{r}_1, \vec{v}_1, t)$ back to the marginal density $p(\vec{r}_1, \vec{v}_1, t)$. In two dimensional domain, the inner region Ω_{in} corresponds to an annulus. Then equation (A.1.1) reads as

$$p(\vec{r}_1, \vec{v}_1, t) = q(\vec{r}_1, \vec{v}_1, t) \int_{\Omega \times V} q(\vec{r}_2, \vec{v}_2, t) d\vec{r}_2 d\vec{v}_2 - \pi \epsilon^2 q(\vec{r}_1, \vec{v}_1, t) \rho(\vec{r}_1, t)$$

where $\rho(\vec{r}_1, t) = \int_V q(\vec{r}_1, \vec{v}_1, t) d\vec{v}_1$. Next applying the normalisation condition to the above and repeating the steps in (A.1.2), we get

$$\left[\int_{\Omega \times V} q(\vec{r}, \vec{v}, t) d\vec{r} d\vec{v} \right]^2 = 1 + \mathcal{O}(\epsilon^2)$$

that produces the required results $p(\vec{r}_1, \vec{v}_1, t) = q(\vec{r}_1, \vec{v}_1, t) + \mathcal{O}(\epsilon^2)$.

A.2 Algorithms

A.2.1 SSA

1: Compute position $X(t + \Delta t)$.

2: If $X(t + \Delta t)$ is outside the domain $[0, L]$, proceed the random walk to the opposite direction.

   a If $X(t + \Delta t) < 0$, $X(t + \Delta t) \leftarrow -X(t) - V(t)\Delta t$ and $V(t + \Delta t) \leftarrow -V(t)$.

   b If $X(t + \Delta t) > L$, $X(t + \Delta t) \leftarrow 2L - X(t) - V(t)\Delta t$ and $V(t + \Delta t) \leftarrow -V(t)$.

3: Calculate λ: if $V(t) > 0$, $\lambda \leftarrow \lambda^+$, else $\lambda \leftarrow \lambda^-$.

4: Generate a uniform random number r.

5: Check for random velocity jumps: if $r < \lambda \Delta t$, then $V(t + \Delta t) \leftarrow -V(t)$.

6: Go back to step 1 for $t \leftarrow t + \Delta t$.

A.2.2 Even-driven KMC algorithm

1: Initialise position vector X and velocity vector V for N spheres.

2: Compute pairwise collision times.

   a Generate uniform random number r.

   b If $r <$ *collision_probability* and particles moving towards each other, calculate collision time $T_{i,j}^{coll}$ for $i \neq j = 1, 2, ..., N - 1$.

   c Else set $T_{i,j}^{coll} \leftarrow large\_value$.

3: Calculate the collision times T_i^{wall} for $i = 1, 2, ..., N$ with the walls 0 and L; otherwise set $T_i^{wall} \leftarrow large\_value$.

4: Compute random turn times T_i^{turn} for $i = 1, 2, ..., N$.

   a If $V_i > 0$, $\lambda \leftarrow \lambda^+$, and $\tau \leftarrow \tau^-$.

   b Else $\lambda \leftarrow \lambda^-$, and $\tau \leftarrow \tau^+$.

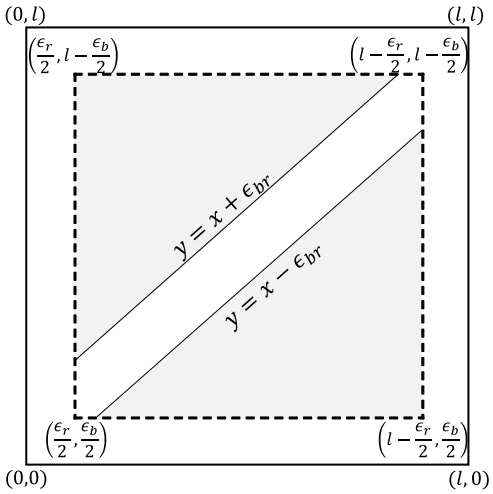

Figure A.3.1: The collision square illustrates the space available for the red particle when the blue particle is fixed at y. The upper left and the lower right triangles represent, respectively, passing below and passing above.

5: Find the minimal time from the event queue: $t_{min} \leftarrow \{\mathbf{T}^{coll}, \mathbf{T}^{wall}, \mathbf{T}^{turn}\}$.

6: Update the positions using time t_{min}.

   a If $X_i(new) < 0$, $X_i(new) \leftarrow -X_i(old) - V_i(old)dt$ and $V_i(new) \leftarrow -V_i(old)$,

   b If $X_i(new) > L$, $X_i(new) \leftarrow 2L - X_i(old) - V_i(old)dt$ and $V_i(new) \leftarrow -V_i(old)$, where $dt = t_{min} - t$

7: Change velocities of the participants of the corresponding event.

   a If i collide with j, $V_i(new) \leftarrow -V_i(old)$ and $V_j(new) \leftarrow -V_j(old)$.

   b If wall-particle interaction, $V_i(new) \leftarrow -V_i(old)$, where $i = 1$ or $N + 1$.

   c If a random turn, $V_i(new) \leftarrow -V_i(old)$.

8: Go back to step 2 for $t \leftarrow t_{min}$

A.3 Collision Probability

In general, the collision probability depends on the sizes of the species and the container. Here we consider two species (blue and red) with hard-cores inside a narrow channel, so it is not to be confused with the case when one species is immersing in a fluid with much smaller particle size. Take a blue particle with diameter ϵ_b and a red with ϵ_r such that $\epsilon_b + \epsilon_r \leq$ the width of the narrow channel (say l). Let's assume that the blue is at y, where $Y \sim U(\frac{\epsilon_b}{2}, l - \frac{\epsilon_b}{2})$. Then the space available for the red particle to unobstructedly move is given by the top and the bottom triangles of Figure A.3.1. The total probability

of red passing blue is

$$\int_{(\epsilon_r+\frac{\epsilon_b}{2})}^{(l-\frac{\epsilon_b}{2})} P(\text{passing below}|Y=y)f_Y(y)dy + \int_{\frac{\epsilon_b}{2}}^{(l-\epsilon_r-\frac{\epsilon_b}{2})} P(\text{passing above}|Y=y)f_Y(y)dy$$

The total space available for the red particle is $l-\epsilon_r$. Given that the blue particle is at y, the probability of the red particle passing the blue particle; below (upper left triangle) is $\frac{max\{0,y-\epsilon_{br}-\frac{\epsilon_r}{2}\}}{l-\epsilon_r}$ and above (lower right triangle) is $\frac{max\{0,l-y-\epsilon_{br}-\frac{\epsilon_r}{2}\}}{l-\epsilon_r}$. The position density function for the blue particle is the constant function $1/(l-\epsilon_b)$. Therefore, the above integrals produces the following result.

$$\int_{(\epsilon_r+\frac{\epsilon_b}{2})}^{(l-\frac{\epsilon_b}{2})} \frac{y-\frac{\epsilon_b}{2}-\epsilon_r}{(l-\epsilon_r)(l-\epsilon_b)}dy + \int_{\frac{\epsilon_b}{2}}^{(l-\epsilon_r-\frac{\epsilon_b}{2})} \frac{l-y-\frac{\epsilon_b}{2}-\epsilon_r}{(l-\epsilon_r)(l-\epsilon_b)}dy = \frac{(l-\epsilon_r-\epsilon_b)^2}{(l-\epsilon_r)(l-\epsilon_b)}$$

Since the collision probability is (1− the total probability of red passing blue), we remark the following special case:

i. When $\epsilon_r, \epsilon_b \to 0$, collision probability vanishes; hence, we obtain the independent system,

ii. When $l = \epsilon_r + \epsilon_b$, particles cannot pass each other; hence, the system becomes a collision system,

iii. When $\epsilon_r = \epsilon_b = \epsilon$, we get the passing probability $(\frac{l-2\epsilon}{l-\epsilon})^2$ for identical particles.

A.4 Two independent particles

We extend the work in section (4.2) for two particles in a rectangular region $S = [a_1, a_2] \times [b_1, b_2]$. When the particles are positioned at x_1 and x_2 with positive velocity c at time t, denoting the two-particle density by $p(x_1, x_2, c, c, t)$, the probability can be written as

$$P\left(X_1(t), X_2(t) \in S, V_1(t), V_2(t) = c\right) = \iint_S p(x_1, x_2, c, c, t)dx_1dx_2.$$

So the rate of change is

$$\begin{aligned}
\iint_S \frac{\partial p^{++}}{\partial t}(x_1,x_2,t)dx_1dx_2 &= c\int_{b_1}^{b_2} p^{++}(a_1,x_2,t)dx_2 + c\int_{a_1}^{a_2} p^{++}(x_1,b_1,t)dx_1 \\
&\quad -c\int_{b_1}^{b_2} p^{++}(a_2,x_2,t)dx_2 - c\int_{a_1}^{a_2} p^{++}(x_1,b_2,t)dx_1 \\
&\quad + \iint_S p^{0+}(x_1,x_2,t)\lambda_+^0(x_1)dx_1dx_2 + \iint_S p^{-+}(x_1,x_2,t)\lambda_+^-(x_1)dx_1dx_2 \\
&\quad + \iint_S p^{+0}(x_1,x_2,t)\lambda_+^0(x_2)dx_1dx_2 + \iint_S p^{+-}(x_1,x_2,t)\lambda_+^-(x_2)dx_1dx_2 \\
&\quad - \iint_S p^{++}(x_1,x_2,t)\lambda_0^+(x_1)dx_1dx_2 - \iint_S p^{++}(x_1,x_2,t)\lambda_-^+(x_1)dx_1dx_2 \\
&\quad - \iint_S p^{++}(x_1,x_2,t)\lambda_0^+(x_2)dx_1dx_2 - \iint_S p^{++}(x_1,x_2,t)\lambda_-^+(x_2)dx_1dx_2
\end{aligned}$$

where first four terms of the right hand side are the rates of change when particles enter at the boundaries a_1 and b_1, and leave at the boundaries a_2 and b_2. The positive terms of the integrals are the contribution to the rate when switching to $+c$ while the negative terms corresponds to velocity changes from $+c$.
By rearranging the terms we get

$$\begin{aligned}
\iint_S \Big(&\frac{\partial p^{++}}{\partial t} + c\frac{\partial p^{++}}{\partial x_1} + c\frac{\partial p^{++}}{\partial x_2} - p^{0+}\lambda_+^0(x_1) - p^{-+}\lambda_+^-(x_1) - p^{+0}\lambda_+^0(x_2) - p^{+-}\lambda_+^-(x_2) \\
&+p^{++}\lambda_0^+(x_1) + p^{++}\lambda_-^+(x_1) + p^{++}\lambda_0^+(x_2) + p^{++}\lambda_-^+(x_2)\Big)\, dx_1dx_2 = 0
\end{aligned}$$

Since the region S is arbitrary, we get

$$\begin{aligned}
&\frac{\partial p^{++}}{\partial t} + c\frac{\partial p^{++}}{\partial x_1} + c\frac{\partial p^{++}}{\partial x_2} - p^{0+}\lambda_+^0(x_1) - p^{-+}\lambda_+^-(x_1) - p^{+0}\lambda_+^0(x_2) - p^{+-}\lambda_+^-(x_2) \\
&\qquad +p^{++}\lambda_0^+(x_1) + p^{++}\lambda_-^+(x_1) + p^{++}\lambda_0^+(x_2) + p^{++}\lambda_-^+(x_2) = 0
\end{aligned}$$

and we derive eight other PDEs similar to the above, starting from the probability P for the combinations of subpopulations.

A.5 Diffusion limit

We consider the long-time dynamics of the model by taking the parabolic limit of (4.19). First, we write the system in terms of the flux function $j(x,t) = c(p^+ - p^-)$ and total density $\rho(x,t) = p^+ + p^0 + p^-$:

$$\begin{aligned}
\frac{\partial \rho}{\partial t} + \frac{\partial j}{\partial x} &= 0 \\
\frac{\partial j}{\partial t} + c^2\frac{\partial \rho}{\partial x} + \xi\frac{\partial}{\partial x}(c^2\rho^2 - j^2) + c^2\xi\frac{\partial}{\partial x}(\rho p^0) + c(\lambda_-^+ - \lambda_+^-)\rho + (\lambda_-^+ + \lambda_+^-)j + & \\
\frac{c}{2}(\lambda_0^+ - \lambda_0^-)\rho + \frac{1}{2}(\lambda_0^+ + \lambda_0^-)j + c(\lambda_-^0 - \lambda_+^0)p^0 &= 0 \\
c\frac{\partial p^0}{\partial t} - c\xi\frac{\partial}{\partial x}(jp^0) - \frac{c}{2}(\lambda_0^+ + \lambda_0^-)\rho - \frac{1}{2}(\lambda_0^+ - \lambda_0^-)j + c(\lambda_-^0 + \lambda_+^0)p^0 &= 0 \\
\text{with no flux boundary condition} &
\end{aligned}$$

where $\xi = \delta\epsilon(N-1)$. From the transition rates (4.28), we can further simplify above equations. We then introduce the parabolic scaling $\zeta = \gamma x$ for space variable and $\tau = \gamma^2 t$ for time variable, where γ is a small dimensionless parameter. This yields the scaled system of equations,

$$\begin{aligned}
\gamma\frac{\partial \rho}{\partial \tau} + \frac{\partial j}{\partial \zeta} &= 0 \\
\gamma^2\frac{\partial j}{\partial \tau} + \gamma c^2\frac{\partial \rho}{\partial \zeta} + \gamma\xi\frac{\partial}{\partial \zeta}(c^2\rho^2 - j^2) + \gamma c^2\xi\frac{\partial}{\partial \zeta}(\rho p^0) - 3\gamma c^2\chi\frac{\partial S}{\partial \zeta}\rho + 3\lambda_0 j &= 0 \\
\gamma^2 c\frac{\partial p^0}{\partial \tau} - \gamma c\xi\frac{\partial}{\partial \zeta}(jp^0) - c\lambda_0\rho + \gamma c\chi\frac{\partial S}{\partial \zeta}j + 2c\lambda_0 p^0 &= 0
\end{aligned}$$

Applying the regular perturbation expansions $\rho = \rho_0 + \gamma\rho_1 + ...$ and $j = j_0 + \gamma j_1 + ...$, we get

$$\begin{aligned}
\mathcal{O}(1): &\frac{\partial j_0}{\partial \zeta} = 0 \\
&2\lambda_0 j_0 = 0 \\
&2c\lambda_0 p^0 - c\lambda_0\rho_0 = 0 \\
&\text{which implies the trivial solution} \quad j_0 = 0 \quad \text{and} \quad p^0 = \frac{\rho_0}{2}
\end{aligned}$$

$$\mathcal{O}(\gamma): \frac{\partial \rho_0}{\partial \tau} + \frac{\partial j_1}{\partial \zeta} = 0$$

$$c^2 \frac{\partial \rho_0}{\partial \zeta} + \xi \frac{\partial}{\partial \zeta}(c^2 \rho_0^2) + \frac{c^2 \xi}{2} \frac{\partial}{\partial \zeta}(\rho_0^2) - 3c^2 \chi \frac{\partial S}{\partial \zeta} \rho_0 + 3\lambda_0 j_1 = 0$$

eliminating j_1 from the equations we get the drift-diffusion equation

$$\frac{\partial \rho_0}{\partial \tau} = \frac{\partial}{\partial \zeta} \left[\frac{c^2}{3\lambda_0}(1 + 3\xi\rho_0) \frac{\partial \rho_0}{\partial \zeta} - \frac{c^2 \chi}{\lambda_0} \frac{\partial S}{\partial \zeta} \rho_0 \right]$$

A.6 Cattaneo approximation

In transport equations, velocity moments of the density are derived by multiplying it with powers of velocity and integrating over velocity space. In general, the n^{th} moment equation will contain $n + 1^{st}$ moment as well. In order get a closed system of n-moments it is necessary to find an approximation for this $n+1$ moment. According to Hillen [39], this estimation can be found using minimization principle. The Cattaneo closure is the second-moment approximation, and we make use of this method to estimate $\int_V p(\mathbf{r}, \mathbf{v}, t)\mathbf{v}\mathbf{v}d\mathbf{v}$. First, define the functional J on p as

$$J(p) = \int_V \Big(\frac{p^2}{2} - \lambda(p - \rho) - \boldsymbol{\mu} \cdot (p\mathbf{v} - \mathbf{j}) \Big) d\mathbf{v} \tag{A.6.1}$$

where $\lambda = \lambda(\mathbf{r}, t)$ and $\boldsymbol{\mu} = \boldsymbol{\mu}(\mathbf{r}, t)$ are Lagrangian multipliers. Then the first-variation of J yields

$$p - \lambda - \boldsymbol{\mu} \cdot \mathbf{v} = 0 \tag{A.6.2}$$

We calculate the Lagrangian multipliers such that the first two moments of the minimizer p_{min} are ρ and $\mathbf{j}$.

$$\rho(\mathbf{r}, t) = \int_V p d\mathbf{v} = \int_V (\lambda + \boldsymbol{\mu} \cdot \mathbf{v}) d\mathbf{v} = c\lambda \int_\Theta d\theta = c|\Theta|\lambda$$

$$\mathbf{j}(\mathbf{r}, t) = \int_V p\mathbf{v} d\mathbf{v} = \int_V (\lambda + \boldsymbol{\mu} \cdot \mathbf{v})\mathbf{v} d\mathbf{v} = \int_V \boldsymbol{\mu} \cdot \mathbf{v}\mathbf{v} d\mathbf{v} = \frac{c^3}{2}|\Theta|\boldsymbol{\mu}$$

Here $\int_V \mathbf{v} d\mathbf{v} = 0$ and $\int_V \mathbf{v}\mathbf{v} d\mathbf{v} = \frac{c^3}{2}|\Theta| I$, where I is the 2×2 identity matrix and $|\Theta| = 2\pi$. Therefore, $\lambda(\mathbf{r}, t) = \frac{\rho}{c|\Theta|}$ and $\boldsymbol{\mu}(\mathbf{r}, t) = \frac{2}{c^3|\Theta|}\mathbf{j}$. From (A.6.2), we can write the minimizer as

$$p_{min}(\mathbf{r}, \mathbf{v}, t) = \frac{1}{c|\Theta|}\big(\rho + \frac{2}{c^2}\mathbf{j} \cdot \mathbf{v}\big),$$

and find the second-moment of p from the second-moment of the minimizer.

$$\int_V p\mathbf{v}\mathbf{v} d\mathbf{v} = \int_V \frac{1}{c|\Theta|}\big(\rho + \frac{2}{c^2}\mathbf{j} \cdot \mathbf{v}\big)\mathbf{v}\mathbf{v} d\mathbf{v} = \frac{c^2\rho}{2} I$$

A.6.1 Boundary condition We also use p_{min} to find the appropriate boundary condition in terms of the velocity moments. From the reflective boundary condition

$$p(\mathbf{r}, \mathbf{v}, t) = p(\mathbf{r}, \mathbf{v}^*, t) \quad \text{on} \quad \partial\Omega,$$

where $\mathbf{v}^* = \mathbf{v} - 2(\mathbf{v} \cdot \boldsymbol{\eta})\boldsymbol{\eta}$ for outward normal $\boldsymbol{\eta}$.
Substituting the minimizer and $\mathbf{v}^*$ we get

$$\begin{aligned} \frac{1}{c|\Theta|}\big(\rho + \frac{2}{c^2}\mathbf{j} \cdot \mathbf{v}\big) &= \frac{1}{c|\Theta|}\big(\rho + \frac{2}{c^2}\mathbf{j} \cdot (\mathbf{v} - 2(\mathbf{v} \cdot \boldsymbol{\eta})\boldsymbol{\eta})\big) \\ (\mathbf{v} \cdot \boldsymbol{\eta})(\mathbf{j} \cdot \boldsymbol{\eta}) &= 0 \end{aligned}$$

Since $\mathbf{v} \cdot \boldsymbol{\eta} \neq 0$, we get $\mathbf{j} \cdot \boldsymbol{\eta} = 0$ on $\partial\Omega$.

Bibliography

[1] M. A. Abdelrahman, *On the shallow water equations*, Zeitschrift für Naturforschung A, 72 (2017), pp. 873–879.

[2] M. Abkenar, K. Marx, T. Auth, and G. Gompper, *Collective behavior of penetrable self-propelled rods in two dimensions*, Physical Review E, 88 (2013), p. 062314.

[3] B.-Q. Ai and J.-C. Wu, *Transport of finite size particles in confined narrow channels: Diffusion, coherence, and particle separation*, The Journal of chemical physics, 139 (2013), p. 034114.

[4] W. Alt, *Biased random walk models for chemotaxis and related diffusion approximations*, Journal of mathematical biology, 9 (1980), pp. 147–177.

[5] R. E. Baker and M. J. Simpson, *Correcting mean-field approximations for birth-death-movement processes*, Physical Review E, 82 (2010), p. 041905.

[6] E. Barkai and R. Silbey, *Diffusion of tagged particle in an exclusion process*, Physical Review E, 81 (2010), p. 041129.

[7] M. S. Bartlett, *A note on random walks at constant speed*, Advances in Applied Probability, 10 (1978), p. 704–707.

[8] J. Bednenko, G. Cingolani, and L. Gerace, *Nucleocytoplasmic transport: navigating the channel*, Traffic, 4 (2003), pp. 127–135.

[9] J. Bernasconi and W. Schneider, *Diffusion in a one-dimensional lattice with random asymmetric transition rates*, Journal of Physics A: Mathematical and General, 15 (1982), p. L729.

[10] T. Bhattacharjee and S. S. Datta, *Bacterial hopping and trapping in porous media*, Nature communications, 10 (2019), pp. 1–9.

[11] M. Bodnar and J. J. L. Velazquez, *Derivation of macroscopic equations for individual cell-based models: a formal approach*, Mathematical methods in the applied sciences, 28 (2005), pp. 1757–1779.

[12] M. Bruna, *Excluded-volume effects in stochastic models of diffusion*, PhD thesis, University of Oxford, 2012.

[13] M. Bruna and S. J. Chapman, *Diffusion of multiple species with excluded-volume effects*, The Journal of chemical physics, 137 (2012), p. 204116.

[14] ——, *Diffusion of finite-size particles in confined geometries*, Bulletin of mathematical biology, 76 (2014), pp. 947–982.

[15] M. Burger, M. Di Francesco, J.-F. Pietschmann, and B. Schlake, *Nonlinear cross-diffusion with size exclusion*, SIAM Journal on Mathematical Analysis, 42 (2010), pp. 2842–2871.

[16] M. Burger, B. Schlake, and M.-T. Wolfram, *Nonlinear poisson–nernst–planck equations for ion flux through confined geometries*, Nonlinearity, 25 (2012), p. 961.

[17] H. Cabannes, R. Gatignol, and L. Luol, *The discrete boltzmann equation*, Lecture Notes at University of California, Berkley, (1980), pp. 1–65.

[18] J. A. Carrillo, M. Fornasier, G. Toscani, and F. Vecil, *Particle, kinetic, and hydrodynamic models of swarming*, in Mathematical modeling of collective behavior in socio-economic and life sciences, Springer, 2010, pp. 297–336.

[19] A. Defina and P. Peruzzo, *Floating particle trapping and diffusion in vegetated open channel flow*, Water Resources Research, 46 (2010).

[20] L. Dyson and R. E. Baker, *The importance of volume exclusion in modelling cellular migration*, Journal of mathematical biology, 71 (2015), pp. 691–711.

[21] L. Dyson, P. K. Maini, and R. E. Baker, *Macroscopic limits of individual-based models for motile cell populations with volume exclusion*, Physical Review E, 86 (2012), p. 031903.

[22] M. R. D'Orsogna, Y.-L. Chuang, A. L. Bertozzi, and L. S. Chayes, *Self-propelled particles with soft-core interactions: patterns, stability, and collapse*, Physical review letters, 96 (2006), p. 104302.

[23] C. Emako, C. Gayrard, A. Buguin, L. Neves de Almeida, and N. Vauchelet, *Traveling pulses for a two-species chemotaxis model*, PLoS computational biology, 12 (2016), p. e1004843.

[24] C. Emako, J. Liao, and N. Vauchelet, *Synchronising and non-synchronising dynamics for a two-species aggregation model*, arXiv preprint arXiv:1505.07659, (2015).

[25] R. Erban, *Stochastic modelling of biological processes*. Lecture Notes, Mathematical Institute, University of Oxford, 2014.

[26] R. Erban and H. G. Othmer, *From individual to collective behavior in bacterial chemotaxis*, SIAM Journal on Applied Mathematics, 65 (2004), pp. 361–391.

[27] ——, *From signal transduction to spatial pattern formation in e. coli: a paradigm for multiscale modeling in biology*, Multiscale Modeling & Simulation, 3 (2005), pp. 362–394.

[28] ——, *Taxis equations for amoeboid cells*, Journal of mathematical biology, 54 (2007), pp. 847–885.

[29] G. Estrada-Rodriguez and H. Gimperlein, *Interacting particles with levy strategies: limits of transport equations for swarm robotic systems*, arXiv preprint arxiv:1807.10124, (2019).

[30] J. Evans and H. Yoldaş, *On the asymptotic behaviour of a run and tumble equation for bacterial chemotaxis*, arXiv preprint arXiv:2103.16524, (2021).

[31] B. Franz, J. P. Taylor-King, C. Yates, and R. Erban, *Hard-sphere interactions in velocity-jump models*, Physical Review E, 94 (2016), p. 012129.

[32] E. Gavagnin and C. Yates, *Modeling persistence of motion in a crowded environment: The diffusive limit of excluding velocity-jump processes*, Physical Review E, 97 (2018).

[33] M. Ghaemi and A. Shahrokhi, *Combination of the cellular potts model and lattice gas cellular automata for simulating the avascular cancer growth*, in International Conference on Cellular Automata, Springer, 2006, pp. 297–303.

[34] C. S. Gillespie, *Moment-closure approximations for mass-action models*, IET systems biology, 3 (2009), pp. 52–58.

[35] S. Goldstein, *On diffusion by discontinuous movements, and on the telegraph equation*, The Quarterly Journal of Mechanics and Applied Mathematics, 4 (1951), pp. 129–156.

[36] G. Grimmett and D. Stirzaker, *Probability and random processes*, Oxford university press, 2020.

[37] C. Gutsche, F. Kremer, M. Krüger, M. Rauscher, R. Weeber, and J. Harting, *Colloids dragged through a polymer solution: Experiment, theory, and simulation*, The Journal of chemical physics, 129 (2008), p. 084902.

[38] S.-Y. Ha and D. Levy, *Particle, kinetic and fluid models for phototaxis*, Discrete & Continuous Dynamical Systems-B, 12 (2009), p. 77.

[39] T. Hillen, *On the l^2 moment closure of transport equations: The cattaneo approximation*, Discrete & Continuous Dynamical Systems-B, 4 (2004), p. 961.

[40] T. Hillen and H. A. Levine, *Blow-up and pattern formation in hyperbolic models for chemotaxis in 1-d*, Zeitschrift für angewandte Mathematik und Physik ZAMP, 54 (2003), pp. 839–868.

[41] T. Hillen and K. J. Painter, *A user's guide to pde models for chemotaxis*, Journal of mathematical biology, 58 (2009), p. 183.

[42] T. Hillen and A. Stevens, *Hyperbolic models for chemotaxis in 1-d*, (1998).

[43] Y. A. Humenyuk, M. Kotrla, K. Netočnỳ, and F. Slanina, *Separation of dense colloidal suspensions in narrow channels: A stochastic model*, Physical Review E, 101 (2020), p. 032608.

[44] C. Irons, M. J. Plank, and M. J. Simpson, *Lattice-free models of directed cell motility*, Physica A: Statistical Mechanics and its Applications, 442 (2016), pp. 110–121.

[45] W. Jin, S. W. McCue, and M. J. Simpson, *Extended logistic growth model for heterogeneous populations*, Journal of Theoretical Biology, 445 (2018), pp. 51–61.

[46] J. E. Jones, *On the determination of molecular fields.—i. from the variation of the viscosity of a gas with temperature*, Proceedings of the Royal Society of London. Series A, Containing Papers of a Mathematical and Physical Character, 106 (1924), pp. 441–462.

[47] M. Kac, *A stochastic model related to the telegrapher's equation*, The Rocky Mountain Journal of Mathematics, 4 (1974), pp. 497–509.

[48] E. F. Keller and L. A. Segel, *Initiation of slime mold aggregation viewed as an instability*, Journal of theoretical biology, 26 (1970), pp. 399–415.

[49] P. L. Krapivsky, K. Mallick, and T. Sadhu, *Tagged particle in single-file diffusion*, Journal of Statistical Physics, 160 (2015), pp. 885–925.

[50] M. Krüger and M. Rauscher, *Diffusion of a sphere in a dilute solution of polymer coils*, The Journal of chemical physics, 131 (2009), p. 094902.

[51] T. Lappas, A. Leonard, and P. E. Dimotakis, *Riemann invariant manifolds for the multidimensional euler equations*, SIAM Journal on Scientific Computing, 20 (1999), pp. 1481–1512.

[52] B. D. Lubachevsky, *How to simulate billiards and similar systems*, Journal of Computational Physics, 94 (1991), pp. 255–283.

[53] P. M. Lushnikov, N. Chen, and M. Alber, *Macroscopic dynamics of biological cells interacting via chemotaxis and direct contact*, Physical Review E, 78 (2008), p. 061904.

[54] F. Lutscher, A. Stevens, et al., *Emerging patterns in a hyperbolic model for locally interacting cell systems*, Journal of Nonlinear Science, 12 (2002), pp. 619–640.

[55] R. I. Macey and R. M. Oliver, *The time dependence of single file diffusion*, Biophysical journal, 7 (1967), pp. 545–554.

[56] C. Mascia, *Exact representation of the asymptotic drift speed and diffusion matrix for a class of velocity-jump processes*, Journal of Differential Equations, 260 (2016), pp. 401–426.

[57] K. Matthies, G. Stone, and F. Theil, *The derivation of the linear boltzmann equation from a rayleigh gas particle model*, arXiv preprint arXiv:1603.07574, (2016).

[58] B. Mazzag, I. Zhulin, and A. Mogilner, *Model of bacterial band formation in aerotaxis*, Biophysical journal, 85 (2003), pp. 3558–3574.

[59] L. Meinecke and M. Eriksson, *Excluded volume effects in on-and off-lattice reaction–diffusion models*, IET systems biology, 11 (2016), pp. 55–64.

[60] A. Miron, D. Mukamel, and H. A. Posch, *Attraction and condensation of driven tracers in a narrow channel*, arXiv preprint arXiv:2012.10733, (2020).

[61] L. Monchick, *Collision integrals for the exponential repulsive potential*, The Physics of Fluids, 2 (1959), pp. 695–700.

[62] P. M. Morse, *Diatomic molecules according to the wave mechanics. ii. vibrational levels*, Physical review, 34 (1929), p. 57.

[63] P. J. Murray, C. M. Edwards, M. J. Tindall, and P. K. Maini, *From a discrete to a continuum model of cell dynamics in one dimension*, Phys. Rev. E, 80 (2009), p. 031912.

[64] P. J. Murray, C. M. Edwards, M. J. Tindall, and P. K. Maini, *Classifying general nonlinear force laws in cell-based models via the continuum limit*, Physical Review E, 85 (2012), p. 021921.

[65] T. Nagatani, *Four species ca model for facing pedestrian traffic at rush hour*, Applied Mathematical Modelling, 36 (2012), pp. 702–711.

[66] T. Nagatani and K. Komada, *Freezing transition in a four-directional traffic model for facing and crossing pedestrian flow*, Physica A: Statistical Mechanics and its Applications, 389 (2010), pp. 1729–1738.

[67] E. M. Nestorovich, C. Danelon, M. Winterhalter, and S. M. Bezrukov, *Designed to penetrate: time-resolved interaction of single antibiotic molecules with bacterial pores*, Proceedings of the National Academy of Sciences, 99 (2002), pp. 9789–9794.

[68] A. Okubo and S. A. Levin, *Diffusion and ecological problems: modern perspectives*, vol. 14, Springer Science & Business Media, 2013.

[69] S. Osher and S. Chakravarthy, *Upwind schemes and boundary conditions with applications to euler equations in general geometries*, Journal of Computational Physics, 50 (1983), pp. 447–481.

[70] H. Othmer and T. Hillen, *The diffusion limit of transport equations derived from velocity-jump processes*, SIAM Journal on Applied Mathematics, 61 (2000), pp. 751–775.

[71] H. G. Othmer, S. R. Dunbar, and W. Alt, *Models of dispersal in biological systems*, Journal of mathematical biology, 26 (1988), pp. 263–298.

[72] H. G. Othmer and T. Hillen, *The diffusion limit of transport equations ii: Chemotaxis equations*, SIAM Journal on Applied Mathematics, 62 (2002), pp. 1222–1250.

[73] K. J. Painter, *Mathematical models for chemotaxis and their applications in self-organisation phenomena*, Journal of theoretical biology, 481 (2019), pp. 162–182.

[74] K. J. Painter and T. Hillen, *Volume-filling and quorum-sensing in models for chemosensitive movement*, Can. Appl. Math. Quart, 10 (2002), pp. 501–543.

[75] K. J. Painter and J. A. Sherratt, *Modelling the movement of interacting cell populations*, Journal of theoretical biology, 225 (2003), pp. 327–339.

[76] Parés, Carlos and Castro, Manuel, *On the well-balance property of roe's method for nonconservative hyperbolic systems. applications to shallow-water systems*, ESAIM: M2AN, 38 (2004), pp. 821–852.

[77] S. Pellegrini, A. Ess, M. Tanaskovic, and L. Van Gool, *Wrong turn-no dead end: a stochastic pedestrian motion model*, in 2010 IEEE Computer Society Conference on Computer Vision and Pattern Recognition-Workshops, IEEE, 2010, pp. 15–22.

[78] Y. Peng, L. Lai, Y.-S. Tai, K. Zhang, X. Xu, and X. Cheng, *Diffusion of ellipsoids in bacterial suspensions*, Physical review letters, 116 (2016), p. 068303.

[79] B. Piccoli and A. Tosin, *Time-evolving measures and macroscopic modeling of pedestrian flow*, Archive for Rational Mechanics and Analysis, 199 (2011), pp. 707–738.

[80] G. Puppo, M. Semplice, A. Tosin, and G. Visconti, *Kinetic models for traffic flow resulting in a reduced space of microscopic velocities*, arXiv preprint arXiv:1507.08961, (2015).

[81] T. Ralph, S. W. Taylor, and M. Bruna, *One-dimensional model for chemotaxis with hard-core interactions*, Physical Review E, 101 (2020), p. 022419.

[82] G. O. Roberts, A. Gelman, and W. R. Gilks, *Weak convergence and optimal scaling of random walk metropolis algorithms*, The annals of applied probability, 7 (1997), pp. 110–120.

[83] C. Rodríguez-Tinoco, D. N. Simavilla, R. D. Priestley, M. Wübbenhorst, and S. Napolitano, *Density of obstacles affects diffusion in adsorbed polymer layers*, ACS Macro Letters, 9 (2020), pp. 318–322.

[84] H. Rost, *Diffusion de sphéres dures dans la droite réelle: comportement macroscopique et équilibre local*, in Séminaire de Probabilités XVIII 1982/83, Springer, 1984, pp. 127–143.

[85] M. P. Rout, J. D. Aitchison, M. O. Magnasco, and B. T. Chait, *Virtual gating and nuclear transport: the hole picture*, Trends in cell biology, 13 (2003), pp. 622–628.

[86] S. D. Ryan, *A model for collective dynamics in ant raids*, Journal of mathematical biology, 72 (2016), pp. 1579–1606.

[87] B. A. Schlake, *Mathematical models for particle transport: Crowded motion*, PhD thesis, Westfälische Wilhelms-Universität Münster, 2011.

[88] M. J. Simpson, B. H. Foy, and S. W. McCue, *Travelling waves for a velocity-jump model of cell migration and proliferation*, Mathematical biosciences, 244 (2013), pp. 98–106.

[89] M. J. Simpson, W. Jin, S. T. Vittadello, T. A. Tambyah, J. M. Ryan, G. Gunasingh, N. K. Haass, and S. W. McCue, *Stochastic models of cell invasion with fluorescent cell cycle indicators*, Physica A: Statistical Mechanics and its Applications, 510 (2018), pp. 375–386.

[90] M. J. Simpson, K. A. Landman, and B. D. Hughes, *Multi-species simple exclusion processes*, Physica A: Statistical Mechanics and its Applications, 388 (2009), pp. 399–406.

[91] J. Smith and A. Martin, *Comparison of hard-core and soft-core potentials for modelling flocking in free space*, arXiv preprint arXiv:0905.2260, (2009).

[92] D. W. Stroock, *Some stochastic processes which arise from a model of the motion of a bacterium*, Zeitschrift für Wahrscheinlichkeitstheorie und verwandte Gebiete, 28 (1974), pp. 305–315.

[93] B. J. Sung and A. Yethiraj, *Lateral diffusion of proteins in the plasma membrane: spatial tessellation and percolation theory*, The Journal of Physical Chemistry B, 112 (2008), pp. 143–149.

[94] A. Surendran, M. J. Plank, and M. J. Simpson, *Spatial structure arising from chase-escape interactions with crowding*, Scientific reports, 9 (2019), pp. 1–12.

[95] P. Taylor, *Stochastic lattice-based models of diffusion in biological systems*, PhD thesis, University of Oxford, 2016.

[96] P. Taylor, C. Yates, M. Simpson, and R. Baker, *Reconciling transport models across scales: The role of volume exclusion*, Physical Review E, 92 (2015), p. 040701.

[97] P. R. Taylor, R. E. Baker, M. J. Simpson, and C. A. Yates, *Coupling volume-excluding compartment-based models of diffusion at different scales: Voronoi and pseudo-compartment approaches*, Journal of The Royal Society Interface, 13 (2016), p. 20160336.

[98] J. P. Taylor-King, B. Franz, C. A. Yates, and R. Erban, *Mathematical modelling of turning delays in swarm robotics*, IMA Journal of Applied Mathematics, 80 (2015), pp. 1454–1474.

[99] K. K. Treloar, M. J. Simpson, and S. W. McCue, *Velocity-jump models with crowding effects*, Physical Review E, 84 (2011), p. 061920.

[100] V. Tyagi, *A non-continuum approach to obtain a macroscopic model for the flow of traffic*, PhD thesis, Texas A&M University, 2007.

[101] R. Tyson, S. Lubkin, and J. D. Murray, *A minimal mechanism for bacterial pattern formation*, Proceedings of the Royal Society of London B: Biological Sciences, 266 (1999), pp. 299–304.

[102] N. G. Van Kampen, *Stochastic processes in physics and chemistry*, vol. 1, Elsevier, 1992.

[103] M. Weiss, M. Elsner, F. Kartberg, and T. Nilsson, *Anomalous subdiffusion is a measure for cytoplasmic crowding in living cells*, Biophysical journal, 87 (2004), pp. 3518–3524.

[104] D. A. Wolf-Gladrow, *Lattice-gas cellular automata and lattice Boltzmann models: an introduction*, Springer, 2004.

[105] S. Wolfram, *Statistical mechanics of cellular automata*, Reviews of modern physics, 55 (1983), p. 601.